

Microstructure Model for Ti-6Al-4V used in Simulation of Additive Manufacturing

Corinne Charles Murgau

Material Mechanics

THESIS FOR DEGREE OF PHILOSOPHY DOCTOR IN ENGINEERING

Microstructure Model for Ti-6Al-4V used in Simulation of Additive Manufacturing

CORINNE CHARLES MURGAU

May 2016

Mechanics of Solid Materials
Department of Engineering Sciences and Mathematics
LULEÅ UNIVERSITY OF TECHNOLOGY
971 87 Luleå, Sweden
Phone number +46 (0)920 491 000

Microstructure Model for Ti-6Al-4V used
in Simulation of Additive Manufacturing
CORINNE CHARLES MURGAU

© 2016 Corinne Charles Murgau

Division of Mechanics of Solid Materials
Department of Engineering Sciences and Mathematics
Luleå University of Technology
Sweden
Phone: +46 (0)920 491 000

Printed by Luleå University of Technology, Graphic Production 2016

ISSN 1402-1544
ISBN 978-917583-579-2 (print)
ISBN 978-91-7583-580-8 (pdf)

Luleå 2016

www.ltu.se

ABSTRACT

This thesis is devoted to microstructure modelling of Ti-6Al-4V. The microstructure and the mechanical properties of titanium alloys are highly dependent on the temperature history experienced by the material. The developed microstructure model accounts for thermal driving forces and is applicable for general temperature histories. It has been applied to study wire feed additive manufacturing processes that induce repetitive heating and cooling cycles. The microstructure model adopts internal state variables to represent the microstructure through microstructure constituents' fractions in finite element simulation. This makes it possible to apply the model efficiently for large computational models of general thermo-mechanical processes. The model is calibrated and validated versus literature data. It is applied to Gas Tungsten Arc Welding -also known as Tungsten Inert Gas welding- wire feed additive manufacturing process.

Four quantities are calculated in the model: the volume fraction of α phase, consisting of Widmanstätten α , grain boundary α , and martensite α . The phase transformations during cooling are modelled based on diffusional theory described by a Johnson-Mehl-Avrami-Kolmogorov formulation, except for diffusionless α martensite formation where the Koistinen-Marburger equation is used. A parabolic growth rate equation is used for the α to β transformation upon heating. An added variable, structure size indicator of Widmanstätten α , has also been implemented and calibrated. It is written in a simple Arrhenius format.

The microstructure model is applied to in finite element simulation of wire feed additive manufacturing. Finally, coupling with a physically based constitutive model enables a comprehensive and predictive model of the properties that evolve during processing.

Keywords: Titanium alloy, Ti-6Al-4V, Welding, Metal deposition, Additive manufacturing, Wire feed, Finite Element Method, Microstructure model, Johnson-Mehl-Avrami-Kolmogorov, Thermally driven

ACKNOWLEDGMENTS

This thesis summarises my doctoral studies carried out at University West (Högskolan Väst, HV), Trollhättan, during the years 2005-2013. During this period I was registered as a graduate student at Luleå University of Technology (LTU), division for Material Mechanics. The work was supervised by Professor Lars-Erik Lindgren at LTU, by Associate Professor Niklas Järvstråt at HV during the years 2005-2009 and by Research Associate Robert Pederson at LTU during the years 2009-2016. An appreciated collaboration with GKN aerospace Sweden AB (Volvo Aero Corporation 2005-2013) throughout this work is to be mentioned.

The work was financed by the European Union through the research project VERDI¹ and the research project AFFIX². The region of Västra Götaland (Sweden) through the project INNSide³ and VINNOVA⁴ foundation through the NFFP project MDReg⁵ are also acknowledged for their financial support. The author would like to thank the research environment Production Technology West at University West for financial support during the years 2008-2012 and 2015-2016.

Professor Lars-Erik Lindgren, and his group, especially Bijish Babu and Andreas Lundbäck, are gratefully thanked for their guidance and collaboration. I wish to express my gratitude to Niklas Järvstråt for his time and support as well as for the advising discussions throughout the first part of this work. I also would like to thank Robert Pederson for all the support and supervision given on the metallurgical field. I appreciated that you stand up when supervision transition were needed. Anna-Karin Christiansson and Mikael Ericsson are thanked for their encouragements and helps along the following up meetings that took me through the end of this work. Thanks to all of you for believing in me more than I do.

Finally, I would like to express my family for their understanding and encouragement. Warm thanks to my friends and colleagues at University West for their technical support as well as for their encouragements throughout this journey. I would also like to express my gratitude to all who have helped me master Swedish language and traditions that became part of me.

Corinne Charles Murgau

Trollhättan, Sweden, May 2016

¹ VERDI: European 6th Framework Programme funded research project "Virtual Engineering for Robust manufacturing with Design Integration" (2002-2006) under contract n° AST4-CT-2005-516046 - <http://www.verdi-fp6.org>

² AFFIX: European 6th Framework Programme funded research project "Aligning, Holding and Fixing Flexible and Difficult to Handle Components" (2006-2010) under contract n° NMP-NI-4-2004-026670- <http://www.affix-ip.eu>

³ INNSide 1-4: Region Västra Götaland 7th Framework programme funded research project (2007-2011). "Innovative svetsning och bearbetning för lättviktsdesign"

⁴ VINNOVA: Swedish Governmental Agency for Innovation Systems - <http://www.vinnova.se/en/>

⁵ MDreg: Swedish VINNOVA Nationella Flygtekniska ForskningsProgrammet funded research project (2009-2013) under contract n° 2009-01330

PUBLICATIONS

The thesis comprises introductory chapters and the five appended papers listed below.

Paper A

Development of a Microstructure Model for Metal Deposition of Titanium Alloy Ti-6Al-4V

Corinne Charles and Niklas Järnstråt

In Proceedings of the 11th World Conference on Titanium (Ti-2007), Kyoto, Japan, 3-7 June 2007

Paper B

Modelling Ti-6Al-4V microstructure by evolution laws implemented as finite element subroutines: Application to TIG metal deposition

Corinne Charles and Niklas Järnstråt

In Proceedings of the 8th International Conference on Trends in Welding Research, Pine Mountain, GA, USA, 1-6 June 2008

Paper C

A model for Ti-6Al-4V microstructure evolution for arbitrary temperature changes

Corinne Charles Murgau, Robert Pederson and Lars-Erik Lindgren

Published in Modelling and Simulation in Materials Science and Engineering, 20(5), 055006

Paper D

Temperature and microstructure evolution in Gas Tungsten Arc Welding wire feed additive manufacturing of Ti-6Al-4V

Corinne Charles Murgau, Andreas Lundbäck, Pia Åkerfeldt and Robert Pederson

To be submitted for publication.

Paper E

Physically based constitutive model of Ti-6Al-4V for arbitrary phase composition

Bijish Babu, Corinne Charles Murgau and Lars-Erik Lindgren

To be submitted for publication.

TABLE OF CONTENTS

ABSTRACT.....	i
ACKNOWLEDGMENTS	iii
PUBLICATIONS	v
TABLE OF CONTENTS	vii

Introductory chapters

1 INTRODUCTION.....	1
1.1 Background.....	1
1.2 Scope, limitations and research approach.....	2
1.3 Structure of the thesis.....	3
2 WELDING AND METAL DEPOSITION.....	5
2.1 Near-net-shape manufacturing and metal deposition.....	5
2.2 Fusion welding processes.....	7
2.2.1 GTAW process information.....	7
2.2.2 LBW process information.....	8
2.3 Considerations for welded titanium alloy fabrication.....	9
2.3.1 Oxygen contamination.....	10
2.3.2 Residual stresses and distortions.....	10
2.3.3 Welding defects	10
3 PROPERTIES, METALLURGY AND MICROSTRUCTURE	13
3.1 Titanium and its alloys	13
3.1.1 Structure	13
3.1.1 Alloying	13
3.2 Microstructure of Ti-6Al-4V titanium alloy.....	16
3.2.1 Morphologies and heat treatments.....	16
3.2.2 Microstructure due to weld thermal cycle	19
3.3 Mechanical properties of Ti-6Al-4V	21
3.3.1 Temperature effects	21
3.3.2 Composition effects	23
3.3.3 Microstructure effects	24
3.3.4 Welding and metal deposition effects.....	25

4	MICROSTRUCTURAL STUDIES OF METAL DEPOSITED Ti-6Al-4V	27
4.1	Temperature cycling due to metal deposition	28
4.2	<i>Qualitative characterisation of microstructure</i>	31
4.2.1	Heat affected region of base plate	31
4.2.2	Prior- β grains in deposited metal	31
4.2.3	Transformed β in the deposited metal	33
4.2.4	Banded pattern	33
4.2.5	Martensite α and massive α	34
4.3	<i>Quantitative characterisation of microstructure</i>	35
4.3.1	Volume fraction of β and α	35
4.3.2	Measurement of α lath thickness	36
5	MICROSTRUCTURE MODEL	39
5.1	Length scales.....	39
5.2	Modelling microstructure evolution.....	39
5.2.1	Statistical models	39
5.2.2	Phase-field models.....	40
5.2.3	Phenomenological models	41
5.3	Transformations diagrams	41
5.4	Transforming isothermal model to varying temperature	42
5.5	Phase transformation modelling.....	44
5.5.1	Diffusional transformations of β to α phases.....	44
5.5.2	Dissolution of α to β phase	45
5.5.3	Martensite and massive transformation	45
5.5.1	Transformation of martensitic α_m to $\alpha+\beta$	46
5.6	Microstructure morphology modelling.....	46
5.6.1	Grain size modelling.....	46
5.6.2	α_w lath thickness	46
5.7	Material input parameters and calibration	47
5.7.1	Equilibrium phase diagram	47
5.7.1	Transformation kinetic parameters for diffusional β to α phases.....	47
5.7.2	Parameters for transformation of α to β phase	49
5.7.3	Martensite transformation parameters	49
5.7.4	Parameters of lath thickness model	50
5.8	Implementation of microstructure model	51
5.9	Microstructure model validation.....	54
6	APPLICATION OF THE MODEL.....	55
6.1	Wire feed additive manufacturing simulation	55
6.2	Coupled microstructure and flow stress models.....	57
7	SUMMARY OF APPENDED PAPERS.....	59
7.1	Paper A	59

7.2 Paper B	59
7.3 Paper C	60
7.4 Paper D	60
7.5 Paper E.....	60
8 DISCUSSIONS AND CONCLUSIONS	63
9 FUTURE WORK.....	65
REFERENCES.....	69

Included Papers

PAPER A.....	81
PAPER B.....	87
PAPER C.....	99
PAPER D	125
PAPER E	143

1 INTRODUCTION

Titanium, and predominantly its alloys, are particularly appreciated in the manufacturing of aero engine components for their attractive, combined properties such as low weight, good strength to density ratio, corrosion resistance (Donachie 2000). Microstructure and material properties of titanium alloys are highly dependent on the thermo-mechanical history of the material. Therefore, understanding of the microstructure evolution during manufacturing processing becomes important when producing high reliability components, such as in the aero engine industry. With the objectives mentioned above, the thesis presents a microstructure model that predicts the microstructure evolution of Ti-6Al-4V subjected to arbitrary thermal histories. It is used in finite element simulations of welding and wire feed additive manufacturing process. A coupling to a physically based plastic flow material model is ultimately proposed.

1.1 Background

Modelling and simulation are becoming appreciated tools in the manufacturing design with the objectives to reduce and complement exhaustive pre-study experiments and costs. Development of modelling tools for microstructure and mechanical properties, here for Ti-6Al-4V, can in a longer term assist in the development of new process parameters and limit the use of physical tests (Boyer and Furrer 2004). Finite Element modelling has been demonstrated to be a powerful technique for simulation of welding and heat treatment processes (Alberg 2005; Järvstråt and Sjöström 1993; Järvstråt and Tjotta 1996; Lindgren 2001a; 2001c). The material model is recognised to be an important factor for accurate simulations (Lindgren 2001b) and it is important to account for the effect of undergoing microstructural changes on material properties.

The starting point of this research was part of the European Union funded research project "*Virtual Engineering for Robust manufacturing with Design Integration*", VERDI. The project included development of production technologies for components by fabrication as an alternative to large one-piece castings in which attachment parts, e.g. bosses and flanges, are usually parts of the casting. There is a potential to reduce cost when choosing to fabricate these components. Figure 1 illustrates the fabrication steps in a virtual manufacturing chain. Then the structure is made up of a combination of small castings, forgings, and sheet metal. They are welded together and features can be added by metal deposition (Short 2009). When it comes to titanium alloys, joining and net-shape manufacturing can be performed using welding technologies, thanks to its good weldability. Since welding induces heat input and temperature variations in the metal, it is vital to understand its influence on component properties to ensure high integrity joints and enable the evaluation of different approaches with respect to robustness and reliability.

INTRODUCTION

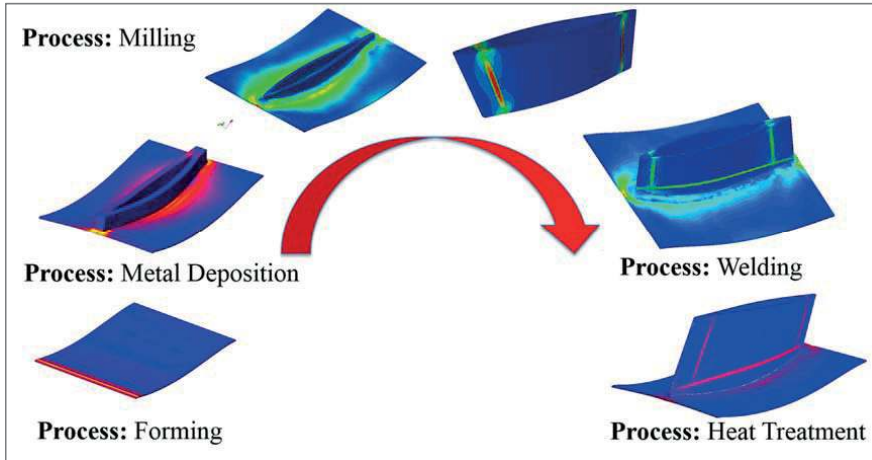


Figure 1. Proposition for virtual fabrication manufacturing chain as alternative to one piece casting.

1.2 Scope, limitations and research approach

The aim of this work was to develop a model to predict the microstructure evolution of the titanium alloy Ti-6Al-4V applicable for general thermal histories and particularly those in welding and metal deposition. The model should calculate relevant quantities that can be useful in a physically based flow stress model. The microstructure description has to be sufficiently detailed to give useful information in the evaluation of the material properties but still be manageable when simulating manufacturing processes for large components.

Given the discussion above the research questions were formulated as:

What are the most important microstructure variables needed to describe changes in flow stress of the titanium alloy Ti-6Al-4V?

How should validated models for the evolution of these variables be formulated and implemented in order to be feasible for large-scale simulations?

The scope is limited to account for thermal driving forces.

To answer the formulated research questions, the following stages have been followed throughout the work. First a literature study as well as evaluation of experimental samples was performed to acquire sufficient understanding of Ti-6Al-4V microstructure and phase transformations during temperature cycling in order to answer the first research question. The second research question corresponds to the larger amount of work in the thesis. The literature review contributed to the selection, development and implementation of the models. They

INTRODUCTION

were calibrated as well as validated by use of experimental work in literature as well as experiments executed during the course of the research.

1.3 *Structure of the thesis*

This thesis consists of introductory chapters followed by five appended papers.

The research presented can be divided into four Research Stages (Rs): (Rs1) the preparatory phase, (Rs2) the development phase, (Rs3) the application phase and (Rs4) the concluding phase.

- (Rs1) The first three chapters relate to the preparatory and subject understanding stage. The *Introduction*, Chapter 1, describes the background to the thesis and contains the overall description and motivation of the research. A presentation of the *welding and metal deposition* is then given in Chapter 2. *Properties, metallurgy and microstructure* review of the considered titanium alloy Ti-6Al-4V are addressed in Chapter 3 where a general presentation of the titanium alloys is first given. Microstructural studies of Ti-6Al-4V metal deposited parts are analysed, interpreted and discussed in Chapter 4.
- (Rs2) *The microstructure model* is described and explained in Chapter 5. Methods for the microstructure modelling are presented and the individual chosen sub-models are clarified. The validation of the microstructure model is eventually discussed.
- (Rs3) Application of the model is developed in Chapter 6. The microstructure model is used in simulation of the wire feed additive manufacturing process and coupled to a flow stress model.
- (Rs4) The concluding phase contains the final analysis and conclusions of the appended papers. *Summary of appended papers* together with the author's contributions are given in Chapter 7. Finally, the usefulness and generality of the results are discussed in the *Conclusion* chapter 8 followed by some suggestions for future work in Chapter 9.

The five appended papers in the second part of the thesis reflect the progression of the work as illustrated in Figure 2. **Paper A** initiates Rs1. The microstructure in deposited material has been quantitatively studied and analysed in **Paper B**. This supplements the Rs1 and initiates Rs2 & Rs3. **Paper C**, presents the completed model and its calibration, large part of Rs2. **Paper D** contains the evaluation of the microstructure model applied to metal deposition more thoroughly with respect to the microstructure. It contributes to Rs2 & Rs3. Finally, **Paper E** includes the coupling of the microstructure model to the flow stress model adding to Rs3.

INTRODUCTION

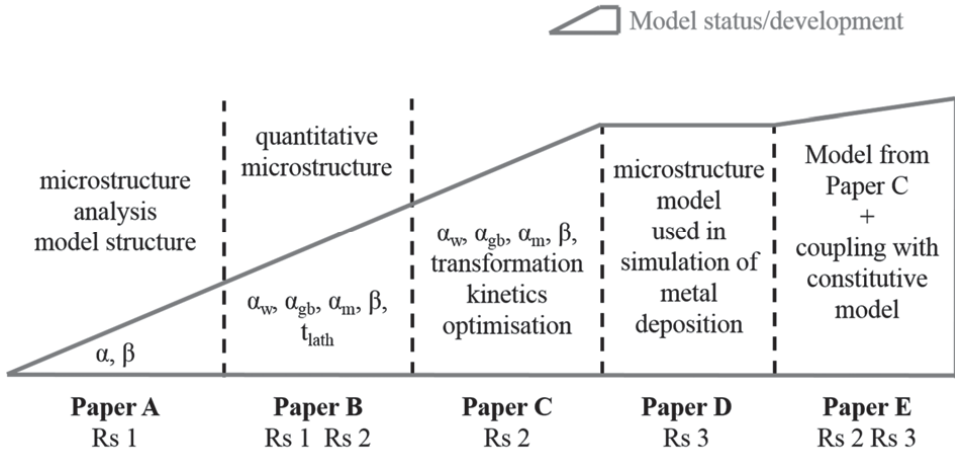


Figure 2. Illustration of the progressive development aiming to the final purpose of the work. Relation to Research stage (Rs).

2 WELDING AND METAL DEPOSITION

There are several processing technologies used in sequence in the fabrication of components. The manufacturing processes of welding and its net-shape fabrication application are selected in this study to support and apply the development of the microstructure model. This net-shape fabrication refers to metal additive manufacturing process for which research and new emerging technologies are continuing (Brice 2011; Frazier 2014; Mazumder et al. 2000). The notation *metal deposition* is used in the thesis. It is classified as Directed Energy Deposition (DED) in ASTM F2792. The DED process, when combined with wire, gives the highest build rates (Ding et al. 2015). DED is particular convenient when adding features to large components.

Because a large part of the microstructure analysis has been studied on metal deposited samples, near-net-shape manufacturing including metal deposition, are briefly presented in Section 2.1. Metal depositions are direct applications of the welding technology. Therefore a short survey of the welding processes, fusion welding process Gas Tungsten Arc Welding (GTAW) and Laser Beam Welding (LBW) that are used for the fabrication of the studied samples, is given in Section 2.2. Details about some typical problems and defects associated with the presented welding methods with Ti-6Al-4V are also pointed out in Section 2.3, since the underlying scope of the thesis is to obtain methods to avoid them already in the design stage.

2.1 *Near-net-shape manufacturing and metal deposition*

There is a strong need for efficient, light and flexible manufacturing techniques. Near-net-shape manufacturing is one alternative (Mendez and Eagar 2001). Complete structures or components may be manufactured directly using near-net-shape approach. A large among of nomenclatures and techniques are today associated with near-net-shape manufacturing; alternatively called Additive Manufacturing (AM), free form fabrication, 3D printing, etc. The main driving forces are cost reduction and flexibility in both manufacturing and product design (Frazier 2014). Better understanding and materials qualifications are still needed (Seifi et al. 2016).

The metal can be supplied in the form of powder or wire and a power source is used to melt it. Welding technology such as laser welding or arc welding is used for this purpose. Most equipment commercially available today uses special nozzles to distribute powder into a laser beam to be melted; Direct Light Fabrication (DLF) (Qian et al. 2005), Selective Laser Melting (SLM) (Bertrand and Smurov 2007), Laser Metal Deposition Shaping (Zhang et al. 2007), and the LENS-system (Wang and Felicelli 2006; Wu and Mei 2003). Robotised Laser Metal wire Deposition (RLMwD) (Heralic et al. 2008), Shaped Metal Deposition (SMD) (Escobar-Palafox et al. 2011; Rooks 2005), Wire and arc additive manufacturing (WAAM) (Wang et al. 2012) or Robotised TIG Metal wire Deposition (RTMwD) are examples of wire-feed metal deposition processes. The deposition efficiency and the cleanliness are increased considerably if wire is used instead of powder (Syed et al. 2005). Quality and accuracy of wire-feed metal deposition are today challenges (Ding et al. 2015; Åkerfeldt 2016)

Metal wire deposition, used in this study, is one of the metal deposition techniques under development in the aero engine industry notably for titanium alloy parts (Escobar-Palafox et

WELDING AND METAL DEPOSITION

al. 2011; Heralic et al. 2010). Metal is deposited as weld beads side-by-side and layer-upon-layer in a desired pattern to build a complete component or add features on a component. The solidified metal gives directly the near-net-shape part. The technology is flexible in that it provides a means for product development, manufacturing of components or specific geometries of components, repair of tools and components, rapid fabrication of prototypes, or for unique tailoring of standard base products. See Figure 3 for potential applications of metal deposited geometries added on an aircraft engine structure.

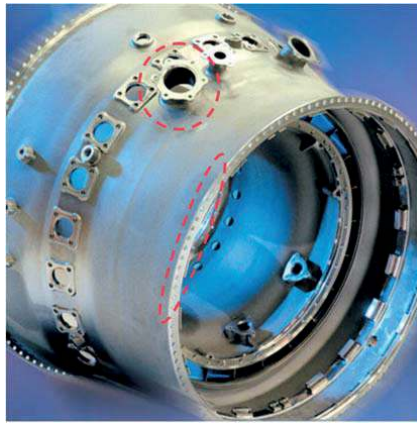


Figure 3: Potential RTMwD/RLMwD geometries, bosses and flanges, on aero engine component (Courtesy Volvo Aero Corporation, 2008).

GTAW metal wire deposition development is focusing on the fabrication of simple features like the ones presented in Figure 4. Simulation of the process is expected to strengthen the understanding and thereby guide the choices for better on-line control of the metal deposition technology. The same reasoning is valid for the development with Laser heat source. This thesis focuses on microstructure simulation during this repeated heating and cooling process.



Figure 4: Different geometries built with GTAW metal wire deposition.

2.2 Fusion welding processes

Several different methods for continuous fusion welding of metal exist based on fundamentally different physical phenomena. They can be applied to different metals and situations (Connor 1987). They all rely on a heat source moving relative to the work piece part to be joined (the work piece can also move relative to a fixed heat source). The heat source heats the metal above melting point creating a weld pool. The weld seam is obtained after cooling and solidification. Sometimes the welding also includes adding metal in the form of powder or wire, which is melted into the weld pool. The heat source varies in intensity depending on the technology (Mendez and Eagar 2001). Focused high power density beam like in LBW will give a “stronger” weld, however the welding is recognized to be more flexible and less costly by using GTAW (Mendez and Eagar 2001; Short 2009). LBW and arc welding such as GTAW are commonly used in the fabrication of titanium and titanium alloy structures (Donachie 2000; Short 2009).

2.2.1 GTAW process information

GTAW, also called Tungsten Inert Gas (TIG) welding, is a process where an electric arc is created between a non-consumable tungsten electrode mounted in a weld torch and a metallic work piece (Weman 2003). The arc is produced by electric current conducted from the electrode tip to the work piece through an ionized gas. The effect of the arc is a local heating of the base metal creating a weld pool by fusion of part of the work piece and, when used, the filler metal. The joint is formed as the metal solidifies.

An advantage with GTAW is that it is a stable and flexible method giving good joint integrity. The cost of the weld equipment is also comparatively low. A down-side is that the large spread of the heat source gives limited mechanical properties due to less controlled and uneven heat treatment of the material. This may cause problems in critical applications (Mendez and Eagar 2001). Welding at higher speeds reduces the specific heat input, increasing the cooling rate, thus changing the metallurgical response giving a finer microstructure. Better properties are thus potentially obtainable through robotic control of welding thanks to the possible increase in welding speed. This robotised GTAW process is discussed below.

A schematic illustration of a GTAW system is given in Figure 5. The system consists of a weld torch supplied by a current controlled power source. A shielding gas can be used and conducted through the weld torch. The filler metal is added by a separate wire feeder. The wire is melting when approaching the arc and feeds the weld pool. A picture of the robotised GTAW setup used to manufacture part of the studied samples is shown in Figure 6. The welding is here performed in a chamber with a protective atmosphere to avoid contamination of the titanium alloy when heated.

WELDING AND METAL DEPOSITION

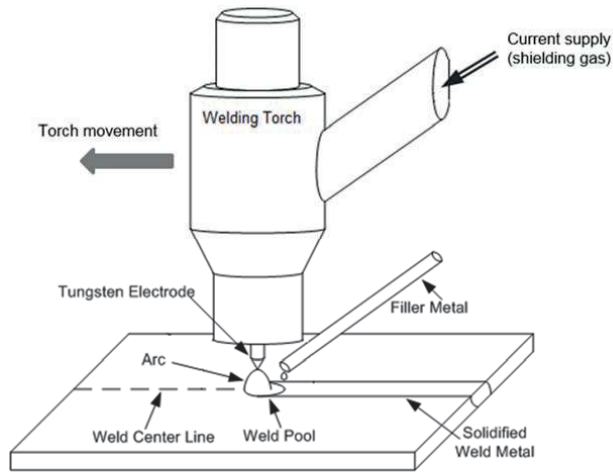


Figure 5. Schematic illustration of GTAW system with filler metal.

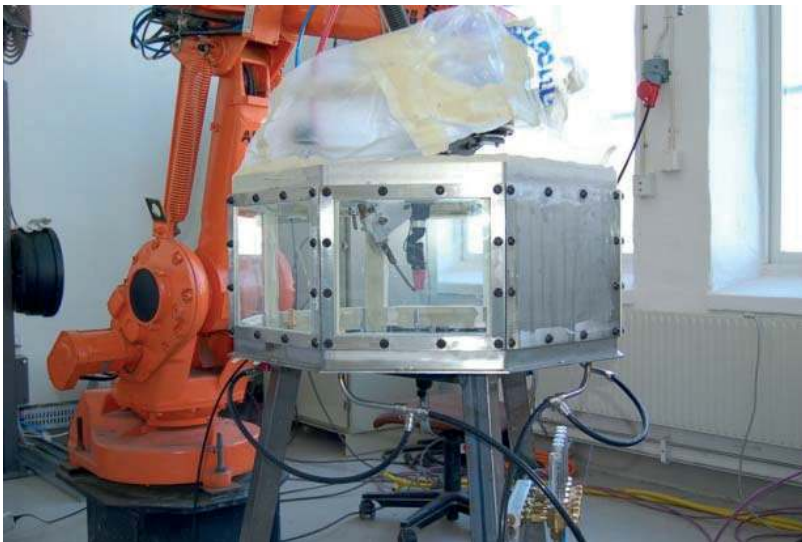


Figure 6: GTAW setup with a robot controlled motion of the heat source, and filler metal. The chamber is filled with an argon gas protective atmosphere.

2.2.2 LBW process information

LBW is a process where the heat input is obtained by a concentrated coherent light beam with a specific wavelength (Duley 1999). The word LASER stands for Light Amplification by Stimulated Emission of Radiation. The energy distribution across the beam is generated by photon oscillation within an optical cavity (arrangement of mirrors that forms a standing wave

WELDING AND METAL DEPOSITION

cavity resonator for light waves) resulting in specific output beam energy patterns. The beam energy is then concentrated and conveyed by optical elements (mirrors, lenses, flexible optical fibres) to a small size focal spot. The focal spot is targeted upon the material surface to be welded to produce a high-power density. At the material surface the controlled electromagnetic (light) energy melts the metal, and may also partly vaporizes it. Two laser systems are used to produce the samples investigated in this thesis: an Nd:YAG lamp-pumped laser and a fibre laser. They both have the flexibility to permit the use of fibre to transmit the beam at the end of the welding tool. Both laser sources are, with their operating wavelength about $1\ \mu\text{m}$, well suited for welding of the material evaluated. LBW can be realized in two modes, namely conduction and keyhole. The conduction mode, for which the weld is performed in the liquid state, is used in this study. LBW power density is about ten times the power density in GTAW; about $100\ \text{kW}/\text{cm}^2$ for LBW against $10\ \text{kW}/\text{cm}^2$ for GTAW. The high power density of LBW has consequently the advantage of resulting in narrow, deep welds. The quality of the weld is of higher accuracy and smaller distortions are observed. A drawback is the high investment cost.

The laser system welding setup is shown in Figure 7. The laser beam is directed by mirrors and optical fibres. The high-power density is conveyed by a fibre, and a welding head focuses the beam onto the work piece. Like with GTAW, the weld is made in a protective chamber as can be seen in the setup presented in Figure 7.

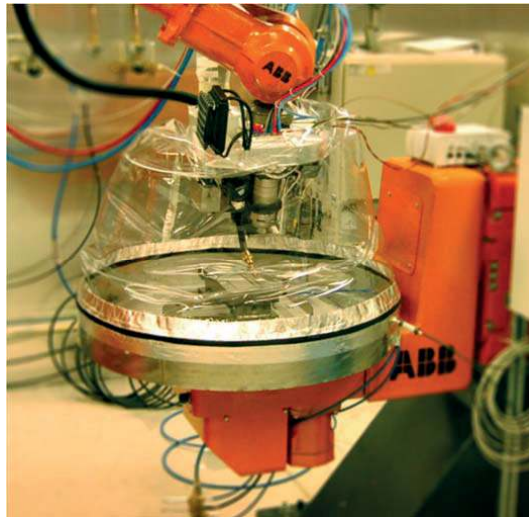


Figure 7. Fibre laser welding setup.

2.3 Considerations for welded titanium alloy fabrication

Several problems in welding can cause poor joint performance and/or deteriorate the structural integrity of a part. Commonly weld related characteristics such as residual stresses and distortions, and defects are discussed below. There is an interest in simulating the manufacturing process already at the design stage in order to determine fixturing or welding

WELDING AND METAL DEPOSITION

parameters to minimise defects or distortions/residual stresses. Ti-6Al-4V is a metal alloy with good weldability. Post-weld lower ductility can however be caused by phase transformations (Donachie 2000).

2.3.1 Oxygen contamination

The strong chemical affinity of titanium for Oxygen leads to a natural protecting oxide layer on a clean surface. At temperatures exceeding around 500°C the oxidation resistance decreases quickly (Donachie 2000). Fusion welding heats the metal to high temperatures around the weld pool. The metal is thus highly susceptible to embrittlement due to interstitial dissolution of Oxygen (Robinson et al. 2002). Therefore, welding must be carried out in protected atmosphere, inert or vacuum environments are required. In this study all samples were welded in a protecting chamber filled with inert gas (Argon) and the Oxygen level was maintained below 20 ppm.

2.3.2 Residual stresses and distortions

Residual stress and distortion are inevitable in welding processes due to the uneven heating/cooling and changes in material properties. The magnitude of these effects depends primarily on the thermal energy contribution of the welding process, typically expressed as input energy per unit length of weld. The interaction between the welded work pieces and the fixture can add significantly to these effects. Usually a highly restrained weld causes large residual stresses whereas less restraint gives more residual deformations. The ideal case would be to have no restraint and an initial shape of the component so that the residual deformations give the wanted shape.

Special post weld heat treatment procedures can be used to mitigate residual stress. A stress-relief operation consisting in holding the piece at low temperatures (480-650°C for Ti-6Al-4V) for a certain time (1-4 hours for Ti-6Al-4V) is often done knowing that such treatment does not affect strength or ductility in Ti-6Al-4V alloy (Donachie 2000).

2.3.3 Welding defects

Instead of weld defects, the term discontinuities is also used (Weman 2003). These include, for example, porosity, incomplete fusion or cracks that are observed in the resulting welds. These problems have a direct negative influence on the mechanical properties of the welded structure, e.g. strength and fatigue. Some of the defects that may be encountered with Ti-6Al-4V are mentioned below.

Porosity is caused by gas bubbles in the weld metal and results from chemical reactions and fluid flow that occur during welding. This discontinuity is caused by e.g. insufficient or contaminated shielding gas coverage, base and/or filler metal contamination. The negative influence of pores is essentially that they reduce the fatigue strength of the weld.

Incomplete fusion occurs when the welding heat does not penetrate the entire thickness of the weld joint. Defective penetration is mainly caused by too low heat input, too high travel speed, incorrect torch or beam angle, variations in joint gap or abrupt changes in the weld geometry. Burn-through, in turn, is caused by excessive heat input. Both phenomena result in poor joint performance, since the joint geometry and strength will degrade. These discontinuities are fatal; sometimes they initiate fatigue cracks, requiring corrective actions.

WELDING AND METAL DEPOSITION

Cracking in the weld joint is categorized as either hot cracking, also called solidification cracking, or cold cracking, also known as contamination cracking. Solidification cracks occur while the weld bead is in the so-called mushy zone between the liquidus and solidus temperatures and is a function of chemical composition. Fortunately the single-phase mode of solidification of Ti-6Al-4V which does not have low-melting point eutectics in its phase-diagram saves the alloy from hot cracks (Donachie 2000). Cold cracks resulting from atmospheric contamination can occur in Ti-6Al-4V because its reactivity increases rapidly above 500°C. Cracks will rapidly cause failure of the weld when subjected to the stresses resulting from the welding.

3 PROPERTIES, METALLURGY AND MICROSTRUCTURE

The titanium in consideration in this thesis is the Ti-6Al-4V alloy. It is the most commonly used titanium alloy in the aero engine industry (Leyens and Peters 2003). However, the microstructure that forms during process route history such as with welding or metal deposition is varying and complex. Fundamental understanding of the formed microstructures during processing is a prerequisite in order to model the static and transient behaviour of the microstructure. This chapter is devoted to necessary understanding of what is needed for the development of a microstructure model presented in Section 4.3.

3.1 Titanium and its alloys

From the today extracted titanium ore, purified and transformed to titanium oxide, only 5 to 10% is further processed to metal form (Leyens and Peters 2003). Titanium in its metal and metal alloys form have 60 years of modern industrial practice since its commercialisation started in 1948. Since then titanium alloys have been key metals for the aircraft industry. 50 to 70% of the titanium and titanium alloys are used by the aero industry. Titanium alloys have high mechanical properties for a light weight, which places them before aluminium alloys or steel alloys when considering the specific properties to weight ratio (Leyens and Peters 2003). Despite their relatively high price, they are used in more diverse applications such as in chemistry and medicine, where their corrosion resistance in a wide range of environments and biocompatibility properties are appreciated.

3.1.1 Structure

In pure titanium two elementary crystal structures are found depending on the temperature, namely alpha (α) and beta (β) shown in Figure 8. The α phase has a hexagonal close-packed (hcp) structure and is the stable phase at low temperature. When heating, the allotropic transformation α to β occurs at around 882°C. This transformation temperature is named the β -transus temperature, denoted T_{β} . The β phase has a body-centred cubic (bcc) structure and is stable at high temperatures up to the melting temperature at around 1725°C. (Donachie 2000; Leyens and Peters 2003)

3.1.1 Alloying

The addition of alloying elements leads to a mixed α + β field in the alloy phase diagram, as indicated the third column of Table 1. These elements dissolve in titanium either as interstitial elements when they have small radii or by solid solutions substitution when they have large radii. The elements have different impact on the phase diagram depending on their stabilizing effect. Some alloying elements are α stabilizers expanding the α phase region and thereby raise the α ↔ β transformation temperature, this is shown in the phase diagram to the right in Table 1. β stabilizers promote the β phase and lower the β -transus temperature. β -isomorphous stabilizers stabilize the phase β at room temperature by forming a continuous solid solution with the β phase, see diagram in Table 1. β -eutectoid stabilizers introduce the intermetallic compound TiX by eutectoid transformation, see corresponding phase diagram in Table 1. Other elements are considered having a neutral effect on the structure but promoting some mechanical properties as stated in Table 1. (Boyer et al. 1994; Donachie 2000)

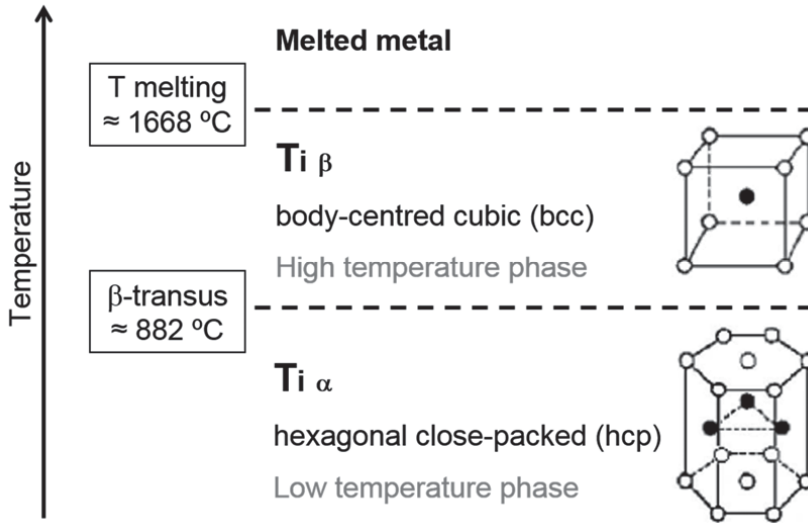


Figure 8. Schematic illustration of titanium phases and principal temperatures.

Titanium alloys are classified according to its phase composition at room temperature, α alloys, β alloys and near- β alloys, $\alpha+\beta$ alloys.

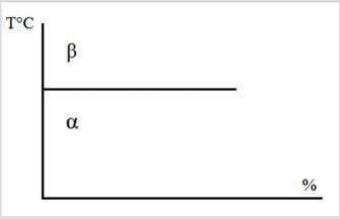
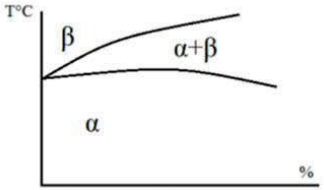
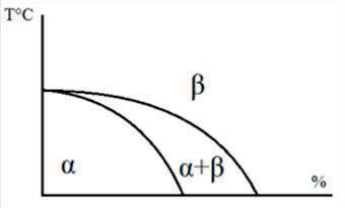
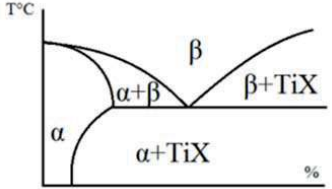
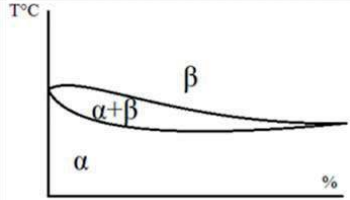
α alloys have almost 100% α phase at room temperature and contain a majority of α stabilizer elements in relatively large amount. The α stabilizer Aluminium is a substitute element present in most of these alloys. They have a limited concentration of β stabilizers. The alloys are generally not responding to normal heat treatments because only restricted β phase content can be reached. For the same reasons they have intrinsically good weldability. However the hexagonal close-packed structure of the α phase make them difficult to cold work.

β alloys and near- β alloys are principally made of metastable β phase. On the contrast to the α alloys, they are rich in β stabilizers and reduced in α stabilizers. They have excellent forgeability and respond well to cold working. The metastable β phase has a tendency to partially transform to $\alpha+\beta$ structure with long time (or aging heat-treatment) or when cold working. The finely dispersed particles of α formed in the β matrix can be used for room temperature strengthening of the alloy.

$\alpha+\beta$ alloys contain at least one α stabilizer and one β stabilizer. These alloys have a mixture of α phase and β phase microstructure at room temperature. Their microstructure can be optimised by using the right thermo-mechanical treatments giving a higher mechanical strength. Their weldability although suitable is limited by the metallurgical transformation induced by temperature cycles. The titanium Ti-6Al-4V studied in this work is part of the $\alpha+\beta$ family alloys.

PROPERTIES, METALLURGY AND MICROSTRUCTURE

Table 1. Effects and schematic variation of the phase diagram for common alloying elements used in titanium (Lütjering and Williams 2003).

Effect on structure	Alloying elements	Corresponding schematic phase diagram as function of the alloying element %
Pure Titanium	-	
α stabilizer	Al, O ₂ , N ₂ , B, C	
β -isomorphous stabilizer	Mo, V, Nb, Ta	
β -eutectoid stabilizer	Si, Mn, Fe, Cr, Co, W, Cu, H ₂	
Neutral (α and β strengthener) (improves creep resistance)	Zr Sn	

3.2 *Microstructure of Ti-6Al-4V titanium alloy*

Ti-6Al-4V titanium alloy is the most commonly used titanium alloy (Donachie 2000). The notation indicates that it has six weight % Aluminium and four weight % Vanadium. It was introduced in the 50's and can be used in applications where the working temperature is below 300°C (Eylon et al. 1984). The alloying with Aluminium (Al) stabilizes the α phase and Vanadium (V) stabilizes the β phase. The equilibrium microstructure mainly consists of α phase with some retained β phase at room temperature. Belonging to the $\alpha+\beta$ alloy, a wide variety of mixture $\alpha+\beta$ microstructure can be obtained depending on the alloy processing history and thermal treatment. It makes it possible to obtain better mechanical properties through thermal or thermo-mechanical processing that controls size, shape and distribution of both α and β phases (Smith 1981). More details about the microstructure effects on the mechanical properties are found in Section 3.3.3. The β -transus temperature, above which only β phase exists, is around 995°C for Ti-6Al-4V. The fusion temperature of the alloy is in the vicinity of 1660°C and the vaporisation temperature is in the surrounding of 3285°C.

3.2.1 Morphologies and heat treatments

During **heating**, the α phase transforms into β phase until the phase content reaches 100% of β for temperatures above the β -transus. If the heating rate is sufficiently low, the transformation $\alpha+\beta\rightarrow\beta$ is following the thermodynamically equilibrium, and the α content will decrease to be zero when the β -transus temperature is reached, Figure 9. If the heating is more rapid, or extremely rapid like in welding, the transformation is not following the expected equilibrium diagram line. The dissolution of the α phase occurs at higher temperatures moving the equilibrium curve to the right as shown in Figure 9.

Depending on the phase field from which the alloy is cooled down and the cooling rate, various microstructures at different microstructural scales are formed.

If the alloy is **rapidly cooled from the β phase field**, martensite α (α_m) forms by martensitic transformation directly from the β phase. The α_m phase has an acicular appearance with small needles as seen in Figure 10 a). It can be noticed that α_m phase has the same chemical composition as β phase and has a crystalline structure which is similar to α phase. α_m is thus a non-equilibrium phase at room temperature and can recover to a ($\alpha+\beta$) structure when the sample is held at medium high temperature.

By **slower cooling rates from the β phase field**, the α formation is controlled by nucleation and growth mechanisms giving the possibility for several morphologies to form depending on the cooling rate (Smallman and Bishop 1999). For fairly rapid cooling, which is the case after welding, the transformation $\beta\rightarrow\alpha+\beta$ is moved from the alloy equilibrium and the dissolution of the β phase takes place at lower temperatures than the equilibrium, see out of equilibrium curve during cooling in Figure 9. The obtained microstructure typically consists of α lamellar structure with an increased lamellae size and thickness for slower cooling rate. The lamellae are frequently found similarly aligned to form “colonies”, as in Figure 10 b). A small amount of retained β phase, enriched in Vanadium (Katzarov et al. 2002, Fig. 1), is present in between the α lamellae. This microstructure is commonly named as “Widmanstätten” microstructure. A “basket weave” microstructure can likewise be used to describe a thinner variant of Widmanstätten structure. In the continuation of the thesis, the denomination of Widmanstätten is used for referring to these structures. In particular

PROPERTIES, METALLURGY AND MICROSTRUCTURE

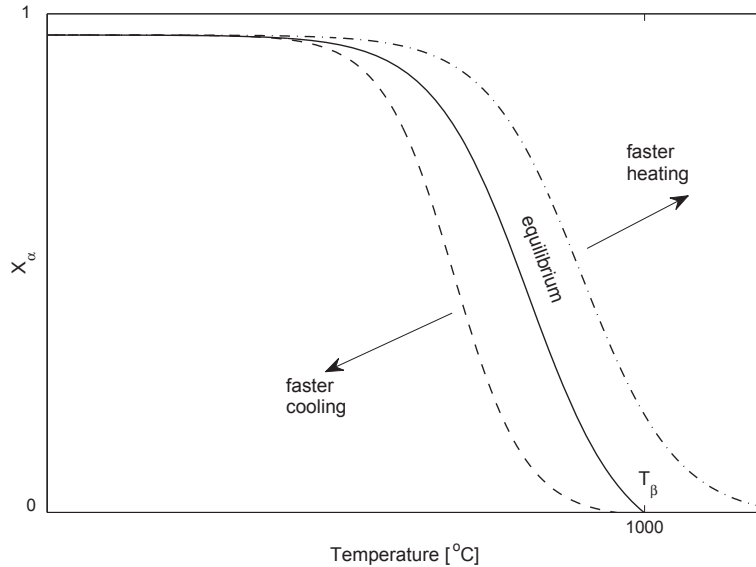


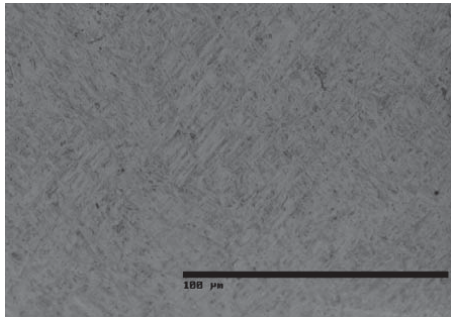
Figure 9. Ti-6Al-4V α/β equilibrium phase diagram. Out of equilibrium curves for $\alpha+\beta\rightarrow\beta$ for ‘fast’ heating and $\beta\rightarrow\alpha+\beta$ for ‘fast’ cooling.

conditions at moderately slow cooling rates and directly when the temperature drops below the β -transus temperature, α phase can first nucleate and grow in the prior β grain boundaries. This α phase, called grain boundary α , marked in Figure 10 c), has an allotriomorph crystal structure.

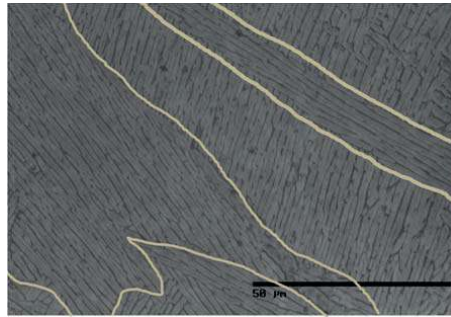
If the alloy is **heated into the $\alpha+\beta$ field and cooled before reaching the β field**, the final microstructure will depend on several factors: the initial microstructure before heating, the heat treatment conditions (heating, holding temperature and holding time at temperature) and the cooling conditions. The initial microstructure can be retained, or increased in size by grain growth when very slow cooling is applied. By faster cooling, new grains can also nucleate.

Even though only thermal effects on microstructure are of concern in this work, the association of thermal and mechanical loads are known to give important microstructure features and therefore shortly mentioned. Further $(\alpha+\beta)$ microstructures, formed during thermo-mechanical treatments, are found in Ti-6Al-4V. Hot working or heat treatment on highly deformed material structures breaks the α lamellae which recrystallize in spherical α primary (α_p) nodules to obtain so-called equiaxed morphology, Figure 10 d). In a similar manner bi-modal or duplex microstructure, seen in Figure 10 e), can be obtained by specific thermo-mechanical treatment under processing (Lütjering 1998; Lütjering and Williams 2003).

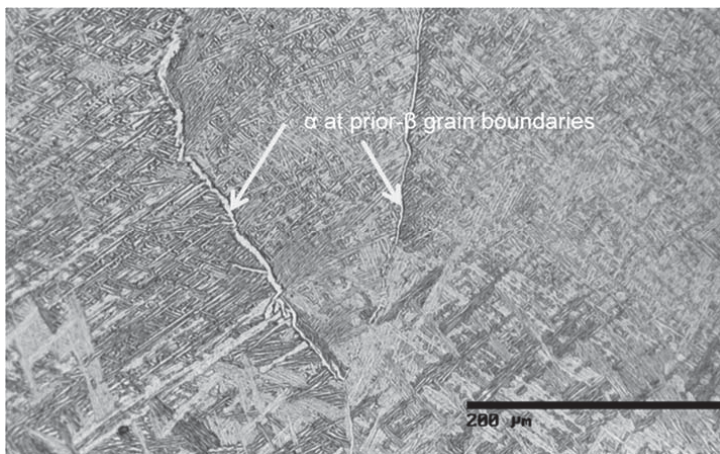
PROPERTIES, METALLURGY AND MICROSTRUCTURE



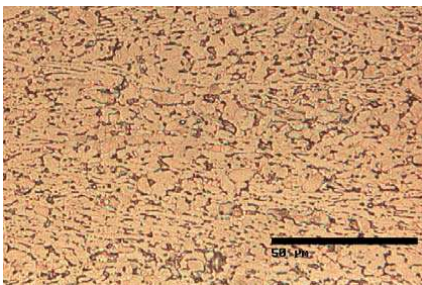
a) Martensitic α microstructure



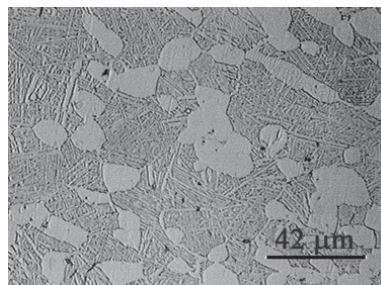
b) Widmanstätten microstructure α colony (marked lighter boundary)



c) continuous α at prior- β grain boundary (arrow)



d) Equiaxed microstructure consisting of more than 90 % primary α (α_p)



e) Bi-modal microstructure consisting of α_p surrounded by transformed α (Widmanstätten structure) of forged Ti-6Al-4V

Figure 10: Optical micrograph of Ti-6Al-4V showing variety of microstructures obtained after different thermal histories.

3.2.2 Microstructure due to weld thermal cycle

Thermal and thermo-mechanical processes determine the microstructure of titanium alloys. Welding as well as metal deposition are examples of such thermal processes that affect the microstructure. The material is subjected to first heating and then cooling in both the substrate and the added metal, in metal deposition this repeats several times. As a result the original microstructure in the base metal is modified in a region close to the weld. This region is usually referred to as the Heat Affected Zone (HAZ). It is conventional in steels to divide the HAZ into sub-zones, and those principles can easily be applied to other metals (Easterling 1993).

Ti-6Al-4V weld shows a progressive variation in the microstructure and sub-zones can be distinct locally depending on the thermal history underwent. The welding metallurgy for the studied alloy is detailed in the following. The schematic drawings in Figure 11 are proposed based on the physical metallurgy of welding by Easterling (1993), a general fusion weld analysis of titanium in Lütjering and Williams (2003), the microstructure investigation in Brandl et al. (2011a), and own microstructure analysis and modelling.

The **Fusion Zone (FZ)**, or solidified weld, is situated in the centre of the joint, Zone 1 in Figure 11. Welding involves melting and solidification (or resolidification of the base metal) of this zone. The transitory liquid state, at which zone 1 has been at one stage of the welding process, is also called weld pool during welding. The solidification takes place when the heat source is extinguished and/or when the welding heat source is remote from the area. β transformed microstructures are consequently composing this zone. Fully lamellar ($\alpha+\beta$) microstructure with potentially α martensite are observed in prior- β grains of large and columnar shapes.

A **solid-liquid transition zone**, for which the temperature reached a peak between solidus and liquidus of the metal, makes the liaison between the FZ and the non-melted metal during welding. In the case of alloys, the effect of a partial melting in between the solidus and liquidus phases may be observed. The solid-liquid transition in Ti-6Al-4V (marked between zone 1 and zone 2 in Figure 11) is usually not observed thanks to the quite low concentration of impurities.

Beyond the transition zone, the base metal which, undergone the thermal cycle from the welding, shows microstructure changes from the original state. This **Heat Affected Zone (HAZ)**, Zones 2-4 in Figure 11, has a different size depending on the intensity of the welding heat source and the welding parameters, such as the welding speed. The metal which, did not reach the liquid state, has been heated either to the β phase field or to the $\alpha+\beta$ phase field. The HAZ directly adjacent to the FZ, sub-zone 2 in Figure 11, exhibits β transformed microstructures and properties considering that the peak temperatures were above the β -transus temperature. The prior- β grains are smaller than in the FZ and fully lamellar ($\alpha+\beta$) microstructure organised in colonies are observed.

Sub-zones 3 and 4 in Figure 11 represent the region where the peak temperature is below the β -transus temperature although it is still high enough to alter the base metal microstructure. Depending on time and the peak temperature reached, primary α (α_p from previous thermo-mechanical process) decreases to the benefit of the lamellar ($\alpha+\beta$) microstructures fraction that is increased in sub-zone 3. With peak temperature further above from the β -transus temperature, sub-zone 4 have a similar to the base plate microstructure with slightly thickened

PROPERTIES, METALLURGY AND MICROSTRUCTURE

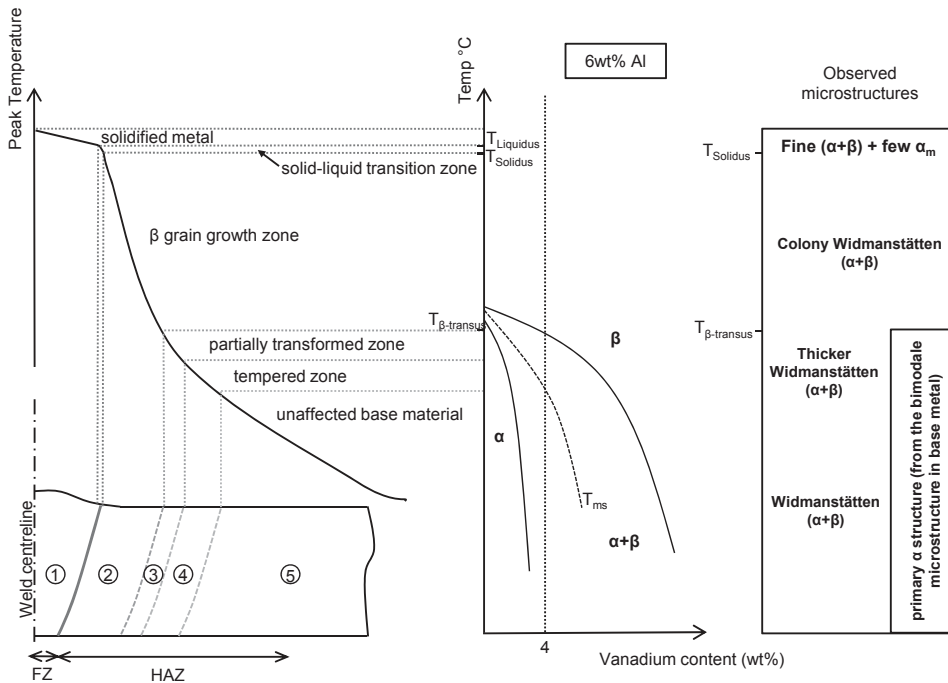


Figure 11. Schematic diagram of the various microstructural sub-zones of the heat-affected zone approximately corresponding to the alloy Ti-6Al-4V indicated on the pseudo-binary (Ti-6Al)-V equilibrium phase diagram.

lamellar matrix. Notice that the extent of the HAZ and its sub-boundaries is difficult to determine for Ti-6Al-4V as the microstructure transitions are smooth.

Further away from the weld centre line, Zone 5 in Figure 11, is the unaffected **base material** microstructure.

Similar variations in the microstructure as for welding are induced by metal deposition with wire (Brandl et al. 2011a). Figure 12 shows an example of such microstructure. Typical prior- β columnar grains are observed from the FZ up to the top of the deposited weld bead following the heat flow direction. Notice that the deposition of several layers will be added to the FZ. Appreciable β grain growth also occurred in the near-HAZ directly adjacent to the weld fusion line showing an equiaxed grain structure. The heat flow during weld solidification determines the size and shape of the grains as will be seen in the metal deposited microstructure study presented in section 4.

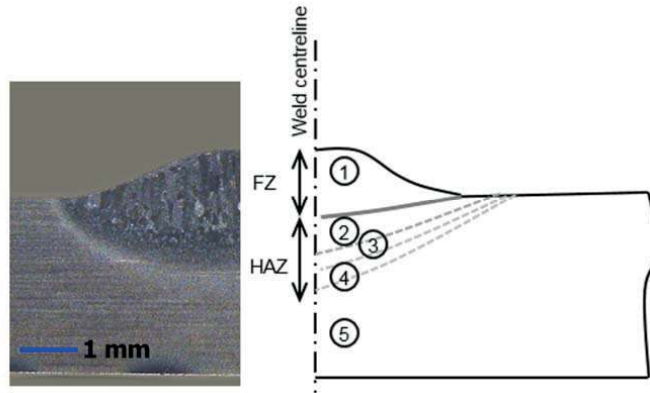


Figure 12. Photo (left) and schematic diagram (right) of the various microstructure sub-zones of the heat affected zones when metal deposited on plate (cross section perpendicular to weld direction). Sub-zone numbers correspond to the microstructure discussion in Figure 11.

3.3 Mechanical properties of Ti-6Al-4V

Ti-6Al-4V is appreciated for its good mechanical properties. However, the variations of the properties with temperature and microstructure is a modelling challenge. These dependencies make the properties a function of the total process history. Some mechanical properties of the alloy at room temperature are summarised in Table 2 from Donachie (2000).

3.3.1 Temperature effects

Metals have a general tendency to soften with increasing temperatures (Smallman and Bishop 1999) without exception for Ti-6Al-4V. The Young's modulus decreases drastically with the temperature as can be observed in Figure 13. The material ductility increases with temperature, see in Figure 14. Strain rate sensitivity is also observed in the stress-strain curves Figure 14. For stress-strain curves at lowest testing temperatures, plastic flow occurs once the yield strength has been exceeded. It can be noticed that, avoiding the fact the curves has been processed to remove the noise from testing, the transition to plastic range is getting more gradual with increased testing temperatures. A regime of flow softening (smooth curve drop) was observed, following yielding and limited hardening, for the higher investigated temperatures (see Figure 14). A near-steady state flow is reached at large strains ($\geq 0,5$) for the highest testing temperatures. Semiatin and co-workers (Semiatin and Bieler 2001a; Semiatin et al. 1999; Shell and Semiatin 1999) mentioned that flow softening behaviour is a consequence of several effects such as the deformation heating effect but also microstructure and texture effects.

PROPERTIES, METALLURGY AND MICROSTRUCTURE

Table 2. Selected mechanical properties at room temperature for Ti-6Al-4V (Donachie 2000).

Property	Notation	Value (typical range)	Comments
Poisson's ratio	ν	0,33	
Modulus of elasticity (Young's modulus)	E	106-146* GPa	*highest value obtained when α -deformation texture, test direction parallel to high density of basal poles
Yield strength	σ_y	895-1250 MPa	Variation by more than 200 MPa by heat treatment, Oxygen content or texture direction
Elongation to failure	ϵ_f	13-16 %	Indicator for the material ductility or its ability to be deformed
Fracture toughness	K_{Ic}	40-100 MPa(m ^{1/2})	

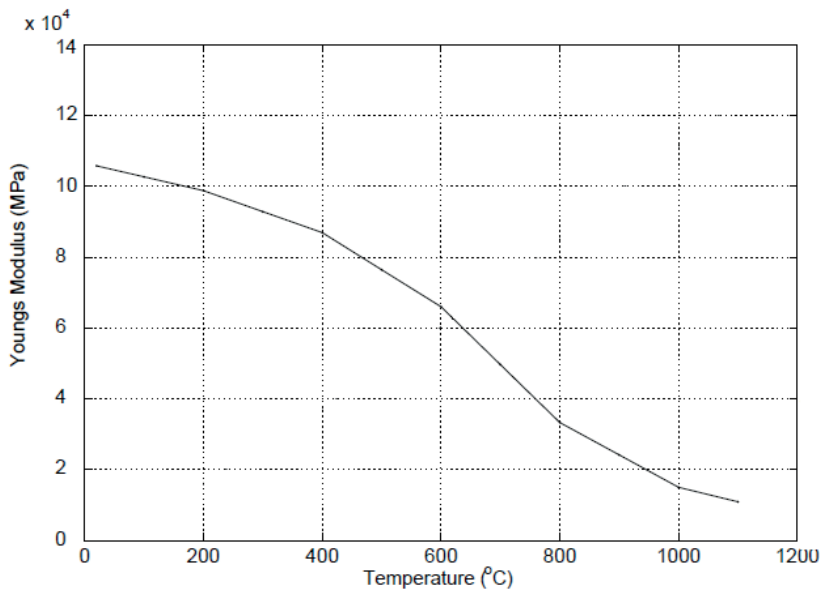


Figure 13. Young's modulus temperature dependency of Ti-6Al-4V, from differential expansion dilatometer measurements (Babu 2008; Babu and Lindgren 2013).

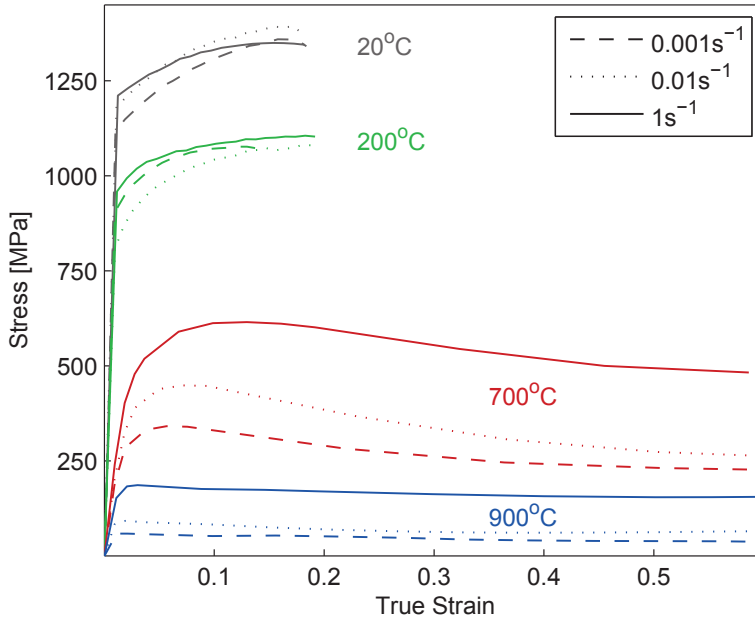


Figure 14. Stress-strain curves from hot compression tests of Ti-6Al-4V at 20°C to 900°C for strain rates of 0.001s⁻¹, 0.01s⁻¹ and 1s⁻¹ (Babu 2008; Babu and Lindgren 2013).

3.3.2 Composition effects

Even though composition effect has not been included directly in the model, one has to be aware of the chemical composition variations that can be an important factor for the equilibrium microstructure or the mechanical properties.

Each of the principal alloying elements, Aluminium (Al) and Vanadium (V), affect the mechanical properties. Aluminium is an effective α -strengthening element, also appreciated for its low density not adding weight to the titanium alloy (Smallman and Bishop 1999). It also lowers the ductility. Vanadium is β -isomorphous structure, i.e. miscible in the β phase and has a limited α -solubility (Smallman and Bishop 1999). For a common titanium alloy Ti-6Al-4V, the impurities and alloying element contents are varying. The allowed variation in the chemical composition is summarised in Table 3. Those variations have consequences on the mechanical properties. Higher content of impurity elements, particularly Oxygen and Nitrogen, will induce a higher strength in the material. Inversely, lower contents will improve ductility, fracture toughness, stress-corrosion resistance as well as resistance against crack growth (Boyer et al. 1994). It is thus of great importance to take the composition in consideration when making comparison between experiments, samples and components. For more advanced and controlled properties an “Extra Low Interstitial (ELI)” grade alloy, Ti-6Al-4V ELI, can be used.

PROPERTIES, METALLURGY AND MICROSTRUCTURE

Table 3. Chemical composition requirements for Ti-6Al-4V titanium alloy (Donachie 2000).

Element	Al	V	Fe	O	N	C	H	Other impurities	Total other impurities
Min composition, wt%	5,5	3,5	-	-	-	-	-	-	-
max composition, wt%	6,75	4,5	0,3	0,2	0,03	0,08	0,0125	0,1	0,4
ELI - Nominal composition, wt%	6	4	0,1	0,11	0,01	0,03	0,006	-	0,2

The Oxygen content, accounted for as an impurity, may vary up to 0.2%. It has the effect of solid solution hardening and increases the mechanical strength to the detriment of ductility (Smallman and Bishop 1999). Titanium affinity for Oxygen increases with the temperature. Deeper than the oxidation layer, the Oxygen stabilises the α phase to form a hard “ α case” layer with brittle properties (Robinson et al. 2002). To avoid Oxygen contamination, titanium alloys are processed in protected atmosphere chamber when treated above about 450°C.

3.3.3 Microstructure effects

Microstructural features such as phase fractions, their morphologies, grain sizes are qualitatively identified to affect mechanical properties as listed by Boyer et al. (1994, Table 1, p 1052). Ti-6Al-4V is a two phases alloy, α and β . Mechanical properties are influenced by the mixture of α and β phases. The α phase shows good creep resistance and greater strength whereas the β phase exhibits a softer behaviour (Tiley 2002). Consequently, large variations in the mechanical behaviour occur in the phase transformation temperature range (Majorell et al. 2002). At temperatures just above the β -transus transitory properties are observed given that 100% β region shows creep behaviour (higher activation energy needed) and higher strain rate sensitivity (Majorell et al. 2002).

Depending on the processing conditions, the alloy can also form metastable phases (α' , α'') or intermetallic phase ($\text{Ti}_3\text{-Al}$ particles). The metastable phases formed during rapid cooling conditions, are either harder than α as for α' martensite, or have mechanical properties close to α as for α'' (Picu and Majorell 2002). α' martensite with extremely fine acicular structure exhibits high strength and hardness but relatively low ductility and toughness (Donachie 2000). Intermetallic particles form when alloy element partitioning occurs during particular conditions below 500°C (Picu and Majorell 2002) or 550°C (Lütjering 1998). These contribute to solid solution hardening at lower temperatures (Picu and Majorell 2002).

G. Lütjering (Lütjering 1998; Lütjering et al. 1994; 1995) explored the relationship between thermal processing, microstructure and obtained mechanical properties of $\alpha+\beta$ alloys. Fully lamellar microstructure with large prior- β grain sizes, similar to the microstructure observed in the deposited metal, is taken as example and microstructures major influence on the mechanical properties are summarised in Figure 15 after Lütjering (1998). Peak temperature and cooling rate are important parameters determining the microstructure. The α colony size or width of lamellae is inversely related to the yield stress, $\sigma_{0,2}$, as well as it contributes to the

ductility, ϵ_f . They also affect the crack propagation resistance of the alloy. Another important parameter with respect to the mechanical properties is the existence of grain boundary α (denoted α_{gb} layer in Figure 15). It has large impact on the material ductility. Fully lamellar microstructures usually have good fatigue crack propagation resistance, fracture toughness (K_{1C}) and creep resistance (Lütjering et al. 1995). This is probably because of the associated large α colony sizes.

To the knowledge of the author, no quantitative tool correlating microstructure to mechanical properties of titanium alloys is yet available except for the work by Kar et al. (2006). Their neural network model is developed to predict yield and ultimate tensile strengths, which are used to identify the influence of individual microstructure features on tensile properties. The α lath thickness, which is shown to be proportional to the colony scale factor (Tiley 2002), has been identified to have the largest effect on the strength properties of Ti-6Al-4V. Increasing volume fraction of total α has shown also to increase the strength. They discovered that formation of basket weave microstructure favours strengthening of the alloy, especially in case of large β grains (larger than $200\mu\text{m}$).

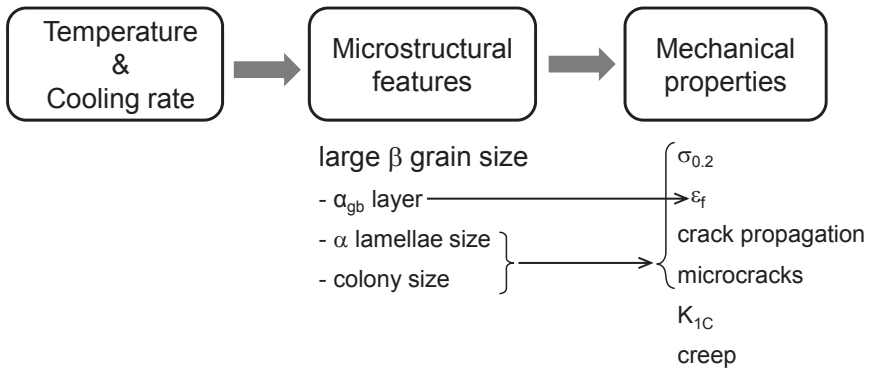


Figure 15. Influences on mechanical properties (major influences are specified by arrows) for fully lamellar microstructure of $\alpha+\beta$ titanium alloy, example for large β grain size (Lütjering 1998).

3.3.4 Welding and metal deposition effects

The thermal cycles induced by the welding and its free-form manufacturing variant metal deposition processing affect the microstructure and consequently the mechanical properties as described above. Ductility can be degraded by the coarse prior- β grain structure obtained depending on the energy input to the weld (Donachie 2000), and the number of passes. Minimising the weld energy input might be a suitable way to maintain a finer grain structure and thus insure better ductility. Weld strength is generally observed to be higher than the welded plate (Boyer et al. 1994). Induced residual stresses and distortions (see also Section 2.3.2), inevitable consequences of the welding or metal deposition processing, might also result in local cracking of the part.


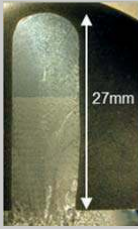
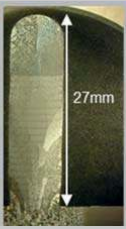


PROPERTIES, METALLURGY AND MICROSTRUCTURE

More specific to layer-by-layer wire deposition processes, mechanical properties that are comparable with cast or even wrought material have been measured (Baufeld et al. 2010; Baufeld et al. 2011; Brandl et al. 2011b; Åkerfeldt et al. 2011). Orientation dependency of the Ultimate Tensile Strength (UTS) and ductility has been noticed when testing deposited wall structures; higher strength in the vertical direction corresponds to the prior- β grains growing direction. Scattered hardness measurements with no direct relation to the position in the walls are suggesting a slight variation of the mechanical strength within the entire samples' structures (Baufeld et al. 2010; Åkerfeldt et al. 2011). This tendency agreed with the observed α lamella width discrepancy in deposited walls in **Paper B**. Although good fatigue properties were obtained, potential source of failure made during the deposition process are highlighted; pores and other apparent defects (Åkerfeldt et al. 2011) and prior- β grain boundaries orientations (Baufeld et al. 2010) would locally lower the resistance to fatigue of the samples.

4 MICROSTRUCTURAL STUDIES OF METAL DEPOSITED Ti-6Al-4V

During the metal deposition process, steep temperature gradients and multiple thermal cycles lead to considerable microstructure variations in the deposited material as discussed in chapter 3. The obtained microstructure depends on the thermal route which itself depends on the welding parameters (such as heat input, welding speed), and on other welding conditions (such as the work piece geometry and fixturing). In addition, at each weld pass, the microstructure in the already deposited material is affected by the energy from the next deposited layer(s). The pass of a new weld on top affects the microstructures on previous deposited layers with possible melting and reheating in the β or $(\alpha+\beta)$ phase field. The final obtained microstructure is the result of the complete thermal history experienced during the entire metal deposition process. The microstructure from built wall structures deposited on base plates have been evaluated both qualitatively and quantitatively. The results below are from **Papers A** and **B**. The chemical composition of the Ti-6Al-4V plate and wire are given in **Paper B**. The selected analysed cases presented in this work have been deposited with GTAW, see Table 4.

Table 4. Selection of experimental GTAW built up walls, layers' height set at 0,9 mm.

	4-2	4-7	4-8	4-11	4-12	5-27
Welding parameters*	75 A 12 V 2 mm/s	86 A 10,7 V 2 mm/s	86 A 10,7 V 2 mm/s	86 A 10,3 V 2 mm/s	90 A 10,8 V 4 mm/s	85 A 10,3 V 2 mm/s
n° of Layers	8 layers	30 layers	30 layers	12 layers	30 layers	30 layers
Inter-pass waiting time	none	none	2 min	none	none	none
Wall type	Single weld bead	Single weld bead	Single weld bead	Single weld bead	Single weld bead	Triple weld bead
Macrographs (same scale)					-	
Studied in	Paper C	Paper A	Paper A	Paper B	-	-

* Complementary welding parameters (ex: wire feeding) were adjusted to permit well behaving deposition

4.1 Temperature cycling due to metal deposition

Temperature history during GTAW metal deposition was on occasion recorded with thermocouples (T/C) spot-welded to the base plate; see **Paper B (Fig. 6)**. A pyrometer was also used to measure in situ the temperature on the side of the wall. See Figure 16 and in **Paper B** for description of the measurement setup. The pyrometer temperature measurements for a fixed position on the wall side for samples 4-7, 4-8 and 4-12 are shown in Figure 17. Note the invalidity of the first three to five peaks in the graphs Figure 17 corresponding to the disturbance from the weld torch when passing by in front of the pyrometer measurement area for the first deposited layers; see Figure 16 b). The sensor measurement range of the pyrometer was set between 400°C and 1920°C explaining the saturated signal observed under the minimal value of 400°C. The cyclic temperature variations are clearly observed and are subsequently inducing repetitive microstructure changes.

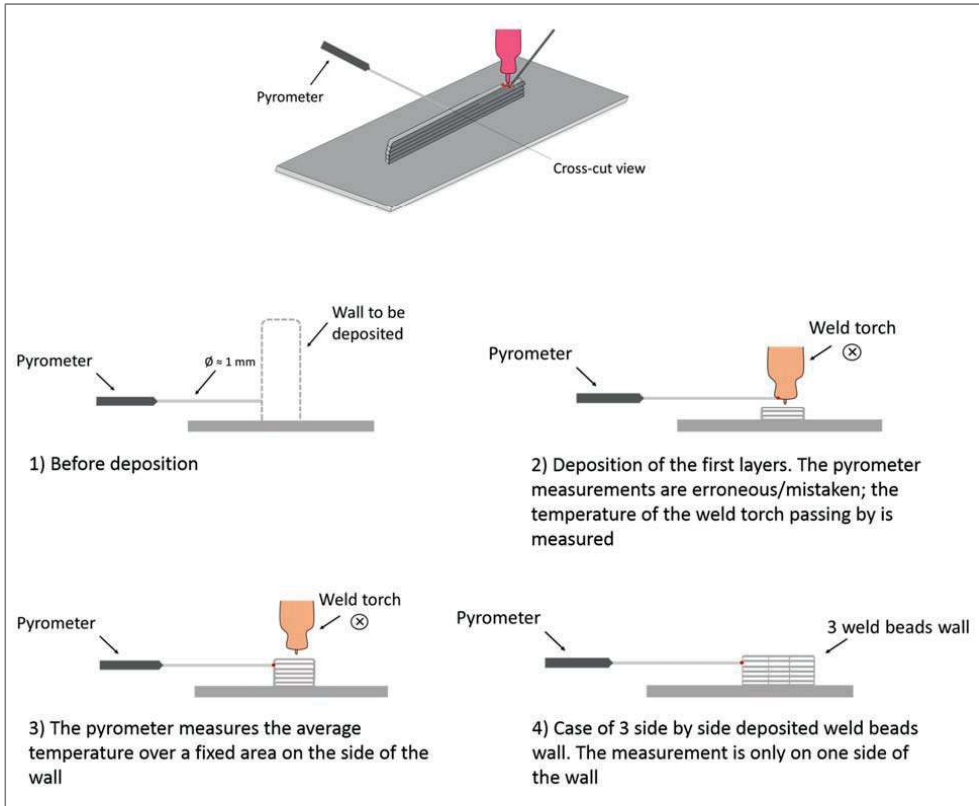


Figure 16. Schematic illustration of temperature measurements setup with pyrometer under GTAW metal deposition of a single weld bead wall and three weld beads wide wall.

MICROSTRUCTURAL STUDIES OF METAL DEPOSITED Ti-6AL-4V

Moreover, inter-pass waiting time between the layers has also an important effect. Indeed accumulation of heat in the already deposited parts is observed when continuous deposition is used (i.e. with no inter-pass waiting time); see Figure 17 a) and c). The microstructure has thus a tendency to be slightly thicker, see **Paper A (Figure 3)**. A longer inter-pass time allows the sample to cool down between each layer, Figure 17 b), and reduces the grain growth.

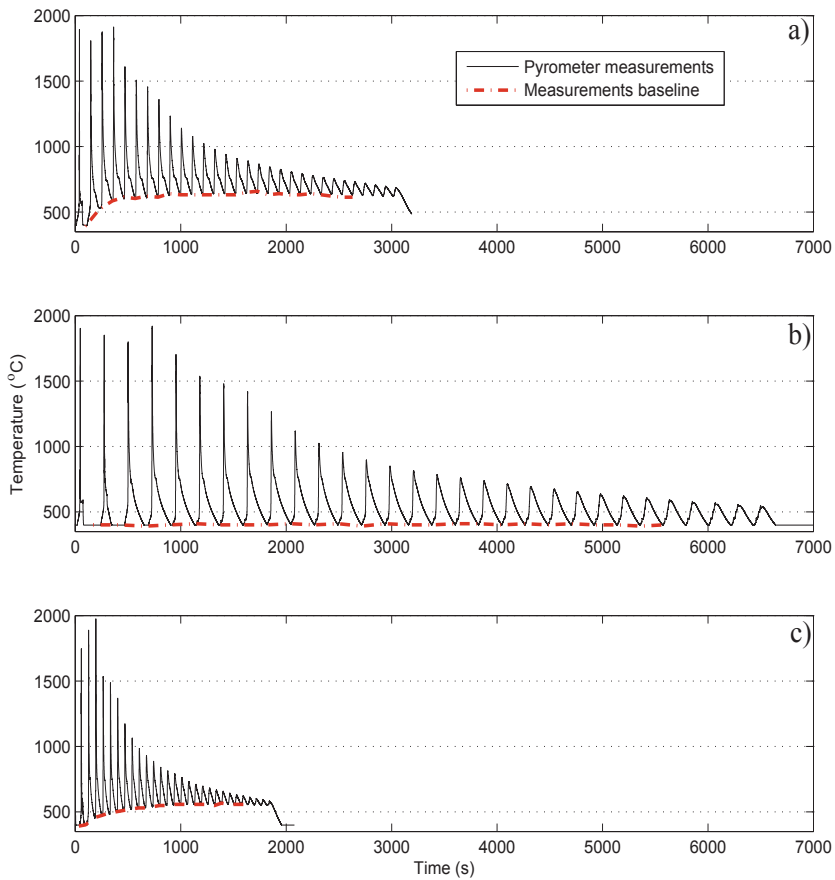


Figure 17. Measured temperature by pyrometer on MD-wall side for samples a) 4-7, b) 4-8 and c) 4-12 presented in Table 4.

MICROSTRUCTURAL STUDIES OF METAL DEPOSITED Ti-6AL-4V

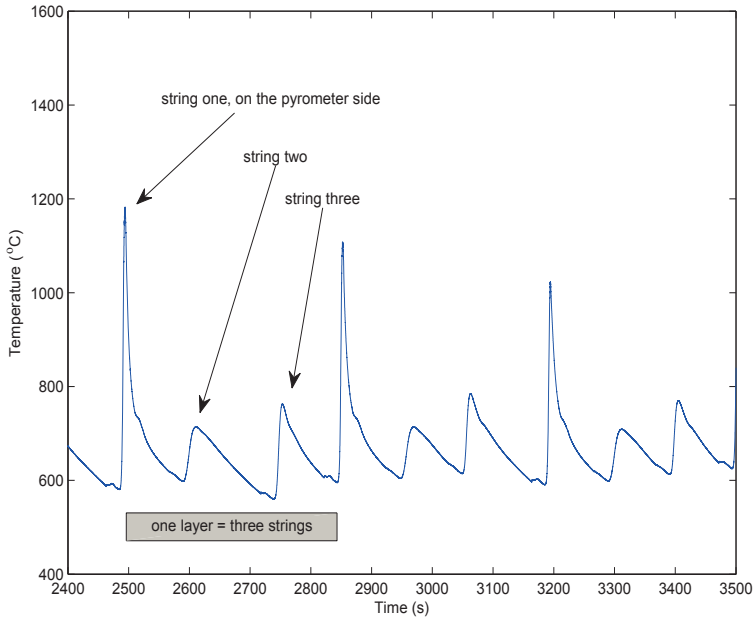


Figure 18. Three deposited layers measured temperature by pyrometer on MD-wall side for sample 5-27, three weld beads wide wall.

The deposition of larger structures side by side as in sample 5-27 adds further heating from neighbouring deposits. Three thermal peaks are registered by the pyrometer of which two of them are due to neighbouring weld beads, see Figure 18. The microstructure of this sample has therefore coarser microstructure than the single weld bead wall, compare with sample 4-7 that was deposited with the same process parameters.

In collaboration with Almir Heralic (Heralic et al. 2012), the change in energy input corresponding to variation in the welding speed have been studied using laser metal deposition process. Similar microstructures to GTAW deposition are observed when laser deposition is performed. The main difference is that the structure sizes are thinner for laser deposition due to its more concentrated heat source. Figure 19 shows cross-sectional micrographs of laser deposited single weld bead with one layer on plate for different welding speeds. Thus, even though laser power is increased, less energy input per unit length is needed when increasing welding speed in order to keep the same breadth and height deposited geometry. Corresponding prior- β grain size variation is clearly noticed between the samples. A larger amount of heat input per unit length of the weld causes more grain growth in the base plate. In the FZ area, the prior- β grain structure is vertically oriented following the induced heat gradients. The grains are larger for slower welding speeds namely when the heat input per unit length is higher.

MICROSTRUCTURAL STUDIES OF METAL DEPOSITED Ti-6Al-4V

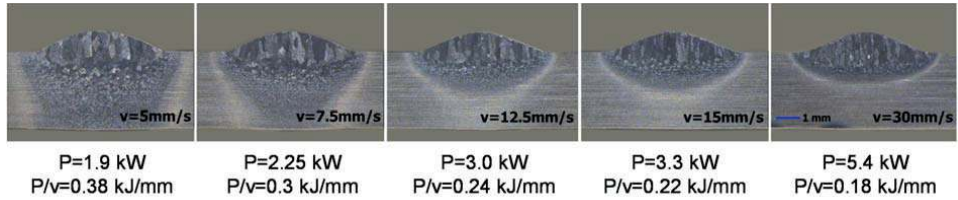


Figure 19. Polished and etched cross-section micrographs of the laser deposited single weld bead on plate for different welding speeds v . [P : Laser power, P/v : energy input indicator (laser energy absorption and other external disturbances are not treated)].

4.2 Qualitative characterisation of microstructure

Optical microscopy was used to investigate and characterise the microstructures. The samples were prepared using conventional grinding and polishing techniques for titanium alloys and etched with a 2% Kroll solution. A selection of deposited wall structures is shown in Table 4, taken from a larger collection of samples. The objective was to identify the different microstructural constituents and their evolution during metal deposition. A selection of the characterised microstructures is discussed in the following. Figure 20 and Figure 21 show both a central cross-section macrograph of a deposit, surrounded by higher magnification micrographs at specific locations in the samples. Variations in the microstructure are clearly observable and some of the microstructure constituents and characteristics are described below.

4.2.1 Heat affected region of base plate

The as-received microstructure of the base plate is unaffected at the far left of the plate in Figure 20 c). It is indeed far enough from the deposition area. The microstructure consists here of equiaxed α microstructure in a transformed β matrix, typical for rolled products. A typical HAZ in the base plate is clearly visible in Figure 20 f) where the microstructure has experienced solid state transformations. The α grains become larger and more of a lamellar shape closer to the deposited metal.

4.2.2 Prior- β grains in deposited metal

The presence of large columnar prior- β grains in the deposit is clearly visible in metal deposited macrographs; see in Figure 20, Figure 21 and Figure 22. At the intersection of the base plate with the first deposited layer, the prior- β grain morphology changes from equiaxed to columnar, as seen in Figure 20 e) and in Figure 21 b). The multidirectional equiaxed β grain morphologies observed near the base plate is a consequence of the three-dimensional heat flow conditions of welding (Donachie 2000).

In the wall part, the prior- β grains are observed nearly perpendicular to the base plate and cross multiple deposited layers as clearly seen in the macrographs of metal deposited samples, see Figure 20 b). The β grain sizes can reach up to several decades of millimetres in the height direction, as seen in **Paper A** or Table 4 for samples with higher walls. The prior- β grains grow in the direction of the thermal gradients (Donachie 2000). Simulation of β phase fraction

MICROSTRUCTURAL STUDIES OF METAL DEPOSITED Ti-6AL-4V

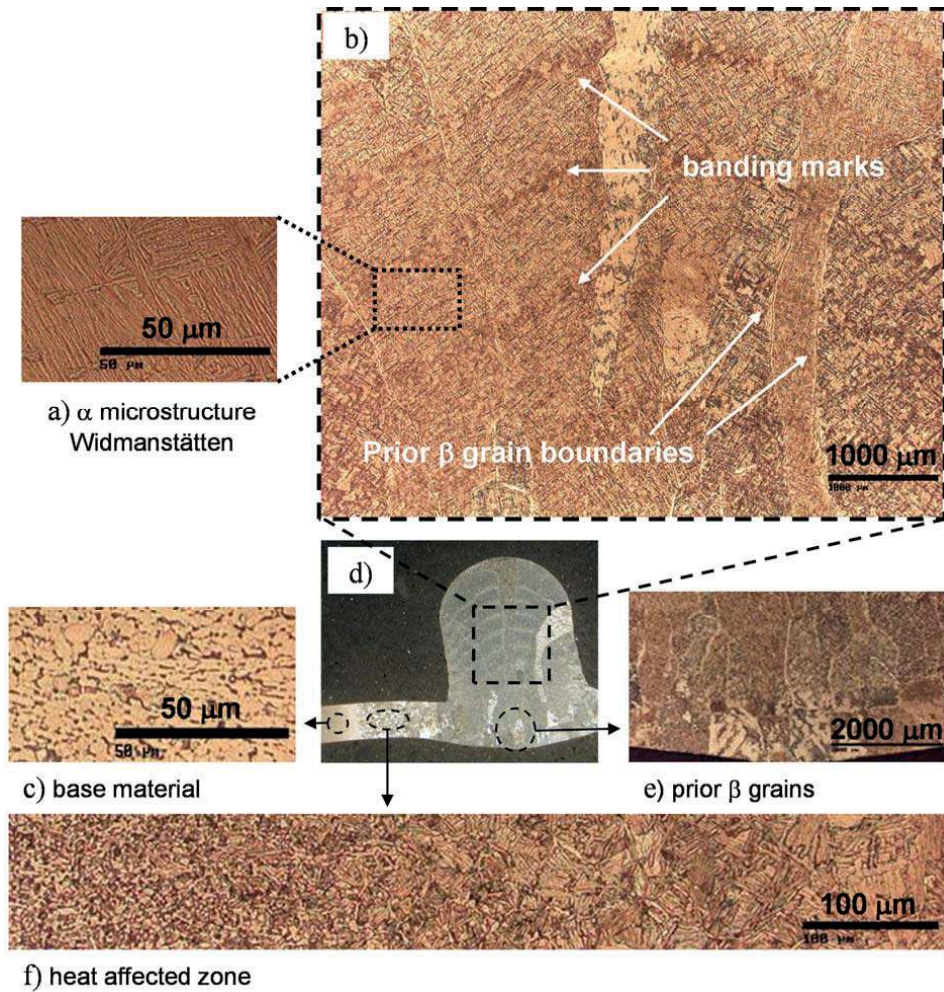


Figure 20. Macro- and micrographs of sample 4-2 presented in Table 4.

in **Paper B** shows that unidirectional propagation in the wall height direction takes place when several layers are deposited. Three simulated image captures at one second interval show, indeed, the 100% β phase fraction propagation for which the propagation front evolved to a horizontal line, see in **Paper B** (Fig.12).

MICROSTRUCTURAL STUDIES OF METAL DEPOSITED Ti-6Al-4V

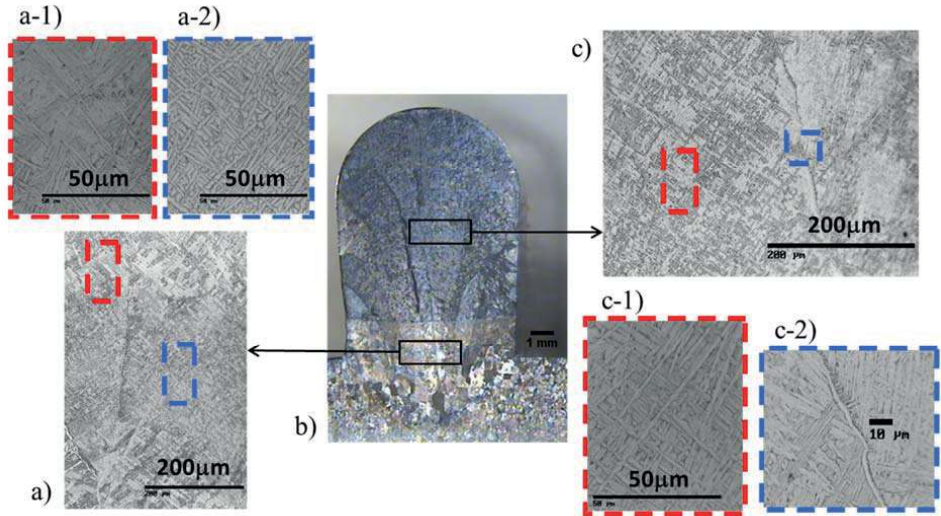


Figure 21. Macro- and micro-graphs of sample 4-11 presented in Table 4 (enlargement of **Fig.7 in Paper B**).

4.2.3 Transformed β in the deposited metal

The presence of continuous α in the prior- β grain boundaries, α_{GB} , is locally outlining the prior- β grain boundaries as shown in Figure 21 c-2). The deposited metal presents a fully lamellar microstructure showing Widmanstätten morphology inside the prior- β grains. Figure 21 a-1), a-2), c-1) and Figure 20 a) are examples of α_W microstructure occupying the main part of the deposited metal.

4.2.4 Banded pattern

A macroscopic banded pattern can be observed in the deposited metal. The pattern can vary between samples and the lower / upper part of the deposited specimens. The observed pattern is shown in Figure 22 for 3 single weld bead walls of different height. Lighter rounded lines can be seen in the wall sample Figure 22 a). For higher deposited structures, straight bands regularly distributed are visible in the lower part of the wall showing darker horizontal lines in Figure 22 c). The upper part of the wall does not show the same banded pattern. Figure 22 b) and c) show macrographs of two walls with different height deposited with the same process parameters. It can be noticed that the upper part has the same size and shape for both of the samples. The banded part is accordingly of higher size for a larger amount of deposited layers. More detailed investigations are needed to find out whether the bands are caused by phase transformation on reheating or annealing effects by extended exposure to intermediate temperatures. Simulations are a very illustrative tool for such investigation as they allow for undergoing observation of the phenomena being difficult to monitor or measure during actual deposition.

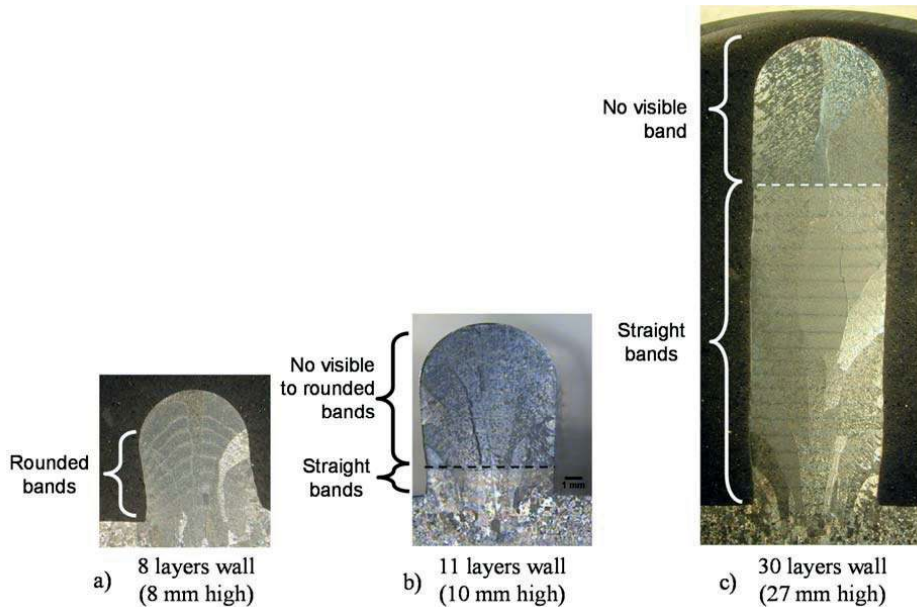


Figure 22. Macrographs of GTAW metal deposited wall – banded patterns.

A potential explanation for this pattern is discussed in **Papers A & B** based on the thermal history. The observed band formation seems to be due to a slight difference in the α lath thickness, Figure 21 a). The same observations can be made when comparing Figure 20 a-1) with a-2) and when comparing Figure 21 a-1) with a-2). Stereology measurements, done in **Paper B (Table 2)** and presented in Table 5, show a difference of about 20% in the α lath thickness when measuring the microstructure sizes within a band and outside it. The slight variations in the lamellar microstructure in shape and sizes are thus inferred to cause the observed banded pattern at a larger observation scale. The α lamellar size variations observed between the lighter and darker band parts may be due to grain growth after the successive heating at low to medium high temperatures. Note that irregularity of the bands distribution can be observed when the conditions for the deposition process vary between the deposited layers. It is important to notice that the bands are, however, not coinciding with the deposited layers' borders. The straight horizontal band lines at the lower part of the higher walls agree in shape with the thermal isotherms. The lack of visual bands in the upper part could be the result of shorter thermal history that did not allow the α lamellar size growth variations to take place.

4.2.5 Martensite α and massive α

Martensite has not been identified with certainty in this study by optical microscopy. However, it is reported to appear when the cooling rate is larger than 410°C/s (Ahmed and Rack 1998). For cooling rates of 20 to 410°C/s , massive transformation would occur in addition to the martensite transformation. Massive α and martensite α does not show

significant difference in composition, and have both hcp crystal structure (Ahmed and Rack 1998). It can be mentioned that hardness measurements on laser beam deposited components show hardness in the range of 430-450 HV for the last top layers deposited and 330-380 HV elsewhere (Baufeld et al. 2011). Fully martensite structure in Ti-6Al-4V has been observed from 330HV and hardness higher up to 410HV when martensite α is decomposed to equilibrium α and β in fine precipitates (Gil Mur et al. 1996). The existence of martensite or massive α in the deposited metal cannot be excluded.

4.3 Quantitative characterisation of microstructure

Quantitative metallographic examination of the microstructure is required in order to obtain useful information about the microstructure of the produced samples. Traditional methods such as the point counting method are low in precision when comparing with image analysis (Dallair and Furrer 2004). Polarized light microscopy is an emerging method tested on titanium alloys to better detect the boundaries of the lamellae colonies (Chraponski and Szkliniarz 2001). Although different standards have been studied for characterising microstructures based on image analysis technology (Russ 2002; Russ and Dehoff 2005), the quantification of microstructure features in $\alpha+\beta$ titanium alloys is still very difficult because the microstructure is quite complex and involves structures at varying size scales. Moreover the information available from a two dimensional section of the microstructure image using optical microscopy is limited in terms of understanding three dimensional aspects. Stereology analysis procedures have been studied for titanium alloy Ti-6Al-4V (Searles et al. 2005; Tiley et al. 2004). The authors suggested measuring methods for most of the microstructure features in titanium alloy Ti-6Al-4V using Adobe Photoshop⁶ with FoveaPro⁷, a set of functions for computer-based image processing and measurement in images.

In this work, procedures including automated, semi-automated and manual stereological measurements were applied. Various specialised image processing software were tested for measurements of the Ti-6Al-4V metal deposited microstructure. The tools suggested by Searles and Tiley (2005), and the ImageJ⁸ freeware for image editing and manual or semi-automated examination were used. The original image quality has a large impact on the accuracy and reliability of any stereology procedure. To obtain the highest quality micrographs, the microstructure was imaged at progressive magnification from x25 to x1000. Easier image analysis was obtained when the pictures were directly taken in grey scale. The methods used to measure the volume fractions of β and α and some of the α lath dimensions on microstructure images from deposited samples are shortly described below.

4.3.1 Volume fraction of β and α

In the original grey scale picture, Figure 23 a), the dark colour is β phase and the brighter parts are α phase. The contrast in the image is increased by using a threshold value that separates the image into black and white pixels. This can be seen in Figure 23 where the

⁶ Adobe Photoshop 7: graphics editor developed and published by Adobe Systems - Adobe Photoshop (2005)

⁷ FoveaPro 4.0. add-in for Adobe Photoshop - Reindeer Graphics Product

⁸ ImageJ version1.34. (2005). "Image processing and analysis in Java". Research Services Branch, NIMH, <<http://rsb.info.nih.gov/ij/>>.

MICROSTRUCTURAL STUDIES OF METAL DEPOSITED Ti-6Al-4V

picture a) is the original grey scale image and the picture b) is obtained after thresholding. Because of the small amounts of grain boundary α , it was not possible to quantify the different α morphology fractions. It was only possible to quantify the amount of β phase fraction, respectively total α phase fraction. The deposited metal samples were measured on pictures that all gives β phase fraction between 10,6% and 14,9%, respectively a total α phase fractions of 85,1 to 89,4%. This result is slightly higher in β phase fraction than the expected 8 to 10%.

4.3.2 Measurement of α lath thickness

A semi-manual method using the software ImageJ was applied. Measurement of the thickness and the length of the α laths were made. A set of grid points, corresponding to the number of measurements to be done in the pictures, is superimposed on the picture by the software. Some of the identified laths are shown in Figure 24. The width and length of the lath at a grid point is identified and measured with the software ImageJ. The mean value of the measured line lengths is taken as estimation of the α lath thickness or length in the picture. This method was used for the results presented in **Paper B**.

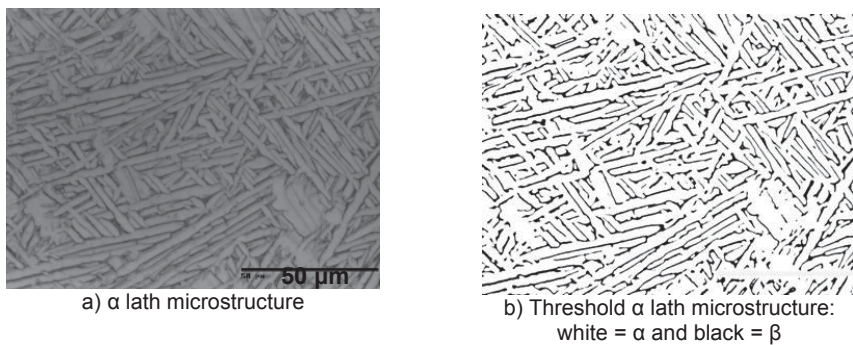


Figure 23: Illustration of thresholding technique in use for α and β phase fraction evaluation in Ti-6Al-4V.

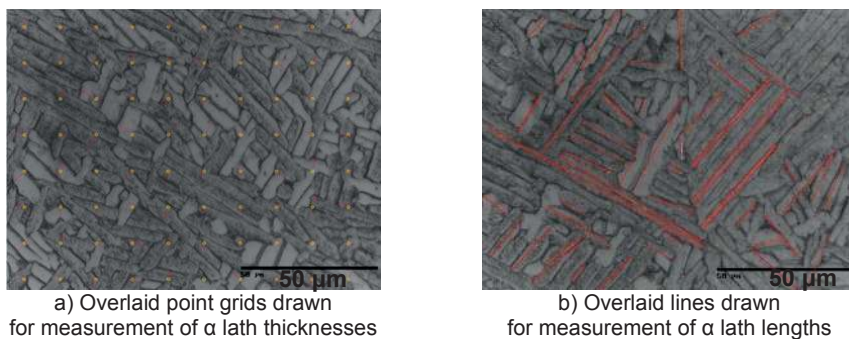


Figure 24: Illustration of the evaluation of the α lath thickness and length in Ti-6Al-4V.

MICROSTRUCTURAL STUDIES OF METAL DEPOSITED Ti-6Al-4V

Using such standard procedures for measurement on microstructure pictures makes the data more repeatable and makes it possible to assign numeric values to the microstructure. In Table 5 the α lath thickness measured for several samples are put together, sample 4-11 is also in **Paper B**. The large divergence observed in the measurements for a single sample has been observed to correspond to a banded pattern that is observed after metal depositions of a certain number of layers, see in **Paper A**.

Table 5. Stereology measurements of α lath thickness using the software ImageJ (see Table 4 for sample specifications).

<i>Sample</i>	<i>Picture specifications (position in the deposited wall and magnification)</i>	<i>α lath thickness (μm) *SD: Standard Deviation</i>	<i>Mean α lath thickness (μm)</i>
4-7	mid wall X200	1.57 (SD:0.38,Min:0.95,Max:3.05)	1.57
	mid wall X200	1.57 (SD:0.45,Min:0.60,Max:3.35)	
4-8	mid wall X200	1.38 (SD:0.30,Min:0.76,Max:2.11)	1.38
	mid wall X200	1.38 (SD:0.30,Min:0.60,Max:1.95)	
4-11	top area X1000	1.14 (SD:0.32,Min:0.53,Max:2.34)	1.16
	mid (light band) X1000	0.97 (SD:0.32,Min:0.30,Max:1.66)	
	mid (dark band) X1000	1.38 (SD:0.36,Min:0.68,Max:2.90)	
4-12	mid (light band) X1000	0.92 (SD:0.23,Min:0.44,Max:1.37)	1.11
	mid (dark band) X1000	1.26 (SD:0.38,Min:0.65,Max:2.35)	
	mid (light band) X1000	0.90 (SD:0.27,Min:0.43,Max:1.47)	
	mid (dark band) X1000	1.35 (SD:0.28,Min:0.85,Max:2.74)	
5-27	top area (several pics)	1.74 (SD:0.85,Min:0.34,Max:-)	1.81
	mid wall (several pics)	2.11 (SD:1.05,Min:0.39,Max:-)	
	side wall (several pics)	1.59 (SD:0.62,Min:0.34,Max:5.16)	

5 MICROSTRUCTURE MODEL

There exist different approaches to study, evaluate and predict the microstructure evolution of Ti-6Al-4V due to welding or metal deposition.

Qian et al. (2005) inferred the microstructures from the equilibrium phase diagrams and published TTT-curves combined with a computed thermal history. This approach gives a qualitative estimate of the variations in microstructure within a given sample due to different cooling times and process heat input.

Bonta et al. (2006) measured microstructure grain morphologies for samples subjected to different solidification conditions. Grain morphologies such as α colony sizes, Widmanstätten or basket weave structures are mapped as functions of heat input and weld velocity. Microstructure predictions are qualitative and can be obtained from the process maps for a measured or computed temperature history (Kobryn and Semiatin 2003). The microstructure estimations are limited to the process window investigated in which the map has been drawn.

The microstructure evolution can be directly calculated by coupling it to the heat transfer simulation. Theories on solid-solid phase transformations are used to obtain microstructure description. The current work is in line with this approach for which the developed model is presented in the following.

5.1 Length scales

Metallurgical phenomena occur at different length scales. The material structures at multiple length scales influence the properties of the material. Figure 25 shows these scales as well as larger scales relevant for the modelling in the current context. The material and process models thus need to describe phenomena on these different length scales. The detail and accuracy of the model will ensue from the metallurgical phenomena to be modelled and the associated length scale chosen. A dislocation density based model, so-called physical based model, has been used to model material plasticity behaviour (Babu 2008; Babu and Lindgren 2013). Information from smaller scales, such as grain size, diffusivity, stacking fault energy, precipitate distribution can be accommodated in this model as they affect the dislocation motion. The current developed microstructure model provides information about the microstructure evolution that is important for the flow stress model.

5.2 Modelling microstructure evolution

Phenomena at the microstructure scale are fairly well studied and several relationships between process variables and resulting microstructure have been proposed (Banerjee and Mukhopadhyay 2007; Porter and Easterling 1992). Material and microstructure behaviour models can be grouped in three broad classes (Furrer and Semiatin 2010).

5.2.1 Statistical models

The statistical models require a large amount of experimental data in order to derive a relation between parameters and predictions. They are limited to the range of data tested and are process independent. Artificial Neural-Networks are one known example; Malinov et al. applied this method to predict TTT-diagrams of titanium alloys (Malinov et al. 2000). Stochastic methods can be applied to the simulation of grain growth thanks to the competing

MICROSTRUCTURE MODEL

nature of the phenomena controlling the process. Monte-Carlo simulations (Mishra and DebRoy 2004; Yang et al. 2000) or cellular automata based methods (Ding and Guo 2004; Grujicic et al. 2001) are models applied for industrial welding and metal deposition. These methods allow exploration of parameter estimation granting a variety of statistical distributions such as normal or exponential distribution. They do also represent the phases explicitly and are thus limited to small domains of analysis.

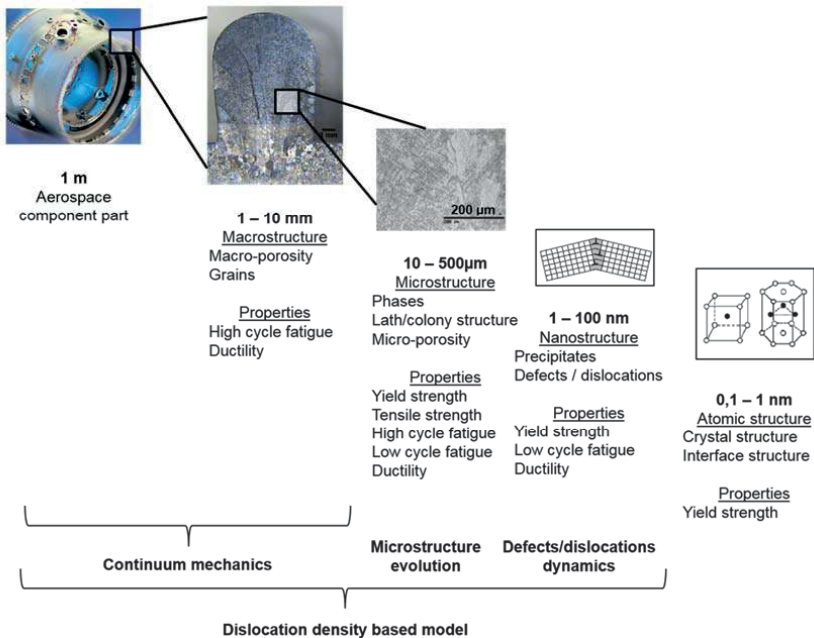


Figure 25. Metallurgical length scales that dominate properties and behaviours in Ti-6Al-4V [inspired and adapted from (Furrer and Semiatin 2010, Fig.3 p10) for Ti-6Al-4V].

5.2.2 Phase-field models

The phase-field approaches for microstructure evolution are included in a form of physics based model class with parameters such as the migration of grains and interfaces energy. The modelling technique resolves the microstructure itself and is therefore limited to study small domains (Chen et al. 2004). The work of Katzarov et al. (2006) can be cited as an example applying this method to compute the lamellar structure formation in γ -TiAl. Gong (2014) shows that the phase field method is also appropriate for modelling columnar structure growth with a dendrite growth approach, yet at the expense of the computational time and resources. It is relevant to underline that phase-field approach is well adapted for mesoscale prediction of dendrite morphology propagating at liquid/solid front.

5.2.3 Phenomenological models

The phenomenological models are typically based on one or several equations that describe the relationship between the process variables and the resulting properties or microstructures. The model focuses primarily on reproducing correctly the beginning and end of transformation, the intermediate steps are not considered. Arrhenius rate-type equation, used to describe the temperature dependence of a phenomena, is a well-known example (Porter and Easterling 1992). The precise underlying mechanism(s) are not incorporated resulting in needs for calibration of the relationship and risk for inaccurate use when the process mechanism(s) changes. The early Avrami equation (Avrami 1939; 1940; 1941) quantifying the nucleation and growth mechanism is another example (Furrer and Semiatin 2010). The Avrami equation or its extensions are frequently used as modelling tool for thermal driven phase transformations.

Models used in structural calculations are mostly phenomenological (Grong and Shercliff 2002) in order to be applicable to large structures. These models are typically used to calculate microstructure variables at a point. Thus they do not represent the microstructure explicitly but will provide microstructure values, typically quantitative fraction of phases, for a representative volume at the point. In accordance with the research question presented in section 1.2, a phenomenological model approach is selected for this thesis work.

5.3 Transformations diagrams

The time and temperature dependence of the transformations are conveniently represented in isothermal transformation diagrams or Time-Temperature-Transformations (TTT) diagrams (Callister 2007). It is worth noting the strong dependency of the diagrams on the exact chemical composition of the tested alloy and on the parent phase grain size. TTT curves are difficult to generate and as well as evaluate accurately. A sample is cooled quickly from the initial temperature, where it has been held a certain time, to the test temperature. Thereafter it is held for a chosen time and then quickly cooled. This structure is post-mortem analysed to determine the microstructure existing before the last quick cooling or alternative indirectly calculated based on volume changes. The results is plotted in a TTT-diagram as in Figure 26(a).

The progress of an isothermal phase transformation is conveniently represented by plotting the fraction transformation (f) as function of time after reading in the TTT-diagram. The schematic TTT-diagram in Figure 26(a) shows the principal transformations that take place in Ti-6Al-4V. The diffusion controlled phase transformation kinetics for $\beta \rightarrow \beta + \alpha_{gb}$ and $\beta \rightarrow \beta + \alpha_w$ are described by C-shaped curves. Two examples for isothermal phase transformation at $T1$ and $T2$ are given in Figure 26(b), at both temperatures the fraction of transformation varies from 0 to 1. Martensite start temperature is marked to notice the instantaneous martensite transformation when rapid cooling passing by this temperature.

Another common case is to subject a sample to a specific cooling rate towards room temperature from the initial state. The microstructure is evaluated in the same way as for TTT-diagrams. The result is plotted in Continuous-Cooling-Transformations (CCT) diagrams (Callister 2007). Times and temperatures of start and finish of transformations related to a specific cooling history are specified in the CCT-diagrams. Percentages of the final formed structure at room temperature can be provided if the transformation is complete.

MICROSTRUCTURE MODEL

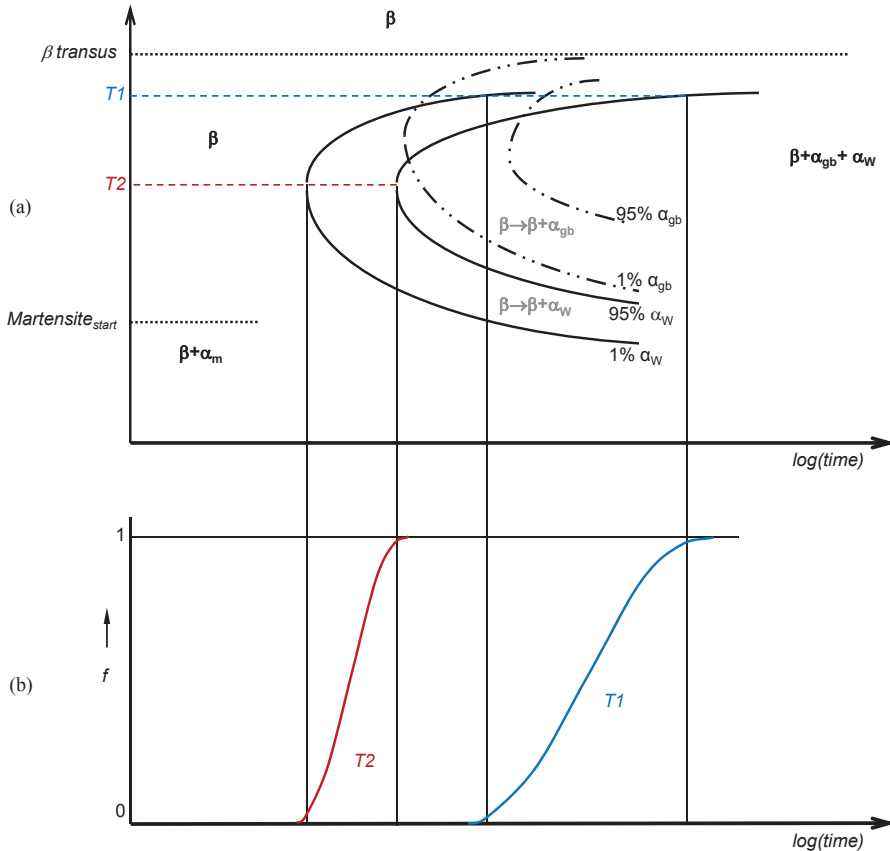


Figure 26: (a) Schematic Temperature-Time-Transformation (TTT) diagram for Ti-6Al-4V
 (b) Percentage transformation versus time for different transformation temperatures.

5.4 Transforming isothermal model to varying temperature

Part of the models used in the current work is formulated for isothermal processes. The current section describes how this is adapted to non-isothermal processes by use of the additivity principle.

The rule of additivity (Cahn 1956) is commonly used to calculate anisothermal transformation from isothermal transformation data using simple rate laws. The additivity rule is only strictly valid under certain conditions (Cahn 1956; Christian 2002; Grong and Shercliff 2002). Avrami (1940) first referred to an isokinetic transformation as one where nucleation rate and growth rate are proportional over the considered temperature range. This is the basis for the

MICROSTRUCTURE MODEL

formulated model in section 5.5. The transformation is then an additive reaction. Cahn (1956) generalised this, and defined a reaction to be additive when the transformation rate, dX/dt , is a function only of the amount of transformation, X , and the temperature, T , written as

$$dX/dt = f(X, T) \quad \text{Equation 1}$$

Thus time and temperature history are not playing any roles. The rate of transformation depends only on the current fraction and the current temperature. This requires “site saturation”, i.e. the nucleation sites are saturated early in the reaction and the growth rate is only dependent on temperature. Several conditions to qualify to be such a transformation must then be fulfilled. The composition of the equilibrium phase should be independent of the temperature (Cahn 1956), i.e. constant. The additivity principle is valid for large undercooling if the last condition is nearly valid (Christian 2002). Grain sizes should be similar for the anisothermal and corresponding isothermal transformations when grain boundary nucleation are involved (Cahn 1956). All these conditions are in general not met. Particular applications, alternatives to the additivity rule and discussions on its validity can be found in Kuban et al. (1986); Lusk and Jou (1997); Reti and Felde (1999); Todinov (1998); Zhu et al. (1997). Grong and Shercliff (2002) show, when modelling welding, that the results were sufficient accurate applying the additivity principle for calculation of microstructure state variables. One should also bear in mind that experimentally determined data themselves, such as the basic TTT-diagrams, are quite uncertain in that they are highly dependent on exact chemical composition and on phase grain sizes (Callister 2007).

The application of the additivity principle is based on the use of a fictitious time (Denis et al. 1992; Grong and Shercliff 2002; Kelly et al. 2005; Malinov et al. 2001a). Demonstration of the use of the additivity rule is presented in Figure 27. The continuous temperature-time path in upper left diagram is approximated by the sum of consecutive isothermal steps denoted $T1$, $T2$, $T3$. For each isothermal step, the phase transformation kinetic is determined from the corresponding TTT-curves. Thus a known state exists after each isothermal step, time and phase fractions are known. However, this time is translated to a fictitious time when performing the next isothermal step. The calculation of the new phase fraction is later reported on the real time scale. The procedure is illustrated in Figure 27. Start at temperature $T1$ with a chosen time step $\Delta t1$, then follow the blue dashed line to the TTT-diagram to the upper right. The information here gives an update in phase fraction, $f1$. This gives the starting fraction for the next increment. However, the starting time for the next increment is the time, $t2_{\text{fictitious}}$, that will give the initial fraction $f1$ in case the whole transformation would have taken place at temperature $T2$. Thereafter the TTT-diagram to the right gives the amount of formed phase for this temperature at time $t2_{\text{fictitious}} + \Delta t2$. This process is then repeated for each new increment. The logic is iterated for $T3$ and the following step-wise temperatures if more subdivisions are intended. The accuracy is improved by shortening the increments in that they will provide a smaller transformation advancement per subdivision minimizing the thermal steps towards isothermal condition.

MICROSTRUCTURE MODEL

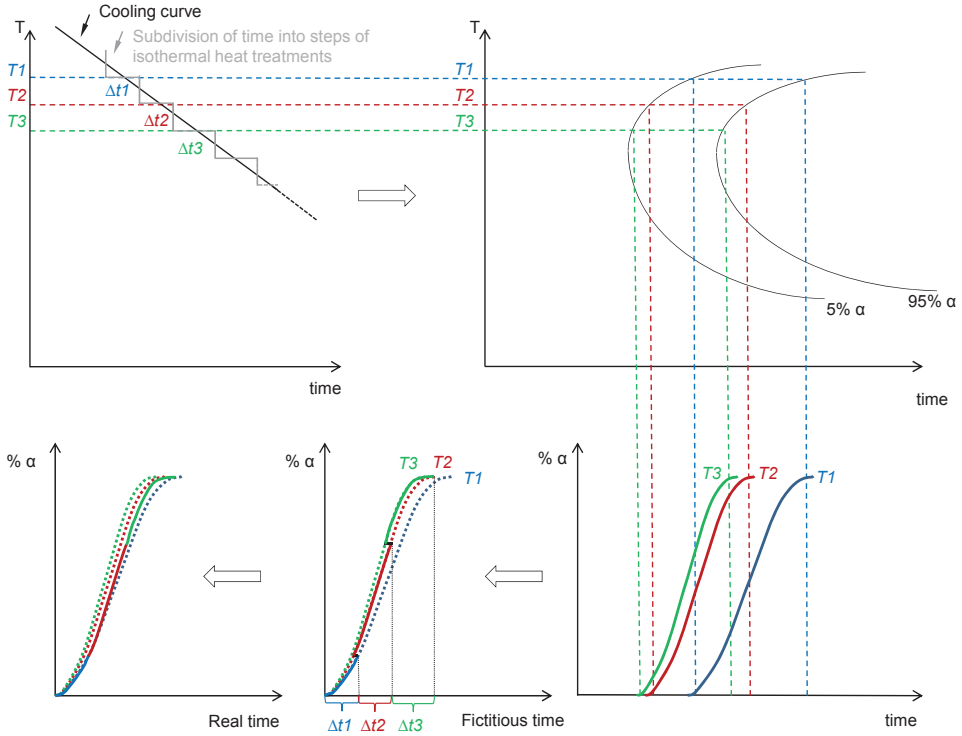


Figure 27. Schematic illustration of the principle of additivity rule, showing the approximation of cooling as the sum of short time step-wise isothermal temperature holding, after (Denis et al. 1992; Grong and Shercliff 2002; Kelly 2004; Malinov et al. 2001a).

5.5 Phase transformation modelling

5.5.1 Diffusional transformations of β to α phases

The Johnson-Mehl-Avrami-Kolmogorov (JMAK) equation given in Equation 2 is used for diffusion controlled transformations and in the current work for the β phase transforming to grain boundary α phase, α_{gb} , and Widmanstätten α phase, α_w .

$$X_i = 1 - e^{-kt^N} \text{ with } i = \alpha_{gb} \text{ or } \alpha_w \quad \text{Equation 2}$$

The nucleation mechanism is reflected in the parameter N , and is therefore independent of temperature for the same nucleation process. The parameter k , on the other hand, is very sensitive to temperature by way of its dependency on the nucleation and growth rates. The model is valid for isothermal conditions. It must be remembered the thermal cycling imposed by the simulated manufacturing processes. Thus the additivity principle described in section 5.4 must be applied for general temperature histories. Adjustments including adaptation to

MICROSTRUCTURE MODEL

5.4 must be applied for general temperature histories. Adjustments including adaptation to incomplete transformation, varying initial phase fraction, multiple phases and incremental formulation, are described in **Paper C**.

5.5.2 Dissolution of α to β phase

JMAK model, as described above for transformations of β to α phases, is also applicable for the dissolution of α to β phase when considering the nature of the transformation as used in **Paper A**. For the specific cases of welding and metal deposition the high heating rates implied give very high transformation rate (Babu et al. 2005; Kelly and Kampe 2004). The phase transformation is approximated as near instantaneous, i.e following the equilibrium phase diagram, in **Paper B**.

At heating, the dissolution of α phases to β phase is essentially controlled by the movement of the α/β interface resulting from the mobility of the Vanadium element at this same interface. No nucleation of the β phase within the α grains is observed (Ivasishin and Teliovich 1999). The alternative to use a simple cell-diffusional model proposed by Kelly (Kelly 2004; Kelly et al. 2005) and model the dissolution by assuming a parabolic growth rate, is finally chosen and used in **Papers C and D**.

$$X_{\alpha} = f_{diss}(T)\sqrt{t} \quad \text{Equation 3}$$

With $f_{diss}(T)$, the dissolution function calibrated by Kelly (2004).

The incremental implementation of the model and the use of fictive time and critical time is explained in (Kelly 2004) and **Paper C**.

5.5.3 Martensite and massive transformation

The martensite transformation is assumed to take place without diffusion and is therefore only temperature dependent and independent of the cooling rate provided it is sufficient high so there still exists some β phase when reaching the start transformation temperature. The article by Koistinen and Marburger (1959) suggest an empirical relationship between the reduction of temperature below T_{ms} (start temperature for martensite transformation) and amount of martensite present. Equation 4 below is therefore used to represent the progress of this reaction for all cooling rates.

$$X_{\alpha_m} = X_{\beta} \left[1 - e^{-coef_{km}(T_{ms}-T)} \right] \quad \text{Equation 4}$$

X_{α_m} is the volume fraction of martensite, X_{β} is the volume fraction of the material that can be transformed (here β phase), $coef_{km}$ is a constant usually taken equal to 0.011 K^{-1} for most of steels, T_{ms} is the start temperature for the transformation, T is the current temperature for which the martensite fraction is calculated. The Koistinen and Marburger model is frequently used when prediction of thermal stresses in a tempering process or welding. This model is adapted to model martensite formations. Its modification for simplifying implementation is described in **Paper B**. The approach was suggested by (Oddy et al. 1996) and shown to be sufficient accurate in (Gyhlesten Back and Lindgren 2016).

Massive α transformation has been observed to occur simultaneously with the martensite formation (Ahmed and Rack 1998). The massive transformation is difficult to separate from the martensitic because of the crystal similitude of the formed phase constituents. The formed

MICROSTRUCTURE MODEL

α phase via massive transformation is here included in the α martensite formation. Also 100% of martensite phase can form at cooling rates above 410°C/s, for cooling rates from 410°C/s to 20°C/s the martensite transformation is gradually replaced with decreasing cooling rate (Ahmed and Rack 1998). This transformation is alternatively proposed to be include through the introduction of the equilibrium fraction of β phase in the equation to prevent a full martensite transformation, see in **Paper C (equation 16)**.

5.5.1 Transformation of martensitic α_m to $\alpha+\beta$

The formation of above described α_m has an unstable crystal structure (Qazi et al. 2003) which is then subjected to evolution with temperature and time. According to Gil Mur et al. (1996) α_m is decomposed into reformed α and/or β according to the current equilibrium proportion of α - and β -phases. The decomposition of α_m is controlled by diffusion depending on the temperature and the heating time and considered complete at the temperature of 800°C.

To avoid an extra variable into the microstructure model, the formed α phase expected having a new morphology that will tend towards the equilibrium one with time, is included into the α_w phase fraction when formed. The classical JMAK, presented in section 5.5.1 Equation 2, is used and adapted to the implementation of the $\alpha_m \rightarrow \alpha_{rec} \rightarrow \alpha_w + \beta$. Details on the incremental form implemented in the model are found in **Paper C**.

5.6 Microstructure morphology modelling

5.6.1 Grain size modelling

A simple grain growth model have been used as part of the physically based plastic flow model, see section 6.2 and **Paper E**. The model is based on the kinetics of normal grain growth for a single-phase metal for which the rate of grain growth is proportional to the mean grain diameter (Porter and Easterling 1992). The following Equation 5 has been used in the model of the hardening process (Babu and Lindgren 2013).

$$g^n - g_0^n = Kt \quad \text{Equation 5}$$

g and g_0 are respectively the mean grain diameter at the current state and at $t=0$. K and n are parameter from the mean driving force for boundary migration; K is typically proportional to the boundary mobility, n is typically equal to 2 for curved boundaries (Porter and Easterling 1992). An incremental version of the Equation 5 have been proposed by Babu and Lindgren (2013) to permit the use in a rate model as follow,

$$g_{i+1} = \sqrt[n]{g_i^n + K\Delta t} \quad \text{Equation 6}$$

5.6.2 α_w lath thickness

The α lath thickness, linearly linked to the colony scale factor (Tiley 2002), is an indicator of the material strength (Lütjering 1998). Indeed, the yield stress have been reported lower for thicker α lath morphology (Kar et al. 2006). α lath thickness would consequently be an interesting microstructure variable to include in a flow stress model. For simplification in the model, the formation temperature is here assumed to be dominant in determining the Widmanstätten α lath thickness. This parameter has been modelled as described in **Papers B**

MICROSTRUCTURE MODEL

and D. The empirical Arrhenius equation, Equation 7, expresses the temperature dependence of the α lath thickness and the incremental form is shown in Equation 8.

$$t_{lath}^{eq} = k_{lath} e^{-R/T} \quad \text{Equation 7}$$

$$\Delta t_{lath} = \frac{t_{lath}^n X_{\alpha_w}^n + t_{lath}^{eq} \Delta X_{\alpha_w}}{X_{\alpha_w}^n + \Delta X_{\alpha_w}} - t_{lath}^n \quad \text{Equation 8}$$

Determination of the k_{lath} and R parameters used is developed in Section 5.7.3.

5.7 Material input parameters and calibration

When dealing with phenomenological model, material input data parameters are very important.

5.7.1 Equilibrium phase diagram

As presented in section 3.2.1 Figure 9, the equilibrium phase diagram is a representation of the equilibrium state of the metal giving the equilibrium phase fraction at thermodynamic equilibrium changes with temperature. It is thus used in the microstructure model as reference in the calculation of the phase fractions.

The high dependency of the equilibrium on the exact chemical composition of the alloy or the original microstructure (i.e. grain size) makes large variations between the sources as seen in Figure 28. Castro and Seraphin (1966) have determined the volume fraction of the phases present at room temperature after quenching depending on the annealing temperature using both techniques, the X-ray diffraction and a micrographic analysis. Different curves are obtained by resistivity measurements (Malinov et al. 2001b) or X-ray diffractometry (Pederson et al. 2003). Thermodynamics and diffusional phase transformation software such as ThermoCalc (Andersson et al. 2002) have the ability to extend the existing microstructural data but the calculations are likewise dependent on microstructure properties such as grain size. Two examples of calculated curves are also given in Figure 28.

Bearing in mind the natural variation of the equilibrium phase fraction with the changes in microstructure and chemical composition of the alloys, a choice is made on one equilibrium curve in **Paper C** where a numerical description of a best fit equilibrium curve was adopted. The same equilibrium curve have been used in **Paper D**, however a new adjustment of the same curve have been done in **Paper E** regarding the knowledge of the complementary experimental data origin (Malinov et al. 2001a) for the coupled plastic flow model.

5.7.1 Transformation kinetic parameters for diffusional β to α phases

As stated in section 5.5.1, the JMAK model is used for the formation of grain boundary and Widmanstätten α phases. For each transformation temperature step, it is necessary to know the fraction of phases in equilibrium (by the end of the transformation), the transformation start time, and the N and k coefficients of the JMAK law (or two characteristic times to determine the values). This type of model has been first established for steels (Denis et al. 1992; Fernandes et al. 1985), and more recently also for titanium alloys (Kelly et al. 2005; Sha and Malinov 2009; Teixeira et al. 2007). Kinetics and physical modelling of TTT-diagrams for Ti-6Al-4V based on JMAK theory is used here to model the diffusional phase transformations. Two approaches can be considered to calculate the kinetics of transformation: the kinetics is described by comprehensive laws derived from experimental

MICROSTRUCTURE MODEL

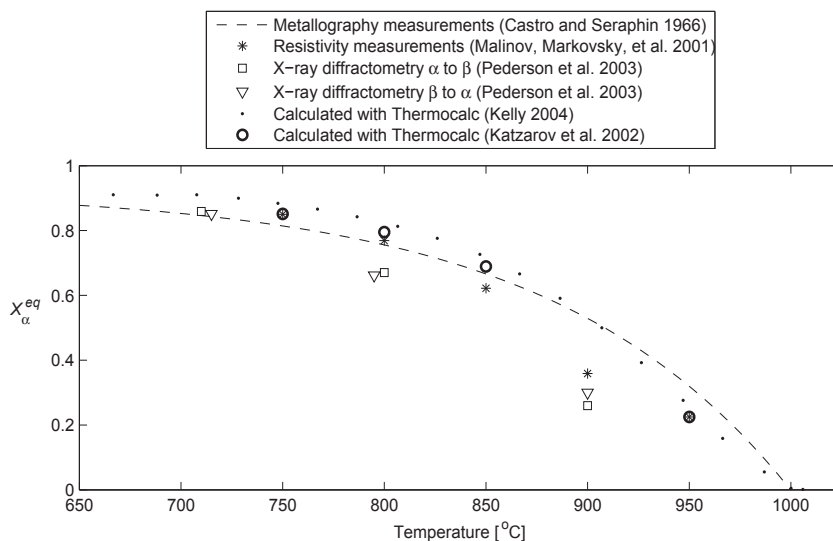


Figure 28. α phase fraction equilibrium diagrams.

TTT-diagrams or experiments that explicitly consider the kinetics of nucleation and growth phases.

The kinetics constants, N and k , in Equation 2 can directly be obtained from several sources. If the difference between grain boundary and Widmanstätten phases is ignored, then the temperature dependent kinetics constants are available in (Malinov et al. 2001a; Malinov et al. 2002) and used in **Paper A**. Although both mechanisms, grain boundary and mixed α structure (that can be assimilated to widmanstätten α in this work) formations have been observed and parameterised (Malinov et al. 2001b), the results do not cover the entire necessary temperature range and transformations. Since the temperature dependency of these parameters do not cover the entire transformation window, in Charles and Järsvstråt (2007), temperature independent parameters, $N=1.4$ and $k=0.025$, evaluated from (Malinov et al. 2001b), was used pending more calibration of the temperature dependence during metal deposition conditions.

TTT-diagrams provide graphical information on the transformations, see Section 5.2.2. However, the published diagrams show large variations for the titanium alloy Ti-6Al-4V (Castro and Seraphin 1966; Malinov et al. 2001a; Malinov et al. 2001b; Vander Voort 1991). Their differences can be appreciated in **Paper C (Figure 4)**. Phase diagram calculation based on thermodynamics are also an alternative (Chang et al. 2004) such as the calculated TTT-diagram used in Kelly (2004). The principle is based on the computational thermodynamics known as the CALPHAD (*CAL*culat*ion of PH*ase *Diagrams*) method (Saunders 1995; Saunders and Miodownik 1998). Then, in **Paper B**, the TTT-diagram published in Kelly (2002) for a Ti-6Al-4V with similar alloy composition is used in the

MICROSTRUCTURE MODEL

calculation of the phase fractions. In **Paper C**, the kinetic parameters for the α_{gb} variant are still estimated from the TTT-diagram in Kelly (2004). The kinetic parameters for the α_w variant are further calibrated as described in **Paper C** (section 4.2).

5.7.2 Parameters for transformation of α to β phase

The JMAK parameters N and k for the transformation of α to β phase have been calculated by Elmer and co-workers (Elmer et al. 2005a; Elmer et al. 2004; Elmer et al. 2005b) based on their experiment results. The obtained parameters are outside the expected ranges based on the nucleation and growth theory (Avrami 1941; Porter and Easterling 1992) and thus questionable. Malinov et al. (2001b) values, although not covering the entire temperature range, have been used in **Paper A** and (Charles and Järsvstråt 2007).

The model in Equation 3, Section 5.5.2, was formulated by (Kelly 2004; Kelly et al. 2005). The kinetic data have been obtained by Kelly (2004) by calculation of the isothermal growth rate based on a simple cell diffusion model in DICTra (Andersson et al. 2002) and using the rules of additivity to determine the non-isothermal dissolution kinetics. The results used for the model of the α dissolution is proposed in a dissolution function, $f_{diss}(T) = 2.2 \times 10^{-31} T^{9.89}$, used in Equation 3. This model is used in **Papers C, D and E**. Details about how the dissolution is implemented is available in **Paper C**.

5.7.3 Martensite transformation parameters

The model in Equation 4 requires the martensitic start temperature. This temperature, as discussed in **Paper C**, has a wide range of values in the literature. It varies from 575°C (Ahmed and Rack 1998) to 800°C (Boyer et al. 1994). Its effect on the computed martensite formation is shown in Figure 29. No large variations in the formed α_m variant are observed. The T_{ms} value of 575°C has been selected in the current work. Only few papers address the topic of the Koistinen-Marburger coefficient, $coef_{km}$. Fan et al. (2005) evaluated the coefficient to 0.003 after experiments by Malinov et al. (2001a). The author of the current thesis evaluated the same parameter from spot weld experiments (Elmer et al. 2005b) to be 0.005. It can nevertheless be observed that numerical tests with a $coef_{km}$ up to 0.015 does not show a large impact on the results when computed in the full model.

Regarding α_m recovery, the only information known to the author at this subject by Gil Mur et al. (1996) has been used in this work. The values for the kinetic parameters, k and N , are thus taken from Gil Mur et al. (1996). They determined the kinetics of the transformation through hardness measurements and obtained the values reported in Table 6.

Table 6. JMAK kinetics parameters for martensite recovery transformation (Gil Mur et al. 1996).

T [°C]	0	400	500	700	800	1900
N	1.019	1.019	1.015	1.025	1.031	1.031
k	0.667	0.667	1.106	1.252	1.326	1.326

MICROSTRUCTURE MODEL

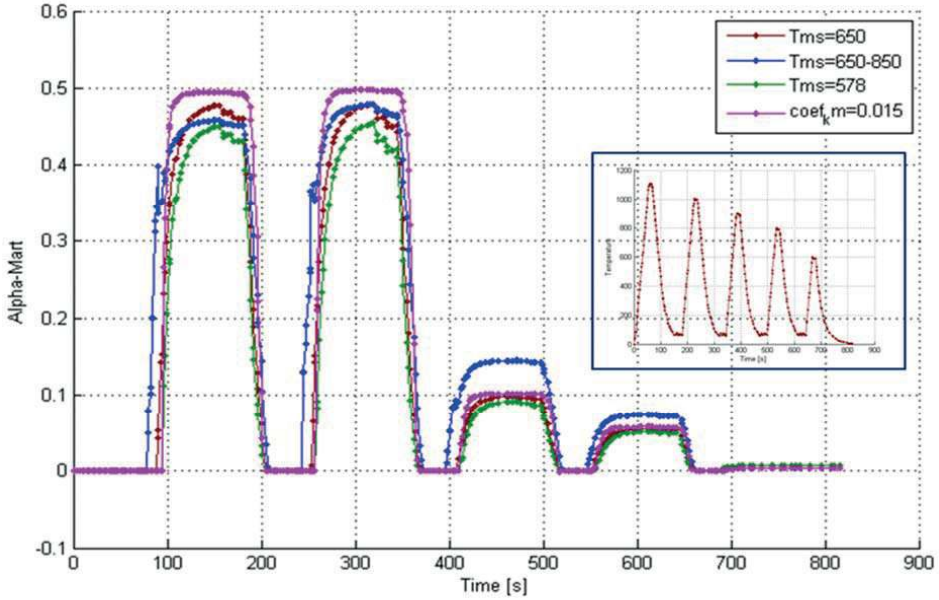


Figure 29. Sensitivity analysis for T_{ms} and coefficient $coef_{km}$ used in the martensite formation equation.

5.7.4 Parameters of lath thickness model

The parameters k_{lath} and R_{lath} in Equation 5, presented in Section 5.6.2, have been evaluated from (Gil et al. 2001) for quenching from the temperatures of 1050 and 1100°C, see Figure 30. Then further calibration have been performed with experimental measurements of single weld bead metal deposited wall samples shown in Figure 31 for the cases listed in Table 4. The 2nd column in Table 7 shows the first set of values. Figure 31 shows simulation results from the calibration tests. Discrepancy in simulation result can be observed when the model is applied for a three weld beads wall samples (see sample 5-27 in Figure 31) showing the limitation of the model. Irwin et al. (2015) proposed other values for the parameters based on calibration with experimental results of their own. The new suggested values are better and are within the expected range, see 3rd column Table 7.

Table 7. Parameters in the calculation of α lath thickness.

	Paper B	(Irwin et al. 2015)
Arrhenius prefactor k_{lath} (μm)	18400	1.42
Activation Temperature R_{lath} (K)	10044	294
Initial condition $t_{\alpha-lath}^0$ (μm)	1	1

MICROSTRUCTURE MODEL

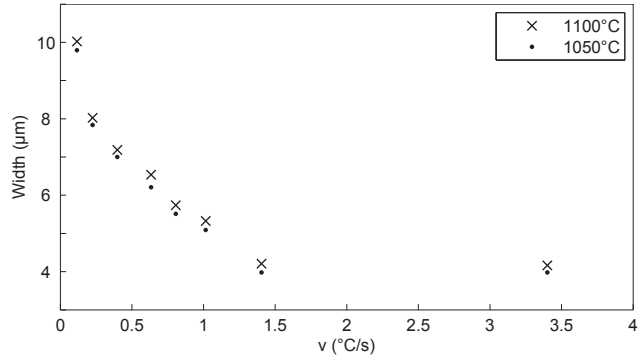


Figure 30. Width of α -Widmanstätten plates in relation to the cooling rate with data from Gil et al. (2001).

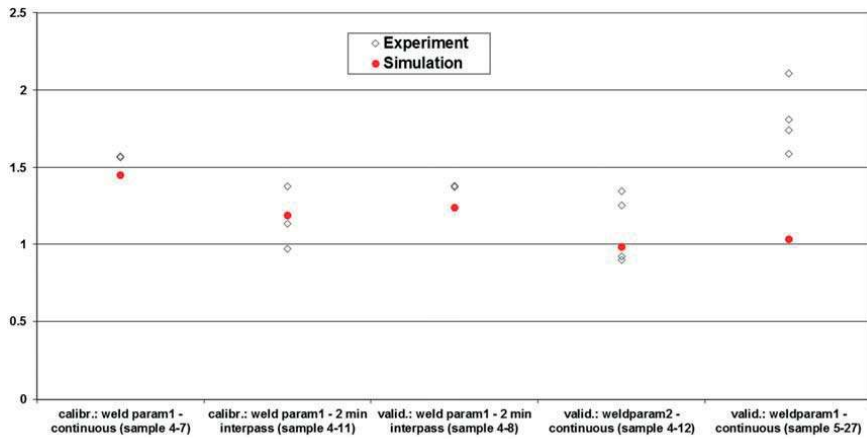


Figure 31. α lath thickness (μm): model versus experiments (see Table 5, Section 3.3).

5.8 Implementation of microstructure model

The microstructure is represented by a set of state variables. There are four phase constituent's fractions and one morphology parameter denoted as

- Grain boundary α_{gb} fraction $X_{\alpha_{gb}}$,
- Widmanstätten α_w fraction X_{α_w} ,
- Martensite and massive α_m fraction X_{α_m} ,
- β phase fraction X_{β} ,
- Widmanstätten lath thickness $t_{\alpha-lath}$.

These variables are updated using the previous described models listed below.

MICROSTRUCTURE MODEL

These variables are updated using the previous described models listed below.

- Diffusional β to α_w transformation, sections 5.5.1 and 5.7.1.
- Diffusional β to α_{gb} transformation, sections 5.5.1 and 5.7.1.
- Diffusional α_w to β transformation, sections 5.5.2 and 0.
- Diffusional α_{gb} to β transformation, sections 5.5.2 and 0.
- Instantaneous β to α_m transformation, sections 5.5.3 and 5.7.2.
- Diffusional α_m to α_{gb} , α_w and β transformation, sections 5.5.1 and 5.7.2.
- Widmanstätten lath thickness formation, sections 5.6.2 and 5.7.3.

In reality, several of the listed transformations can occur simultaneously and are potentially interacting with each other. The logic used to determine what transformations are active at a given temperature is described in the next section.

The basic models are concerned with a phase 1 transforming to a phase 2. Their fractions start with 100% and 0% and end with 0% and 100%, respectively. The adaptations of the models to incomplete transformations as well as the presence of more than two phases are detailed in **Paper C**.

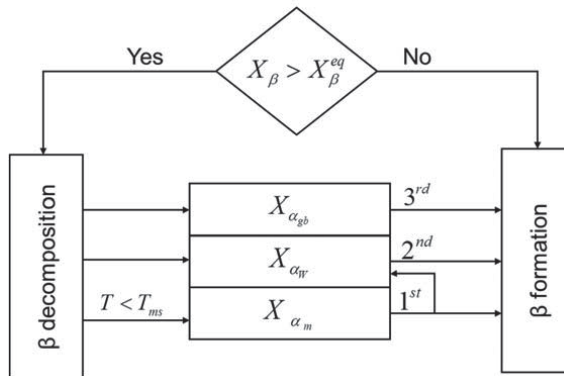


Figure 32. Overall model logic from **Paper C**.

A certain order for the transformations has been adopted for the model. The logic is shown in Figure 32 and the flowchart in Figure 33. The solid or liquid state is checked first. If the temperature is higher or equal to the melting temperature, T_{melt} , then each state variable are is set to zero value as they are describing the microstructure only at the solid state of the material; the phase fractions are later reset on solidification. If the temperature is below T_{melt} , the β equilibrium fraction for the current temperature is computed. This determines whether β phase will form or decompose. The existing amount of β phase is compared with the current equilibrium value. If it is larger than the current equilibrium value, then β is dissolved into α_{gb} and/or α_w followed by an eventual martensite formation. If the β fraction is below the equilibrium value, then existing martensite is recovered to α_w and β phases. The martensite formation, detailed in Figure 34, is computed according to the Koistinen-Marburger equation. If martensite exists and the temperature is higher than the martensite start temperature (T_{ms}), then martensite recovery is computed. The α lath thickness is then evaluated using the updated α_w phase fraction and the current temperature.

MICROSTRUCTURE MODEL

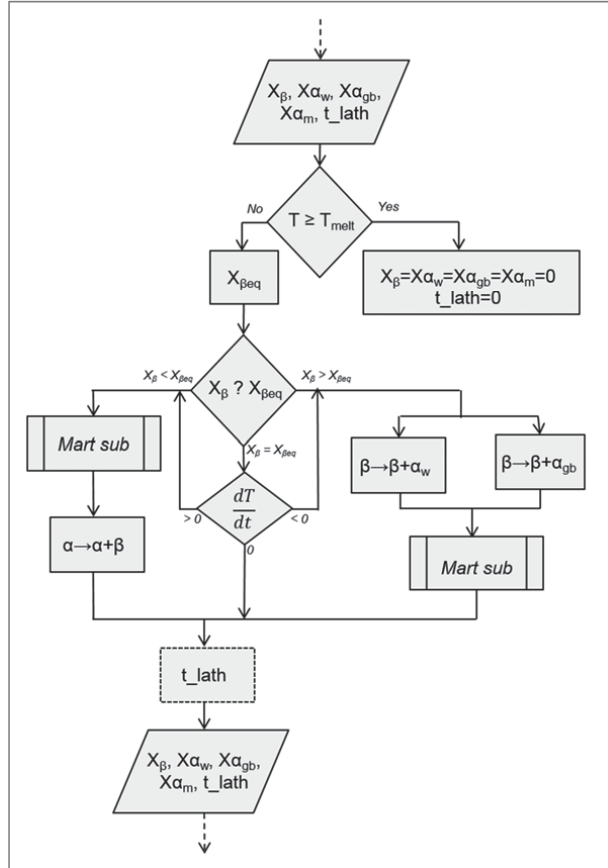


Figure 33. Flowchart for microstructure model implementation.

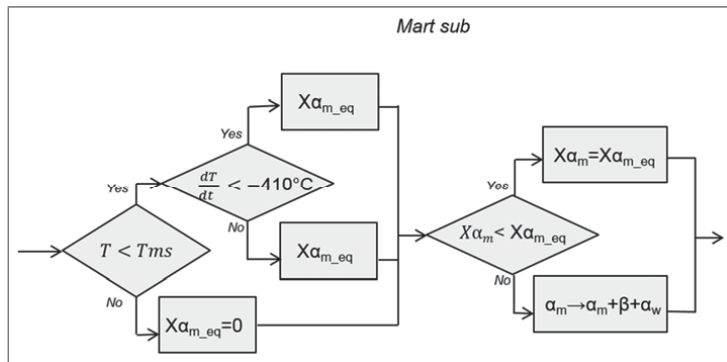


Figure 34. Flowchart of the martensite model part.

MICROSTRUCTURE MODEL

The microstructure model is applicable for general temperature histories. It is implemented as user subroutine for MSC.Marc, a finite element analysis tool to simulate the additive manufacturing process. The user subroutine is called at each time increment for each integration point of the finite element model. Temporal substeps are used in **Paper D** to assure that the computing steps are adapted to the microstructure model demand individually per integration point. This alleviates the need for very small global time step in the simulation.

5.9 *Microstructure model validation*

The difficulty to accurately measure the microstructure when evolving with steep temperature history must be considered in implementation as model calibration and validation. Striving for extreme numerical accuracy is a waste as well as trying to make a perfect fit in model calibration versus a specific set of tests. **Paper B** gives computed α fraction for cycling heating tests. Alternatives have been to use published experimental measurements during temperature variations with differential scanning calorimetry, X-ray or synchrotron X-ray diffraction such as specified in **Paper C**. Qualitative validation by graphical comparison was presented in **Paper C**. Results from microstructure model simulation are estimated to be accurate enough for the application in consideration in this thesis. The variations and discrepancies observed are explained through the previous choices made during the calibration steps where it has been necessary to select a medium behaviour to keep the model more general in its application on the type of thermal histories that can be applied and simulated with.

Some microstructure constituents in Ti-6Al-4V are particularly difficult to determine with microscopy as observed in **Paper D**. The grain boundary alpha α_{gb} exists in very small quantities and thus is difficult to separate optically, making any quantitative measurements imprecise. Thus, neither calibration nor validation was possible for the predicted separation between different types of α . A much larger amount of measurements or fitting parameters would be appreciable to accomplish a better fitting.

The validation of the Widmanstätten lath thickness model for metal deposition simulations have been done in **Paper D** with success. The simulations results agree well with the experimental measurements made on several selected cross sections of deposited walls.

6 APPLICATION OF THE MODEL

6.1 Wire feed additive manufacturing simulation

Wire feed additive manufacturing is a complex process involving thermal, mechanical and microstructural changes in the built pieces. Computational Welding Mechanics (CWM) have established methods and models, originally developed for welding processes, to obtain optimal material performances (Lindgren 2007). Similar to multipass welding, the wire feed metal deposition process can be simulated using CWM. The process is typically divided into different fields; thermal field, microstructure field and mechanical field, as illustrated in Figure 35 and **Paper E (Figure 1)**. The metal deposition process is thermally modelled in **Papers B and D** and the microstructure model is only post processed. That means that it is computed from temperature fields.

A single weld bead wall was modelled in **Papers A and B**. The experimental set-up, developed in **Papers A and B**, consist of wire feed deposited with tungsten inert gas heat source in argon flow chamber, see Figure 36. The wall is deposited on a 1.2 mm thick plate of Ti-6Al-4V. The simulation provides thermal histories at all points of the structure and phase fraction mapping at all time during the deposition process. Phase fractions α and β , **Paper A**, are simulated with the heat input model and thermal simulations from (Lundbäck and Lindgren 2011). Results during deposition of the 4th layer are illustrated in Figure 37. A finer 2D simulation mesh, **Paper B**, is also used for the microstructure simulation. Figure 38 shows a photograph of more complex geometry that is simulated using the microstructure model from **Paper C**. Several weld bead walls have been deposited on plate under the set-up conditions in **Paper D**. Figure 39 shows the 3D simulation of the deposited walls and the obtained results for α_w phase amount.

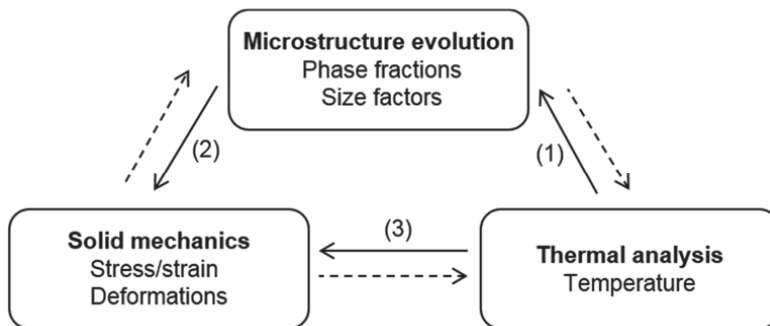


Figure 35. Multiphysics domains in CWM. The arrows represent the potential coupling effects between physic domains; the dotted arrows are likely to have no or little effect comparing to the plain arrows that have stronger coupling effects.

APPLICATION OF THE MODEL



Figure 36. TIG-torch in argon chamber after depositing of the third layer.

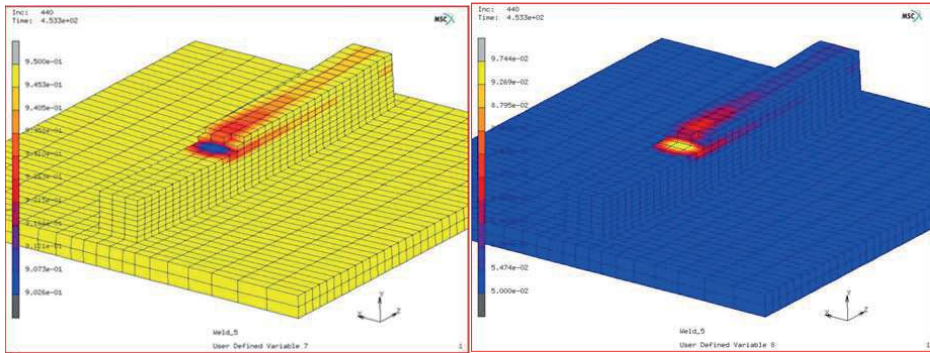


Figure 37. 3D simulation of 4th layer deposition.
Left: Total α phase fraction, Right: β phase fraction.



Figure 38. TIG wire feed deposited wall features in **Paper D**.

APPLICATION OF THE MODEL

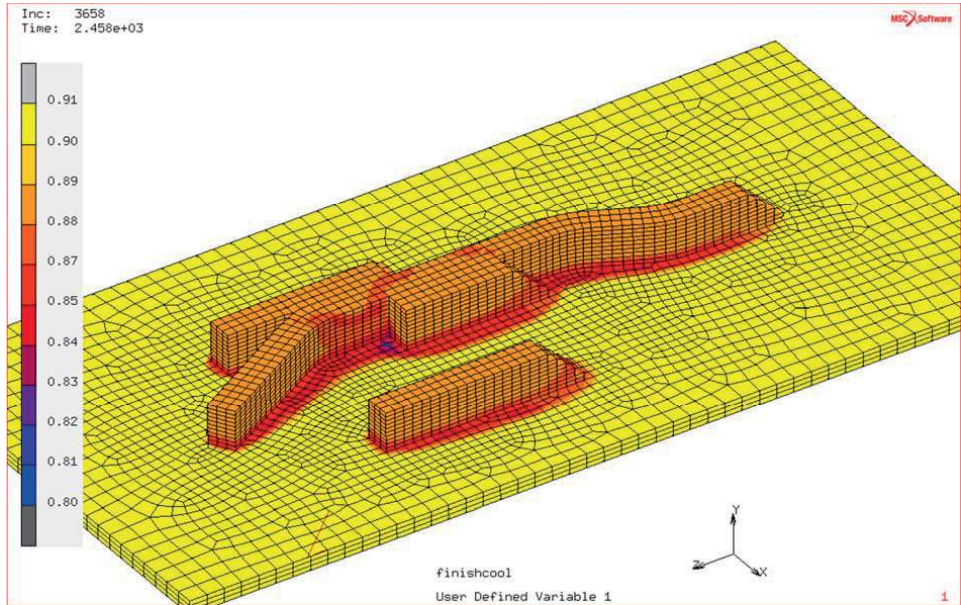


Figure 39. Simulated α_w phase amount at the end of the entire deposition.

6.2 Coupled microstructure and flow stress models

Processes for fabrication, such as welding and metal deposition studied in the present work, do influence the material properties partly via microstructure changes (Donachie 2000). The properties have a temperature dependency even for a fixed microstructure. Further complications in modelling the material properties occur when the microstructure changes. Therefore, coupling microstructure model within the material model for modelling thermo-mechanical processes is of interest. This is particularly important for thermal expansion and plastic properties in the current context of welding and metal deposition. By coupling the models, modelled microstructures are complementing the parameters for the constitutive model (Lindgren et al. 2010).

The constitutive material model is a “dislocation density based model” (Babu 2008; Babu and Lindgren 2013) formulated to cover plasticity and creep properties and taking in consideration the dislocations movements. It is a model utilizing dislocation density and vacancy concentration as internal state variables. It includes globularisation, which is assumed to be responsible for flow-softening and stress relaxation (Babu and Lindgren 2013) through annihilation of dislocation decreasing dislocation density in the material. The phenomenon of globularisation is identified as a two stage process: boundary slipping and edge spheroidisation followed by grain coarsening (Stefansson and Semiatin 2003). It can also be noticed that flow softening rate should not largely be affected by the nature of the originally transformed microstructure (Shell and Semiatin 1999). At temperatures where phase changes

APPLICATION OF THE MODEL

occur, the nucleation and growth of the new phase dissipates the defects of the substructures and results in resetting the material deformation and properties (Babu 2008).

The flow stress model is coupled to the microstructure model in **Paper E** as indicated by arrow 2 in Figure 35. The microstructure model is also used for calculation of the thermal strain. A mixture rule is applied based on the β and the total α phase fractions.

7 SUMMARY OF APPENDED PAPERS

Five papers are appended to the thesis, see Figure 2 for an overview. All the papers have been written in collaboration with co-authors.

7.1 *Paper A*

Development of a Microstructure Model for Metal Deposition of Titanium Alloy Ti-6Al-4V

Corinne Charles and Niklas Järnstråt

The paper presents two principal ideas. It includes a discussion of observed microstructures in samples from RTMwD deposited Ti-6Al-4V. A macroscopically “banded” pattern, considered induced by the consecutive heat input from the fabrication process, reinforced the need for the parallel thermal analysis. The implementation strategy in a FEM thermal simulation is described. A simplified volume phase fraction model (total α , β and α -martensite) is tested in a simulation of a deposited single weld bead wall.

Contribution of the thesis author

The thesis author carried out the metallurgy analysis, major part of the modelling and implemented the metallurgical model for phase transformations using some earlier subroutines developed by the second author. The thesis author wrote major part of the paper.

7.2 *Paper B*

Modelling Ti-6Al-4V microstructure by evolution laws implemented as finite element subroutines: Application to TIG metal deposition

Corinne Charles and Niklas Järnstråt

The paper describes a test case for 2D simulation of an 11 layer metal deposited sample. Distinctions between three α phases’ constituents are added to the microstructure model in paper A. Furthermore, an equation for temperature dependent α lath size formation is implemented. Measured temperatures and evaluated microstructure are compared with calculations. The β phase-front progression induced by the heat transfer profile is identified as a possible correlation to the “banded” pattern. Results of the microstructure simulation are applied to explain fatigue properties.

Contribution of the thesis author

The thesis author carried out major part of the microstructure modelling, implemented the model and carried out the modelling and simulation of the metal deposition process. The thesis author wrote the paper after suggestions from the co-authors.

7.3 Paper C

A model for Ti-6Al-4V microstructure evolution during cyclic temperature changes

Corinne Charles Murgau, Robert Pederson and Lars-Erik Lindgren

The paper described the detailed formulation and implementation of the complete microstructure model. Dissolution of the β phase out of equilibrium is added to the model at heating. The phase representative state variables and the corresponding phase transformations are mathematically formulated in a discretized context for finite element simulation. Sensitivity of the material parameters for the kinetics of phase transformations are discussed and evaluated throughout the calibration. A validation test case with controlled temperature history resembling metal deposition by Babu et al. (2005), is analysed and compared with the microstructure model.

Contribution of the thesis author

The thesis author carried out major part of the microstructure modelling, implemented and calibrated the model and carried out the modelling. The thesis author wrote the paper after suggestions from the co-authors.

7.4 Paper D

Temperature and microstructure evolution in Gas Tungsten Arc Welding wire feed additive manufacturing of Ti-6Al-4V

Corinne Charles Murgau, Andreas Lundbäck, Pia Åkerfeldt and Robert Pederson

A thermo-mechanical finite element model is used to simulate the process of wire feed additive manufacturing. It includes the microstructure model that is evaluated at each integration point in all elements. Temperature field and microstructure evolution are solved for a specific experimental sample comprising of a single, double and three weld beads wall deposited on plate. Predicted phases fractions and α lath thicknesses are compared to experimental measurements.

Contribution of the thesis author

The author contributed in the planning of the simulation work. The author evaluated the results together with the co-authors. The author wrote the major part of the paper after suggestions from the co-authors.

7.5 Paper E

Physically based constitutive model of Ti-6Al-4V for arbitrary phase composition

Bijish Babu, Corinne Charles Murgau and Lars-Erik Lindgren

The paper proposes a physically based flow stress models coupled with microstructure evolution models. The flow stress model is calibrated separately for each phase. It is then combined with the microstructure model. A simple, linear mixture rule is used to compute the macroscopic flow stress. The computed phase fractions from the microstructure model are

SUMMARY OF APPENDED PAPERS

used in this mixture rule. The same principle is used to calculate thermal expansion. The flow stress thus depends not only on the current temperature but also on its complete history embodied in the current phase fractions.

Contribution of the thesis author

The author contributed to the implementation of the microstructure model. The author evaluated the results with the co-authors.

8 Discussions and Conclusions

The following main conclusions can be drawn based on the results presented in the appended papers.

A microstructure model for Ti-6Al-4V has been developed and implemented. The model is thermally driven. It is appropriate for application to large-scale industrial cases. Arbitrary temperature histories, e.g. cyclic thermal loadings as in metal deposition, are well supported by the model. The microstructure of metal deposited material has been investigated contributing to an increased understanding about Ti-6Al-4V behaviour in welding based additive manufacturing. Available solid-solid phase transformation kinetics data in the literature has been collected and compared to each other. Substantial variations between different sources and measurements have been found. This leads to uncertainties in parameter calibration. Sensitive studies have been performed to evaluate this.

The research questions, section 1.2, have been answered by the choice of state variables representing the microstructure constituents, and subsequently by implementation of the corresponding models. The models have been calibrated as well as validated and applied to metal deposition. Moreover, it is applicable to general thermal histories. The microstructure model for Ti-6Al-4V has been successfully coupled to a dislocation density based flow stress model contributing to the improvement of it. The lath size parameter is currently not included in the flow stress model by Babu and Lindgren (2013).

9 Future work

The phase fraction and morphology models have been compared with the metal deposited microstructure and found to be sufficient accurate considering uncertainties in microstructural characterisation. However, a more quantitatively accurate model maybe achieved while revising several of the simplifying assumptions made.

The alloying chemical species' composition, mainly Aluminium and Vanadium, of the phases varies during their formation. This is influencing the kinetics of the phase transformations and the morphologies that are formed; Appolaire et al. (2005) have modelled the β phase formation using the diffusion of the alloying chemical species. Vanadium and Aluminium are in the case of Ti-6Al-4V the elements of interest. This could be applied to the phase formation in Ti-6Al-4V providing that the same assumption stands for diffusion controlled by the elements. Knowing the local chemical composition of the phases will also make it possible to improve the flow stress model accounting for varying solute hardening.

The Widmanstätten and grain boundary α phases were differentiated in the model using two different set of JMAK parameters adapted to integrate the competitive simultaneous transformations. It is however necessary to underline the difficulties encountered when validating the corresponding individual phase fractions. Efforts to quantify the α_{gb} phase fraction in **Paper D** show no-conclusive validation when comparing the experimentally and simulated results. The calculated α_{gb} phase fraction may not correspond to the identified and measured α_{gb} structure in microstructure samples. Is α_{gb} only the thin layer covering the boundary or, as suggested in Malinov et al. (2001b), includes small portion of grain boundary α -phase as well as α -plates diffusionaly grown from the grain boundary. α_w will accordingly be nucleated and grown within the grains. It is thus important to define further the associated definition to α_{gb} and how to measure it for model validation.

Although the microstructure model is has been focus on modelling the phase fractions, it has been shown in section 3.3 that more than one morphology in the microstructure have effect on the properties. It is thus of interest to develop the microstructure model to get information about the formed morphologies such as the prior β grain size and distribution, the α colony sizes, etc... However, to keep the microstructure model efficient for process simulations of large products, simplified grain growth models similar to the α -lath thickness should be accounted for.

The coupling of the microstructure and material models is presented in **Paper E**. Thus utilizing this model in simulation of additive manufacturing cases is the next logical step. Several extensions of the coupling between microstructure and plastic flow models are possible. Semiatin and Bieler (2001b) have shown that the α lath thickness do affect the plastic flow. Their work could be the starting point for incorporating the α lath thickness into the constitutive modelling.

Although microstructure is known to affect the mechanical properties of the material, the reverse is also to be considered. Forming is inducing mechanical loading on the material that causes microstructure changes even at a constant temperature. In such processes, the effect of deformation (plastic energy, dislocations movement) on phase transformations may have a significant impact.

Future work

A preferred orientation of the prior β crystal related to the heat flow has been observed, see Figure 40. This causes a strong anisotropy of the mechanical properties. Development of additive manufacturing for tailoring a more homogeneous microstructure are on-going; minimizing the banding formation by varying the process parameters during the deposition (Cerjak 2008), minimizing the microstructure discontinuities by mechanically rolling processing between the deposition of each layer (Donoghue et al. 2016), post heat treatments outside the standardised frames to obtain a more homogenised microstructure (Brandl and Greitemeier 2012) and improve ductility (Vrancken et al. 2012). The microstructure model may assist in this development.

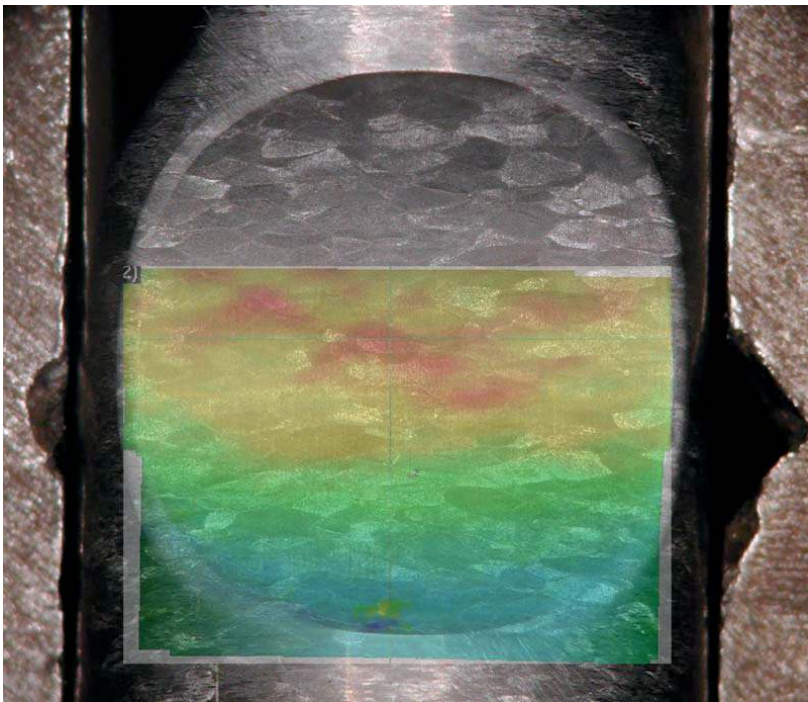


Figure 40. Optically measured surface strain in the direction of applied load (vertical in the figure).

REFERENCES

- Ahmed, T., and Rack, H. J. (1998). "Phase transformations during cooling in $\alpha+\beta$ titanium alloys". *Mater. Sci. Eng., A*, 243(1-2), 206-211.
- Alberg, H. (2005). "Simulation of welding and heat treatment : modelling and validation". PhD thesis, Luleå University of Technology, Sweden, 2005:33, Luleå.
- Andersson, J. O., Helander, T., Höglund, L., Shi, P., and Sundman, B. (2002). "Thermo-Calc and DICTRA, computational tools for materials science". *Calphad*, 26(2), 273-312.
- Appolaire, B., Hericher, L., and Aeby-Gautier, E. (2005). "Modelling of phase transformation kinetics in Ti alloys - Isothermal treatments". *Acta Mater.*, 53(10), 3001-3011.
- Avrami, M. (1939). "Kinetics of phase change, I. General theory". *J. Chem. Phys.*, 7, 1103-1112.
- Avrami, M. (1940). "Kinetics of phase change, II. Transformation-time relations for random distribution of nuclei". *J. Chem. Phys.*, 8, 212-224.
- Avrami, M. (1941). "Kinetics of phase change, III. Granulation, phase change, and microstructure". *J. Chem. Phys.*, 9, 177-184.
- Babu, B. (2008). "Physically based model for plasticity and creep of Ti-6Al-4V". Licentiate thesis, Luleå University of Technology, Luleå, Sweden, 2008:40.
- Babu, B., and Lindgren, L.-E. (2013). "Dislocation density based model for plastic deformation and globularization of Ti-6Al-4V". *International Journal of Plasticity* 50, 94-108.
- Babu, S. S., Kelly, S. M., Specht, E. D., Palmer, T. A., and Elmer, J. W. (2005). "Measurement of phase transformation kinetics during repeated thermal cycling of Ti-6Al-4V using time-resolved X-ray diffraction". In: *International Conference on Solid-Solid Phase Transformations in Inorganic Materials*, Phoenix, AZ, United States, Minerals, Metals and Materials Society, Warrendale, PA 15086, United States, Vol. 2, 503-508.
- Banerjee, S., and Mukhopadhyay, P. (2007). *Phase transformations : examples from titanium and zirconium alloys*, Elsevier/Pergamon, Amsterdam ; Oxford.
- Baufeld, B., Biest, O. V. d., and Gault, R. (2010). "Additive manufacturing of Ti-6Al-4V components by shaped metal deposition: Microstructure and mechanical properties". *Materials & Design*, 31, Supplement 1(0), S106-S111.
- Baufeld, B., Brandl, E., and van der Biest, O. (2011). "Wire based additive layer manufacturing: Comparison of microstructure and mechanical properties of Ti-6Al-4V components fabricated by laser-beam deposition and shaped metal deposition". *Journal of Materials Processing Technology*, 211(6), 1146-1158.

REFERENCES

- Bertrand, P., and Smurov, I. (2007). "Laser assisted direct manufacturing". In: *International Conference on Lasers, Applications, and Technologies 2007: Laser-assisted Micro- and Nanotechnologies*, Minsk, Proc. SPIE (Society of Photographic Instrumentation Engineers), Vol. 6732, 67320H.
- Bontha, S., Klingbeil, N. W., Kobryn, P. A., and Fraser, H. L. (2006). "Thermal process maps for predicting solidification microstructure in laser fabrication of thin-wall structures". *Journal of Materials Processing Technology*, 178(1-3), 135-142.
- Boyer, R., Collings, E. W., and Welsch, G. (1994). *Materials properties handbook : titanium alloys*, ASM International, Materials Park, OH.
- Boyer, R. R., and Furrer, D. U. (2004). "The potential advantages of microstructure modeling of titanium to the aerospace industry". In: *Materials Processing and Design: Modeling, Simulation and Applications - NUMIFORM 2004*, Columbus, Ohio (USA), American Institute of Physics Conference Series, Vol. 712, 1694-1699.
- Brandl, E., and Greitemeier, D. (2012). "Microstructure of additive layer manufactured Ti-6Al-4V after exceptional post heat treatments". *Materials Letters*, 81(0), 84-87.
- Brandl, E., Michailov, V., Viehweger, B., and Leyens, C. (2011a). "Deposition of Ti-6Al-4V using laser and wire, part I: Microstructural properties of single beads". *Surface and Coatings Technology*, 206(6), 1120-1129.
- Brandl, E., Palm, F., Michailov, V., Viehweger, B., and Leyens, C. (2011b). "Mechanical properties of additive manufactured titanium (Ti-6Al-4V) blocks deposited by a solid-state laser and wire". *Materials & Design*, 32(10), 4665-4675.
- Brice, C. A. (2011). "Net shape processing of titanium alloys for enhanced performance and improved affordability". In: *Ti-2011, the 12th world conference on Titanium*, Beijing, China.
- Cahn, J. W. (1956). "Transformation kinetics during continuous cooling". *Acta metall.*, 4(6), 572-575.
- Callister, W. D. (2007). *Materials science and engineering : an introduction*, 7th ed. Ed., Wiley, New York ; Chichester.
- Castro, R., and Seraphin, L. (1966). "Contribution in the metallographic and structural study of the alloy of titanium TA6V (in French)". *Les mémoires scientifiques de la Revue de métallurgie/Scientific memories seen again by metallurgy*, 63(12), 1025-1058.
- Cerjak, H. (2008). "Aspects on the joinability for advanced designs - Keynote 6: Properties and structural integrity of weldments". In: *8th international conference on Trends in Welding Research*, Pine Mountain, Georgia USA.

REFERENCES

- Chang, Y. A., Chen, S., Zhang, F., Yan, X., Xie, F., Schmid-Fetzer, R., and Oates, W. A. (2004). "Phase diagram calculation: past, present and future". *Prog. Mater. Sci.*, 49(3-4), 313-345.
- Charles, C., and Järsvstråt, N. (2007). "Modelling microstructure evolution in weld deposited titanium". In: *the 4th NAFEMS Nordic Seminar: MATERIALS MODELING - FEA Simulations of the Behavior of Modern Industrial Materials Including their Failure*, Oslo (Sandvika), Norway.
- Chen, Q., Ma, N., Wu, K., and Wang, Y. (2004). "Quantitative phase field modeling of diffusion-controlled precipitate growth and dissolution in Ti-Al-V". *Scripta Materialia*, 50(4), 471-476.
- Chraponski, J., and Szkliniarz, W. (2001). "Quantitative metallography of two-phase titanium alloys". *Materials Characterization*, 46(2-3), 149-154.
- Christian, J. W. (2002). *The theory of transformations in metals and alloys. Part I*, Pergamon, Amsterdam.
- Connor, L. P. (1987). *Welding handbook. Vol. 1, Welding technology*, American Welding Society, Miami, Fla.
- Dallair, m., and Furrer, D. (2004). "Quantitative metallography of ti alloys". *Advanced Materials and Processes*, 162(12), 25-28.
- Denis, S., Farias, D., and Simon, A. (1992). "Mathematical model coupling phase transformations and temperature evolutions in steels". *ISIJ International*, 32(3), 316-325.
- Ding, D., Pan, Z., Cuiuri, D., and Li, H. (2015). "Wire-feed additive manufacturing of metal components: technologies, developments and future interests". *The International Journal of Advanced Manufacturing Technology*, 1-17.
- Ding, R., and Guo, Z. X. (2004). "Microstructural evolution of a Ti-6Al-4V alloy during β -phase processing: experimental and simulative investigations". *Materials Science and Engineering A - Multiscale Materials Modelling*, 365(1-2), 172-179.
- Donachie, M. J. (2000). *Titanium : a technical guide*, Second Ed., ASM International, Materials Park, Ohio.
- Donoghue, J., Antonyamy, A. A., Martina, F., Colegrove, P. A., Williams, S. W., and Prangnell, P. B. (2016). "The effectiveness of combining rolling deformation with Wire-Arc Additive Manufacture on β -grain refinement and texture modification in Ti-6Al-4V". *Materials Characterization*, 114, 103-114.
- Duley, W. W. (1999). *Laser welding*, Wiley, New York.
- Easterling, K. (1993). *Introduction to the physical metallurgy of welding*, Second Ed.
- Elmer, J. W., Palmer, T. A., Babu, S. S., and Specht, E. D. (2005a). "In situ observations of lattice expansion and transformation rates of α and β phases in Ti-6Al-4V". *Mater. Sci. Eng., A*, 391(1-2), 104-113.

REFERENCES

- Elmer, J. W., Palmer, T. A., Babu, S. S., Zhang, W., and DebRoy, T. (2004). "Phase transformation dynamics during welding of Ti-6Al-4V". *J. Appl. Phys.*, 95(12), 8327-8339.
- Elmer, J. W., Palmer, T. A., Babu, S. S., Zhang, W., and DebRoy, T. (2005b). "In-situ observations of phase transformations in the fusion zone of Ti-6Al-4V alloy transient welds using synchrotron radiation". In: *Mathematical Modelling of weld phenomena 7*, H. Cerjak, H. K. D. H. Bhadeshia et al., eds., Verlag der Technischen Universität Graz, 343-361.
- Escobar-Palafox, G., Gault, R., and Ridgway, K. (2011). "Robotic manufacturing by shaped metal deposition: state of the art". *Industrial Robot: An International Journal*, 38(6), 622-628.
- Eylon, D., Postans, P. J., Fujishiro, S., and Froes, F. H. (1984). "High-temperature titanium alloys - a review". *Journal of Metals*, 36(11), 55-62.
- Fan, Y., Cheng, P., Yao, Y. L., Yang, Z., and Eglund, K. (2005). "Effect of phase transformations on laser forming of Ti-6Al-4V alloy". *J. Appl. Phys.*, 98(1), 013518.
- Fernandes, F., Denis, S., and Simon, A. (1985). "Mathematical model coupling phase transformation and temperature evolution during quenching of steels". *Mater. Sci. Technol.*, 1(Oct), 838-844.
- Frazier, W. E. (2014). "Metal Additive Manufacturing: A Review". *Journal of Materials Engineering and Performance*, 23, 1917-1928.
- Furrer, D. U., and Semiatin, S. L. (2010). *ASM handbook. Vol. 22A, Fundamentals of modeling for metals processing*, ASM international, Materials Park, Ohio.
- Gil, F. J., Ginebra, M. P., Manero, J. M., and Planell, J. A. (2001). "Formation of α -Widmanstatten structure: effects of grain size and cooling rate on the Widmanstatten morphologies and on the mechanical properties in Ti-6Al-4V alloy". *J. Alloys Compd.*, 329(1-2), 142-152.
- Gil Mur, F. X., Rodriguez, D., and Planell, J. A. (1996). "Influence of tempering temperature and time on the alpha prime Ti-6Al-4V martensite". *J. Alloys Compd.*, 234(2), 287-289.
- Gong, X. (2014). "Microstructural characterizations and modeling of Ti-6Al-4V parts made by electron beam additive manufacturing (EBAM)". The University of Alabama.
- Grong, O., and Shercliff, H. R. (2002). "Microstructural modelling in metals processing". *Prog. Mater. Sci.*, 47(2), 163-282.
- Grujicic, M., Cao, G., and Figliola, R. S. (2001). "Computer simulations of the evolution of solidification microstructure in the LENSTM rapid fabrication process". *Appl. Surf. Sci.*, 183(1-2), 43-57.

REFERENCES

- Gyhlesten Back, J., and Lindgren, L.-E. (2016). "Simplified Implementation of the Koistinen-Marburger Model for Use in Finite Element Simulations". In: *11th International Congress on Thermal Stresses 2016*, Salerno, Italy.
- Heralic, A., Charles Murgau, C., Christiansson, A.-K., and Lennartson, B. (2012). "Towards stable high-speed metal-wire deposition, Part I: Process window development". *Optics & Lasers in Engineering*, Submitted Feb. 2012.
- Heralic, A., Christiansson, A.-K., Ottosson, M., and Lennartson, B. (2010). "Increased stability in laser metal wire deposition through feedback from optical measurements". *Optics and Lasers in Engineering*, 48(4), 478-485.
- Heralic, A., Ottosson, M., Hurtig, K., Danielsson, F., and Christiansson, A.-K. (2008). "Automation of a robotised metal deposition system using laser melting of wire". In: *18th International Conference on Flexible Automation and Intelligent Manufacturing (FAIM 2008)*, University of Skövde, Sweden, L. J. d. Vin, ed., Runit AB, Skövde, 122-129.
- Irwin, J., W. Reutezel, E., Michaleris, P., Keist, J., and R. Nassar, A. (2015). "Predicting Microstructure from Thermal History during Additive Manufacturing for Ti-6Al-4V". In: *Materials Science & Technology*, To be published.
- Ivashishin, O. M., and Teliovich, R. V. (1999). "Potential of rapid heat treatment of titanium alloys and steels". *Mater. Sci. Eng., A*, 263(2), 142-154.
- Järvstråt, N., and Sjöström, S. (1993). "Current status of TRAST; a material model subroutine system for the calculation of quench stresses in steel". In: *ABAQUS users' conference 1993*, Aachen, Germany.
- Järvstråt, N., and Tjotta, S. (1996). "Mechanical material model for aluminium extrusions during on-line quenching". *Journal of Engineering Materials and Technology, Transactions of the ASME*, 118(1), 114-119.
- Kar, S., Searles, T., Lee, E., Viswanathan, G. B., Tiley, J., Banerjee, R., and Fraser, H. L. (2006). "Modeling the tensile properties in β -processed α/β Ti alloys". *Metall. Mater. Trans. A*, 37(3), 559-566.
- Katzarov, I., Malinov, S., and Sha, W. (2002). "Finite element modeling of the morphology of β to α phase transformation in Ti-6Al-4V alloy". *Metall. Mater. Trans. A*, 33(4), 1027-1040.
- Katzarov, I., Malinov, S., and Sha, W. (2006). "A phase-field model for computer simulation of lamellar structure formation in γ -TiAl". *Acta Mater.*, 54(2), 453-463.
- Kelly, S. M. (2004). "Thermal and Microstructure Modeling of Metal Deposition Processes with Application to Ti-6Al-4V". PhD thesis, Faculty of the Virginia Polytechnic Institute and State University, United States, Blacksburg, Virginia.
- Kelly, S. M., Babu, S. S., David, S. A., Zacharia, T., and Kampe, S. L. (2005). "A microstructure model for laser processing of Ti-6Al-4V". In: *7th International*

REFERENCES

- Conference on Trends in Welding Research*, Pine Mountain, GA, United States, ASM International, Vol. 2005, 65-70.
- Kelly, S. M., and Kampe, S. L. (2004). "Microstructural evolution in laser-deposited multilayer Ti-6Al-4V builds: Part II. Thermal Modeling". *Metall. Mater. Trans. A*, 35 A(6), 1869-1879.
- Kobryn, P. A., and Semiatin, S. L. (2003). "Microstructure and texture evolution during solidification processing of Ti-6Al-4V". *Journal of Materials Processing Technology (Special Issue containing paper from the conference "Research and Development in Net shape Manufacturing")*, 135(2-3), 330-339.
- Koistinen, D. P., and Marburger, R. E. (1959). "A general equation prescribing the extent of the austenite-martensite transformation in pure iron-carbon alloys and plain carbon steels". *Acta metall.*, 7(1), 59-60.
- Kuban, M. B., Jayaraman, R., Hawbolt, E. B., and Brimacombe, J. K. (1986). "An assessment of the additivity principle in predicting continuous-cooling austenite-to-pearlite transformation kinetics using isothermal transformation data". *Metallurgical Transactions A*, 17(9), 1493-1503.
- Leyens, C., and Peters, M. (2003). *Titanium and titanium alloys: fundamentals and applications*, WILEY-VCH.
- Lindgren, L. E. (2001a). "Finite element modeling and simulation of welding. Part 1: Increased complexity". *Journal of Thermal Stresses*, 24, 141-192.
- Lindgren, L. E. (2001b). "Finite element modeling and simulation of welding. Part 2: Improved material modeling". *Journal of Thermal Stresses*, 24, 195-231.
- Lindgren, L. E. (2001c). "Finite element modeling and simulation of welding. Part 3: Efficiency and integration". *Journal of Thermal Stresses*, 24, 305-334.
- Lindgren, L. E. (2007). *Computational welding mechanics: thermomechanical and microstructural simulations*, Woodhead Publishing Ltd, Boca Raton, CRC Press, Cambridge, England.
- Lindgren, L. E., Babu, B., Charles, C., and Wedberg, D. (2010). "Simulation of manufacturing chains and use of coupled microstructure and constitutive models". In: *International Symposium on Plasticity 2010 and its current applications*, St Kitts, Saint Kitts och Nevis, A. S. Khan and B. Farrokh, eds., NEAT Press.
- Lundbäck, A., and Lindgren, L.-E. (2011). "Modelling of metal deposition". *Finite Elements in Analysis and Design*, 47(10), 1169-1177.
- Lusk, M., and Jou, H.-J. (1997). "On the rule of additivity in phase transformation kinetics". *Metall. Mater. Trans. A*, 28(2), 287-291.
- Lütjering, G. (1998). "Influence of processing on microstructure and mechanical properties of $\alpha+\beta$ titanium alloys". *Mater. Sci. Eng., A*, 243(1-2), 32-45.
- Lütjering, G., Albrecht, J., and Ivasishin, O. M. (1994). "Microstructure and mechanical properties of conventional titanium-alloys". In: *Proceedings of the*

REFERENCES

- TMS Spring Meeting, Feb 27-Mar 3 1994, San Francisco, CA, USA, Minerals, Metals & Materials Soc (TMS), 65.
- Lütjering, G., Albrecht, J., and Ivasishin, O. M. (1995). "Influence of cooling rate and β grain size on the tensile properties of $\alpha+\beta$ Ti-alloys". In: *Titanium '95: Science and Technology*, Birmingham, UK, London Institute of Material, 1163-1170.
- Lütjering, G., and Williams, J. C. (2003). *Titanium*, Springer - Verlag.
- Majorell, A., Srivatsa, S., and Picu, R. C. (2002). "Mechanical behavior of Ti-6Al-4V at high and moderate temperatures - Part I: Experimental results". *Mater. Sci. Eng., A*, 326(2), 297-305.
- Malinov, S., Guo, Z., Sha, W., and Wilson, A. (2001a). "Differential scanning calorimetry study and computer modeling of β to α phase transformation in a Ti-6Al-4V alloy". *Metall. Mater. Trans. A*, 32(4), 879-887.
- Malinov, S., Markovsky, P., Sha, W., and Guo, Z. (2001b). "Resistivity study and computer modelling of the isothermal transformation kinetics of Ti-6Al-4V and Ti-6Al-2Sn-4Zr-2Mo-0.08Si alloys". *J. Alloys Compd.*, 314(1-2), 181-192.
- Malinov, S., Sha, W., and Guo, Z. (2000). "Application of artificial neural network for prediction of time-temperature-transformation diagrams in titanium alloys". *Mater. Sci. Eng., A*, 283(1-2), 1-10.
- Malinov, S., Sha, W., Guo, Z., Tang, C. C., and Long, A. E. (2002). "Synchrotron X-ray diffraction study of the phase transformations in titanium alloys". *Materials Characterization*, 48(4), 279-295.
- Mazumder, J., Dutta, D., Kikuchi, N., and Ghosh, A. (2000). "Closed loop direct metal deposition: art to part". *Optics and Lasers in Engineering*, 34(4-6), 397-414.
- Mendez, P. F., and Eagar, T. W. (2001). "Welding processes for aeronautics". *Advanced Materials & Processes*, may 2001, 39-43.
- Mishra, S., and DebRoy, T. (2004). "Measurements and Monte Carlo simulation of grain growth in the heat-affected zone of Ti-6Al-4V welds". *Acta Mater.*, 52(5), 1183-1192.
- Oddy, A. S., McDill, J. M. J., and Karlsson, L. (1996). "Microstructural predictions including arbitrary thermal histories, re-austenization and carbon segregation effects". *Can. Metall. Q.*, 35(3), 275-283.
- Pederson, R., Babushkin, O., Skystedt, F., and Warren, R. (2003). "Use of high temperature X-ray diffractometry to study phase transitions and thermal expansion properties in Ti-6Al-4V". *Mater. Sci. Technol.*, 19(11), 1533-1538.
- Picu, R. C., and Majorell, A. (2002). "Mechanical behavior of Ti-6Al-4V at high and moderate temperatures - Part II: constitutive modeling". *Mater. Sci. Eng., A*, 326(2), 306-316.
- Porter, D. A., and Easterling, K. E. (1992). *Phase transformations in metals and alloys*, Second Ed., Chapman & Hall, London.

REFERENCES

- Qazi, J. I., Senkov, O. N., Rahim, J., and Froes, F. H. (2003). "Kinetics of martensite decomposition in Ti-6Al-4V-xH alloys". *Mater. Sci. Eng., A*, 359(1-2), 137-149.
- Qian, L., Mei, J., and Wu, X. (2005). "The effects of thermal history on microstructures of direct-laser-fabricated Ti-6Al-4V alloy". In: *24th International Congress on Applications of Lasers and Electro-Optics, ICALEO 2005, Oct 31-Nov 3 2005*, Miami, FL, United States, Laser Institute of America, Orlando, FL 32826, United States, 502-511.
- Reti, T., and Felde, I. (1999). "A non-linear extension of the additivity rule". *Comput. Mater. Sci.*, 15(4), 466-482.
- Robinson, M., Lippold, J. C., Harwig, D. D., and Lawmon, J. (2002). "Thermal cycle effects on α -case characteristics in titanium welds". In: *Trends in Welding Research: Proceedings of the 6th International Conference, Apr 15-19 2002*, Phoenix, AZ, United States, ASM International, 768-772.
- Rooks, B. (2005). "Assembly in aerospace features at IEE seminar". *Assembly Automation*, 25(2), 108-111.
- Russ, J. C. (2002). *The image processing handbook [Elektronisk resurs]*, Fourth Ed., CRC, Boca Raton.
- Russ, J. C., and Dehoff, R. T. (2005). *Practical Stereology*, Second Ed., Plenum Press, New York.
- Saunders, N. (1995). "Modelling of phase equilibria in Ti-alloys". In: *Titanium '95: Science and Technology*, Institute of Materials, London 1996, P.Bleckinsop, W.J.Evans et al., eds., 2167.
- Saunders, N., and Miodownik, A. P. (1998). *CALPHAD : CALculation of PHase Diagrams : a comprehensive guide*, Pergamon, New York ; London.
- Searles, T., Tiley, J., Tanner, A., et al. (2005). "Rapid characterization of titanium microstructural features for specific modelling of mechanical properties". *Measurement Science and Technology*, 16(1), 60-69.
- Seifi, M., Salem, A., Beuth, J., Harrysson, O., and Lewandowski, J. J. (2016). "Overview of Materials Qualification Needs for Metal Additive Manufacturing". *JOM*(march 2016).
- Semiatin, S. L., and Bieler, T. R. (2001a). "The effect of α platelet thickness on plastic flow during hot working of Ti-6Al-4V with a transformed microstructure". *Acta Mater.*, 49(17), 3565-3573.
- Semiatin, S. L., and Bieler, T. R. (2001b). "The effect of alpha platelet thickness on plastic flow during hot working of Ti-6Al-4V with a transformed microstructure". *Acta Materiala*, 49, 9.
- Semiatin, S. L., Seetharaman, V., and Weiss, I. (1999). "Flow behavior and globularization kinetics during hot working of Ti-6Al-4V with a colony alpha microstructure". *Mater. Sci. Eng., A*, 263(2), 257-271.

REFERENCES

- Sha, W., and Malinov, S. (2009). *Titanium alloys: modelling of microstructure, properties and applications*, Woodhead Publishing Ltd, Cambridge, England.
- Shell, E., and Semiatin, S. (1999). "Effect of initial microstructure on plastic flow and dynamic globularization during hot working of Ti-6Al-4V". *Metall. Mater. Trans. A*, 30(12), 3219-3229.
- Short, A. B. (2009). "Gas tungsten arc welding of titanium alloys: a review". *Mater. Sci. Technol.*, 25(3), 309-324.
- Smallman, R. E., and Bishop, R. J. (1999). *Modern physical metallurgy and materials engineering : science, process, applications*, Sixth Ed., Butterworth-Heinemann, Oxford.
- Smith, W. F. (1981). *Structure and properties of engineering alloys*, McGraw-Hill, New York ; London.
- Syed, W. U. H., Pinkerton, A. J., and Li, L. (2005). "A comparative study of wire feeding and powder feeding in direct diode laser deposition for rapid prototyping". *Appl. Surf. Sci.*, 247(1-4), 268-276.
- Teixeira, J. D. C., Appolaire, B., Aeby-Gautier, E., Denis, S., Cailletaud, G., and Späth, N. (2007). "Transformation kinetics and microstructures of Ti17 titanium alloy during continuous cooling". *Mater. Sci. Eng., A*, 448(1-2), 135-145.
- Tiley, J. (2002). "Modeling of microstructure property relationships in Ti-6Al-4V". PhD thesis, The Ohio State University, Ohio.
- Tiley, J., Searles, T., Lee, E., Kar, S., Banerjee, R., Russ, J. C., and Fraser, H. L. (2004). "Quantification of microstructural features in α/β titanium alloys". *Mater. Sci. Eng., A*, 372(1-2), 191-198.
- Todinov, M. (1998). "Alternative approach to the problem of additivity". *Metallurgical and Materials Transactions B*, 29(1), 269-273.
- Vander Voort, G. F. (1991). *Atlas of time-temperature diagrams for nonferrous alloys*, ASM International, Metals Park.
- Wang, F., Williams, S., Colegrove, P., and Antonysamy, A. A. (2012). "Microstructure and Mechanical Properties of Wire and Arc Additive Manufactured Ti-6Al-4V". *Metall. Mater. Trans. A*, 44(2), 968-977.
- Wang, L., and Felicelli, S. (2006). "Analysis of thermal phenomena in LENSTM deposition". *Mater. Sci. Eng., A*, 435-436, 625-631.
- Weman, K. (2003). *Welding processes handbook*, CRC Press ; Woodhead Publishing Ltd, Boca Raton, Cambridge, England.
- Vrancken, B., Thijs, L., Kruth, J.-P., and Van Humbeeck, J. (2012). "Heat treatment of Ti6Al4V produced by Selective Laser Melting: Microstructure and mechanical properties". *J. Alloys Compd.*, 541(0), 177-185.
- Wu, X., and Mei, J. (2003). "Near net shape manufacturing of components using direct laser fabrication technology". *Journal of Materials Processing Technology*, 135(2-3), 266-270.

REFERENCES

- Yang, Z., Sista, S., Elmer, J. W., and DebRoy, T. (2000). "Three dimensional Monte Carlo simulation of grain growth during GTA welding of titanium". *Acta Mater.*, 48(20), 4813-4825.
- Zhang, K., Liu, W., and Shang, X. (2007). "Research on the processing experiments of laser metal deposition shaping". *Optics & Laser Technology*, 39(3), 549-557.
- Zhu, Y. T., Lowe, T. C., and Asaro, R. J. (1997). "Assessment of the theoretical basis of the Rule of Additivity for the nucleation incubation time during continuous cooling". *J. Appl. Phys.*, 82(3), 1129-1137.
- Åkerfeldt, P. (2016). "Additive Manufacturing of Ti-6Al-4V: Relationship between Microstructure, Defects and Mechanical Properties". PhD thesis, Luleå University of Technology, Luleå, Sweden.
- Åkerfeldt, P., Pederson, R., and Antti, M.-L. (2011). "Microstructure and mechanical properties of laser metal deposited Ti-6Al-4V". In: *Ti-2011, the 12th world conference on Titanium*, Beijing, China.

Included Papers

**Development of a Microstructure Model for Metal Deposition
of Titanium Alloy Ti-6Al-4V**

Corinne Charles and Niklas Järvstråt

Proceedings of the 11th World Conference on Titanium (Ti-2007), Kyoto, Japan,
3-7 June 2007

Development of a Microstructure Model for Metal Deposition of Titanium Alloy Ti-6Al-4V

Corinne Charles, Niklas Järvestråt

Department of Technology, Mathematics and Computer Science, University West, SE-461 86 Trollhättan, Sweden

Metal deposition of titanium alloys has received an increasing interest in the aero-engine industry during this decade. Deposition of melted metal layer by layer leads to successive thermal cycles within the material. To ensure required knowledge of the material properties, increased understanding and control of the microstructure are necessary. This study is devoted to the development of a microstructure model for metal deposited titanium alloy Ti-6Al-4V with the intention of coupling it with the constitutive models.

In single bead walls built using Robotised TIG (tungsten inert gas) Metal-wire Deposition (RTMwD), large oriented columnar grains as well as basket-weave and Widmanstätten microstructures were observed using microscopy. Phase fractions and morphology size parameters, such as alpha platelet size, are suggested as representative variables. It is suggested to combine equations based on diffusional and thermodynamic theories with martensitic transformation for a full description. Heating, cooling, as well as successive re-heating involved in the process of metal deposition were taken into account for the modelling.

Numerical simulations of the microstructure evolution have been performed for metal deposited samples. Microstructure observations are discussed, and in their light, adjustments for further improving the prediction of metal deposited material properties are suggested.

Keyword: titanium alloys, metal deposition, microstructure, phase transformation, Ti-6Al-4V

1. Introduction

The structural integrity of components is essential for safety critical products, especially in the aerospace industry. The titanium alloy Ti-6Al-4V is therefore extensively employed in this industry because of its excellent mechanical properties for moderate density. However, the mechanical properties of titanium alloys are very sensitive to the microstructure. Thus, modelling the microstructure development during manufacturing processes such as welding, heat treatment and metal deposition will enable significant advances in the control and optimisation of product quality and reliability.

The thermal history during such manufacturing processes, and in particular during weld metal deposition, is highly complex, including heating, cooling, and re-heating at different and sometimes very rapid temperature changes. Thus, diffusional beta to alpha transformation compete with martensitic transformation, while reverse transformation into beta phase is significant in reheating stages as adjacent layers are deposited.

Despite earlier modelling of similar behaviour in materials such as steel^{1,2)} and the considerable industrial interest in microstructural modelling of titanium alloys, however, microstructural simulation of Ti-6Al-4V for welding, heat treatment and metal deposition seems not to have been attempted until recently³⁻⁵⁾.

The presented modelling approach focuses on the development of the microstructure in solid state, modelling the liquid phase as homogeneous and solidifying into pure beta phase. Further, a point-wise and fully deterministic logic will be employed, implementing the metallurgical model as a set of subroutines for a commercial finite element program, MSC.Marc⁶⁾. This approach dispenses with the need for detailed geometrical description of features such as texture, dendritic structure and grain boundary interactions, at a modest cost in modelling resolution.

The microstructure will be described by a set of scalars and the metallurgy is consequently considered

homogeneous at the nodes. Choices made regarding the modelling of the microstructure for Ti-6Al-4V are presented in this paper. Observation of the Ti-6Al-4V microstructure over a range of process parameters provided a set of quantifiable state variables. The considered phase variables are the relative phase content of beta, alpha, grain boundary alpha and martensite. It is further suggested that one size parameter is associated with each of those phases.

2. Metal Deposition of Ti-6Al-4V

2.1. Experimental procedure of fabrication

Within this study metal deposition refers to Robotised TIG Metal-wire Deposition (RTMwD). The metal deposited titanium alloy is wire feed deposited using a tungsten inert gas (TIG) heat source on a 1.2 mm thick plate as presented in figure 1. Each sample was manufactured in a chamber keeping an oxygen level less than 10 ppm by an argon flow to avoid alpha-case and oxidation.

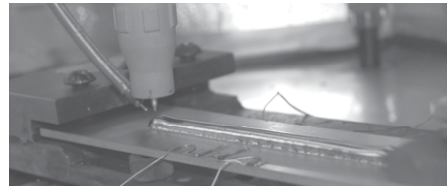


Figure 1. TIG-torch in argon chamber after depositing the third layer.

2.2. As deposited Ti-6Al-4V microstructure

During the metal deposition (MD) process, steep temperature gradients and multiple thermal cycles lead to considerable microstructural changes within a very short time and depending on the position in the sample. Ti-6Al-4V exhibits a variety of microstructures depending on the conditions experienced during cooling transformation from the high-temperature β form to the low-temperature α

form of the alloy, and for the reverse transformations upon reheating.

A microscopic examination of single-walls MD metal cross-sections is used as a representative of the MD microstructures to be modelled. The samples shown were prepared using conventional grinding and polishing techniques and etched by a 2% Kroll solution. Figure 2 represents two optical micrographs in transverse cuts of metal deposited Ti-6Al-4V. Each sample is built in 30 layers of weld metal, each 0.9 mm high. The two walls were made with identical welding parameters, the only difference being a waiting time of 2 minutes between layers for the sample shown in figure 2b. The difference in width is due to the higher material feed required to keep the same layer height.

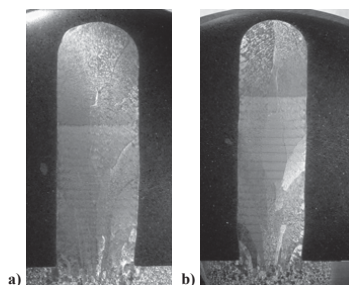


Figure 2. Photographs of metal deposited specimen with clear banding and prior beta grains. The two walls are 27 mm high. **a)** No waiting time between deposition passes. **b)** 2 min waiting time between deposition passes.

A very dense structure with no porosities or defects was observed. The large columnar prior beta grains start out perpendicular to the base plate and widens as they cross multiple deposit layers. Indeed, the size of the prior beta grains is often observed to be as large as 100 μm . The prior beta grains are also outlined by the presence of a continuous alpha phase at the grain boundaries depending on the welding parameters. The visible banding feature observed in figure 2 represents a difference in the alpha morphology sizes. Figure 3 shows a higher magnification of the banding structure; the upper part of the pictures is situated in an inter-band area with the lower part within the band itself. The deposit microstructure shows basket-weave Widmanstätten morphology with an irregular size distribution. The inter-band area shows slightly larger alpha platelets tending to organise in colonies.

It is an interesting observation that a banded structure is visible in the lower part of the specimens, but not in the upper layers. This is not only consistent over the two samples shown here, but have also been observed in other specimens with fewer layers, always with a very similar “band-free” region at the top of the specimen. As each new deposited layer has the same convex shape as the specimen top, we conclude that the horizontal banding is not caused during deposition solidification, but later through supplementary annealing caused by the consecutive heat input at new layers. As further support for this hypothesis, the two samples, although having

different temperature histories do not present the same height of the un-banded top area.

As can be expected by considering that a waiting time between weld passes provides a cooler substrate and thus a quicker quench of the liquid metal, sample b) presents thinner features than sample a). (see figure 3) The 2 minutes waiting time between passes during the manufacturing of sample b) allowed the sample to cool quicker, thus reducing the exposure time at higher temperatures.

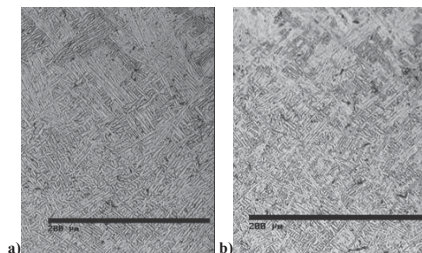


Figure 3. Banding area, black bar is 200 μm . **a)** No waiting time between deposition passes. **b)** 2min waiting time between deposition passes.

No martensite was observed with certainty in our samples, although that could be argued regarding the structure in the top area. A more detailed analysis would probably reveal trace amounts within this area.

3. Metallurgical model

Based on the current understanding of the as-deposited Ti-6Al-4V microstructure presented above, micro-structural features are identified for quantification and as parameters (state variables) for the microstructural model.

The aim of the microstructure modelling is important when selecting representative state variables. In this work, the main aim of the microstructural modelling is to provide information capable of parametrising mechanical properties (thus providing a more physically based constitutive model) in order to predict mechanical behaviour. Initially, the alpha and beta phase fraction has to be followed upon temperature changes in the metal. Also, a distinction between the different alpha morphologies is an important issue for the modelling of the mechanical properties. Although martensitic formation is not observed with certitude in this sample, martensitic transformation is previously reported in Ti-6Al-4V⁷⁾ for cooling rates higher than 410°C/s. This is close to what is experienced in RTMwD, and will probably be exceeded in laser metal deposition⁸⁾, and is therefore considered important for inclusion in the model. Then, associated geometrical or dimensional parameters such as the grain sizes will participate in the determination and calculation of the mechanical properties. As a result, a set of scalar quantities⁹⁾ assignable to integration points in a finite element calculation, are needed.

3.1. Diffusional phase transformations

For diffusion controlled transformations, the Johnson-Mehl-Avrami equation^{10,11)} is adopted, which for pure and isothermal transformation from phase j to phase k , can be written as in equation 1.

$$v_k = \left(1 - \exp^{-B_{jk} t^{N_{jk}}}\right) v_j^0 v_k^{eq} \quad (1)$$

Here, v_j is the current fraction of phase j , v_k is the current fraction of phase k , B_{jk} and N_{jk} are temperature dependent material constants that can be determined e.g. from a TTT-diagram; t is the time since start of transformation, v_j^0 and v_k^{eq} are initial fractions of phase j and the equilibrium fraction of phase k , respectively.

The Finite Element Method allows using isothermal kinetics data by time and space discretisation, so the equation 1 is easily used for both the α to β and β to α transformations. Some of the necessary parameters are available in the literature¹²⁻¹⁶⁾. However, often only some temperature ranges have been studied. As a first approximation, considering the divergence between the available parameters in the literature, a set of arbitrary temperature independent parameters was used, awaiting more accurate parameter determination. The accuracy in the simulation results will of course increase considerably by the future use of properly determined temperature dependent parameters.

3.2. Martensitic transformation

For modelling the martensitic transformation, it is common practice for titanium to assume instantaneous transformation at a specific temperature for any cooling rate higher than approximately 410°C/s⁷⁾. We will, however, employ the for steel established Koistinen-Marburger equation¹⁷⁾, which for transformation of phase j into phase k in the absence of diffusional transformations can be written as:

$$v_k = \left(1 - \exp^{-0.003(T_{ms} - T)}\right) v_j^0 \quad (2)$$

Here, T_{ms} is the start temperature for martensitic transformation, while T is the current temperature and the constant -0.003 is taken from³⁾, and used instead of -0.011 as commonly employed for steels.

According to Gil Mur et al.¹⁸⁾ α^m is decomposed into α and/or β depending on the temperature and the heating time. The decomposition of α^m is controlled by diffusion and considered complete at the temperature of 800°C¹⁸⁾.

4. Numerical simulations

A set of microstructure evolution subroutines has been adapted for use in the Finite Element commercial software MSC.Marc⁶⁾ supporting the computation of the thermo-metallurgical evolution.

4.1. Implementation strategy

The modelling of the microstructure takes into account heating, cooling, as well as successive reheating involved in the process of metal deposition. The thermal

history driving the phase transformations is calculated using Finite Element Method with the commercial software MSC.Marc. Since this method employs a continuum formulation with properties and state variables represented as values in integration points, it is necessary to represent phase transformations and size parameter evolution according to a point-wise logic.

The implementation structure is described in the flowchart, figure 4, as elaborated in a previous paper¹⁹⁾. Transformation data, material properties and initial states are read by the user subroutine USDATA at the first increment and stored in common blocks. During the simulation, the temperature and the time step are supplied by MSC.Marc. The phase contents are calculated in the user subroutine USPCHT, returned to MSC.Marc and stored at each material point between time steps.

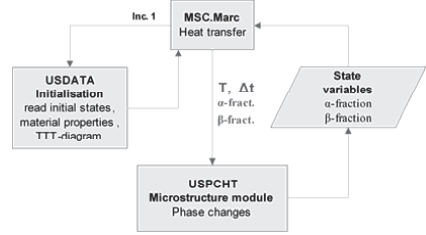


Figure 4. Flowchart of the implementation in MSC.Marc.

4.2. Discretisation of phase transformation

The incremental form, equation 3, used in our model was derived according to Järvestråt & Sjöström¹⁾.

- The diffusion process is assumed to depend on the temperature trough the kinetics parameters B and N .
- The phase fraction at the beginning of the time step is denoted by superscript n . The length of the time step is Δt and the concentration time, t_c , is defined as the time it would have taken to reach the current concentration at the current temperature.
- The sum of original and resultant phase fraction ($v_j + v_k$) is employed to correct for the case of more than one transformation product.

$$\Delta v_k = -\Delta v_j = \left(1 - e^{-B_{jk}(t_c + \Delta t)^{N_{jk}}}\right) \left(v_j^n + v_k^n\right) v_k^{eq} - v_k^n$$

$$t_c = \left[-\ln \left(1 - \frac{v_k^n / v_k^{eq}}{v_j^n + v_k^n}\right) / B_{jk} \right]^{1/N_{jk}} \quad (3)$$

4.3. Numerical test case simulation

As a proof of concept for the simulation tool, a single bead wall metal deposition was modelled employing a reduced model with alpha phase representing a one state variable with one beta to alpha transformation law and one "reverse" alpha to beta transformation law. The simulation provided thermal histories at all

points of the structure and phase content maps, continuously during the process.

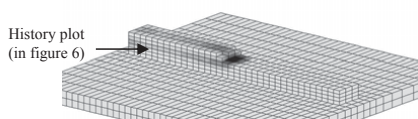


Figure 5. Contour plot of beta to alpha phase content (black to white colour) during deposition of the third layer.

A snapshot of alpha phase / beta content can be seen in figure 5, while a typical temperature and phase history plot is shown in figure 6. It can be noted that for this temperature history, reverse (α into β) transformation only occur once.

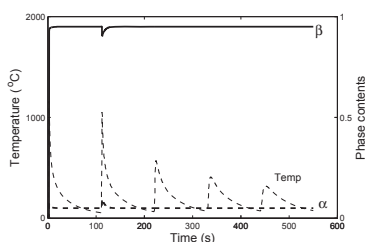


Figure 6. History plot of temperature and phase content history at a node of the FE-model.

5. Concluding remarks

A strategy is presented for modelling the microstructure of Ti-6Al-4V, separating phase transformation models from grain growth models for the different phases. A preliminary implementation in the FE-code MSC.Marc shows promising results, and will also enable simulating metal deposition of more complex geometries, such as multiple-weld walls, flanges or bosses on real aero engine components.

A banded structure is observed in the lower part of MD-specimens that is not present in the upper part. These bands must form late in the thermal history, because they are straight horizontal lines which agree with isotherms only at a certain distance from the curved weld front. Further, the lack of banding in upper parts of the structure indicates that the reheating caused by successive layer additions plays a significant role. More detailed investigations are needed to find out whether the bands are caused by beta formation on reheating or just annealing effects by extended exposure to intermediate temperatures.

Although further experimental data is needed for a complete characterisation of the transformation kinetics and growth laws of MD microstructure, the present observations provide an initial insight in the evolution of a microstructural mixture of Widmanstätten, basket weave and grain boundary alpha. The coupling of experimental quantification to numerical simulation seems a promising approach for gaining deeper understanding of microstructure evolution mechanisms of Titanium alloys.

For this paper, no distinction was initially made between alpha types in the simulations. However, two types of alpha precipitates are planned for consideration: the grain boundary α^{gb} appearing at the prior beta grain boundaries; and the Widmanstätten α^w developing in the matrix²⁰. The difference in kinetics will be modelled by using two different diffusion parameter sets.

Acknowledgements

The authors express gratitude to Mr. Andreas Lundbäck from Luleå University of Technology, Sweden, for performing the weld deposition simulation using our subroutines, and Prof. Lars-Erik Lindgren for his help in the implementation of the model.

The authors acknowledge the financial support from the European 6th Framework Programme through the research project VERDI (Virtual Engineering for Robust manufacturing with Design Integration). See <http://www.verdi-fp6.org>.

REFERENCES

- 1) N. Järsvsträt and S. Sjöström: *ABAQUS users' conference* (Aachen, Germany, 1993).
- 2) N. Järsvsträt and S. Tjøtta: *J. Eng. Materials & Technology* **118** (1996) pp. 114-119.
- 3) Y. Fan, P. Cheng, Y. L. Yao, Z. Yang and K. Egland: *J. Appl. Phys.* **98** (2005) 013518.
- 4) S. M. Kelly, S. S. Babu, S. A. David, T. Zacharia and S. L. Kampe: *Proc. 7th International Conference on Trends in Welding Research*, (ASM International, United States, 2005) pp. 65-70.
- 5) R. G. Thiessen and I. M. Richardson: *Metallurgical & Materials Transactions B* **37** (2006) pp. 293-299.
- 6) MSC Software: *Marc overview*, see <http://www.mssoftware.com/products/marc.cfm>
- 7) T. Ahmed and H. J. Rack: *Mat. Sc. & Eng. A* **243** (1998) pp. 206-211.
- 8) L. Qian, J. Mei and X. Wu: *24th International Congress on Applications of Lasers and Electro-Optics, ICALEO 2005* (Laser Institute of America, United States, 2005) pp. 502-511.
- 9) C. Charles and N. Järsvsträt: *Proc. joint 16th International Conference Computer Technology in Welding and Manufacturing and 3rd International Conference Mathematical Modelling and Information Technologies in Welding and Related Processes*, ed. by Makhnenko, P. W. L. a. P. V. I., (E.O. Paton Electric Welding Institute, NAS of Ukraine, 2006) pp. 151-156.
- 10) M. Avrami: *J. Chem. Phys.* **7** (1939) pp. 1103-1112.
- 11) M. Avrami: *J. Chem. Phys.* **8** (1940) pp. 212-224.
- 12) S. S. Babu, S. M. Kelly, E. D. Specht, T. A. Palmer and J. W. Elmer: *Proc. International Conference on Solid-Solid Phase Transformations in Inorganic Materials 2005*, (Minerals, Metals and Materials Society, Phoenix, United States, 2005) Vol. 2, pp. 503-508.
- 13) J. W. Elmer, T. A. Palmer, S. S. Babu, W. Zhang and T. DebRoy: *J. Appl. Phys.* **95** (2004) pp. 8327-8339.
- 14) S. Malinov, Z. Guo, W. Sha and A. Wilson: *Metallurgical & Materials Transactions A* **32** (2001) pp. 879-887.
- 15) S. Malinov, W. Sha, Z. Guo, C. C. Tang and A. E. Long: *Materials Characterization* **48** (2002) pp. 279-295.
- 16) W. Sha and Z. Guo: *J. Alloy Comp.* **290** (1999) pp. L3-L7.
- 17) D. P. Koistinen and R. E. Marburger: *Acta Metall.* **7** (1959) pp. 59-60.
- 18) F. X. Gil Mur, D. Rodriguez and J. A. Planell: *J. Alloy Comp.* **234** (1996) pp. 287-289.
- 19) C. Charles and N. Järsvsträt: *Proc. 4th NAFEMS Nordic Seminar: MATERIALS MODELING - FEA Simulations of the Behavior of Modern Industrial Materials Including their Failure* (Oslo, Norway, 2007).
- 20) N. Saunders, X. Li, A. P. Miodownik and J.-P. Schille: *Proc 10th World Conference on Titanium, Ti-2003* (Hamburg, Germany, 2003)

**Modelling Ti-6Al-4V microstructure by evolution laws implemented
as finite element subroutines: Application to TIG metal deposition**

Corinne Charles and Niklas Järvstråt

Proceedings of the 8th International Conference on Trends in Welding Research,
Pine Mountain, GA, USA, 1-6 June 2008

Modelling Ti-6Al-4V microstructure by evolution laws implemented as finite element subroutines: Application to TIG metal deposition

C. Charles, N. Järnstråt

University West, Dept of engineering science, Production Technology Centre, Trollhättan, Sweden
corinne.charles@hv.se, +46 520 223315

Abstract

In this paper, microstructure evolution laws for the titanium alloy Ti-6Al-4V have been formulated and adapted for use in finite element simulations of Robotised TIG Metal-wire Deposition (RTMwD). State variables representing the relative phase contents are included, as well as the α lath thickness. Phases considered are the β and α phases, the α phase being further subdivided in colony/grain boundary α , Widmanstätten α and martensite. Heating, cooling, as well as successive re-heating involved in the repetitive process of metal deposition are treated, taking care of the different phase interactions. Diffusional transformations implemented according to the traditional Johnson-Mehl-Avrami and instantaneous formulations are discretised. The metallurgical model is implemented as a set of subroutines, employing a point-wise and fully deterministic logic. The microstructure subroutines are coupled to thermal history simulation of the RTMwD process. The model is applied to TIG metal deposition of Ti-6Al-4V component-like features to provide further understanding of the underlying metallurgical process. The simulation of phase fractions and α lath thickness are exploited to explain observed banding features, and fatigue endurance variations between different manufacturing process settings.

Introduction

Titanium alloy Ti-6Al-4V is extensively used in aerospace applications because of its very good material properties combination, its mechanical properties, however, are very sensitive to the microstructure [1, 2]. When meeting a recently developed fabrication process such as RTMwD it is hence important to consider the microstructure development during the process to support the final material quality evaluation.

Metal deposition, from a process view similar to multi-pass welding, is considered for repairing parts but also as an alternative in component fabrication [3]. The aero-engine industry has shown an interest in the development and understanding of metal deposition processes since the beginning of the 80s. The saving in buy-to-fly material cost is of great interest, especially when using advanced and expensive materials such as Titanium alloys. Laser Metal Deposition has drawn

much attention lately [4], and several laser processes with metal powders have been commercialised in the last few years. However, the use of wire shows a higher deposition rate and lower waste ratio [5]. In the present study, metal wire is fed through a conventional wire feeder and deposited as features on a metal plate using a standard Tungsten Inert Gas (TIG) power source. During the RTMwD process, steep temperature gradients and multiple thermal cycles lead to considerable microstructural changes within a very short time which in turn determines the final material properties. Modelling and simulation are intended for understanding and future control of the metal deposition process.

Consequently to the rapid increase of computing capacities and the last 50 years in research and development of manufacturing processes [6], simulations are considered a powerful tool in modern design including productivity capabilities associated to quality focus. The material model is an important factor in welding simulations [7] and thus in metal deposition simulations. Simulation of the microstructure is a method to understand the complex metallurgy of a deposited metal. Kelly et al. [8] already simulated the thermal history and phase transformations of Ti6Al4V in Laser Metal Deposition (LMD). In association to the purpose of evaluating the final microstructure of the simulated part, the model provides information capable of parametrising mechanical properties in the simulation of the manufacturing process. The density-type microstructure model developed is suitable for large-scale simulations and thus pertinent to real-case applications.

Model for Ti-6Al-4V microstructure

The model is based on the Finite Element Method supported by the feature of the software Msc.Marc [9] used for the temperature history simulations. The microstructure model will thus be introduced through user-subroutines according to Msc.Marc rules. It follows that the modelling is oriented to Finite Element Method and the theoretical model for the microstructure is written in FORTRAN language as Msc.Marc user sub-routines. The description of the microstructure follows a point-wise homogeneous description. As a result state variables representing the microstructure at each node will be described through scalar quantities. Such representation of the

microstructure also facilitates future coupling of the microstructure model with the mechanical behaviour. Based on the current understanding of the RTMwD metal deposited Ti-6Al-4V microstructure [10, 11], microstructural features are identified for quantification as state variables for the microstructural model. A typical cycling temperature history as experienced by the material is shown in Fig. 1, representing a temperature measurement of an 11 layers deposited wall. Heating, cooling, and successive re-heating have to be modelled throughout the metal deposition process, driven by the temperature history.

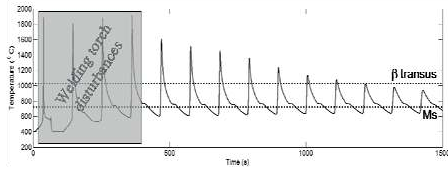
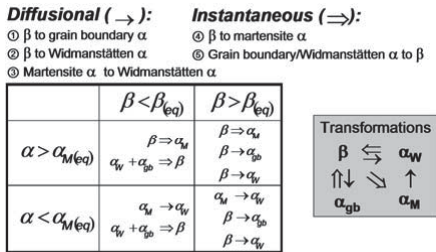


Fig. 1 Temperature measurements – with pyrometer spot low on the side of the built wall, as described in the Temperature measurements section. (The first four cycles are inaccurate due to the heat emitted from the welding torch.)

Thus, diffusional β to α transformation compete with martensitic transformation, while reverse transformation into β phase is significant in reheating stages as adjacent layers are deposited. The five state variables identified for the representation of the microstructure in the model are: Widmanstätten α fraction (α_w), Colony/Grain boundary α fraction (α_{gb}), Martensite α fraction (α_M), β fraction (β) and α lath thickness ($\alpha\text{-lath}$). Diffusional and instantaneous transformations are used in the calculation of the phase fractions according to the logic presented in Fig. 2.



Alpha lath size: Formation temperature dependence
 Fig. 2 Microstructure and morphology modelling logic

The selection of the transformations which are active in the simulation is determined by comparison with the equilibrium of the β and martensitic phases at the present temperature. The interaction between the four considered phases is thus taken into account. Consequently, the phases that are assumed to be interacting with the active transformations are considered in the equilibrium described in equation 1

and 2 below. In the diffusional Widmanstätten and grain boundary transformations, except in the back transformation to β phase, martensite is considered inert, and removed from the equations. Thus, the fraction of β that will approach the equilibrium state is defined in equation 1.

$$\frac{\beta}{\beta + \alpha_w + \alpha_{gb}} \left(= \frac{\beta}{1 - \alpha_M} \right) \rightarrow \beta_{(eq)}(T) \quad (1)$$

On the other hand, in the martensite transformations, formation and recovery to Widmanstätten, the Widmanstätten and grain boundary α are considered inert, and removed from the equations. Thus, the fraction of martensite that will be used in calculations is:

$$\frac{\alpha_M}{\beta + \alpha_M} \left(= \frac{\alpha_M}{1 - \alpha_w - \alpha_{gb}} \right) \rightarrow \alpha_{M(eq)}(T) \quad (2)$$

The presented modelling approach focuses on the development of the microstructure in solid state, modelling the liquid phase as homogeneous and solidifying into pure β phase. The evolution equations have been discretised for the finite element implementation.

Diffusional phase transformations:

① β to α_{gb} and ② β to α_w

The classic diffusional Johnson-Mehl-Avrami formulation (JMA) [12-14] has been selected and adapted to the Widmanstätten and grain boundary α phase transformations. For pure and isothermal transformation from phase j (β in the present case) to phase k (α_w or α_{gb} in the present case), the transformation can be written according to equation 3:

$$v_k = \left(1 - e^{-B_{jk} t^{N_{jk}}} \right) v_j^0 v_k^{eq} \quad (3)$$

Here, v_j is the current fraction of phase j , v_k is the current fraction of phase k , B_{jk} and N_{jk} are temperature dependent material constants which are determined from TTT-diagram; t is the time since start of transformation, v_j^0 and v_k^{eq} are initial fractions of phase j and the equilibrium fraction of phase k , respectively.

The Finite Element Method allows using isothermal kinetics data by time and space discretisation, so equation 3 is easily used for both the β to α_{gb} and β to α_w transformations. As a first choice, considering the divergence in parameters found in the literature, a set of temperature dependent parameters, B_{jk} and N_{jk} , were calculated using interpolation over the TTT-diagram made for a specified Ti64 and published in [15]. Also the equilibrium curve of total α fraction has been implemented going from a maximum of 90% at low temperature and decreasing to 0 at high temperature. The incremental form presented in

equation 4 was derived according to the logic used by Järnstråt & Sjöström [16]:

- The diffusion process is assumed to depend on the temperature through the kinetics parameters B and N .
- The phase fraction at the beginning of the time step is denoted by superscript n . The length of the time step is Δt and the concentration time, t_c , is defined as the time it would have taken to reach the current concentration at the current temperature.
- Normalisation with respect to the sum of original and resultant phase fraction ($v_j + v_k$) is employed to correct for the case of more than one transformation product, considering phases not involved as inert.

$$\Delta v_k = -\Delta v_j = \left(1 - e^{-B_{jk}(t_c + \Delta t)^{N_{jk}}}\right) \left(v_j^n + v_k^n\right) v_k^{eq} - v_k^n$$

with $t_c = \left[-\ln \left(1 - \frac{v_k^n / v_k^{eq}}{v_j^n + v_k^n}\right) / B_{jk} \right]^{1/N_{jk}}$ (4)

③ α_M recovery to α_w

According to Gil Mur et al. [17] α_M is decomposed into reformed α and/or β depending on the temperature and the heating time. The decomposition of α_M is assumed to be a diffusion process and considered complete at a temperature of 800°C. As a simplification, avoiding an extra state variable with unknown properties, the recrystallized or precipitated fraction from martensite will be considered equivalent to Widmanstätten α and added to the state variable α_w . Thus, the JMA-formulation in equation 3 presented above is used in the implementation of this transformation and the values for the Avrami constants determined from hardness measurements in [17] are applied.

Instantaneous transformations:

④ β to α_M

For modelling the martensitic transformation, it is common practice for titanium to assume instantaneous transformation at a specific temperature for any cooling rate higher than approximately 410°C/s [18]. For improved accuracy and consistency, however, we will employ the Koistinen-Marburger equation [19], used extensively for martensitic transformation in steel. For transformation of phase j (β in the present case) into phase k (α_M in the present case) in the absence of diffusional transformations, the equation can be written as:

$$v_k = \left(1 - e^{-0.003(T_{ms} - T)}\right) v_j^0 \quad (5)$$

Here, T_{ms} is the start temperature for martensitic transformation, while T is the current temperature and

the constant -0.003 is taken from [20], and used instead of -0.011 as commonly employed for steels. Martensitic transformation according to equation 5 can be written in incremental form as:

$$\Delta v_k = -\Delta v_j = \left(1 - e^{-0.003(-\Delta T)}\right) \left(v_j^n + v_k^n\right) \quad (6)$$

where $-\Delta T$ is the step in increased undercooling below T_{ms} , the martensite start temperature. When the temperature increases, or when above martensite start temperature, no martensitic transformation is assumed to occur.

⑤ Back transformation to β

S.S.Babu et al. [21] have shown by time-resolved x-ray diffraction investigation with synchrotron radiation that the transformation during heating, at a rate of 20°C/s, closely follows the equilibrium phase diagram. Consequently, the back transformation $\alpha + \beta \rightarrow \beta$ under re-heating is approximated and implemented as instantaneous according to the β equilibrium phase fraction.

Morphology parameter: Alpha lath size

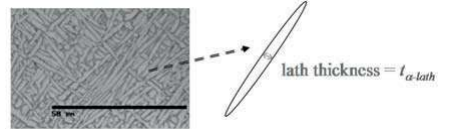


Fig. 3 lath thickness state variable

The alpha lath thickness, as defined in Fig. 3, is calculated as temperature dependent formation size, using the classic Arrhenius energy formulation for the calculation of the equilibrium size at temperature T .

$$t_{\alpha-lath}^{eq} = k e^{-R/T} \quad (7)$$

And the incremental calculation of the alpha lath size has been implemented as follow:

$$\Delta t_{\alpha-lath} = \frac{t_{\alpha-lath}^n \times \Delta v_{\alpha_{total}}^n + t_{\alpha-lath}^{eq} \times \Delta v_{\alpha_{total}}}{v_{\alpha_{total}}^n + \Delta v_{\alpha_{total}}} - t_{\alpha-lath}^n \quad (8)$$

The parameters k and R in equation 7, have been estimated using quenches from 1050/1100°C [22] disregarding the higher starting temperatures because slower cooling rates give long hold times at high temperature that do not agree with metal deposition conditions. Consequently, the parameters $k = 18433$ and $R = 10044$, after calibration against single-bead deposited walls, are considered reasonable first approximations.

For proper modelling of post-deposition heat treatment, a grain growth model should be included.

However, during metal deposition, the alpha formation temperature is considered dominant in determining the lath thickness, and thus grain growth is not modelled in the present version of the software.

Model

The microstructure model takes into account heating and cooling, as well as successive reheating involved in the RTMwD process. The thermal history, driving the phase transformations, can either be given or measured (for point results) or calculated (for more complex geometry or phase field results) using Finite Element Method. The implementation structure of the model subroutine is described as a flowchart in Fig. 4. The microstructure evolution user subroutine is called by Msc.Marc at each temperature and time increment, thus allowing nonlinear evolution laws and access to the state variables including the temperature. The martensite transformation criterion is tested first. The choice regarding α phase dissolution ($\alpha \rightarrow \beta$) or α phase nucleation and growth ($\beta \rightarrow \alpha$) is done by comparison with the equilibrium β phase level, as seen in Fig. 4. If the fraction of β phase is greater than equilibrium, β is dissolved into α_{gb} and/or α_w according to the current temperature range. α lath size is, finally, calculated separately using the calculated change in α content and the current temperature. As mentioned in the model description, the evolution laws are written in incremental form.

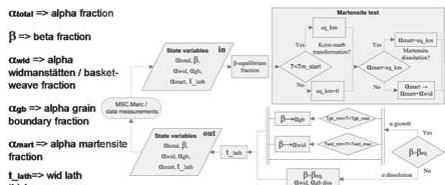


Fig. 4 Flow chart – Microstructure module logic

Experimental work

Robotised TIG Metal-wire Deposition

The Tungsten Inert Gas power source is used to electrically heat and melt the metal wire, which then solidifies to form a fully dense layer on the clamped base plate as can be seen in Fig. 5. The addition of multiple layers produces a fully dense part having the near net shape. Both base plate and filler metal are aerospace grade titanium alloy Ti6Al4V. The chemical composition of the plate and the feeding wire were according to the specifications in Table 1.

Table 1 Chemical composition of the plate and wire.

Element (wt%)	Al	V	Fe	C	O	N	H	Fi
Plate	6.01	3.87	0.18	0.009	0.14	0.006	<50ppm	balance
Wire	6.045	3.89	0.12	0.022	0.15	0.004	<0.001	balance

Therefore, the entire RTMwD sequence including the final cooling was performed within a chamber to

prevent formation of α -case or oxidation. A protective atmosphere of less than 20 ppm of oxygen was maintained by injecting argon into the chamber. Single bead walls as shown in Fig. 6, were built on 3.2 mm thick base plates. A two minute hold time between each layer was employed, allowing the deposited material to cool down before the deposition of the next layer. Fig. 6 shows the finished specimen, a 7.6 mm wide wall, 11 layers high, which is analysed and simulated for this study.

Temperature measurements

The microstructure is evolving during the temperature changes throughout the deposition process and in particular the cooling and heating rates are determining the microstructure. RTMwD as well as multipass welding involves a complex metal temperature history as seen in Fig. 1 and Fig. 10. The metal is heated up each time a pass is made, which means that the microstructure transformations are reversed by each passage of the weld torch until the peak is below transition temperature. The temperature ranges as well as the heating and cooling rates depend on the process parameters used.

Consequently, the temperature was experimentally measured during the deposition process. Four thermocouples of type K (NiCr/NiAl) were spot-welded on the base plate; two on the top surface of the plate as close as possible to the deposited weld (5 mm from the centre of the weld), and two on the back face of the plate positioned at the centre of the weld (see Fig. 6). In addition pyrometer measurements, Fig. 1, were used systematically throughout the deposition experiments. The pyrometer, forehead calibrated on heated Ti6Al4V, measured on a 1 mm diameter area spot with focus low on the side of the built wall as shown in Fig. 5. Because of the position of the measurement area, radiation from the passing welding torch produces an unphysical high temperature peak to be registered for the first 4 layers - the disturbances are marked in Fig. 1. Fig. 5 shows the thermocouples and pyrometer in place after the deposition of the second layer.

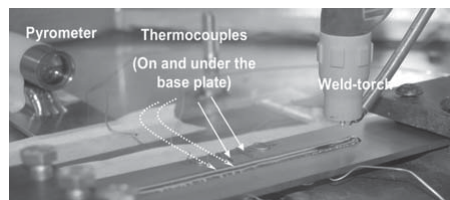


Fig. 5 Experimental setup for single-string wall deposition with pyrometer and thermocouples after the second layer deposited

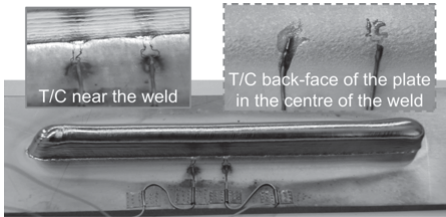


Fig. 6 Deposited 11-layer wall with thermocouples mounted

RTmWd metal deposited microstructure

Ti-6Al-4V is a two-phase, HCP- α and BCC- α , heat-treatable alloy, which exhibits a variety of microstructures dependent on the conditions experienced during cooling transformation from the high-temperature β form to the low-temperature α form of the alloy, and for the reverse transformation upon reheating [1]. Microscope examinations of single-wall MD cross-sections as seen in Fig. 7 are used as a representative of the MD microstructures to be modelled. The samples were prepared using conventional grinding and polishing techniques and etched by a 2% Kroll solution. In all observed MD cases, the large columnar prior beta grains start out perpendicular to the base plate and widens as they cross multiple deposit layers as it can be seen in Fig. 7. Indeed, the size of the prior beta grains is often observed to be as large as the wall height, or 100 μm . A more or less coarse α_W microstructure is observed depending of the thermal history of the sample. The lower part of the wall, left hand side of Fig. 7, presents a layering structure observable on the optical micrograph of the area, which appears to be caused by a difference in the α lath thickness. On the other hand, the upper part of the wall does not present such observable variation in the α lath sizes.

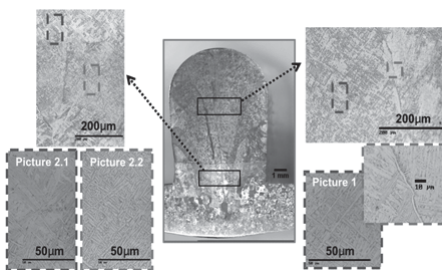


Fig. 7 Microstructure exploration of two zones on a 11 layers wall

In order to get useful information on the microstructure of the produced samples to be used for comparison with the simulation results, quantitative metallographic examination of the microstructure has been performed. Stereology procedures to measure the microstructural features from micrographs were considered and used in the evaluation of the model parameters quantities. Although different standards have been developed for

characterizing microstructures based on images [23-25], the quantification of microstructural features in α/β Ti alloys is still very difficult because the microstructure is quite complex and involves features spanning a wide range of size scales. The stereology procedures used for Ti64 microstructure analysis have been inspired from previous publications on the subject by T. Searles, J. Tiley et al. [26, 27]. The information available from cross-sections of the microstructure imaged using optical microscopy was processed with the image processing software ImageJ [28] in semi-automated mode. Statistical numeric values extracted from the optical pictures could thus be assigned to the observed microstructure. Table 2 includes the results from stereology measurements of the α lath thicknesses corresponding to the optical pictures edited in Fig. 7. The variation in measured α lath thicknesses within the sample has been interpreted to be a layering structure formed during metal depositions by the thermal cycling after a certain number of layers as previously discussed in [11].

Table 2 Stereology measurements of alpha lath thickness using ImageJ [28]

Fig. 7	α lath thickness(μm)
Picture 1	1.14 (SD: 0.32, Min: 0.53, Max: 2.34)
Picture 2.1	0.97 (SD: 0.32, Min: 0.30, Max: 1.66)
Picture 2.2	1.38 (SD: 0.36, Min: 0.68, Max: 0.2.9)

Experimental fatigue life

The manufacturing route has major impact on the fatigue endurance of metal deposited material. Low cycle fatigue tests were thus performed at Volvo Aero Corporation [29] on samples manufactured from 3x30 layer deposited walls. The welding parameters and the heat treatment were varied to induce changes in the final microstructure. Indeed, Fig. 8 shows a difference of an order of magnitude in life between different manufacturing conditions. The major influence seems to be from the use of different process parameters, and in particular, allowing the metal to cool before depositing the next layer seems highly beneficial for fatigue life.

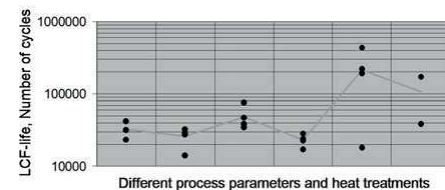


Fig. 8 Experimental fatigue life for different process parameters and different post-deposition heat treatment

Metal deposition simulation

The commercial finite element software MSC.Marc is used for the simulations of the temperature field evolution during the RTMwD operation. The thermal and microstructural analyses of the process are discussed in this paper.

The temperature history simulation

A 2D model is used to represent the experimentally investigated geometry. In order to model successive material layers while building up the wall, the mesh for the plate as well as for the complete wall, must be established before the simulation. The Altair Hypermesh finite element pre-processor was used for meshing the geometry with quadratic (base plate) and triangular (deposited metal) full integration element types. The mesh used, shown in Fig. 9, is rather dense in order to capture the microstructure changes within a single layer of the wall. This explains the choice of 2D-simulation, equivalent to a cross-section in the middle of a long wall providing huge savings in element numbers and computation time.

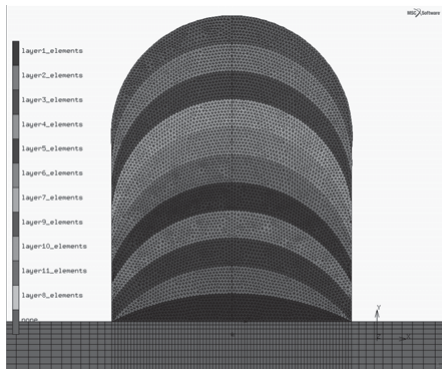


Fig. 9 Mesh over the 11 layers

The welding process is modelled by applying spatially varying temperature boundary condition following the deposition of each layer, including a pre-set formation temperature of the created elements representing each deposited new layer. All the wall elements are initially “quiet”, i.e. with 10^{-10} scaled down material properties to ensure that they do not contribute to the load calculation. As a new wall layer (c.f. fig 9) is created, the properties of the elements in the new layer are fully restored and boundary conditions are assigned to the created elements. A predefined deposition temperature of 1800°C is employed, higher than melting temperature to include the full energy provided by the heat source. The thermal properties were implemented as temperature dependent as suggested in [30]. The latent heat of melting has been accounted for separately in the model for temperatures between the solidus (1600°C) and the liquidus (1670°C). Film convection has been retained as boundary conditions

on the entire plate surface and deposited layer surfaces, since the work-piece is maintained in a controlled atmosphere chamber during the Metal Deposition. The heat conduction into the fixture has been neglected in these calculations since it was designed to have very small contact area with the plate.

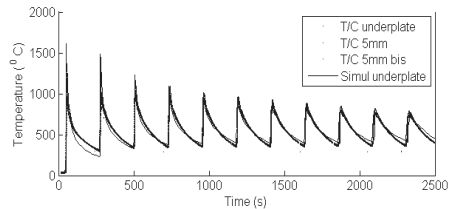


Fig. 10 Calibration heat transfer simulation against thermocouple measurements

The thermal simulation was calibrated based on experimentally measured temperatures. Fig. 10 depicts the measured and calculated temperature history during metal deposition of the 11 layer wall, showing satisfactory agreement.

The microstructure simulation

Numerical simulations of the microstructure evolution have been performed for the experimentally produced 11-layer single bead wall test case described above. The microstructure is calculated through the microstructure subroutine from the temperature and time step supplied by MSC.Marc. The microstructure state variables returned to MSC.Marc are stored at each material point between time steps.

The cyclic characteristic of metal deposition process already evident in the temperature history experienced by the material influences also the microstructure. Fig. 11, illustrates the temperature range for transformations as beta is formed going up in temperature at 1000°C, while the diffusional formation of α on cooling varies a bit with quenching speed, increasing with each cycle as the cooling rate decreases with increasing distance to the latest deposited layer.

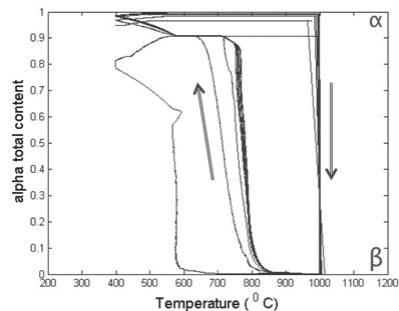


Fig. 11 Microstructure simulation results - Total alpha content versus temperature at one computation node

The conduction of heat within the already deposited layers and the base plate is a predominant heat propagation and cooling factor. Phase transformations, driven by the temperature changes, are directly influenced. Fig. 12 shows the β -front progression in the sample at the deposition of the 11th layer. Directly after the deposition of the layer (Fig. 12: ①), the β -front progress according to the initial curvature of the layer, but as the thermal wave penetrates deeper into previously deposited material (Fig. 12: ②) the curve gradually straightens, and at the furthest beta transformation (Fig. 12: ③), the beta front is completely straight as heat propagation is now uni-axial downwards and the energy is expended to the level that the temperature is not raised above beta transus. The extension of the beta phase in Fig. 12: ③ is not as deep as the highest observed banding mark in Fig.13, indicating that the banding is caused at temperatures lower than beta transus.

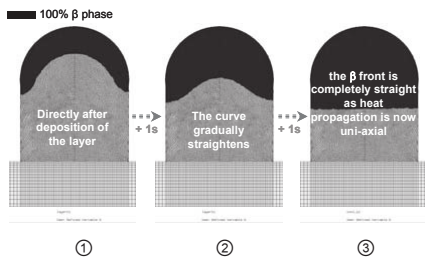


Fig. 12 β (black)-front progression after deposition of the 11th layer.

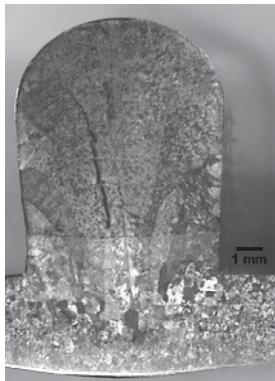


Fig. 13 Cross-section on a 11 layers deposited wall

The α lath thickness model is based on the hypothesis of temperature dependent formation. During deposition the thickness of α lath formed at high temp can be as large as 7 μm but because most alpha is formed at lower temp, the final size is typically less than 2 μm , as shown in Fig. 14 and Fig. 15.

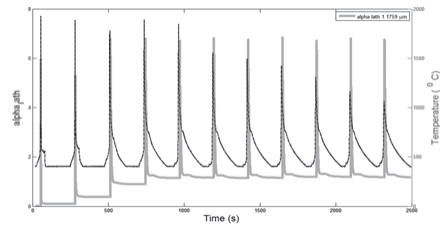


Fig. 14 α lath thickness with the pyrometer measurements

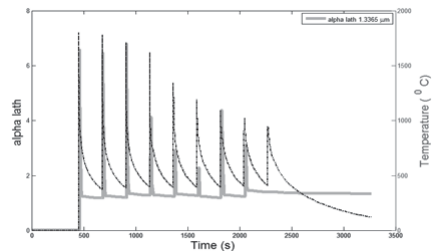


Fig. 15 α lath thickness with temperature history at a node taken within the 3rd layer

Applications and discussions

Impact of microstructure on fatigue properties

For predicting the safe life of metal deposited components, it is important to assess and quantify the impact variations in thermal history will have on component fatigue endurance. From Fig. 16, it can be seen that there is strong correlation to both the substrate metal temperature at deposition of a new layer and the α lath thickness.

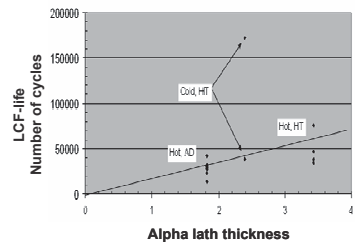
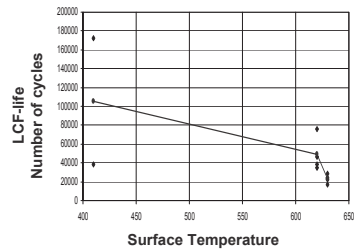


Fig. 16 – Top: Life versus estimated surface temperature (stabilised minimum temperature in the

deposition cycle) and Bottom: Life versus α lath thickness

Thus, a simple linear parameterisation in surface temperature and α lath thickness is suggested, here applied as a scalar multiplication to the strain:

$$\frac{\Delta \varepsilon}{2} = k_{process} \left(\frac{\sigma_f}{E} N^b + \varepsilon_f N^c \right) \quad (9)$$

$$k_{process} = 136 t_{\alpha\text{-lath}} (730 - T_{surface})$$

Interestingly enough, this crude model seems to provide very good agreement with experimental data, as indicated in Fig. 10. However, although it was possible to obtain an excellent fit through the three first points of the figure, the validation test using a different set of welding parameters shows a somewhat less good agreement. Thus, it would be advisable to perform a more thorough study of the underlying principles for the differences in fatigue strength.

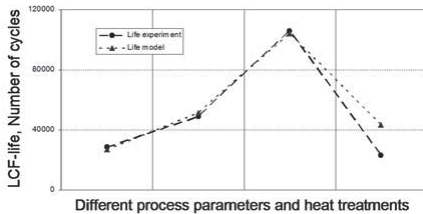


Fig. 17 Model versus experimental results

Further, although the use of alpha lath thickness and surface temperature at deposition correlates very well with the performed tests, it must be emphasised that the number of tests available were too limited to draw any solid conclusions.

Application to a coupled mechanical simulation

We can observe, c.f. Fig. 1, that the material is subjected to brief stress release heat treatments, as the temperature goes above 600°C for each additional level. This could explain that metal deposition processes like Shape Metal Deposition have been reported to give better-than-cast material properties [3].

Thus, an interesting future application of the present modelling would be the integration into a fully coupled thermal-metallurgical-mechanical simulation model for use in predicting distortions, residual stresses and structural integrity. Such simulations could be used for optimising parameters such as welding speed and interpass time to achieve improved product properties.

Possible causes of the observed banding

It is concluded from the straight shape of the bands that the banding is not caused during solidification or the first quench, by rather during a later reheating stage. Actually, since the topmost observed band is lower than the beta transformation front from the simulation, we conclude that the temperature of importance for

band creation must be lower than beta transus. We believe that the instantaneous transformation to beta at beta transus on heating is not accurate and beta is partially reformed at lower temperatures. This reformation of beta would be very sensitive to the exact height of the last temperature wave to reform beta, and thus the amount of reformed beta would vary within the layer. The alpha formed during cooling of this low-temperature beta would automatically be thinner, because of the lower formation temperature, and thus a difference in alpha size would be observed. Although we consider this formation temperature hypothesis the most likely cause of the banding, an alternative explanation could be alpha grain growth during the brief high temperature parts of the cycle. If the growth rate changes very rapidly in a certain temperature range, that would also cause banding of the type observed.

Conclusions

A microstructural evolution model for titanium has been developed, implemented as MSC.Marc subroutines and applied to metal deposition of Ti-6Al-4V. The model considers phase changes during cooling, heating, and re-heating. Diffusional and instantaneous models are employed as appropriate to the various occurring transformations. The evolution equations are parameterised to account for varying temperature histories, providing appropriate response at different temperature change rates and temperature cycling.

Preliminary simulations using literature data and fitting parameters to the limited data available show promise for predicting the impact on fatigue endurance from manufacturing history, for coupled thermal-microstructural-mechanical simulations, and for explaining the characteristic banded sections observed in weld deposited titanium.

Acknowledgments

The authors acknowledge the financial support from the European 6th Framework Programme through the research project VERDI (Virtual Engineering for Robust manufacturing with Design Integration). See <http://www.verdi-fp6.org>.

The authors would like to address their thanks to Mats Högström and Mattias Ottoson for performing the Metal Deposition experiments and making possible the recording of thermal data, and to Fredrik Niklasson and Volvo Aero Corporation for performing the fatigue testing.

References

1. M.J. Donachie, *Titanium: A Technical Guide*, Second Edition ed.: ASM International (2000)
2. C. Leyens and M. Peters, *Titanium and Titanium Alloys: Fundamentals and Applications*: WILEY-VCH (2003)

Paper B

3. B. Rooks, *Assembly in aerospace features at IEE seminar 25* (2005)
4. L. Dubourg and J. Archambeault, *Technological and scientific landscape of laser cladding process in 2007*, *Surface and Coatings Technology*, In Press, Accepted Manuscript
5. W.U.H. Syed, A.J. Pinkerton, et al., *A comparative study of wire feeding and powder feeding in direct diode laser deposition for rapid prototyping*, *Applied Surface Science*, 247, 268-76 (2005)
6. J.A. Goldak and M. Akhlaghi, *Computational welding mechanics*. New York: Springer (2005)
7. L.E. Lindgren, *Computational welding mechanics : thermomechanical and microstructural simulations*, Boca Raton, FL, Cambridge, England: CRC Press, Woodhead (2007)
8. S.M. Kelly, S.S. Babu, et al., *A microstructure model for laser processing of Ti-6Al-4V*, in *7th International Conference on Trends in Welding Research, May 16-20 2005*, Pine Mountain, GA, United States, 65-70 (2005)
9. MSC.Software.
10. C. Charles and N. Järviesträt, *Finite Element Modelling of Microstructure on GTAW Metal Deposition of Ti-6Al-4V alloy*, in *3rd International Conference "Mathematical Modelling and Information Technologies in Welding and Related Processes"*, Kiev, E.O. Paton Electric Welding Institute, NAS of Ukraine, 151-56 (2006)
11. C. Charles and N. Järviesträt, *Development of a Microstructure Model for Metal Deposition of Titanium Alloy Ti-6Al-4V*, in *The 11th World Conference on Titanium (Ti-2007)* at the International Conference Center in Kyoto, Japan, (2007)
12. M. Avrami, *Kinetics of phase change, I. General theory*, *Journal of Chemical Physics*, 7, 1103-12 (1939)
13. M. Avrami, *Kinetics of phase change, II. Transformation-time relations for random distribution of nuclei*, *Journal of Chemical Physics*, 8, 212-24 (1940)
14. M. Avrami, *Kinetics of phase change, III. Granulation, phase change, and microstructure*, *Journal of Chemical Physics*, 9, 177-84 (1941)
15. S.M. Kelly, *Characterization and Thermal Modeling of Laser Formed Ti-6Al-4V*, in *materials Science and Engineering* Blacksburg, Virginia: Faculty of the Virginia Polytechnic Institute and State University (2002)
16. N. Järviesträt and S. Sjöström, *Current status of TRAST; a material model subroutine system for the calculation of quench stresses in steel*, in *ABAQUS users' conference 1993*, Aachen, Germany (1993)
17. F.X. Gil Mur, D. Rodriguez, et al., *Influence of tempering temperature and time on the [alpha]'-Ti-6Al-4V martensite*, *Journal of Alloys and Compounds*, 234, 287-89 (1996)
18. T. Ahmed and H.J. Rack, *Phase transformations during cooling in [alpha]+[beta] titanium alloys*, *Materials Science and Engineering A*, 243, 206-11 (1998)
19. D.P. Koistinen and R.E. Marburger, *A general equation prescribing the extent of the austenite-martensite transformation in pure iron-carbon alloys and plain carbon steels*, *Acta Metallurgica*, 7, 59-60 (1959)
20. Y. Fan, P. Cheng, et al., *Effect of phase transformations on laser forming of Ti-6Al-4V alloy*, *Journal of Applied Physics*, 98, 013518 (2005)
21. S.S. Babu, S.M. Kelly, et al., *Measurement of phase transformation kinetics during repeated thermal cycling of Ti-6Al-4V using time-resolved X-ray diffraction*, in *International Conference on Solid-Solid Phase Transformations in Inorganic Materials 2005, May 29-Jun 3 2005*, Phoenix, AZ, United States (2005)
22. F.J. Gil, M.P. Ginebra, et al., *Formation of [alpha]-Widmanstatten structure: effects of grain size and cooling rate on the Widmanstatten morphologies and on the mechanical properties in Ti6Al4V alloy*, *Journal of Alloys and Compounds*, 329, 142-52 (2001)
23. R. John C. and D. Robert T., *Practical Stereology*, 2nd Edition ed. New york: Plenum Press (2005)
24. *Annual book of ASTM standards 03.01* (1998)
25. J.C. Russ, *The image processing handbook*, 4. ed. Boca Raton: CRC, (2002)
26. J. Tiley, T. Searles, et al., *Quantification of microstructural features in [alpha]/[beta] titanium alloys*, *Materials Science and Engineering A*, 372, 191-98 (2004)
27. T. Searles, J. Tiley, et al., *Rapid characterization of titanium microstructural features for specific modelling of mechanical properties*, *Measurement Science and Technology*, 16, 60-69 (2005)
28. Research Services Branch, NIMH, ImageJ 1.34 (2005)
29. N. Järviesträt, F. Niklasson, C. Charles; *to be published*
30. R. Pederson, *The microstructures of Ti-6Al-4V and Ti-6Al-2Sn-4Zr-6Mo and their Relationship to Processing and Properties*, PhD thesis in Department of Applied Physics and Mechanical Engineering, Division of Engineering Materials Luleå, Sweden: Luleå University of Technology (2004)

**A model for Ti-6Al-4V microstructure
evolution during cyclic temperature changes**

Corinne Charles Murgau, Robert Pederson and Lars-Erik Lindgren

In Modelling and Simulation in Materials Science and Engineering, 20(5), 055006

Erratum

Page 110 (Page 10 of the article)

Equation (19), Section 3.3.3

The equation should be written as follow,

$$t_c = \left[-\ln \left(\frac{n_X \alpha_m^{-n+1} X_{\alpha_m}^{eq}}{(n_X \beta^+)^{n_X} \alpha_m^{-n+1} X_{\alpha_m}^{eq}} / K \alpha_m \right) \right]^{1/N_{\alpha_m}} \quad (19)$$

A model for Ti–6Al–4V microstructure evolution for arbitrary temperature changes

C Charles Murgau¹, R Pederson^{2,3} and L E Lindgren⁴

¹ Department of Engineering Science, University West, 461 29 Trollhättan, Sweden

² Division of Material Science, Luleå University of Technology, 97181 Luleå, Sweden

³ Department of Materials Technology, Volvo Aero Corporation, 46181 Trollhättan, Sweden

⁴ Division of Material Mechanics, Luleå University of Technology, 97187 Luleå, Sweden

E-mail: corinne.charlesmurgau@gmail.com

Received 21 November 2011, in final form 4 May 2012

Published 13 June 2012

Online at stacks.iop.org/MSMSE/20/055006

Abstract

This paper presents a microstructure model for the titanium alloy Ti–6Al–4V designed to be used in coupled thermo–metallurgical–mechanical simulations of, e.g., welding processes. The microstructure evolution is increasingly taken into consideration in analyses of manufacturing processes since it directly affects the mechanical properties. Thermally driven phase evolutions are accounted for in the model. A state variable approach is adopted to represent the microstructure with the objective to integrate the microstructure changes with a thermo–mechanical model of manufacturing process simulation such as welding. The model is calibrated using the literature data and also validated against a cyclic temperature history during multi-pass welding.

1. Introduction

Titanium alloy Ti–6Al–4V is widely used in aero-engines because of its excellent strength, toughness and corrosion resistance [1]. Its mechanical properties are directly affected by the microstructure. Understanding and control of the microstructure evolution are therefore important in order to maintain high quality at each manufacturing step and in the final product. Multi-pass welding and metal deposition (layer-by-layer deposition in a free-form manufacturing fashion) are manufacturing steps, which induce severe temperature variations to the material and consequently changes in the microstructure.

This work provides a model for thermally driven phase transformations to be used, coupled with a physically based constitutive model [2], in thermo–metallurgical–mechanical simulations of large aerospace components [3]. It is valuable to be able to perform this simulation based analysis before the actual manufacturing takes place in order to evaluate the effect on the microstructure, stresses and deformations of the produced component for tentative manufacturing routes. This requires a sufficiently accurate microstructure

model. 'Sufficiently' accommodates not only the uncertainties in other parts of the thermo-mechanical model and the manufacturing process itself, but also uncertainties in the available microstructure information for model calibration and validation. Furthermore, the requirement of being able to model large components also limits the modelling approaches that are suitable for acceptable computation time and power. The modelling of microstructure can be tackled at different scales. Microscale modelling [4–7] is more precise but considerably computation demanding. A density type of model, also called internal state variable approach by Grong and Shercliff [8], is preferred here because it requires less computing time. The density fields, such as phase fractions, are computed at the integration points of the elements discretizing the computed volume [3]. The microstructure model in this paper is formulated as incremental relations to be used for arbitrary temperature histories such as in the cases of multi-pass welding or metal deposition manufacturing. This work is an improvement of the model in [9, 10] and follows the same logic adopted by Kelly *et al* [11]. The coupling of the microstructure model with the constitutive model will be presented in a forthcoming publication.

This paper is structured as follows: first, the microstructure evolution and some microstructure features observed in metal deposited parts [12] are presented. Then the formulation and implementation of the model are detailed. The phases and corresponding phase transformations and their mathematical formulations are described. Calibration of the model and a discussion about sensitivity of the material parameters for the kinetics of phase transformations are also presented. The model is investigated against a controlled temperature history resembling metal deposition by Babu *et al* [13], which is used for validation of the proposed microstructure model. Finally, conclusions regarding the applicability of the model are given.

2. Background

2.1. Titanium alloy Ti–6Al–4V

The titanium alloy Ti–6Al–4V is a two-phase, hexagonal close packed (hcp) α -phase and a body centred cubic (bcc) β -phase [14], heat-treatable titanium alloy (6 wt% aluminium and 4 wt% vanadium). The alloy is up to 80–95% composed of the α -phase at room temperature with the remaining being β -phase. The ($\alpha + \beta$)-phase mixture exhibits a variety of microstructures depending on the thermal and mechanical conditions experienced. During multi-pass welding processes and metal deposition the microstructure undergoes phase transformations between α and β during successive reheating and cooling. Transformations from the low-temperature $\alpha + \beta$ form of the alloy to the high-temperature β form during heating, and the reverse transformations upon cooling are accounted for in the model presented in this paper.

The heating and cooling cycles imposed during multi-pass welding or metal deposition induce cyclic phase transformations between α and β . This paper first discusses cooling effects followed by heating effects. On cooling from the liquid state, β grains nucleate and grow. The ΔT undercooling below the solidification temperature, T_{solidus} , is the driving force for this growth. The β -phase is fully stable at temperatures larger than the β -transus temperature, T_{β}^{trans} [14]. Quenching from β homogeneous state produces massive and martensitic α -phases [15]. Alternatively, if the cooling rate is lower below T_{β}^{trans} grain boundary α -phase may grow at the β -grain boundaries, or plate-like grown α structure may form within the prior β grains when lower temperatures are reached [14, 16]. The plate-like grown α structure, also called Widmanstätten α , are grouped in α -colonies presenting the same crystallographic orientations. The cycles of β formation and decomposition include homogenization or segregation for many of the alloying elements. Particularly, the effect of vanadium and aluminium distribution

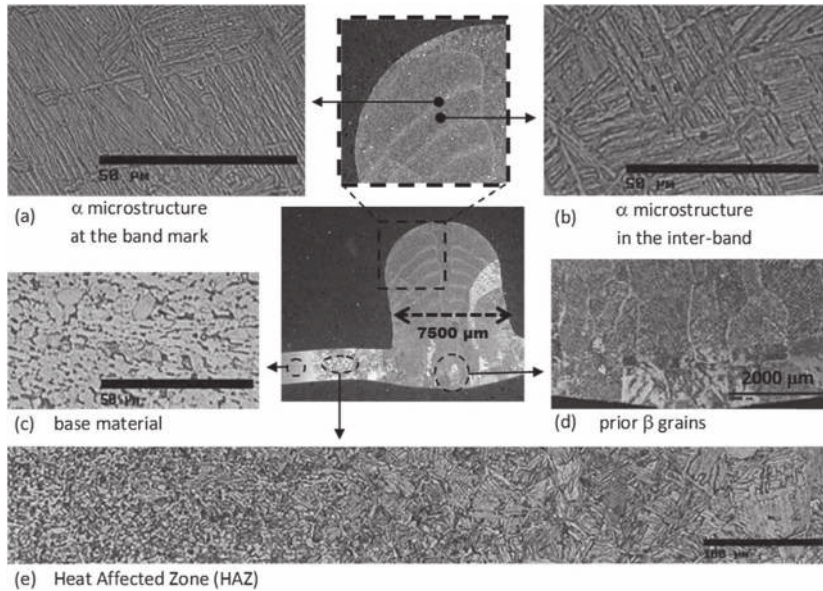


Figure 1. Macro- and micrographs of a Ti-6Al-4V TIG arc welding metal deposited wall (height of eight layers).

controls most of the transformations by diffusion [14], which permits the use of diffusion-based models.

2.2. Microstructure studies

Optical microscopy was used to observe and record the microstructure features present in tungsten inert gas (TIG) arc welding metal deposited titanium alloy Ti-6Al-4V. The deposition layers were laid as single beads on top of each other. The samples were cross-cut and prepared using conventional grinding and polishing techniques for titanium alloys and etched with a 2% Kroll solution. Optical microscopy was performed with the objective to collect and quantify the microstructure features present, see figure 1. A cross-section macrograph of the deposit, one bead width and eight layers height wall, is shown at the centre of figure 1. The boundaries between the deposited layers cannot be seen due to the partial re-melting of the previously deposited layer by the subsequent layer. However, this repeated thermal history can be seen as a banding in figure 1. The variations in the microstructure can be seen in the higher magnification micrographs in figure 1. The presence of large columnar prior β grains in the deposit is visible in the macrograph at the centre of figure 1. The prior β grain morphology changes from equiaxed to columnar at the intersection of the first layer with the base plate, which can be seen in figure 1(d). The prior β grains are nearly perpendicular to the plate and cross multiple deposit layers. The β grain sizes can reach more than ten millimetres in the height direction as can be seen in [12] for samples with higher walls. The prior β grains are locally outlined by the presence of non-continuous α -phase at the grain boundaries, α_{gb} -phase. Note that the α_{gb} -phase is not desired as it gives rise to poorer fatigue properties [14]. The deposited metal

presents a fully lamellar microstructure showing basketweave-Widmanstätten α/β morphology inside the prior β grains. Brighter bands are seen in the macrograph at the centre of figure 1. The observed banding formation seems to present a difference in the α lath thickness when figures 1(a) (brighter band) and (b) (in between bands) are compared. As suggested in [12], these bands must form late in the thermal history as they do not correspond to the new layers' deposition border. Furthermore, the lack of banding in upper parts of the structure indicates that the reheating caused by successive layer additions plays a significant role. More detailed investigations are required to find out whether the bands are caused by β formation on reheating or just annealing effects by extended exposure to intermediate temperatures during deposition. Although martensite was not observed in this investigation by optical microscopy, it is reported that a complete transformation to martensite can appear when the cooling rate is higher than 410°C s^{-1} [15], and that partial transformation to a similar structure can be observed from 20°C s^{-1} [15]. Martensite formation will thus be included in the microstructure model.

Variations in the α/β fraction in the microstructure and the texture of the phases both contribute to influence on the mechanical properties of the Ti-6Al-4V titanium alloy [17, 18]. Yield and ultimate tensile strengths, fracture toughness or creep resistance are important factors while delivering manufactured components. There are a few demanding techniques to observe the microstructure without a total or partial destruction of the component [19, part I]. In fact, modelling of the microstructure is an efficient and low cost complement to destructive experimental techniques [20].

2.3. Material modelling

There is an increasing interest towards simulation of manufacturing processes. Material modelling is a crucial part in these models and that is why a considerable amount of effort is devoted to this, see e.g. [21]. Material modelling is particularly challenging for materials experiencing solid-state transformations, so combining constitutive models with microstructure models is an option under consideration. Microstructure models have been successfully applied to steel alloys, as in [22–27]. Studies concerned with titanium or titanium alloys are mostly case specific. General models for computing microstructure evolution while simulating welding and metal deposition of Ti-6Al-4V seem not to have been addressed until recently [10, 28–31]. Diverse modelling methods are applied to model phase transformations and some of the transformation kinetics associated have been evaluated for titanium alloys [19]. The phase transformation kinetics during either isothermal or cooling processes have been successfully described with the JMAK model (Johnson–Mehl [32], Avrami [26] and Kolmogorov [33]) for titanium alloys [34], especially for Ti-6Al-4V [11, 19, 35]. Nevertheless, phase transformations during heating have been studied by a few authors [28, 36]. The martensite formation for Ti-6Al-4V is still not well understood [15, 37, 38] and the Koistinen–Marburger equation [23] has been used for this transformation.

3. Microstructure model

The microstructure model focuses on the solid-state transformations of the titanium alloy Ti-6Al-4V when subjected to arbitrary temperature changes.

3.1. Modelling approach

The liquid–solid phase changes are not modelled in detail. Instead, a simplified model for transition between the liquid and solid state is implemented to take care of temperatures above

the melting temperature T_{melt} . In the liquid state, each of the solid phases is consequently set to zero. In the solid state, Ti-6Al-4V microstructure is composed of two main phases: the high-temperature stable β -phase and the lower temperature stable α -phase. Depending on the formation conditions [14], a variety of α/β textures can be obtained by heat treatment giving varying mechanical properties. Lütjering *et al* [17, 39] explored the relationship between processing, microstructure and mechanical properties. A large number of features have been identified to be relevant with respect to the mechanical properties such as the α -phases, the β -phase, their morphologies and grain sizes.

An internal state variable approach [3, 8] is adopted in this paper to represent the model's microstructure evolution. This microstructure model uses a combination of models applied in a sequential logic in order to handle general temperature histories [3].

3.1.1. Representative state variables. The microstructure is represented by the phase fractions (X_i), which are the representative state variables in the model. The subscript i indicates the phase considered. Four phase contents are chosen for calculation. They are the β -phase and three variants of α -phases. These are the grain boundary α -phase, α_{gb} , Widmanstätten α -phase, α_{W} , and martensitic α -phase, α_{m} . The total α -phase fraction, X_{α} , is calculated as the sum of these three state variables denoted by $X_{\alpha_{\text{gb}}}$, $X_{\alpha_{\text{W}}}$ and $X_{\alpha_{\text{m}}}$, respectively. α_{gb} represents a more globular α -phase texture and forms first during cooling on the boundaries of the prior β grains at temperatures directly below T_{β}^{trans} . α_{W} represents the α -phase part, which is nucleated from the prior β grain boundary and grows into the prior β grains as long thin plates, also called lamellas, and becomes a plate-like α structure. Moreover, diffusionless transformations can take place at high cooling rates passing below the martensite start temperature, T_{ms} . A full martensite transformation, considered to form instantaneously [16], occurs for cooling rates faster than $410\text{ }^{\circ}\text{C s}^{-1}$ [15]. A similar diffusionless transformation, to massive α , is also observed to form for slower cooling rates down to $20\text{ }^{\circ}\text{C s}^{-1}$ together with diffusion controlled α . The diffusion is favoured for much slower cooling rates [15]. The two diffusionless formations, martensitic and massive α -phase, have similar aluminium and vanadium chemical compositions and show the same crystal structure [15]. It is consequently assumed that they have the same mechanical behaviour and therefore one single state variable, $X_{\alpha_{\text{m}}}$, includes both martensitic and massive α fractions in the model. Grain sizes and detailed oriented morphology features such as α -colonies, are left for further studies.

3.1.2. Arbitrary temperature histories. The principle of additivity [40], commonly used to calculate non-isothermal transformation using the isothermal transformation models, is used for incremental calculation of the transformations during a small time step. Any arbitrary temperature variation is handled provided that time steps are much shorter than the time constant of the transformation. In that case, a sum of small consecutive isothermal steps replaces continuous temperature variations. This concept has been used in many works and has successfully been applied to describe the kinetics of phase transformations in titanium alloys [4, 10, 19, 28, 31]. The additivity approach is also found to be sufficiently accurate when modelling microstructures using state variables for applications such as heat treatment and welding [8].

Incremental calculations over the temperature histories (heat conduction simulations or continuous temperature measurements) are invoked. The phase fractions at each time step depend on the result from the previous time and temperature steps. The current phase status thus depends on the current microstructure, the increment in time and the corresponding temperatures. The incremental variants of the used models are detailed in section 3.3.

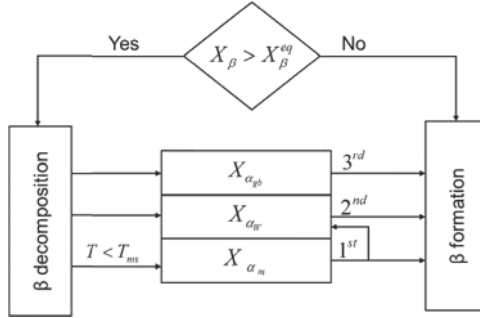


Figure 2. β decomposition and formation.

3.1.3. *Overall model logic.* Diffusion-controlled and instantaneous phase transformations occur during cooling and heating. The JMAK model (Johnson–Mehl [32], Avrami [26] and Kolmogorov [33]) is used for the diffusion-controlled formations and the Koistinen–Marburger [23] equation for the diffusionless formations. In addition, a simplified one-dimensional plate dissolution according to a parabolic rate law is also used to model the α to β transformation [11]. Note that although some phase formations may act simultaneously, the model assumes a certain order for the phase transformations.

The overall model logic for each computation step is shown in figure 2. First it is decided whether the β -phase will form or decompose. This depends on whether the current β -phase fraction X_β is below or above the current equilibrium value X_β^{eq} , denoted by $X_\beta > X_\beta^{\text{eq}}$ in figure 2. The β -phase decomposes if its fraction is higher than the equilibrium value at the current temperature X_β^{eq} . The decomposition of β into α is considered in the order indicated in the left part of figure 2. The diffusion-controlled decomposition of β starts when the temperature goes below T_β^{trans} , since $X_\beta^{\text{eq}} \rightarrow 100\%$ above T_β^{trans} . The logic of the decomposition algorithm is performed in the following order: $X_{\alpha_{\text{gb}}}$ is first updated since α_{gb} has a higher transformation rate at the highest temperatures, $X_{\alpha_{\text{w}}}$ is thereafter calculated. The remaining β -phase fraction, which has not transformed to the α -phase when the martensite start temperature, T_{ms} , is reached, forms α_{m} according to the Koistinen–Marburger equation [23]. The formation of the β -phase from the α -phase is illustrated in the right part of figure 2. The possible recovery of α_{m} is first checked as it forms back ($\beta + \alpha_{\text{w}}$). α_{m} dissolves to β and α_{w} proportional to the current X_β^{eq} and X_α^{eq} . Next, it is assumed that the α_{w} fraction is transformed to β . α_{gb} is the last α -phase to transform into the β -phase after the α_{w} has been extinguished.

3.2. The JMAK model and its generalization

The JMAK model for nucleation and growth of a phase is usually formulated for isothermal processes as

$$X_2 = 1 - e^{-k_{12}\tau^{N_{12}}} \quad \text{or} \quad X_1 = e^{-k_{12}\tau^{N_{12}}}, \quad (1)$$

where X_1 and X_2 are the fractions of phase 1 decomposing to form phase 2, the total phase content being $X_1 + X_2 = 1$. The time, τ , is a relative time measured from the start of the transformation. k_{12} and N_{12} are material-dependent parameters and reflect the kinetics of the nucleation and growth process of the diffusion transformation from phase 1 to phase 2. The equation can also be derived from assuming that the change in Gibb's free energy is the driving

force of the transformation, and that it is proportional to the assumed constant transformation rate [16, 41].

The following subsections describe in more detail the different modifications that are needed in order to apply the model to the application in consideration.

3.2.1. Adaptation of JMAK model to incomplete transformation. The JMAK model is formulated for a phase transformation where the initial phase is 100%, $X_1 = 1$, and disappears completely at infinite time. The opposite holds for the formed phase X_2 . The equation therefore cannot describe cases of incomplete transformations, which finishes on reaching an equilibrium value less than 100%. Thus, we need to modify the earlier given JMAK relations for cases when $X_1(t \rightarrow \infty) \rightarrow X_1^{\text{eq}}$. This problem is circumvented by normalizing equations (1) [41–45] to

$$\begin{aligned} X_2 &= (1 - e^{-k_{12}\tau^{N_{12}}})X_2^{\text{eq}} \quad \text{or} \\ X_1 &= 1 - (1 - e^{-k_{12}\tau^{N_{12}}})X_2^{\text{eq}} = 1 - X_2^{\text{eq}} + e^{-k_{12}\tau^{N_{12}}}X_2^{\text{eq}} = X_1^{\text{eq}} + e^{-k_{12}\tau^{N_{12}}}(1 - X_1^{\text{eq}}). \end{aligned} \quad (2)$$

3.2.2. Adaptation of JMAK model for varying initial phase fractions. The JMAK model must also be modified to be useful for cases where the initial fraction of phase 1 to decompose is not 100% but X_1^0 . X_1^0 refers to the available amount of decomposing phase 1 at the beginning of the considered transformation stage and is augmented to equation (2) according to the following:

$$X_2 = (1 - e^{-k_{12}\tau^{N_{12}}})X_2^{\text{eq}}X_1^0. \quad (3)$$

The modification with X_1^0 corresponds to assuming that this current fraction of phase 1 would behave as a 100% fraction of phase 1 in terms of transformation rates according to the JMAK model.

3.2.3. A note regarding simultaneous transformation of multiple phases. The JMAK model is also limited as it considers only one phase change and needs to be modified in case of multiple phases. The model is applied to the diffusive formation of α from the β -phase in Ti–6Al–4V. Thus phase 1 in equations (1)–(3) denotes the β -phase and 2 denotes the α -phase used in the following. The β -phase can decompose into the grain boundary, α_{gb} , and Widmanstätten, α_{w} , α -phases. Jones and Bhadeshia [46] propose an extension of the JMAK model to handle the simultaneous decomposition of two phases. They applied their approach to allotriomorphic ferrite, forming at grain boundaries, and Widmanstätten ferrite, forming in grain interior. We use a simpler approach where the two phases are calculated subsequently within each time step in our incremental implementation.

3.2.4. Incremental formulation of the JMAK model. We first apply the JMAK model and equation (3) to the β to α transformation without making any distinction between different variants of α -phases. The JMAK model gives

$$X_\alpha = (1 - e^{-k_{\beta\alpha}(\tau)^{N_{\beta\alpha}}})X_\alpha^{\text{eq}}X_\beta^0, \quad (4)$$

where X_α is the calculated fraction of the α -phase at the current temperature. $k_{\beta\alpha}$ and $N_{\beta\alpha}$ are material parameters; $N_{\beta\alpha}$ can vary from 1 to 4 and is related to the shape of the formed grain, $k_{\beta\alpha}$ depends on the nucleation and growth rates and is therefore sensitive to the temperature [24–26]. X_α^{eq} is the equilibrium fraction of the α -phase, which represents the fraction of the α -phase expected to remain after an infinite time at the current temperature. X_β^0 is the initial fraction of the β -phase, and is set to be the available proportion of the β -phase for the considered transformation before start of the transformation.

The model is adapted to a general computational framework as explained in section 3.1.3, following the additivity principle [8]. Equation (4) is updated supposing that for each incremental time step, Δt , ${}^{n+1}X_\alpha = \Delta^n X_\alpha + {}^n X_\alpha$. The superscript n denotes the beginning of the current time step and the superscript $n + 1$ the end of the current increment. $\Delta^n X_\alpha$ corresponds to the small variation of the phase fraction at the current increment step.

The value of X_α^{eq} is taken for the temperature at the end of the increment. X_β^0 represents the fraction of the β -phase when the decomposition has started. It will depend on the course of the temperature history which can involve multiple heating-cooling cycles. The fraction of the transforming phase X_β^0 is taken here to be the total content of the transforming and resultant phases at the beginning of the increment: (${}^n X_\beta + {}^n X_\alpha$). With these assumptions, equation (4) can be written in the incremental form [47]:

$${}^{n+1}X_\alpha = \Delta^n X_\alpha + {}^n X_\alpha = (1 - e^{-k_{\beta\alpha}(t_c + \Delta t)^{N_{\beta\alpha}}})({}^{n+1}X_\alpha^{\text{eq}})({}^n X_\beta + {}^n X_\alpha), \quad (5)$$

where a fictive time, t_c , is introduced to be the time it would have taken to reach the current concentration if the current temperature is taken as constant throughout the transformation. This implies that

$${}^n X_\alpha = (1 - e^{-k_{\beta\alpha}(t_c)^{N_{\beta\alpha}}})({}^n X_\beta + {}^n X_\alpha)({}^{n+1}X_\alpha^{\text{eq}}), \quad (6)$$

which results in an explicit expression for the fictive time,

$$t_c = \left[-\ln \left(1 - \frac{{}^n X_\alpha / {}^{n+1} X_\alpha^{\text{eq}}}{{}^n X_\beta + {}^n X_\alpha} \right) / k_{\beta\alpha} \right]^{1/N_{\beta\alpha}}. \quad (7)$$

This case is adapted for α_{gb} and α_{W} formations described in section 3.3.1, and for α_{m} recovery described in section 3.3.3.

3.3. Proposed set of models

Our choice of state variables and the fundamental equations outlined above are described in more detail here. We give their incremental formulation and specify them for each of the transformations notified in figure 2.

3.3.1. Formation of grain boundary and Widmanstätten α -phases. The α_{gb} and α_{W} are formed from the β -phase and are treated as two separate diffusional transformations. According to the incremental formulation of the JMAK model in section 3.2.4 and by adapting equation (5) to calculate the transformation of β to α_{gb} , the following equation is found:

$${}^{n+1}X_{\alpha_{\text{gb}}} = \Delta^n X_{\alpha_{\text{gb}}} + {}^n X_{\alpha_{\text{gb}}} = (1 - e^{-k_{\beta\alpha}(t_c + \Delta t)^{N_{\beta\alpha}}})({}^{n+1}X_{\alpha_{\text{gb}}}^{\text{eq}})({}^n X_\beta + {}^n X_{\alpha_{\text{gb}}}). \quad (8)$$

The parameters $k_{\beta\alpha}$ and $N_{\beta\alpha}$ are the JMAK transformation kinetic parameters. The temperature-dependent $X_{\alpha_{\text{gb}}}^{\text{eq}}$ is the equilibrium fraction of the α_{gb} -phase. $X_{\alpha_{\text{gb}}}^{\text{eq}}$ is difficult to determine experimentally since the α_{gb} -phase exists only in small amounts in the microstructure. Therefore, $X_{\alpha_{\text{gb}}}^{\text{eq}}$ is proposed to be calculated as part of the available data X_α^{eq} representing the equilibrium amount of diffusional α -phase. This leads to the following modification to equation (8):

$${}^{n+1}X_{\alpha_{\text{gb}}} + {}^{n+1}X_{\alpha_{\text{W}}} = \Delta^n X_{\alpha_{\text{gb}}} + {}^n X_{\alpha_{\text{gb}}} = (1 - e^{-k_{\beta\alpha}(t_c + \Delta t)^{N_{\beta\alpha}}})({}^{n+1}X_\alpha^{\text{eq}})({}^n X_\beta + {}^n X_{\alpha_{\text{gb}}} + {}^n X_{\alpha_{\text{W}}}). \quad (9)$$

More than one transformation product is thus involved in the transformation. In fact, by introducing X_α^{eq} equilibrium fraction, $X_{\alpha_{\text{W}}}$ must also be introduced in the original amount of β available for the transformation. Note that ${}^{n+1}X_{\alpha_{\text{W}}} = {}^n X_{\alpha_{\text{W}}}$ is assumed here, since the model

adopts a certain order for the phase transformations and the α_w formation is treated separately in the next step. The transformation equation explicitly used in the model for the fraction of the α_{gb} -phase is now

$${}^{n+1}X_{\alpha_{gb}} = \Delta^n X_{\alpha_{gb}} + {}^n X_{\alpha_{gb}} = (1 - e^{-k_{gb}(t_c + \Delta t)^{N_{gb}}}) ({}^n X_{\beta} + {}^n X_{\alpha_w} + {}^n X_{\alpha_{gb}}) ({}^{n+1}X_{\alpha}^{eq}) - {}^n X_{\alpha_w}. \quad (10)$$

The corresponding fictive time t_c is calculated:

$$t_c = \left[-\ln \left(1 - \frac{({}^n X_{\alpha_w} + {}^n X_{\alpha_{gb}}) / {}^{n+1} X_{\alpha}^{eq}}{{}^n X_{\beta} + {}^n X_{\alpha_w} + {}^n X_{\alpha_{gb}}} \right) / k_{\alpha_{gb}} \right]^{1/N_{\alpha_{gb}}}. \quad (11)$$

The normalization by $({}^n X_{\beta} + {}^n X_{\alpha_w} + {}^n X_{\alpha_{gb}})$ corresponds to the correction used when more than one phase is involved in the diffusional process. The fraction of the α_m -phase, X_{α_m} , is not involved as it does not participate in the transformation. Indeed, α_m , following a time-independent transformation process during faster cooling, is considered as being an inert phase in the diffusional process.

Following the same reasoning as for α_{gb} , the transformation equation explicitly used in the model for α_w formation from the β -phase is

$${}^{n+1}X_{\alpha_w} = \Delta^n X_{\alpha_w} + {}^n X_{\alpha_w} = (1 - e^{-k_w(t_c + \Delta t)^{N_w}}) ({}^{n+1}X_{\alpha}^{eq}) ({}^n X_{\beta} + {}^n X_{\alpha_w} + {}^n X_{\alpha_{gb}}) - {}^n X_{\alpha_{gb}} \quad (12)$$

with

$$t_c = \left[-\ln \left(1 - \frac{({}^n X_{\alpha_w} + {}^n X_{\alpha_{gb}}) / {}^{n+1} X_{\alpha}^{eq}}{{}^n X_{\beta} + {}^n X_{\alpha_w} + {}^n X_{\alpha_{gb}}} \right) / k_{\alpha_w} \right]^{1/N_{\alpha_w}}. \quad (13)$$

3.3.2. Formation of massive and martensitic α -phase. The martensite and massive formations to α_m are temperature-dependent diffusionless transformations. The standard choice of using the empirical Koistinen–Marburger equation [23] is made, and the following format is used:

$$X_{\alpha_m} = (1 - e^{-b_{KM}(T_{ms} - T)}) X_{\beta}, \quad (14)$$

X_{β} is the β -phase amount available at the start of the martensite transformation, T is the temperature to reach and T_{ms} is the temperature when the transformation begins [23]. The parameter b_{KM} is material dependent.

The diffusionless nature of the transformation makes it time independent and consequently open to several possibilities for implementation in a model. For cooling rates faster than 410°C s^{-1} , 100% of martensite in the microstructure can be formed [15,48]. Here equation (14) is used directly and is discretized, see equation (15), for its implementation in incremental logic. The current α_m -phase amount, ${}^n X_{\alpha_m}$, is thus added to the current amount of β -phase, ${}^n X_{\beta}$, in order to recalculate the amount of β -phase originally available at the start of the cooling, X_{β} . On cooling from 410°C s^{-1} to 20°C s^{-1} , diffusion-controlled α formation also occurs [15]. Given the lack of precise data on the subject, an alternative choice is made and the current equilibrium fraction of the β -phase, X_{β}^{eq} , is subtracted from the β -phase amount available for the transformation in order to prevent a full transformation to martensite, see in equation (16).

For cooling rate $>410^\circ\text{C s}^{-1}$

$${}^{n+1}X_{\alpha_m} = {}^n X_{\alpha_m} + \Delta X_{\alpha_m} = (1 - e^{-b_{KM}(T_{ms} - T)}) ({}^n X_{\beta} + {}^n X_{\alpha_m}). \quad (15)$$

For cooling rate between 410 and 20°C s^{-1}

$${}^{n+1}X_{\alpha_m} = {}^n X_{\alpha_m} + \Delta X_{\alpha_m} = (1 - e^{-b_{KM}(T_{ms} - T)}) ({}^n X_{\beta} + {}^n X_{\alpha_m} - X_{\beta}^{eq}) \quad (16)$$

α_m , formed under cooling conditions, has an unstable crystal structure [49] which is then subjected to evolution with temperature and time as described in the next section.

3.3.3. *Recovery of massive and martensitic α -phase.* The decomposition of α -phases according to the right-hand side of figure 2 starts with the α_m -phase. It dissolves to ($\alpha + \beta$) when the temperature rises after martensite formation [37]. The martensite dissolution occurs by diffusional process according to the current equilibrium proportion of α - and β -phases at the current temperature [37]. The α -phase formed from the recovery of α_m , together with an equilibrium proportion of the β -phase, presents a new morphology which will tend to an ‘equilibrium’ α -phase composition with time. It is ignored that the α -phase from recovered α_m has a different crystallography and composition from α_w . Thereby we avoid adding an extra α -phase (state variable) into the model. The classical JMAK, presented in equation (2), is used and adapted to the implementation of the $\alpha_m \rightarrow (\alpha_w + \beta)$ transformation. The values for the kinetic parameters, k_{α_m} and N_{α_m} are taken from Gil Mur *et al* [37]. They determined the kinetics of the transformation through hardness measurements. The expected martensite equilibrium, $X_{\alpha_m}^{eq}$, is used to determine the expected amount of martensite left at the current temperature. The dissolved α_m -phase from the recovery transformation (superscript r), $\Delta X_{\alpha_m}^r$, is then divided between the formed α_w - and β -phases, ΔX_{α_w} and ΔX_{β} , according to the current equilibrium of α - and β -phases, X_{β}^{eq} , see in equation (18).

$${}^n X_{\alpha_m} + \Delta^n X_{\alpha_m}^r = {}^{n+1} X_{\alpha_m}^{eq} - (e^{-k_{\alpha_m}(t_c + \Delta t)^{N_{\alpha_m}}}) ({}^n X_{\alpha_m} + {}^n X_{\beta} - {}^{n+1} X_{\alpha_m}^{eq}), \quad (17)$$

$$\begin{aligned} \Delta^n X_{\alpha_w}^r &= \Delta^n X_{\alpha_m}^r (1 - {}^{n+1} X_{\beta}^{eq}), \\ \Delta^n X_{\beta}^r &= \Delta^n X_{\alpha_m}^r {}^{n+1} X_{\beta}^{eq}, \end{aligned} \quad (18)$$

with

Erratum

$$t_c = \left[-\ln \left(\frac{{}^n X_{\alpha_m} - {}^{n+1} X_{\alpha_m}^{eq}}{({}^n X_{\beta} + {}^n X_{\alpha_m} - {}^{n+1} X_{\alpha_m}^{eq})} \right) / k_{\alpha_m} \right]^{1/N_{\alpha_m}}. \quad (19)$$

3.3.4. *Dissolution of the α -phases to the β -phase.* α dissolves back to β under heating conditions or when the α/β equilibrium is not reached. The α dissolution can be assimilated to a diffusional process as the dissolution appears to be controlled by the mobility of the vanadium element at the α - β interface [50]. Kelly and co-workers modelled the dissolution of α assuming a parabolic β growth rate, $X_{\alpha} = f_{diss}(T)\sqrt{t}$ with $f_{diss}(T) = 2.2 \times 10^{-31} T^{9.89}$ with T in kelvin [11, 28]. The model described in [11] has been used in the implementation. For the same reason as in the JMAK model, a fictive time, t^* , corresponding to the equivalent time necessary to transform at ${}^{n+1} T$ the amount of material already transformed at ${}^n T$, is introduced. A critical time, t_{crit} , is also calculated to be the time for which the reaction is equal to 1. In the current model, the transformation is first handled for one single α -phase which represents the sum of the α_w - and α_{gb} -phases.

$${}^{n+1} (X_{\alpha_w} + X_{\alpha_{gb}}) = \begin{cases} 1 - {}^{n+1} X_{\beta}^{eq} f_{diss}(T) \sqrt{(\Delta t + t^*)} & 0 < \Delta t + t^* < t_{crit}, \\ 1 - {}^{n+1} X_{\beta}^{eq} = {}^{n+1} X_{\alpha}^{eq} & \Delta t + t^* > t_{crit}, \end{cases} \quad (20)$$

$$t^* = \left(\frac{{}^n X_{\beta}}{{}^{n+1} X_{\beta}^{eq} f_{diss}(T)} \right)^2, \quad (21)$$

$$t_{crit} = (f_{diss}(T))^{-2}. \quad (22)$$

The calculated amount of dissolved α thus needs to be transferred to the fraction of the α_w -phase and α_{gb} -phase. Consulting the pseudo-binary titanium phase diagram, the α_{gb} -phase that forms at high temperature has a composition slightly enriched in the α -stabilizer element aluminium [4]. The temperature gradient at cooling provides the driving force for diffusion of

aluminium, which stabilizes the α_{gb} -phase. Correspondingly, the α_{W} -phase with a composition closer to the β -phase is considered more favourable to transform to the β -phase. Therefore, the α_{gb} -phase is chosen to start dissolving after all α_{W} has been consumed.

4. Simulation results and discussion

The models described above are implemented and tested in an in-house Matlab® toolbox for calibration and validation against experimental measurements available in the literature [13, 36, 51, 52].

4.1. Material input data

Different input material data, mostly temperature dependent, are necessary for the simulations. They are the equilibrium α -phase fraction X_{α}^{eq} , the JMAK coefficients k and N for each diffusional phase transformation, and the Koistinen–Marburger coefficients T_{ms} and b_{KM} . Despite the fact that Ti–6Al–4V is the most commonly used titanium alloy, its microstructure transformation kinetics is not as well documented as for steel alloys. Malinov *et al* [51, 52], Babu *et al* [13], Elmer *et al* [36] and Pederson *et al* [53] measured phase changes during controlled temperature histories. Their experimental data are used in the evaluation of the transformation kinetic parameters used in this work. Alternatively, material data can be calculated with the help of thermodynamic-based software such as Thermocalc [54] or JMatPro [55]. Both methods have uncertainties and are specific to the composition and initial alloy structure considered. Unfortunately, the transformation kinetics and the equilibrium phase fractions are also known to vary with the chemical composition of nominally the same Ti–6Al–4V alloy, the type of temperature history considered and the start morphology before transformation [16]. Such variations in the alloy are expected in manufacturing, and these also influence the accuracy of a general microstructure model. The material data used in the model are discussed below.

$X_{\alpha}^{\text{eq}}(T)$ can be measured or calculated according to the alloy composition [54]. Variations up to 10% are directly observed for $X_{\alpha}^{\text{eq}}(T)$ data in Ti–6Al–4V collected from the literature [4, 28, 48, 52, 53]. Some of these are shown in figure 3. The Kelly calculated data are from [28], the Malinov β to α isothermal data are from experimental measurements in [52], the Katarov calculated data are Thermocalc calculated data in [4, 19], the Pederson α to β and β to α isothermals are from experimental measurements in [53] and the Castro first approximation data are a first approximation in [48]. All the above authors' data, collected in figure 3, are the basis for a polynomial curve fitting, which are used in the current microstructure model as in

$$X_{\alpha}^{\text{eq}}(T) = \sum_{i=0}^8 P(i) \left(\frac{T}{1000} \right)^{8-i}, \quad (23)$$

where

$$P = \{-31\,188.514, 170\,526.26, -388\,991.69, 471\,927.45, -315\,178.49, 99\,079.891, 1667.1991, -9726.8403, 1884.7280\}$$

and T is the temperature in degree Celsius. A polynomial description avoids repetitive interpolation procedures during calculation.

A few papers [30, 36, 37, 48, 56] take into consideration the study of the martensite formation in Ti–6Al–4V. The material parameter b_{KM} is calculated to be 0.005 from recorded welding experiments by Elmer *et al* [36]. Different values for the martensite start of Ti–6Al–4V, T_{ms} , are found in the literature. Ahmed and Rack [15] used 575 °C after Majdic

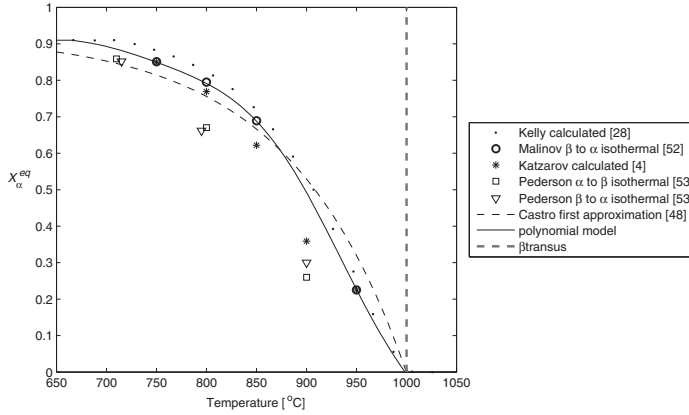


Figure 3. $X_{\alpha}^{csq}(T)$ data from the literature [4, 28, 48, 52, 53] and the polynomial model in (22).

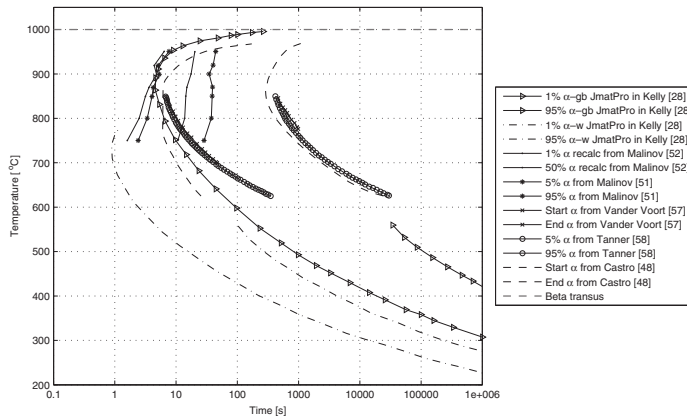


Figure 4. TTT-diagram data for Ti-6Al-4V collected from the literature [28, 48, 51, 52, 57, 58].

and Ziegler [38], Crespo *et al* [30] used 650 °C, and Castro and Seraphin [48] evaluated the martensite start to be around 625 °C. A sensitivity analysis has been performed for the different reported values in order to investigate the impact of T_{ms} . It showed only small variations in the calculated martensite fractions, so a T_{ms} value of 575 °C [15] is chosen in the model.

The JMAK coefficients k and N have been evaluated from differential scanning calorimetry (DSC) study and resistivity measurements by Malinov *et al* [51, 52]. They can also be extracted from the existing TTT-diagram data by inverse calculation with the JMAK model. We used the latter approach in our work. The parameters k and N are calculated using the times of beginning and completion of the transformation obtained from the TTT-diagram. Figure 4 shows several of the published TTT-curves that can be found in the literature, and large variations of the TTT-data are observed between the diverse sources. Calculated JMatPro curves from Kelly [28]

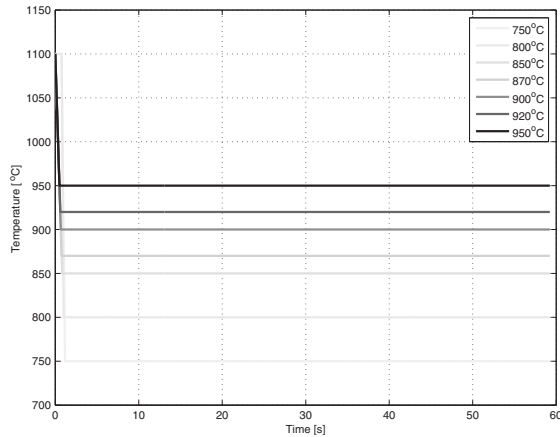


Figure 5. Isothermal conditions [52]—rapid cooling (around $300\text{ }^{\circ}\text{C s}^{-1}$) from $1110\text{ }^{\circ}\text{C}$ to the chosen isotherm temperatures.

are also included in figure 4 and it is observed that they fit into the fluctuation range of the experimental results. The differences observed are partly explained by the variations in the conditions with which the curves have been obtained. The phase transformations do not follow exactly the same mechanism depending on, for example, the temperature history [19] such as for the isotherms [52] or the continuous cooling experiments [51] by Malinov *et al.* Moreover, it is noted that experimental data are not available over larger temperature ranges or for specific morphologies such as α_{gb} . The JMatPro curves calculated by Kelly [28] are thus used for the morphology α_{gb} in the model. For the same reason, the curves calculated by Kelly [28] for the temperatures below $750\text{ }^{\circ}\text{C}$ are used for the considered α_{W} morphology. The upper part of the α curves in the temperature domain spread from $750\text{ }^{\circ}\text{C}$ to $850\text{ }^{\circ}\text{C}$ or $950\text{ }^{\circ}\text{C}$ are available from several references. Calibration of the α_{W} curves in the temperature domain above $750\text{ }^{\circ}\text{C}$ are proposed in the next section.

4.2. Verification and further calibration of material input data

For calibration purposes of the β to α transformation kinetics, resistivity measurements during isothermal heat treatment [52] and DSC measurements during continuous cooling [51] are compared with the modelled transformation. These measurements were used to further refine the material input data discussed in the previous section. The temperature histories are shown in figure 5 for isothermal heat treatment, and in figure 6 for continuous cooling. Measurement data are not available for each of the morphologies considered in the model. The calculated total α -phase amount ($X_{\alpha} = X_{\alpha_{\text{gb}}} + X_{\alpha_{\text{W}}} + X_{\alpha_{\text{m}}}$) is used while comparing with experimental values. Note that no martensite or massive formation is observed for the tested thermal histories in [51, 52]. The fraction of the α_{m} -phase is thus zero for those cases, and therefore not discussed in the following. For comparison between the calculated total α -phase and the measured α -phase [51, 52] see figure 7 to figure 13.

The α -phase fractions from [52] and the proposed model are shown in figure 7 and figure 8 for the isothermal conditions shown in figure 5. the two alternatives for transformation kinetic

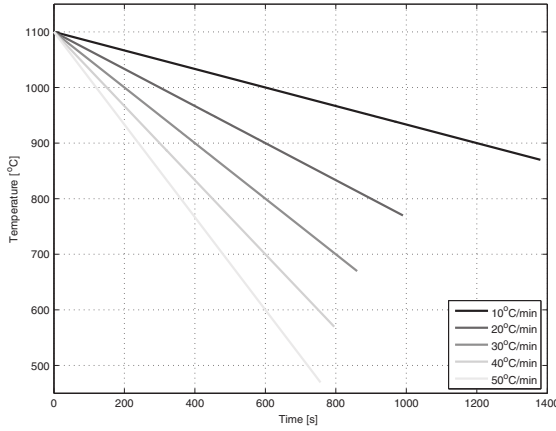


Figure 6. Continuous cooling conditions [51]—cooling from 1100 °C at the chosen cooling rate.

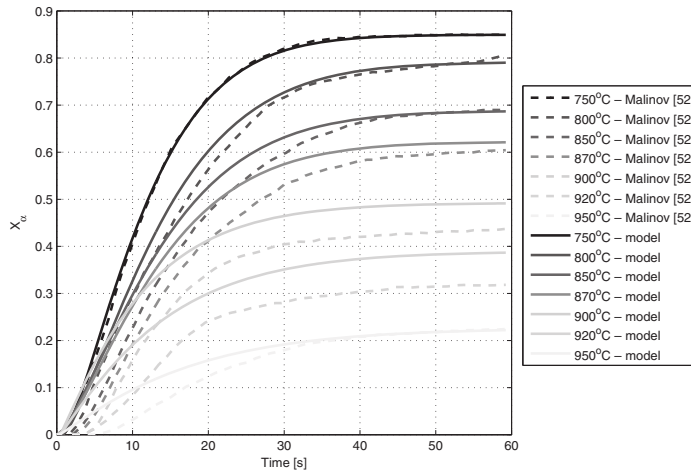


Figure 7. X_{α} from [52] and modelled with JMAK material parameters, $k_{\beta\alpha}$ and $N_{\beta\alpha}$, from [52].

parameters of the transformation $\beta \rightarrow \alpha + \beta$ from Malinov *et al* [52] and Malinov *et al* [51] are analysed. Very good agreements between measured and modelled α -phase fractions are obtained, see figure 7, when the parameters extracted from the isothermal experiments by Malinov *et al* [52] are directly used. Applying the parameters extracted from the cooling experiments in [51] in the simulation of the isothermal conditions does not give the same good agreement, see figure 8. The model shows a slower transformation at the highest temperatures and a very fast start of the transformation for 750 °C and 800 °C isotherms compared with the experimental data. Variations in the nucleation and growth conditions are expected when isothermal and continuous cooling conditions are considered [16]. Differences

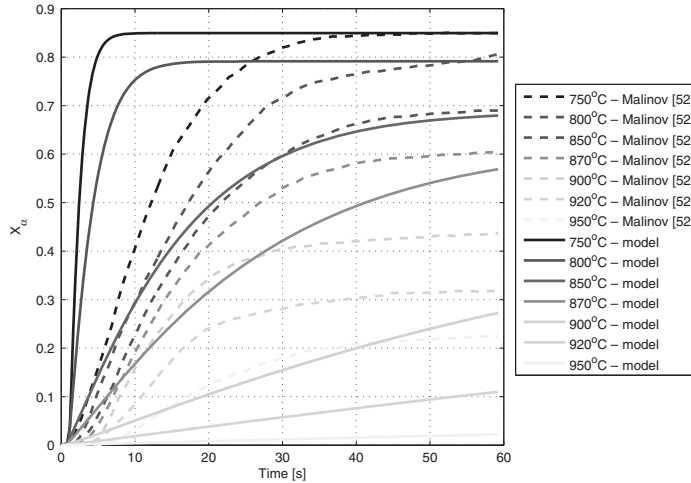


Figure 8. X_α from [52] and modelled with JMAK material parameters, $k_{\beta\alpha}$ and $N_{\beta\alpha}$, from [51].

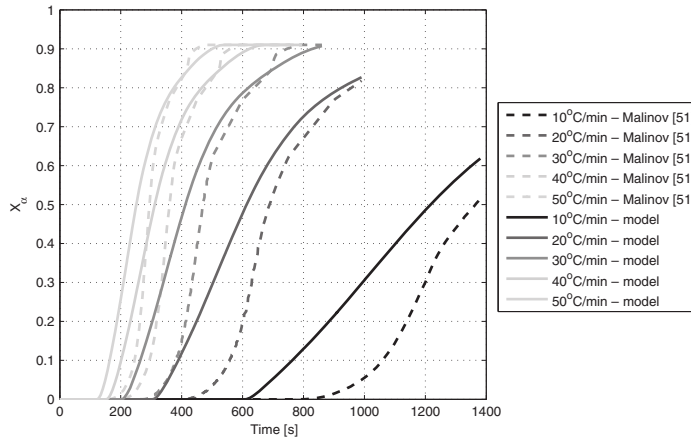


Figure 9. X_α from [51] and modelled with JMAK material parameters, $k_{\beta\alpha}$ and $N_{\beta\alpha}$, from [52].

in transformation mechanisms might reflect in the morphology of the α -phase formed and consequently affect the JMAK material parameters [19, see section 6.7.1].

Simulation results for continuous cooling seen in figure 6 are shown in figure 9 and figure 10, where the two different alternatives for transformation kinetic parameters of the transformation $\beta \rightarrow \alpha + \beta$ from Malinov *et al* [52] and Malinov *et al* [51] were applied. The transformation kinetic parameters extracted from the isothermal heat treatment experiments in [52] are used for the model in figure 9. The experimental S-shape at the transformation start is lacking in the modelled behaviour. Similarly to the observations made in figure 8, the difference

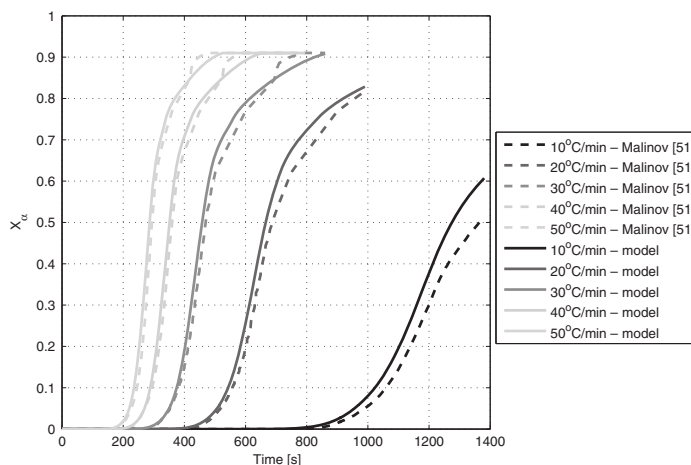


Figure 10. X_α from [51] and modelled with JMAK material parameters, $k_{\beta\alpha}$ and $N_{\beta\alpha}$, from [51].

in the mechanism of transformation causes the observed discrepancies in figure 9. The model with JMAK material parameters, $k_{\alpha\beta}$ and $N_{\alpha\beta}$, extracted from the isothermal exposure [52] might not properly account for the already existing nucleation sites formed during the previous cooling steps from the β -transus, and which are preferred sites for further growth [19, see section 6.7.1]. There is however expected good agreement between the measured α -phase fraction by Malinov *et al* [51] and the output from the model when transformation kinetics from the corresponding continuous cooling experiments are used [51].

From simulations above, the two sets of transformation kinetic parameters for the transformation $\beta \rightarrow \alpha + \beta$, which are extracted from isothermal and continuous cooling experiments [51, 52], are not a good choice for a general temperature history. On the one hand, in figure 7 and figure 10, verification of the model for use under a specific heat treatment condition is accepted through the expected good agreement between experiments and the modelled α -phase. On the other hand, in figure 8 and figure 9, disagreements are obtained when simulating with JMAK material parameters that are not indexed for the same kind of heat treatment condition. Therefore, we propose alternative TTT-curves, shown in figure 11, which are chosen in line with the objective to model general temperature histories. Notice that the TTT-curves have been extended almost asymptotically to meet the β -transus line where the incubation time is large and should not result in unobserved α formation close to the β -transus temperature. This extension is necessary in order to have complete data for the numerical algorithm. Reasonably acceptable results over a variety of temperature histories are in focus against a limitation to one heat treatment condition for modelling. For efficiency reasons we also give analytical expressions instead of using tabulated TTT-curves. Piecewise polynomial formulations, described in the appendix, are suggested to model the TTT-curves seen in figure 11. The TTT-curves, representing the two sets of transformation kinetic parameters for the transformations $\beta \rightarrow \alpha + \beta$ from the experiments by Malinov *et al* [51, 52], are also shown in figure 11.

The proposed transformation kinetic parameters calculated via the TTT-curves presented in figure 11 are used for the simulation results presented in figures 12 and figure 13. agreements

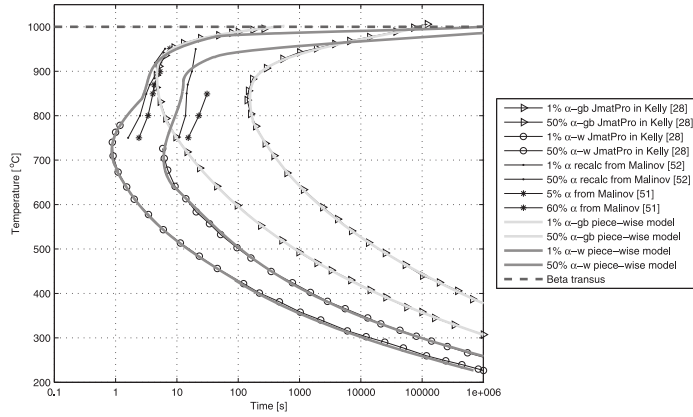


Figure 11. TTT-diagram for Ti-6Al-4V from collected literature sources [28, 51, 52] and the proposed piece-wise polynomial model.

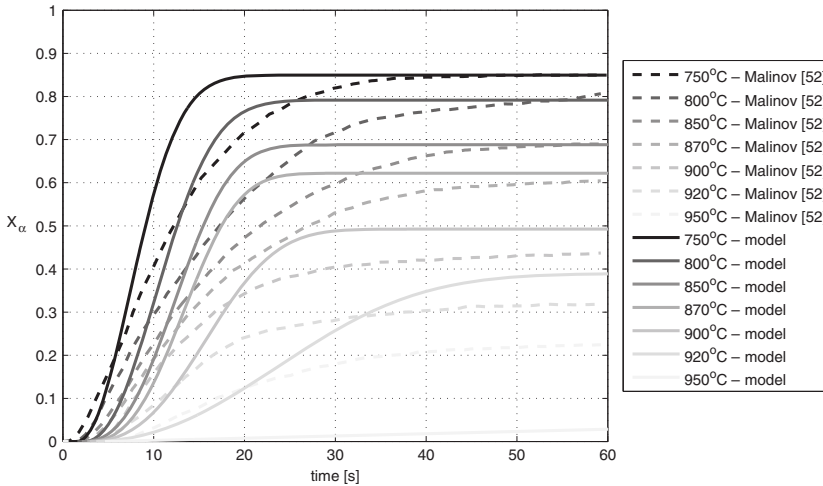


Figure 12. X_α from [52] and modelled with JMAK material parameters, $k_{\beta\alpha_{gb}}$, $N_{\beta\alpha_{gb}}$, and $k_{\beta\alpha_w}$, $N_{\beta\alpha_w}$ calculated from piece-wise polynomial TTT-curves.

between measured [51, 52] and simulated total α -phase fractions are good enough to be acceptable for both isothermal and continuous cooling conditions. Figure 12 shows the isothermal condition tests [52] and it is observed that the simulation predicted a more S-shaped start for the transformation than in figure 8 with kinetic parameters extracted from the continuous cooling conditions [51]. Figure 13 shows the continuous cooling condition tests from [51]. The simulated results give the correct transformation start point. However, the transformation is slightly too fast in the first part of the transformation.

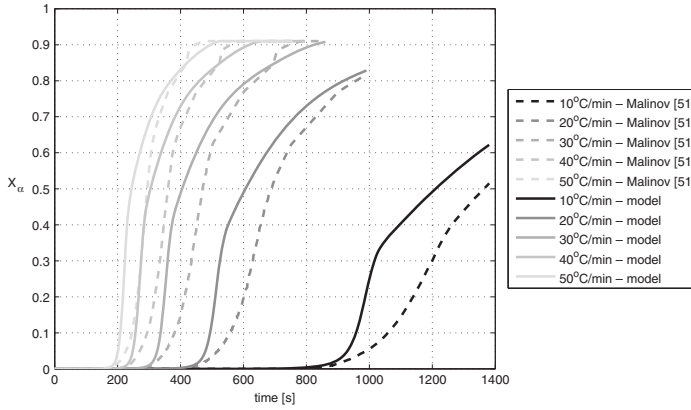


Figure 13. X_α from [51] and modelled with JMAK material parameters, $k_{\beta\alpha_{gb}}$, $N_{\beta\alpha_{gb}}$, and $k_{\beta\alpha_w}$, $N_{\beta\alpha_w}$ calculated from piece-wise polynomial TTT-curves.

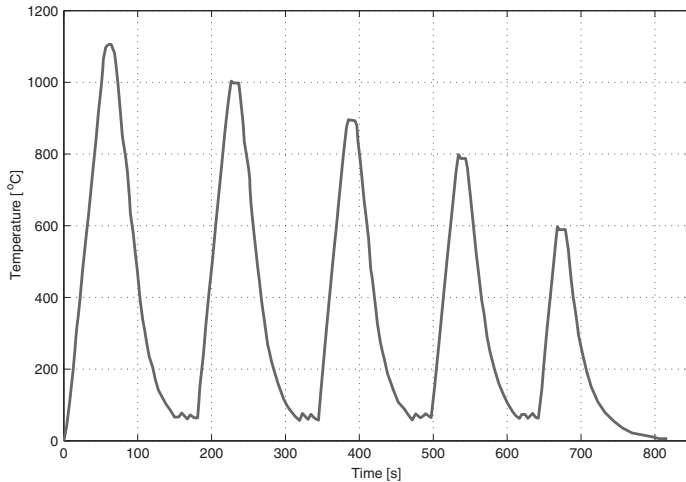


Figure 14. Temperature history—laser metal deposition [13].

4.3. Validation of the microstructure model

Babu *et al* [13] measured the total α -phase amount using time-resolved x-ray diffraction during a replicated Laser Metal Deposition (LMD) temperature history. Figure 14 shows the temperature history of the metal deposition experiments [13] which are simulated for validation purposes.

The experimental results [13] are compared with the model calculation results. Figures 15–16 show measured [13] and simulated total α -phase fractions for metal deposition thermal history shown in figure 14. The transformation kinetic parameters from the proposed TTT-curves are used and show satisfactory good agreement in figure 15. The different variants

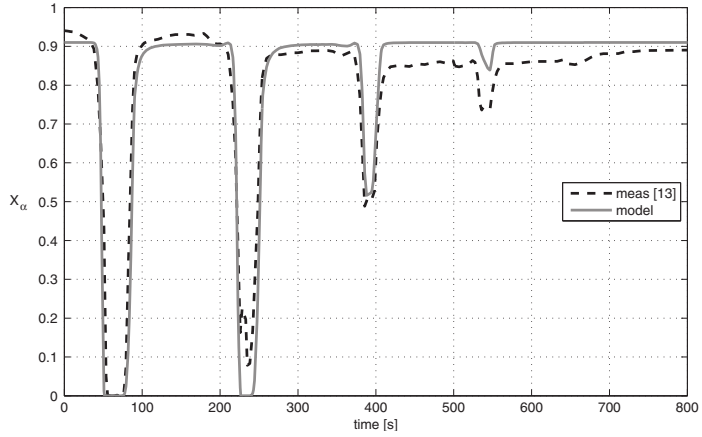


Figure 15. X_{α} from [13] and modelled with JMAK material parameters, $k_{\beta\alpha_{gb}}$, $N_{\beta\alpha_{gb}}$, and $k_{\beta\alpha_w}$, $N_{\beta\alpha_w}$ calculated from piece-wise polynomial TTT-curves.

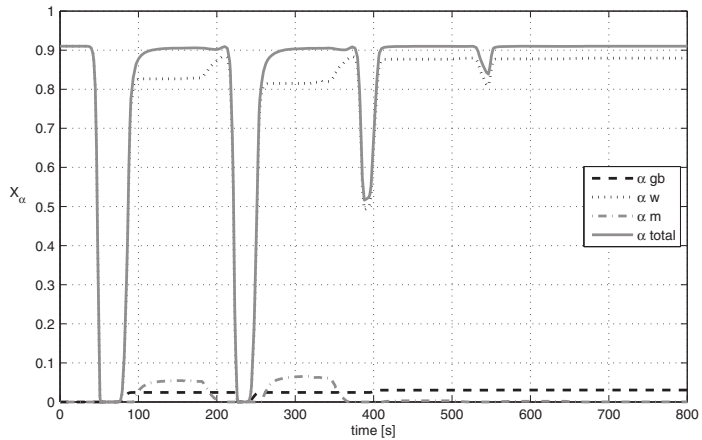


Figure 16. Modelled $X_{\alpha_{gb}}$, X_{α_w} , X_{α_m} , and $X_{\alpha_{total}}$ for the metal deposition test case with JMAK material parameters, $k_{\beta\alpha_{gb}}$, $N_{\beta\alpha_{gb}}$, and $k_{\beta\alpha_w}$, $N_{\beta\alpha_w}$ calculated from piece-wise polynomial TTT-curves.

of α -phases, which are also modelled, are shown in figure 16. A small proportion of α_{gb} stays in the material over the thermal cycles and it can be noted that α_m , which forms at the first thermal cycles, is consumed after reheating of the material.

5. Conclusions

This paper presents a calibrated temperature-driven microstructure model to describe the evolution of α -phase fractions in Ti-6Al-4V alloy for general arbitrary temperature changes.

The α -phase is of utmost important for material properties, and for manufacturing processes with cyclic temperature changes a microstructure model facilitates fair production planning. The α -phase is subdivided into three α -phases, which represent different morphologies: Widmanstätten, grain boundary and martensite. Each of them is handled as individual phases for the calculations in the model. The phase transformations were modelled based on a diffusional theory described by a Johnson–Mehl–Avrami–Kolmogorov formulation, a parabolic rate law for the α dissolution on heating, as well as diffusionless transformation for the martensite formation. Moreover, analytical alternatives for Ti–6Al–4V TTT-curves used in the calculation of the JMAK material parameters in the β to α transformations are proposed. The TTT-data were developed for the model to be used for arbitrary temperature histories, especially cyclic.

To permit coupling within a transient thermo-metallurgical finite element model of large industrial parts where temperature gradients are likely to be encountered, state variables are used to represent the phase fractions. This coupling work with a physically based constitutive model [2] is currently under progress. In this way, a more complete thermo-mechanical model of industrial parts is available accounting for the microstructure.

Acknowledgments

This work was supported in part by the Swedish National Aviation Engineering Research Programme (NFFP), which is highly acknowledged. The authors would like to express their gratitude to Professor Kenneth Eriksson for mathematical guidance.

Appendix. Piece-wise polynomial description of the TTT-curves used in the model

For the 1% transformation curve of α_{gb} , see figure 11: left full line in light grey,

$$t_{\alpha_{gb}}^{1\%}(T) \begin{cases} T \leq 1060 & \sum_{i=1}^4 P_1(i) \left(\frac{T}{1000}\right)^{4-i}, \\ 1060 < T \leq 1275 & \sum_{i=1}^6 P_2(i) \left(\frac{T}{1000}\right)^{6-i}, \end{cases} \quad (\text{A.1})$$

where

$$P_1 = \{20.563, -86.779, 146.36, -120.00, 40.973\},$$

$$P_2 = \{41\,059.764, -262\,322.94, 697\,207.00, -986\,711.93, 784\,229.81, -331\,901.06, 58\,440.4796\}$$

with T in kelvin and t in second.

For the 50% transformation curve of α_{gb} , see figure 11: right full line in light grey,

$$t_{\alpha_{gb}}^{50\%}(T) \begin{cases} T \leq 1060 & \sum_{i=1}^4 P_3(i) \left(\frac{T}{1000}\right)^{4-i}, \\ 1060 < T \leq 1275 & \sum_{i=1}^6 P_4(i) \left(\frac{T}{1000}\right)^{6-i}, \end{cases} \quad (\text{A.2})$$

where

$$P_3 = \{-4.9866, 5.2617, 24.168, -49.111, 27.168\},$$

$$P_4 = \{-123\,057.49, 823\,987.50, -2294\,367.6, 3400\,803.7, -2830\,274.4, 1254\,010.3, -0.231\,099.49\}$$

with T in kelvin and t in second.

For the 1% transformation curve of α_w , see Figure 11: left full line in dark grey,

$$t_{\alpha_w}^{1\%}(T) \begin{cases} T \leq 700 & \sum_{i=1}^5 P_5(i)(T - 600)^{i-1}, \\ 700 < T \leq 950 & \sum_{i=1}^5 P_6(i)(T - 800)^{i-1}, \\ 950 < T \leq 1110 & \sum_{i=1}^5 P_7(i)(T - 1000)^{i-1}, \\ 1110 < T \leq 1250 & \sum_{i=1}^5 P_8(i)(T - 1150)^{i-1}, \\ 1250 < T & \sum_{i=1}^5 P_9(i) \frac{(T - 1250)^{i-1}}{\sqrt{1300 - T}}, \end{cases} \quad (\text{A.3})$$

where

$$\begin{aligned} P_5 &= \{3.5, -0.019, 4.2 \times 10^5, -2.8 \times 10^8, 9.3 \times 10^{11}\}, \\ P_6 &= \{0.92, -9 \times 10^3, 2.2 \times 10^5, -1.6 \times 10^8, 21.1\}, \\ P_7 &= \{-0.062, 5.5 \times 10^4, 4.5 \times 10^5, -7.5 \times 10^8, -1.7 \times 10^{10}\}, \\ P_8 &= \{0.52, 2 \times 10^3, 7.1 \times 10^6, 5.4 \times 10^7, 2.7 \times 10^9\}, \\ P_9 &= \{11.4, -0.149, 0.123, -3.22 \times 10^3, -1.05 \times 10^5\} \end{aligned}$$

with T in kelvin and t in second.

For the 50% transformation curve of α_w , see Figure 11: right full line in dark grey,

$$t_{\alpha_w}^{50\%}(T) \begin{cases} T \leq 915 & \sum_{i=1}^4 P_{10}(i)(T - 600)^{i-1}, \\ 915 < T \leq 1150 & \sum_{i=1}^4 P_{11}(i)(T - 1000)^{i-1}, \\ 1150 < T \leq 1205 & \sum_{i=1}^4 P_{12}(i)(T - 1000)^{i-1}, \\ 1205 < T & \sum_{i=1}^4 P_{13}(i) \frac{(T - 1250)^{i-1}}{\sqrt[10]{1300 - T}}, \end{cases} \quad (\text{A.4})$$

where

$$\begin{aligned} P_{10} &= \{4.41, -0.02, 4.58 \times 10^5, -5.48 \times 10^8\}, \\ P_{11} &= \{0.8, 1.31 \times 10^3, 2.33 \times 10^5, -1.23 \times 10^7\}, \\ P_{12} &= \{2.09, -2.97 \times 10^3, -9.71 \times 10^5, 4.87 \times 10^7\}, \\ P_{13} &= \{7.41, 0.144, -3.88 \times 10^4, -2.64 \times 10^5\}[-2pt] \end{aligned}$$

with T in kelvin and t in second.

References

- [1] Leyens C and Peters M 2003 *Titanium and Titanium Alloys: Fundamentals and Applications* (Weinheim: Wiley-VCH)
- [2] Babu B 2008 Physically based model for plasticity and creep of Ti-6Al-4V *Licentiate Thesis* Division of Material Mechanics, Luleå University of Technology, Sweden, 2008:40
- [3] Lindgren L E 2007 *Computational Welding Mechanics: Thermomechanical and Microstructural Simulations* (Cambridge, England/Boca Raton, FL: Woodhead Publishing Ltd/CRC Press)
- [4] Katarzov I, Malinov S and Sha W 2002 Finite element modeling of the morphology of beta to alpha phase transformation in Ti-6Al-4V alloy *Metall. Mater. Trans. A* 33 1027-40

- [5] Grujicic M, Cao G and Figliola R S 2001 Computer simulations of the evolution of solidification microstructure in the LENS™ rapid fabrication process *Appl. Surf. Sci.* **183** 43–57
- [6] Gandin C-A and Rappaz M 1997 A 3D Cellular Automaton algorithm for the prediction of dendritic grain growth *Acta Mater.* **45** 2187–95
- [7] Thiessen R G and Richardson I M 2006 A strategy for modeling microstructure in macroscopic simulations of welded material *Metall. Mater. Trans. B* **37** 293–9
- [8] Grong O and Shercliff H R 2002 Microstructural modelling in metals processing *Prog. Mater. Sci.* **47** 163–282
- [9] Charles C 2008 Modelling microstructure evolution of weld deposited Ti–6Al–4V *Licentiate Thesis* Division of Material Mechanics, Luleå University of Technology, Sweden, 2008:47
- [10] Charles C and Järnstråtr N 2008 Modelling Ti–6Al–4V microstructure by evolution laws implemented as finite element subroutines: application to TIG metal deposition. *8th Int. Conf. on Trends in Welding Research (Pine Mountain)* (Materials Park, OH: ASM International)
- [11] Kelly S M, Babu S S, David S A, Zacharia T and Kampe S L 2005 A microstructure model for laser processing of Ti–6Al–4V. *7th Int. Conf. on Trends in Welding Research (Pine Mountain)* (Materials Park, OH: ASM International)
- [12] Charles C and Järnstråtr N 2007 Development of a microstructure model for metal deposition of titanium alloy Ti–6Al–4V. *11th World Conf. on Titanium (Ti-2007) (Kyoto)* (Sendai: The Japan Institute of Metals)
- [13] Babu S S, Kelly S M, Specht E D, Palmer T A and Elmer J W 2005 Measurement of phase transformation kinetics during repeated thermal cycling of Ti–6Al–4V using time-resolved x-ray diffraction *Int. Conf. on Solid-Solid Phase Transformations in Inorganic Materials (Phoenix)* (Warrendale, PA: Minerals, Metals and Materials Society)
- [14] Donachie M J 2000 *Titanium: A Technical Guide* (Materials Park, OH, ASM International)
- [15] Ahmed T and Rack H J 1998 Phase transformations during cooling in $\alpha + \beta$ titanium alloys *Mater. Sci. Eng. A* **243** 206–11
- [16] Porter D A and Easterling K E 1992 *Phase Transformations in Metals and Alloys* (London: Chapman and Hall)
- [17] Lütjering G 1998 Influence of processing on microstructure and mechanical properties of $\alpha + \beta$ titanium alloys *Mater. Sci. Eng. A* **243** 32–45
- [18] Lütjering G 1999 Property optimization through microstructural control in titanium and aluminum alloys *Mater. Sci. Eng. A* **263** 117–26
- [19] Sha W and Malinov S 2009 *Titanium Alloys: Modelling of Microstructure, Properties and Applications* (Cambridge, England: Woodhead Publishing Ltd)
- [20] Boyer R R and Furrer D U 2004 The potential advantages of microstructure modeling of titanium to the aerospace industry *Materials Processing and Design: Modeling, Simulation and Applications—NUMIFORM 2004 (Columbus)* (College Park, MD: American Institute of Physics Conference Series)
- [21] Guo Z X, Pettifor D, Kubin L and Kostorz G 2004 Multiscale materials modelling *Mater. Sci. Eng. A* **365** 1–354
- [22] Oddy A S, McDill J M J and Karlsson L 1996 Microstructural predictions including arbitrary thermal histories, re-austenization and carbon segregation effects *Can. Metall. Q.* **35** 275–83
- [23] Koistinen D P and Marburger R E 1959 A general equation prescribing the extent of the austenite-martensite transformation in pure iron-carbon alloys and plain carbon steels *Acta metall.* **7** 59–60
- [24] Avrami M 1939 Kinetics of phase change: I. General theory *J. Chem. Phys.* **7** 1103–12
- [25] Avrami M 1940 Kinetics of phase change: II. Transformation-time relations for random distribution of nuclei *J. Chem. Phys.* **8** 212–24
- [26] Avrami M 1941 Kinetics of phase change: III. Granulation, phase change, and microstructure *J. Chem. Phys.* **9** 177–84
- [27] Kirkaldy J S 1991 Diffusion-controlled phase transformations in steels. Theory and applications *Scand. J. Metall.* **20** 50–61
- [28] Kelly S M 2004 thermal and microstructure modeling of metal deposition processes with application to Ti–6Al–4V *PhD Thesis* Materials Science and Engineering, Faculty of the Virginia Polytechnic Institute and State University, USA
- [29] Robert Y 2007 Simulation numérique du soudage du TA6V par laser YAG impulsif : caractérisation expérimentale et modélisation des aspects thermomécaniques associés à ce procédé (in french) *PhD Thesis* Centre des Matériaux P.M. Fourt, Mines ParisTech (ENSM), France
- [30] Crespo A, Deus A and Vilar R 2009 Modeling of phase transformations and internal stresses in laser powder deposition. *17th Int. Symp. on Gas Flow, Chemical Lasers, and High-Power Lasers (Lisboa, Portugal)*
- [31] Longuet A, Robert Y, Aeby-Gautier E, Appolaire B, Mariage J F, Colin C and Cailletaud G 2009 A multiphase mechanical model for Ti–6Al–4V: Application to the modeling of laser assisted processing *Comput. Mater. Sci.* **46** 761–6

- [32] Johnson W and Mehl R 1939 Reaction Kinetics in processes of nucleation and growth *Trans. Am. Inst. Min. Metall. Eng.* **135** 416–58
- [33] Kolmogorov A 1937 Statistical theory of crystallization of metals (in Russian) *Izv. Akad. Nauk SSSR Ser. Math.* **1** 355–9
- [34] Teixeira J D C, Appolaire B, Aeby-Gautier E, Denis S, Cailletaud G and Späth N 2007 Transformation kinetics and microstructures of Ti17 titanium alloy during continuous cooling *Mater. Sci. Eng. A* **448** 135–45
- [35] Fan Y, Cheng P, Yao Y L, Yang Z and Eglund K 2005 Effect of phase transformations on laser forming of Ti–6Al–4V alloy *J. Appl. Phys.* **98** 013518
- [36] Elmer J W, Palmer T A, Babu S S, Zhang W and DebRoy T 2005 In-situ observations of phase transformations in the fusion zone of Ti–6Al–4V alloy transient welds using synchrotron radiation *Mathematical Modelling of weld phenomena* vol 7 ed H Cerjak *et al* (Graz: Verlag der Technischen Universität Graz)
- [37] Gil Mur F X, Rodriguez D and Planell J A 1996 Influence of tempering temperature and time on the alpha prime Ti–6Al–4V martensite *J. Alloys Compounds.* **234** 287–9
- [38] Majdic M and Ziegler G 1973 Effect of the metastable beta phase transformations in the Ti–6Al–4V alloy *Z. Metallk./Mater. Res. Adv. Tech.* **64** 751–8 (in German)
- [39] Lütjering G, Albrecht J and Ivasishin O M 1995 Influence of cooling rate and beta grain size on the tensile properties of $\alpha + \beta$ Ti-alloys *Titanium '95: Science and Technology (Birmingham)* (London Institute of Material)
- [40] Cahn J W 1956 Transformation kinetics during continuous cooling *Acta Metall.* **4** 572–5
- [41] Ronda J and Oliver G J 2000 Consistent thermo-mechano-metallurgical model of welded steel with unified approach to derivation of phase evolution laws and transformation-induced plasticity *Comput. Methods Appl. Mech. Eng.* **189** 361–418
- [42] Fernandes F, Denis S and Simon A 1985 Mathematical model coupling phase transformation and temperature evolution during quenching of steels *Mater. Sci. Technol.* **1** 838–44
- [43] Hildenwall B 1979 *Prediction of the Residual Stresses Created During Quenching PhD Thesis* Linköping Studies in Science and Technology, Linköping University, Sweden
- [44] Leblond J B and Devaux J 1984 A new kinetic model for anisothermal metallurgical transformations in steels including effect of austenite grain size *Acta Metall.* **32** 137–46
- [45] Leblond J-B 1985 Mathematical models of anisothermal phase transformations in steels, and predicted plastic behaviour *Mater. Sci. Technol.* **1** 815–22
- [46] Jones S J and Bhadeshia H K D H 1997 Kinetics of the simultaneous decomposition of austenite into several transformation products *Acta Mater.* **45** 2911–20
- [47] Järsvstråt N and Tjotta S 1996 Mechanical material model for aluminium extrusions during on-line quenching *J. Eng. Mater. Technol., Trans. ASME* **118** 114–9
- [48] Castro R and Seraphin L 1966 Contribution in the metallographic and structural study of the alloy of titanium TAGV *Les Mémoires scientifiques de la Revue de métallurgie/Scientific Memories Seen Again by Metallurgy* **63** 1025–58 (in French)
- [49] Qazi J I, Senkov O N, Rahim J and Froes F H 2003 Kinetics of martensite decomposition in Ti–6Al–4V–xH alloys *Mater. Sci. Eng. A* **359** 137–49
- [50] Szkliniarz W and Smolka G 1995 Analysis of volume effects of phase transformation in titanium alloys *J. Mater. Process. Technol. Adv. Mater. Technol.* **53** 413–22
- [51] Malinov S, Guo Z, Sha W and Wilson A 2001 Differential scanning calorimetry study and computer modeling of β to α phase transformation in a Ti–6Al–4V alloy *Metall. Mater. Trans. A* **32** 879–87
- [52] Malinov S, Markovsky P, Sha W and Guo Z 2001 Resistivity study and computer modelling of the isothermal transformation kinetics of Ti–6Al–4V and Ti–6Al–2Sn–4Zr–2Mo–0.08Si alloys *J. Alloys Compounds* **314** 181–92
- [53] Pederson R, Babushkin O, Skystedt F and Warren R 2003 Use of high temperature X-ray diffractometry to study phase transitions and thermal expansion properties in Ti–6Al–4V *Mater. Sci. Technol.* **19** 1533–8
- [54] Andersson J O, Helander T, Höglund L, Shi P and Sundman B 2002 Thermo-Calc and DICTRA, computational tools for materials science *Calphad* **26** 273–312
- [55] Saunders N, Li X, Miodownik A P and Schille J-P 2003 An integrated approach to the calculation of materials properties for Ti-alloys *10th World Conf. on Titanium (Hamburg, Germany)*
- [56] Elmer J W, Palmer T A, Babu S S, Zhang W and DebRoy T 2004 Phase transformation dynamics during welding of Ti–6Al–4V *J. Appl. Phys.* **95** 8327–39
- [57] Vander Voort G F 1991 *Atlas of Time–Temperature Diagrams for Nonferrous Alloys* (Metals Park, OH: ASM International)
- [58] Tanner L E 1959 Time–Temperature–Transformation diagrams of the titanium sheet-rolling-program alloys D.M.I.C. *Report* 46 G

**Temperature and microstructure evolution in Gas Tungsten Arc
Welding wire feed additive manufacturing of Ti-6Al-4V**

Corinne Charles Murgau, Andreas Lundbäck, Pia Åkerfeldt and Robert Pederson

To be submitted

Temperature and microstructure evolution in Gas Tungsten Arc Welding wire feed additive manufacturing of Ti-6Al-4V

Corinne CHARLES MURGAU ¹, Andreas LUNDBÄCK ²,
Pia ÅKERFELDT ³, Robert PEDERSON ^{3,4}

¹Department of Engineering Science, University West, 461 29 Trollhättan, Sweden

²Division of Mechanics of Solid Materials, Luleå University of Technology, 971 81 Luleå, Sweden

³Division of Materials Science, Luleå University of Technology, 971 81 Luleå, Sweden

⁴GKN Aerospace Engine Systems, 461 81 Trollhättan, Sweden

Abstract

The Finite Element Method (FEM) is used to solve temperature field and microstructure evolution during GTAW wire feed additive manufacturing process. The microstructure of titanium alloy Ti-6Al-4V is computed based on the temperature evolution in a point-wise logic. The methodology concerning the microstructural modeling is presented. A model to predict the thickness of the α lath morphology is also implemented. The results from simulations are presented together with qualitative and quantitative microstructure analysis.

Key words: Additive manufacturing, Titanium, Ti-6Al-4V, modeling, metal deposition, Finite Element

1. Introduction

Gas Tungsten Arc Welding (GTAW) wire feed additive manufacturing (AM) process is deposition of metal using a tungsten arc energy source. It belongs to the group of Direct Energy Deposit (DED) methods in AM. A solid metal wire is fed through a conventional wire feeder and deposited layer-by-layer onto a substrate using a standard GTAW energy source. The energy source is used to electrically heat and

PAPER D

melt the metal wire and base material. The addition of multiple layers produces a fully dense near-net-shape part. GTAW wire feed additive manufacturing has a high deposition rate [1]. Flexibility and cost saving in manufacturing are a large driving force in the development of such techniques [2].

The titanium alloy Ti-6Al-4V is extensively used in aerospace applications because of its good combination of mechanical properties. It is a well appreciated metal in the aerospace industry thanks to its good strength to weight ratio [3]. Its good weldability makes it suitable for AM processes. However, the microstructure and consequently the mechanical properties are highly dependent on the temperature history of the built material. Ti-6Al-4V is a two-phase material consisting of an hcp- α phase and bcc- β phase. It is a heat-treatable titanium alloy, which exhibits a variety of microstructures dependent on the conditions experienced during cooling transformation from the high-temperature β phase to the low-temperature α phase of the alloy, and for the reverse transformation upon reheating. Complete understanding of resulting material properties and mechanical behavior are prerequisites for successful qualification of parts for aerospace applications.

Process simulations provide information about how to manufacture components in order to achieve the required properties, and also to support the development and understanding of the manufacturing process itself. Finite Element (FE) simulation, which is a conventional method used in modeling of welding processes, particularly for larger components, are applied at macro scale. In the present work, the FE modeling is used to predict the thermal field and that in turn determines the microstructure evolution. A number of different strategies exist for how to include detailed and explicit modeling at a microscopic scale in a macroscopic simulation. One such strategy is to use sub-meshes located at the nodes of the FE model [4] or dual-mesh method by placing microstructure domains at nodes of a macroscopic FE calculation [5, 6]. However, the calculations become very cumbersome if a large component is to be simulated. Therefore, for industrial needs it is more pragmatic to use a density type of model, also called internal state variable approach by Grong and Shercliff [7]. A density type approach is here used in order to be able to model the microstructure at a larger scale. Moreover, it facilitates the future combination of the microstructure model with a mechanical model to compute material properties.

2. Process description and microstructure characterization

2.1. Experimental setup

The Ti-6Al-4V metal is wire feed deposited on a 3.25 mm thick plate using a tungsten arc weld heat source. 4 weld sequences of 10 layers height are continuously added on the plate as presented in Figure 1. Each layer is approximately 0.7 mm in height. Continuously here means that no waiting time between each deposited layer has been used except that for the welding torch movement to move to the new

PAPER D

starting position. In order to avoid oxidation and alpha case formation during the building process, the oxygen level is kept under 10 ppm within the building chamber. This is achieved by having an over-pressurized argon gas flowing through the chamber. The weld passes are numbered 1 to 4, corresponding to respective starting point as shown in Figure 1 (left). The building sequence is such that walls 1 through 4 are deposited layer by layer, one wall at a time. Totally 10 layers are deposited for each wall.

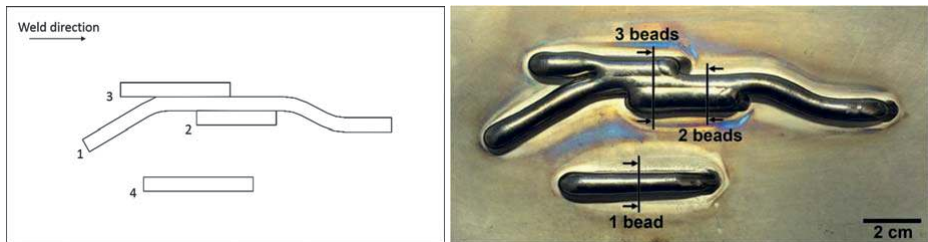


Figure 1. **Left:** Schematic sketch of starting positions for the building of each wall as well as their respective sequence order. **Right:** The real built feature consisting of the 4 different walls of 10 layers height. The arrows indicate the point of view for microstructural characterization of each cross section.

2.2. Microstructure characterization

In order to validate the predicted results from the microstructure model, the microstructure of selected cross sections were characterized. The location of each cross section was selected so that different widths of the built material could be evaluated. In total three cross sections were metallographically evaluated, corresponding to widths of 1, 2 and 3 weld beads, respectively. The cross sections were cut at the locations shown in Figure 1 (right). Thereafter, each sample was mounted, ground and polished using conventional methods for titanium alloys, and finally etched with Kroll's reagent (1 ml HF, 2ml HNO₃ and 100ml distilled H₂O) to reveal the microstructure.

The microstructural characterization was carried out in a light optical microscope (NIKON eclipse MA200) equipped with image analysis software (NIS Elements Basic Research). First large area mapping was carried out to capture overview images of the cross sections. Thereafter the microstructural characterization was planned in detail and the areas to be analyzed were decided. In each area ten images at 1000 times magnification were captured and in each image the α lath thickness was measured at 25 randomly selected sites. I.e. per area in total 250 α lath measurements were carried out. In addition, the fraction of grain boundary α was assessed for the single weld bead cross section. The measurement of the grain boundary α was carried

PAPER D

out manually. At first, large area mapping (approximate 110 images) of the selected region at 500 times magnification was carried out at the highest resolution (2560x1920). Thereafter, the grain boundary α was carefully marked and colored red by using an image editing software (Adobe Photoshop CC 2015) and digital zoom. The fraction of grain boundary α was subsequently calculated by comparing total number of pixels to the number of red pixels in the images.

3. Process modeling

The similarities between the here considered additive manufacturing process with multipass welding permit applying welding simulation techniques. Computational Welding Mechanics (CWM) establishes methods and models that are applicable for control of welding processes to obtain optimal mechanical performance. The book by Lindgren [8] describes different modeling options and strategies.

3.1. Thermal model

For the thermal model, the weld pool details are replaced by a heat input model. The modeling is thus considerably simplified but still being able to create a model fit for its purpose. The implementation logic is thoroughly described in [9]. Some noteworthy clarifications to the process model are shortly mentioned below.

The heat input model is the commonly used double ellipsoid with Gaussian distribution proposed by Goldak *et al.* [10]. An adaptive rescaling of the heat input through the efficiency factor is, when needed, used to control the variation of the heat input function due to the rather coarse mesh used for the discretization of the model. The heat input model has been calibrated on a simplified model of a 10-layer single wall. The parameters values are found in [9].

The number of nodes and elements in this model are approximately 19000 and 13000 respectively. The element type is 8-noded fully integrated hexahedral elements. The FE-software used in this work, MSC.Marc and its pre- and post-processor Mentat, has a number of interfaces for user defined subroutines. The heat input is defined via user subroutines. The microstructural model that will be described in subsequent chapter is also defined via these user subroutines.

3.2. Microstructure model

Phase evolution is computed during heating, cooling, and repeated re-heating and cooling. During heating up, when temperature exceeds about 700°C [11], α phase starts to transform to β phase. Normally during AM as well as welding, the heating rates are too fast for equilibrium to exist, which means that $X_{\beta} < X_{\beta\text{-eq}}$, even at temperatures exceeding the so-called β -transus of the alloy. Above the β -transus temperature at equilibrium only β phase exist. During cooling, existing β phase transforms through diffusion into α phases. For slow-to moderate cooling rates the initial α phase normally nucleates at the prior β grain boundaries, and continues to

PAPER D

grow along these grain boundaries before starting to grow into the prior β grain, in a lamellar morphology. This lamellar type of microstructure is here called Widmanstätten microstructure. For very high cooling rates, non-diffusional transformation of β to α phase takes place and this type of α phase is therefore defined as martensitic α , i.e. martensitic microstructure. Solid-solid phase changes, on heating as well as on cooling, are mostly characterized by transformation mechanisms of nucleation and growth processes. The β phase decomposition to α Widmanstätten and α at prior β grain boundaries, as well as the β formation during heat up are all diffusion controlled processes [12]. On the opposite, α martensite formation from β phase is a diffusionless transformation.

Solid-solid phase change model

The diffusional phase transformations of β to α and α to β are evaluated using a modified Johnson-Mehl-Avrami theory. The equation is strictly valid only under isothermal transformation, therefore the additivity principle has been adopted and discretization into a series of smaller isothermal steps is used during temperature variations. The rule of additivity [11] is commonly used to calculate non-isothermal transformation from isothermal transformation data using simple rate laws. It should be noticed that the additivity rule should be applied only under certain conditions at which the reaction is additive [7, 11, 12]. Grong and Shercliff [7] compared the additivity approach to numerical solutions when modeling microstructure state variables with the focus on applications in heat treatments and welding. Although discrepancies are observed, the approximation is evaluated to be sufficient for many problems and particularly when the constant data is estimated against experimental data for microstructure. The generalization steps of the Johnson-Mehl-Avrami equation used in this work are thoroughly detailed in Murgau et al. [13]. The incomplete transformations toward equilibrium at the current temperature is circumvented by normalizing the equations. The interaction between simultaneous transformations is handled by assuming that the current fraction of the resultant phase is taken relative to the total content of the transforming phase.

The diffusionless martensite formation has been chosen to be modeled using the classical Koistinen-Marburger equation for which a direct incremental formulation of the equation, shown to be simpler and equally well accurate [14], is chosen. The altogether model's equations and their discretization are found detailed in Murgau et al. [13].

Morphology parameter: alpha lath thickness

The morphology size parameter associated with Widmanstätten α phase, i.e. the α lath thickness parameter, has been modeled by a simplified energy model approach [15]. The α phase formation temperature is here, as a first approximation, considered dominant in determining the α lath thickness. The empirical Arrhenius equation is used to express the temperature dependence of the α lath thickness. A first

PAPER D

approximation for kinetics parameters have been used in [15], the proposed values seemed out of the expected parameters' dimensions. Irwin et al. [16] updated the values for the parameters after additional optimization supported by a new set of experimental results of their own. The new suggested values, Arrhenius prefactor $k=1.42\mu\text{m}$ and activation temperature $R=294\text{K}$, appear having fair dimensions and are thus used in this work. The equation and its explicit form used in the model can be found in Charles and Järsvsträt [15].

Implementation strategy

The development of the microstructure model is based on the finite element method and is supported by the feature of the software MSC.Marc. The microstructure is homogeneously described by state variables associated at each of the integration points of the finite element mesh. This approach means that Representative Volume Elements (RVE), see Figure 2, are considered at each integration point of the elements. The calculated value corresponds to an average behavior over this domain. For example, the phase fraction in an integration point then corresponds to the fraction of the phase in the RVE connected to this integration point.

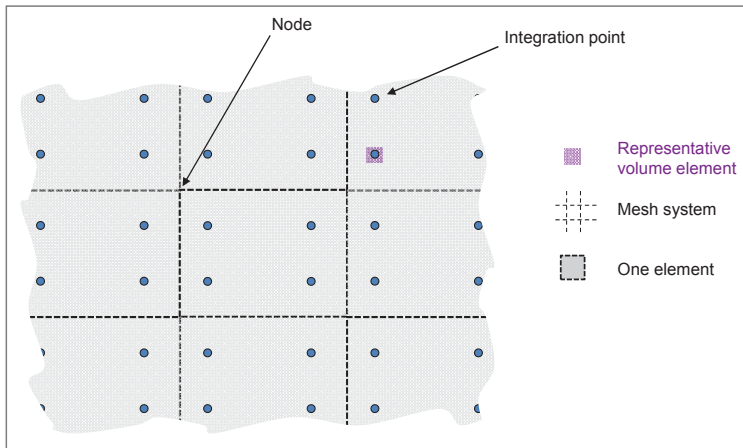


Figure 2. Schematic illustration of density type of model.

4 state variables are used in the model to represent the fraction of microstructure constituent phases. 1 more state variable is used for the α lath thickness parameter. The state variable denominations can be seen in Table 1. The α phase can form a number of different types of microstructures, but for the modeling purpose the choice to approximate the diffusively formed α into twofold different microstructure is made, namely i) grain boundary α (α_{gb}), and ii) Widmanstätten (α_{w}) microstructure. The grain boundary α (α_{gb}) is the α phase that is formed in the prior β grain boundaries. The Widmanstätten (α_{w}) structure represents the α phase that forms

PAPER D

inside the prior β grains (thus is here considered to include both *colony* type and *basket weave* microstructures). The α martensite (α_m) structure and the β phase are also represented.

Table 1. Microstructure parameters and morphology description used in this work.

Phase constituents	Type	State Variable	Size parameters
α	Diffusional α	Grain boundary	$X_{\alpha gb}$
		Intergranular, Basket-weave, Colony	$X_{\alpha w}$
	Non diffusional α	Martensite	$X_{\alpha m}$
β		X_{β}	

The interactions between the constituents are schematically presented in the upper right square of Figure 3. In this work, 4 different diffusional transformations and 1 non-diffusional transformation are implemented. The transformation processes and microstructure constituents' interactions that are implemented in the model are shown in the table of Figure 3. The detailed overall model logic can be found in Murgau et al. [13].

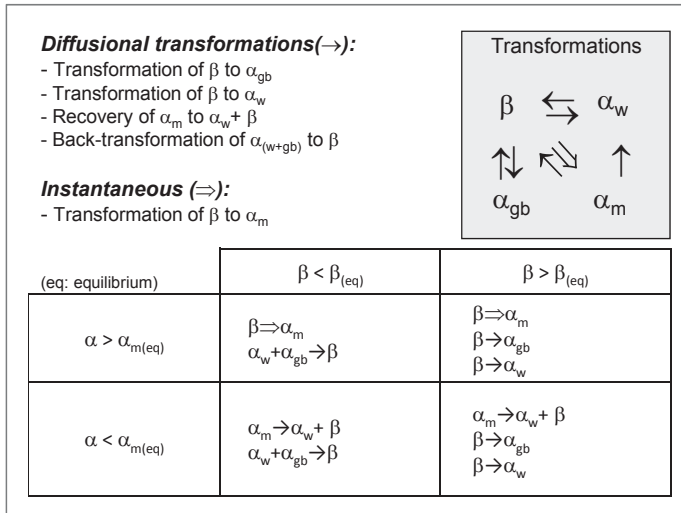


Figure 3. Transformation process and constituents' interactions.

3.3. Adaptive sub-stepping

To optimize the solution routine and reducing computational time, an adaptive sub-stepping for calculating microstructure model has been adopted. To improve accuracy, a refined time stepping is used when the temperature is in the fastest phase

transformations region. When necessary each thermal step is thus divided into several smaller thermal sub-steps assuming a linear temperature variation inside the original thermal step.

4. Results and discussion

4.1. Microstructure analysis

The microstructural analysis was performed on the areas highlighted in Figure 4 and denoted A, B, C, D, and E. In general the microstructure of the GTAW wire fed built Ti-6Al-4V consist of large columnar prior β grains that grow in the temperature gradient direction, through several layers. The directions of the columnar prior β grains can be seen in Figure 4. The prior β grains, seen as large areas of different color and/or contrast in Figure 4, are more and more deflected towards the sides of the cross section because of the temperature gradient. Within the prior β grain, fine α laths are observed in the form of either *basketweave* α structure (see Figure 5a) or *colony* α structure (see Figure 5b). However, only small regions of colony α are observed for the GTAW wire fed Ti-6Al-4V, the main part of the α laths is in the form of basketweave α structure. The prior β grain boundaries are decorated by grain boundary α as shown in Figure 5c. Noteworthy is that the thickness and prevalence of grain boundary α varied in different cross sections. In some regions the grain boundary α is continuous like in Figure 5c, whilst absent or discontinuous in other grain boundaries.

The result of the quantitative microstructural characterization is summarized in Table 2. In general only a small difference is observed when comparing the different areas. The variation is within the range of the standard deviation. One tendency however is that slightly thicker α laths form with increasing thickness of deposited material (number of beads). This could be explained by the increased number of heating cycles due to the additional beads that allow the diffusional growth of the α laths to continue for a longer time. In contrast to the α lath thickness, a large variation of the grain boundary α fraction is observed. The fraction of grain boundary α depends on the location of the prior β grains and furthermore of the prior β grain size. As seen in Figure 4, the width of the prior β grains vary significantly within the cross sections, making the fraction estimation highly sensitive to the location of the evaluated area. Moreover, because of its limited thickness, the grain boundary α is difficult to discern, which may have been the case for some limited regions of the areas investigated in the present study. For future work it is therefore recommended to carry out the validation of the grain boundary α on a deposited material with slower cooling rate, for which a thicker grain boundary α is expected that is more well defined and thus easier to measure.

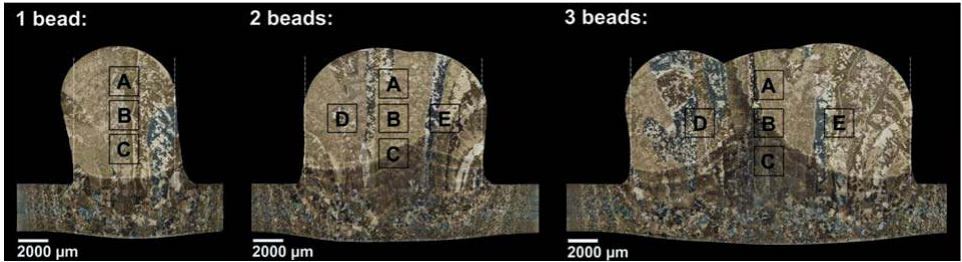


Figure 4. The characterized cross-sections indicated in Figure 1. The different areas denoted A, B, C, D and E, correspond to the location of the measurements presented in Table 2.

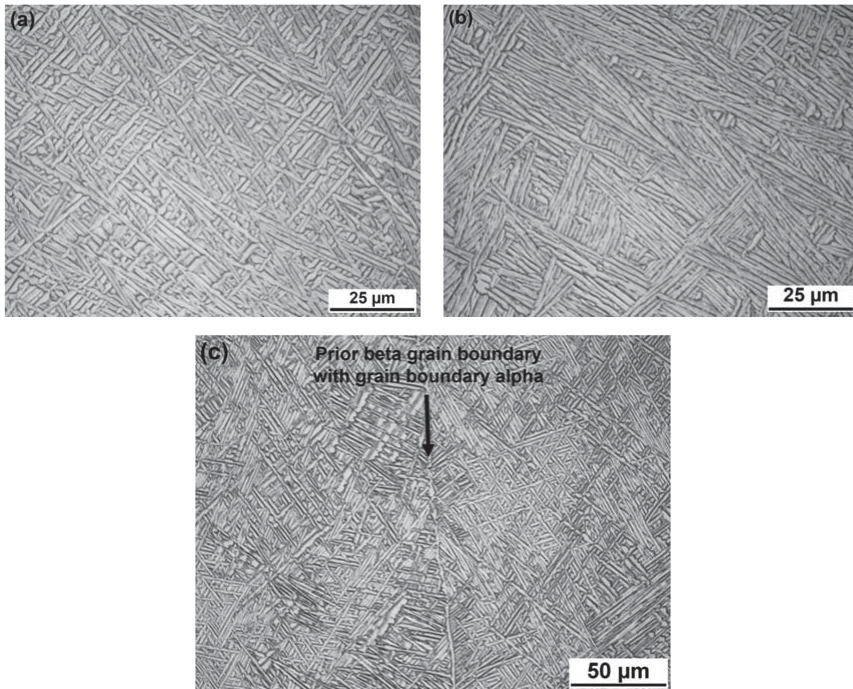


Figure 5. The microstructure of the GTAW wire fed built Ti-6Al-4V consist fine α laths in the form of (a) basketweave α structure or (b) colony α . The prior β grain boundary is decorated with grain boundary α (c).

PAPER D

Table 2. The result of the quantitative material characterization of the three cross sections containing 1 bead, 2 beads and 3 beads width, respectively.

Cross section	Area	Average α lath thickness	Grain boundary α
	A	1.1 ± 0.4	0.21
	B	1.0 ± 0.3	0.11
	C	0.9 ± 0.3	0.05
	All	1.0 ± 0.3	
2 beads	A	1.1 ± 0.4	
	B	1.0 ± 0.4	
	C	1.0 ± 0.3	
	D	1.0 ± 0.3	
	E	1.0 ± 0.4	
	All	1.0 ± 0.4	
3 beads	A	1.0 ± 0.3	
	B	1.1 ± 0.5	
	C	1.3 ± 0.5	
	D	0.9 ± 0.3	
	E	1.0 ± 0.3	
	All	1.1 ± 0.4	

4.2. Microstructure simulation

The additive manufacturing process is characterized by cyclic temperature variations, leading to repetitive phase transformations and microstructure changes in the deposited material and substrate. Temperature history is thus the main factor when modeling the microstructure. Continuous microstructure modeling enables to follow the microstructural changes during processing. While microstructure analysis gives information about the results after the additive manufacturing process, the microstructure model, by following the entire deposition process, gives information about the microstructure changes undergone during the additive manufacturing process. The temperature history experienced at a selected point during additive manufacturing, see Figure 6a), is representative of a typical temperature profile experienced by the deposited material. The location of this point is in area B in the single weld bead sample in Figure 4. In Figure 6b) and 6c) the simulated phase transformations versus time and temperature respectively can be seen. As explained earlier, during cooling from elevated temperature the β phase transforms to a mixture of α_{gb} and α_{wid} (the phase fraction of each microconstituent depends on the cooling rate, i.e. faster cooling rate promotes more α_{wid} than α_{gb} , and vice versa); during the following heating up sequence the α_{gb} and α_{wid} transforms to β phase which cyclically transforms again to α_{gb} and α_{wid} over the temperature history.

PAPER D

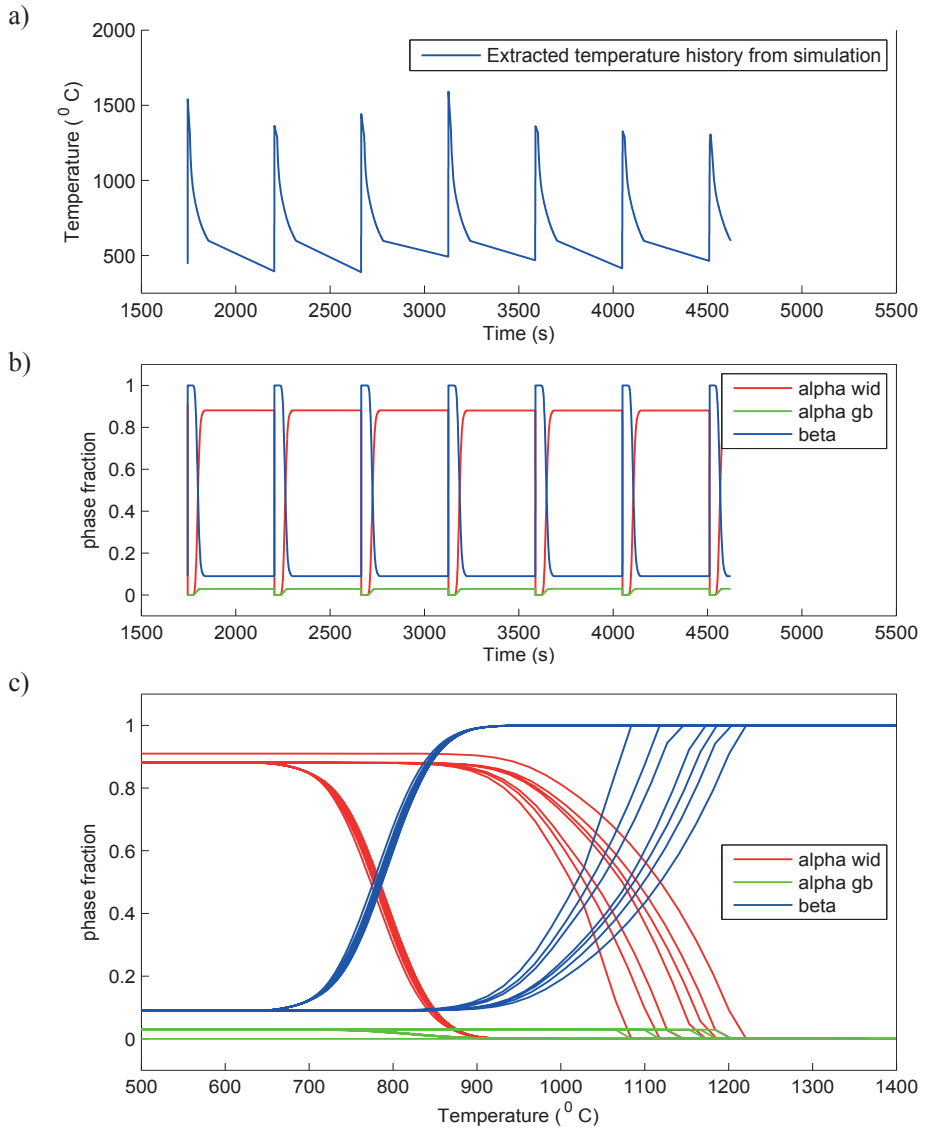


Figure 6. Simulation results at a node positioned in 1 weld bead cross section positioned in the B area (Figure 4). **a)** Temperature variations vs time. **b)** Corresponding simulated α_{gb} , α_{wid} and β phase fractions vs time. **c)** Corresponding simulated α_{gb} , α_{wid} and β phase fractions vs temperature.

Figure 7 and Figure 8 shows the simulated results of the α lath thickness. Despite the simplicity of the chosen model, the simulation results agree well with the

PAPER D

experimental measurements. The simulated thickness, evaluated to be approximately $1.1\mu\text{m}$, is in agreement with the 1 to $1.1\mu\text{m}$ obtained by microstructure analysis. It is also interesting to notice that the α lath thickness show a tendency to increase with increasing wall width, i.e. when built with more weld beads, are deposited. Similar trend was found in the experimental evaluation.

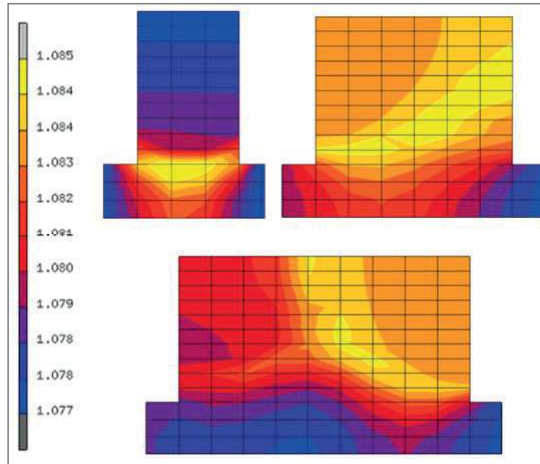


Figure 7. Simulated α lath thickness (μm), cross sections 1, 2 and 3 weld beads wide walls.

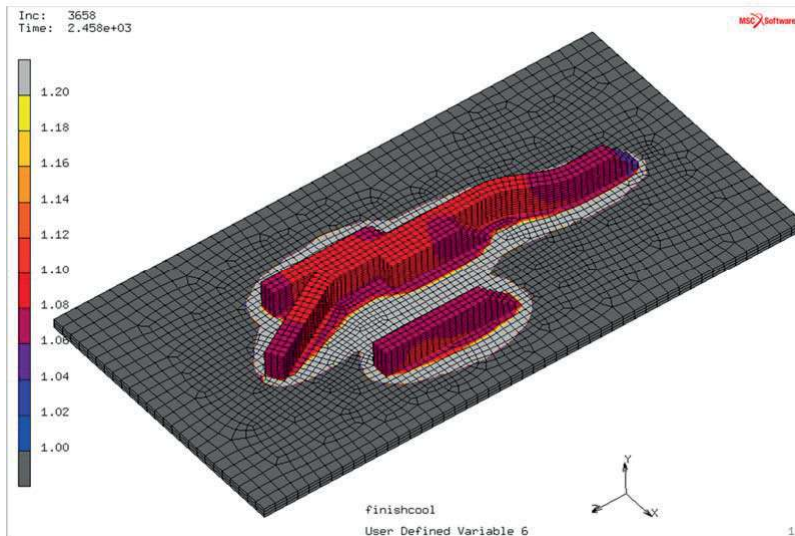


Figure 8. Simulated α lath thickness (μm) variation in the additive manufactured part.

The model predicts 3% α_{gb} , seen in Figure 9, and the experimental measurements indicate α_{gb} fractions between 0.05-0.2%, seen in Table 2. Due to the small amount of

PAPER D

α_{gb} phase and the large variation of the α_{gb} amount that was observed experimentally, it is difficult to conclude on the model results. As already advised in the microstructure analysis section, a more accurate validation case could be achieved by using deposited material containing thicker grain boundary α which could be obtained in slower cooled deposited material.

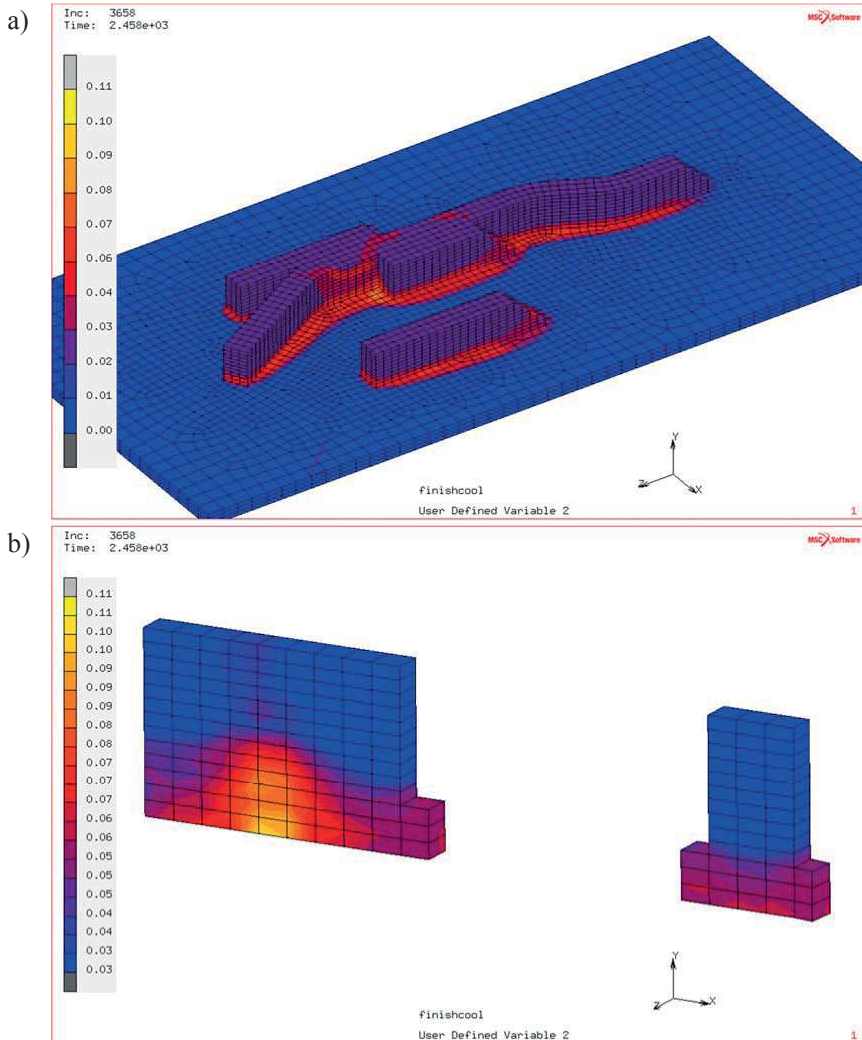


Figure 9. Simulated α_{gb} amount after wire feed additive manufacturing. a) Complete view of the sample. b) Cross sections of the 3 and 1 weld beads wall sections.

PAPER D

An example of the results that can be obtained during the additive manufacturing process by using simulations is shown in Figure 10. The effect of the new deposited layer on the previously deposited layers is here presented. The simulated β phase fraction illustrates the ongoing phase transformations that are taking place while depositing the consecutive metal layers. The model as well as the microstructure characterization shows no martensitic areas in the microstructure for the current manufacturing parameters.

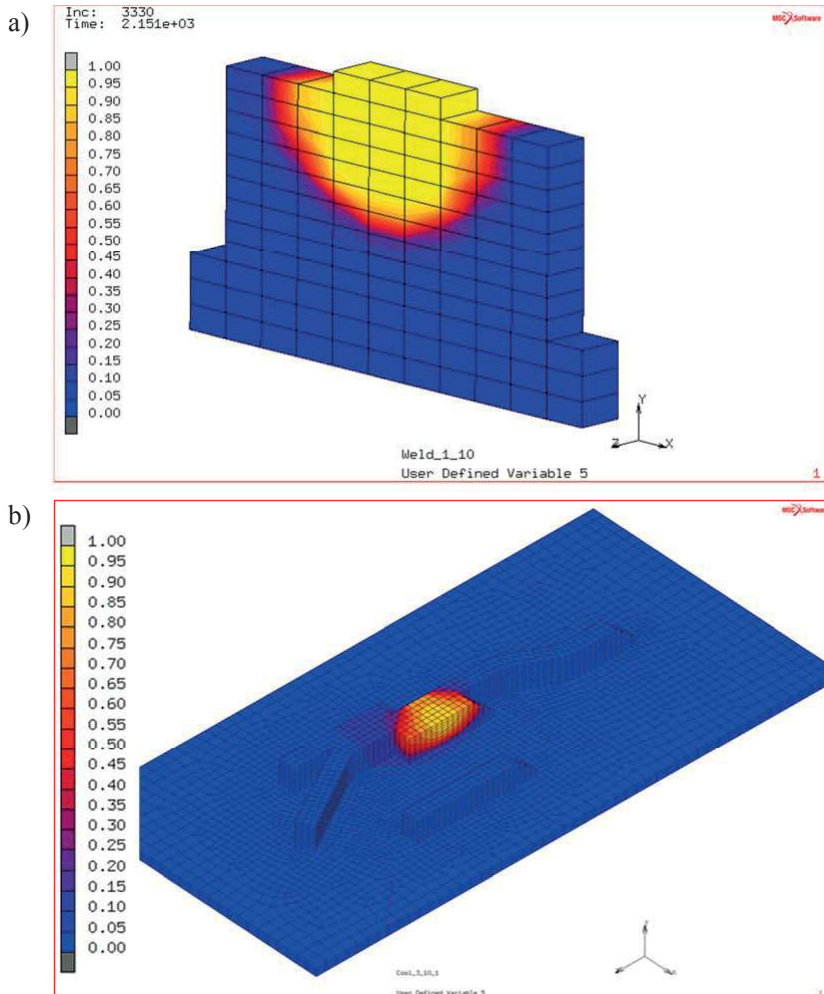


Figure 10. Simulated β phase amount during wire feed additive manufacturing. **a)** crosscut of the 3 weld beads wall section. **b)** complete view of the sample.

PAPER D

The presented method for modeling of wire feed additive manufacturing has been implemented into subroutines that can be evoked from a commercial finite element software. Moreover, microstructure modeling increases the understanding of microstructure evolution for not only post building but also during the additive manufacturing process. The α lath thickness has been successfully predicted. The β phase transformation model (equivalent to the complementary total α phase transformation model) has been validated in a previous publication [13]. However the α_{gb} phase transformation part of the model is still not validated.

In addition, the microstructure model is an important tool that enables continued additive manufacturing process development to obtain improved material properties. Because physical and mechanical properties are dependent on the microstructure, it is interesting to consider the microstructure development also during the AM process. Then the model can be coupled with a flow stress model needed in a thermo-mechanical analysis. The plastic properties will then depend on current temperature and microstructure. Work in progress aims at couple it with the dislocation density based plasticity model in [17].

Acknowledgements

The authors thank the financial support from the European 6th Framework Program through the research project VERDI (Virtual Engineering for Robust manufacturing with Design Integration). The authors also acknowledge the financial support from VINNOVA foundation (Swedish Governmental Agency for Innovation Systems) through the NFFP program (the National Aviation Engineering Research Program) in Sweden. The authors are also grateful for the financial support from the Swedish National Space Board through the NRFP2 program (Swedish National Space Research Program). The Graduate School in Space Technology for supporting and encouraging the project. The close collaboration with GKN Aerospace Engine Systems in supporting this work is highly recognized. The authors would like to express their gratitude to Professor Lars-Erik Lindgren at the Division of Mechanics of Solid Materials, Luleå University of Technology, for his valuable discussions about the microstructure model and to Mats Högström at University West, Sweden for performing the additive manufacturing trials.

References

1. D. Ding, Z. Pan, D. Cuiuri, and H. Li, *Wire-feed additive manufacturing of metal components: technologies, developments and future interests*. The International Journal of Advanced Manufacturing Technology, 2015: p. 1-17.
2. C.A. Brice, *Net shape processing of titanium alloys for enhanced performance and improved affordability*, in *Ti-2011, the 12th world conference on Titanium*. 2011: Beijing, China.
3. C. Leyens and M. Peters, *Titanium and titanium alloys: fundamentals and applications*. 2003: WILEY-VCH.

PAPER D

4. C.-A. Gandin and M. Rappaz, *A 3D Cellular Automaton algorithm for the prediction of dendritic grain growth*. Acta Materialia, 1997. **45**(5): p. 2187-2195.
5. I. Katarov, S. Malinov, and W. Sha, *Finite element modeling of the morphology of β to a phase transformation in Ti-6Al-4V alloy*. Metallurgical and Materials Transactions A: Physical Metallurgy and Materials Science, 2002. **33**(4): p. 1027-1040.
6. R.G. Thiessen, I.M. Richardson, and J. Sietsma. *A dual-mesh strategy for microstructure development in a macroscopic heat affected zone: Studies on AISI316L and AISI1005*. in *7th International Conference on Trends in Welding Research, May 16-20 2005*. 2005. Pine Mountain, GA, United States: ASM International, 9639 Kinsman Road, OH 44073-0002, United States.
7. O. Grong and H.R. Shercliff, *Microstructural modelling in metals processing*. Progress in Materials Science, 2002. **47**(2): p. 163-282.
8. L.-E. Lindgren, *Computational welding mechanics. Thermomechanical and microstructural simulations*. 2007: Woodhead Publishing.
9. A. Lundbäck and L.-E. Lindgren, *Modelling of metal deposition*. Finite Elements in Analysis and Design, 2011. **47**(10): p. 1169-1177.
10. J. Goldak, A. Chakravarti, and M. Bibby, *A New Finite Element Model for Welding Heat Sources*. Metallurgical Trans B, 1984. **15B**: p. 299-305.
11. J.W. Cahn, *Transformation kinetics during continuous cooling*. Acta Metallurgica, 1956. **4**(6): p. 572-575.
12. J.W. Christian, *The theory of transformations in metals and alloys. Part I*. 2002, Amsterdam: Pergamon.
13. C.C. Murgau, R. Pederson, and L.E. Lindgren, *A model for Ti-6Al-4V microstructure evolution for arbitrary temperature changes*. Modelling and Simulation in Materials Science and Engineering, 2012. **20**(5): p. 055006.
14. J. Gyhlestén Back and L.-E. Lindgren, *Simplified Implementation of the Koistinen-Marburger Model for Use in Finite Element Simulations*, in *11th International Congress on Thermal Stresses 2016*. Salerno, Italy.
15. C. Charles and N. Järnström, *Modelling Ti-6Al-4V microstructure by evolution laws implemented as finite element subroutines: Application to TIG metal deposition*, in *8th International Conference on Trends in Welding Research*. 2008, ASM International: Pine Mountain, GA, United States.
16. J. Irwin, E. W. Reutezel, P. Michaleris, J. Keist, and A. R. Nassar, *Predicting Microstructure from Thermal History during Additive Manufacturing for Ti-6Al-4V*, in *Materials Science & Technology*. 2015, To be published.
17. B. Babu and L.-E. Lindgren, *Dislocation density based model for plastic deformation and globularization of Ti-6Al-4V*. International Journal of Plasticity 2013. **50**: p. 94-108.

**Physically based constitutive model of Ti-6Al-4V
for arbitrary phase composition**

Bijish Babu, Corinne Charles Murgau and Lars-Erik Lindgren

To be submitted

Physically Based Constitutive Model of Ti-6Al-4V for Arbitrary Phase Composition

Bijish Babu

Mechanics of Sold Materials, Luleå University of Technology, SE-971 87, Luleå, Sweden

Corinne Charles

Department of Industrial Production, Högskolan Väst, SE-461 86, Trollhättan, Sweden

Lars-Erik Lindgren

Mechanics of Sold Materials, Luleå University of Technology, SE-971 87, Luleå, Sweden

Abstract

The main challenge in producing aerospace components using Ti-6Al-4V alloy is to employ the optimum process window of deformation rate and temperature in order to achieve desired material properties. Understanding the microstructure property relationship qualitatively is not enough to achieve this goal. Developing advanced material models to be used in manufacturing process simulation is the key to iteratively compute and optimize the process. The focus in this work is on physically based flow stress models coupled with microstructure evolution models. Such a model can be used to simulate processes involving complex and cyclic thermo-mechanical loading.

Keywords: Finite Element Method, Dislocation density, Vacancy concentration, Ti-6Al-4V, Alpha, Beta

1. Introduction

The most widely used Titanium alloy, Ti-6Al-4V, has an α (HCP) + β (BCC) phase composition. This allotropic property of Titanium allows it to posses diverse microstructures/morphologies thereby giving a large variation of thermo-mechanical properties. This paper features a physically based thermo-mechanical-microstructural model for plastic flow of Ti-6Al-4V for arbitrary phase composition. It is an enhancement of an earlier model (Babu and Lindgren, 2013) that has been improved with respect to handling non-equilibrium phase compositions. Such a model can be used in the simulation of manufacturing processes involving a wide range of temperatures and strain rates.

Simulation of manufacturing process using FEM employing advanced material models can give a deeper understanding as well as be used in process optimization. This allows us to predict and control local microstructure and properties within components thereby meeting complex design specifications demanded by the aerospace industry. Such a strategy has facilitated rapid advancement in technology related to manufacturing process as well as alloy design (Committee on Integrated Computational Materials Engineering, 2008; Backman et al., 2006).

The model developed here can be used in coupled thermo-mechanical-microstructural simulations that can predict the material state for arbitrary thermo-mechanical loading. Owing to its wide range of applicability, this model can be used to simulate processes involving complex histories.

Email addresses: bijish.babu@ltu.se (Bijish Babu), corinne.charles@hv.se (Corinne Charles), lars-erik.lindgren@ltu.se (Lars-Erik Lindgren)
URL: www.ltu.se/research/subjects/Materialmekanik (Bijish Babu)

2. State of the art in models for Ti-6Al-4V

Several different approaches were followed by researchers to model the constitutive behavior of Ti-6Al-4V. Shafaat et al. (2011) proposed an empirical flow stress model for Ti-6Al-4V by combining the Cingara model during hardening up to the peak stress and a softening model identical to JMAK equation thereafter. A similar approach was followed by Karpat (2011) by mixing a modified Johnson-Cook model for hardening and a hyperbolic model for softening which is used during machining simulation of Ti-6Al-4V. Pornadawit et al. (2014) incorporated the Cingara model for hardening and the Shafiei-Ebrahimi model for softening by dynamic recrystallization. Calamaz et al. (2011) proposed a model including the strain softening and thermal softening to be used in simulation of machining. A modified Zerilli-Armstrong model together with a failure model was proposed by Liu et al. (2013). A microstructure simulation of Ti-6Al-4V using Representative Volume Element (RVE) has been employed by Przybyla and McDowell (2011) to generate probabilistic data and developed a model for fatigue crack formation. Anisotropic flow rule for Ti-6Al-4V based on the Khan-Huang-Liang model were developed by Khan and Yu (2012); Khan et al. (2012). Dislocation density based models have been used by Nemat-Nasser et al. (1999) for commercially pure Titanium and Picu and Majorell (2002) & Gao et al. (2011) for Ti-6Al-4V. A model utilizing dislocation density and vacancy concentration as Internal State Variables (ISV) was developed by Babu and Lindgren (2013) that included globularization which is assumed to be responsible for flow-softening and stress relaxation.

There are relatively few published papers about microstructure models for Ti-6Al-4V. Using resistivity measurements and Differential Scanning Calorimetry (DSC), Malinov et al. (2001a,b) quantified the $\beta \rightarrow \alpha$ isothermal transformation of the alloy and modeled the phenomenon. Katzarov et al. (2002) using FEM, modeled the morphology changes of the alloy during transformation. Kelly (2004); Kelly et al. (2005) developed a FEM based thermo-microstructural model for metal deposition process. This was later extended to thermo-mechanical-microstructural domains by Crespo et al. (2008); Longuet et al. (2009). Charles Murgau et al. (2012) compared many available models and evaluated their applicability in simulation of metal deposition. Lately Mi et al. (2014) developed a fully coupled thermo-microstructural FE model for welding of Ti-6Al-4V using the JMAK formulation for phase transformation.

In the current work, the constitutive model by Babu and Lindgren (2013) and microstructure model by Charles Murgau et al. (2012) are combined to provide a model for arbitrary temperature and mechanical loading. An internal state variable approach is adopted in this work to represent the model's microstructure evolution. This microstructure model uses a combination of models for formation and dissolution of various phases applied in a sequential logic in order to handle general temperature histories. Compared to the previous work (Babu and Lindgren, 2013), the current model has a wider window of applicability since the non-equilibrium phase compositions can be included. The model parameters in Babu and Lindgren (2013) were a function of temperature and they were obtained by calibration using tests with constant equilibrium phase composition for each temperature. In the current work, a separate set of parameters of the flow stress model for each phase is calibrated. This is combined with the microstructure model and a mixture rule to include any arbitrary microstructure.

3. Thermo-Mechanical-Microstructural Coupling

A staggered approach is used here to compute the multi-physics problem. For each time step and material point, the microstructure model computes the phase composition (X_α, X_β) using explicit formulation after receiving the temperature (T) from the thermal pass which is followed by the mechanical pass that is based on X_α, X_β and T (see figure1). Thermo-mechanical problem is solved implicitly using an iterative scheme. Phase change can be exo/endo-thermic. This is included in the current model using temperature dependent specific heat in the thermal field. Another source of heat is plastic dissipation from the internal friction which is included in the mechanical domain and added to the thermal field during the subsequent time step. This methodology can be adapted to any of the standard commercial FE softwares.

4. A dislocation density based flow stress model

An incompressible von Mises model is used here with the assumption of isotropic plasticity. The flow stress is split to two parts (Seeger, 1956; Bergström, 1969; Kocks, 1976; Babu and Lindgren, 2013),

$$\sigma_y = \sigma_G + \sigma^* \quad (1)$$

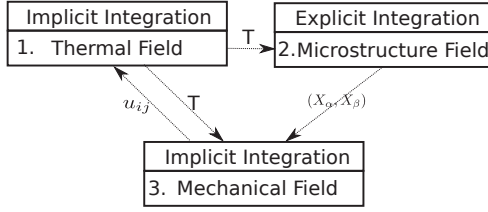


Figure 1: Solving the multi-physics problem.

where, σ_G is the athermal stress contribution from the long-range interactions of the dislocation substructure. The second term σ^* , is the friction stress needed to move dislocations through the lattice and to pass short-range obstacles. Thermal vibrations can assist dislocations to overcome these obstacles. This formulation is very much in accordance to the material behavior demonstrated by Conrad (1981).

4.1. Long range stress component:

The long-range term from equation (1) is derived by Seeger (1956) as,

$$\sigma_G = m\alpha Gb\sqrt{\rho_i} \quad (2)$$

where m is the Taylor orientation factor translating the effect of the resolved shear stress in different slip systems into effective stress and strain quantities. Furthermore, α is a proportionality factor, b is the magnitude of Burger's vector, G is the temperature dependent shear modulus and ρ_i is the immobile dislocation density.

4.2. Short range stress component:

The strain rate dependent part of the yield stress from equation (1) can be derived according to the Kocks-Mecking formulation (Kocks et al., 1975; Mecking and Kocks, 1981) as,

$$\sigma^* = \tau_0 G \left[1 - \left[\frac{kT}{\Delta f_0 G b^3} \ln \left(\frac{\dot{\epsilon}^{ref}}{\dot{\epsilon}^p} \right) \right]^{1/q} \right]^{1/p} \quad (3)$$

Here, $\tau_0 G$ is the shear strength in the absence of thermal energy and $\Delta f_0 G b^3$ is the activation energy necessary to overcome lattice resistance. Some guidelines for selection of Δf_0 and τ_0 are given in (Frost and Ashby, 1982). The shape of the obstacle barrier for dislocation motion is defined by p and q . Further, k is the Boltzmann constant, T is the temperature in Kelvin and $(\dot{\epsilon}^{ref}$ and $\dot{\epsilon}^p)$ are the reference and plastic strain rates.

4.3. Evolution of immobile dislocation density

The basic components for the yield stress in equation (1) are obtained from equations (2) and (3). However, the evolution of ρ_i in equation (2) needs to be computed. The model for evolution of the immobile dislocation density has two parts; hardening and restoration.

$$\dot{\rho}_i = \dot{\rho}_i^{(+)} - \dot{\rho}_i^{(-)} \quad (4)$$

4.3.1. Hardening Process

It is assumed that mobile dislocations move, on average, a distance Λ (mean free path), before they are immobilized or annihilated. According to the Orowan equation, density of mobile dislocations and their average velocity are proportional to the plastic strain rate. It is reasonable to assume that increase in immobile dislocation density also follow the same relation. This leads to,

$$\dot{\rho}_i^{(+)} = \frac{m}{b} \frac{1}{\Lambda} \dot{\epsilon}^p \quad (5)$$

where m is the Taylor orientation factor. The mean free path can be computed from the grain size (g) and dislocation subcell or subgrain diameter (s) as,

$$\frac{1}{\Lambda} = \left(\frac{1}{g} + \frac{1}{s} \right) \quad (6)$$

The formation and evolution of subcells has been modeled using a relation proposed by Holt (1970).

$$s = K_c \frac{1}{\sqrt{\rho_i}} \quad (7)$$

4.3.2. Restoration Processes

Motion of vacancies is related to recovery of dislocations. This occur usually at elevated temperatures and therefore is a thermally activated reorganization process. Creation of vacancy increases entropy but consumes energy and its concentration increases with temperature and deformation. In high stacking fault materials, recovery process might balance the effects of strain hardening leading to a constant flow stress. The primary mechanisms of restoration are dislocation glide, dislocation climb and globularization.

$$\dot{\rho}_i^{(-)} = \dot{\rho}_i^{(glide)} + \dot{\rho}_i^{(climb)} + \dot{\rho}_i^{(globularization)} \quad (8)$$

The model for recovery by glide can be written based on the formulation by Bergström (1983) as,

$$\dot{\rho}_i^{(glide)} = \Omega \rho_i \dot{\epsilon}^p \quad (9)$$

where Ω is a function dependent on temperature. This is analogous to the model by Kocks et al. (1975) as ρ_i and $\dot{\epsilon}^p$ are proportional to ρ_m and \bar{v} respectively.

Militzer et al. (1994) proposed a model for dislocation climb based on Sandstrom and Lagneborg (1975) and Mecking and Estrin (1980). With a modification of the diffusivity according to Babu and Lindgren (2013), the model can be written as,

$$\dot{\rho}_i^{(climb)} = 2c_\gamma D_{app} \frac{Gb^3}{kT} (\rho_i^2 - \rho_{eq}^2) \quad (10)$$

where, c_γ is a material coefficient, D_{app} is the apparent diffusivity and ρ_{eq} is the equilibrium value of the dislocation density.

A model for the evolution of dislocation density during globularization is proposed in Babu and Lindgren (2013). According to this model, the effect of grain growth on the reduction of flow stress is included only when the stored deformation energy is above a critical value.

$$\begin{aligned} &\text{if } \rho_i \geq \rho_{cr} \\ &\dot{\rho}_i^{(globularization)} = \psi \dot{X}_g (\rho_i - \rho_{eq}); \text{ until } \rho_i \leq \rho_{eq} \end{aligned} \quad (11)$$

$$\begin{aligned} &\text{else} \\ &\dot{\rho}_i^{(globularization)} = 0 \end{aligned} \quad (12)$$

Here, ρ_{cr} is the critical dislocation density above which globularization is initiated, ρ_{eq} is the equilibrium value of dislocation density, \dot{X}_g is the globularization rate and ψ is a calibration constant.

4.4. Evolution of excess vacancy concentration

Militzer et al. (1994) proposed a model for excess vacancy concentration with generation and annihilation components. Assuming that only long range stress contributes to vacancy formation and introducing a component for temperature change, the Militzer model can be rewritten as,

$$\begin{aligned} \dot{c}_v^{ex} = & \left[\chi \frac{m\alpha Gb^2 \sqrt{\rho_i}}{Q_{vf}} + \zeta \frac{c_j}{4b^2} \right] \frac{\Omega_0}{b} \dot{\epsilon} - D_{vm} \left[\frac{1}{s^2} + \frac{1}{g^2} \right] (c_v - c_v^{eq}) \\ & + c_v^{eq} \left(\frac{Q_{vf}}{kT^2} \right) \dot{T} \end{aligned} \quad (13)$$

Here, $\chi = 0.1$ is the fraction of mechanical energy spent on vacancy generation, Ω_0 is the atomic volume and ζ is the neutralization effect by vacancy emitting and absorbing jogs. The concentration of jogs (c_j) and D_{vm} , the diffusivity of vacancy are given in Babu and Lindgren (2013). Additionally Q_{vf} is the activation energy of vacancy formation.

5. Model for phase evolution

The liquid–solid phase changes are not modeled in detail. Instead, a simplified model for transition between the liquid and solid state is implemented to take care of temperatures above the melting temperature T_{melt} . In the liquid state, each of the solid phases is consequently set to zero. In the solid state, Ti–6Al–4V microstructure is composed of two main phases; the high-temperature stable β -phase and the lower temperature stable α -phase. Depending on the formation conditions, a variety of α/β textures can be obtained by heat treatment giving varying mechanical properties. Lütjering (1998); Williams and Lutjering (2003) explored the relationship between processing, microstructure and mechanical properties. Based on the literature (Semiatiin et al., 1999b,a; Seetharaman and Semiatiin, 2002; Thomas et al., 2005) few microstructural features have been identified to be relevant with respect to the mechanical properties. The three separate α -phase fractions; Widmanstätten (X_{α_w}), grain boundary ($X_{\alpha_{gb}}$), Martensite (X_{α_m}) and the β -phase fraction (X_{β}) are included in the current model. Though in the current flow stress model, the individual α -phase fractions are not included separately, it is possible to incorporate them when more details about their respective strengthening mechanisms are known.

5.1. Phase Transformations

Depending on the temperature, heating/cooling rates, Ti-6Al-4V undergoes allotropic transformation. The mathematical model for transformation is described schematically in the figure 2. The transformations denoted by F1, F2 and F3 represent formation of α_{gb}, α_w and α_m phases respectively and D3, D2, and D1 shows the dissolution of the same phases. If the current volume fraction of β phase is more than β_{eq} , the excess β phase transforms to α phase. Here α_{gb} formation which occurs in high temperature is most preferred followed by the α_w . The remaining excess β fraction is transformed to α_m if the temperature is lower than T_m , the martensite start temperature. Conversely, if the current volume fraction of β is lower than β_{eq} , the excess α phase is converted to β . Primary, the α_m phase dissolves to β and α_w phases in the same proportion as the α_{eq} and β_{eq} . The remaining excess α_w and α_{gb} transforms to β in that order.

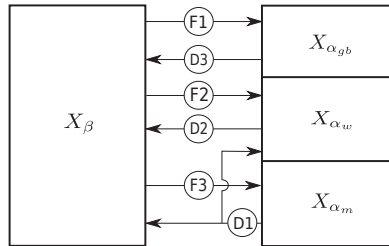


Figure 2: The Mechanism of phase change.

5.2. Adaptation of JMAK Model for Diffusional Transformation

The JMAK- Model (Johnson and Mehl, 1939; Avrami, 1939; Kolmogorov, 1937) originally formulated for nucleation and growth during isothermal situations can be adapted to model any diffusional transformations. Employing the additivity principle, and using sufficiently small time steps ensures that any arbitrary temperature changes be computed. JMAK model assumes that a single phase X_1 which is 100% in volume from the start will transform to 100% of second phase X_2 in infinite time. However in the case of Ti-6Al-4V, this is not the case as it is a $\alpha - \beta$ dual phase alloy below β -transus temperature. Hence, in order to accommodate incomplete transformation, the product fraction is normalized with the equilibrium volume. Conversely, the starting volume of a phase can also be less than 100% which is circumvented by assuming that the available phase volume is the total phase fraction. Another complication is the existence of simultaneous transformation of various α phases ($\alpha_w, \alpha_{gb}, \alpha_m$) to β phase and back. This can be modeled by calculating each transformation in a sequential fashion within the time increment.

5.3. Equilibrium Phase Fraction

Charles Murgau et al. (2012) compared various measurements for equilibrium phase fraction of β^{eq} -phase ($X_{\beta^{eq}}$) available in the literature and identified that the data showed scatter. Compared to the measurements of phase fractions during cooling by Malinov et al. (2001a), the literature data showed an opposite trend. Therefore, in this work, the authors computed $X_{\beta^{eq}}$ by calibrating the model given by the equation 14 and figure 8, where T is the temperature in Kelvin.

$$\begin{aligned} X_{\beta^{eq}} &= 1 - 0.89349e^{\left(-\frac{T^* + 1.8284}{1.7272}\right)^2} + 0.27628e^{\left(-\frac{T^* + 0.59257}{0.66949}\right)^2} \\ T^* &= (T - 1200.0)/24.0 \end{aligned} \quad (14)$$

5.4. Formation of α Phase

During cooling from β -phase, α_{gb} and α_w phases are formed by a diffusional transformation. According to the incremental formulation of JMAK model described by Charles Murgau et al. (2012), the formation of α_{gb} and α_w can be modeled by the set of equations in rows F1 and F2 respectively of table 1. When cooling at rates above 20°C/s, α_m is formed by a diffusion-less transformation. An incremental formulation of Koistinen-Marburger equation described by Charles Murgau et al. (2012) is used here (see equation set in row F3 of table 1).

F1	${}^{n+1}X_{\alpha_{gb}} = \left(1 - e^{-k_{gb}(t_{gb}^* + \Delta t)^{N_{gb}}}\right) \left({}^nX_{\beta} + {}^nX_{\alpha_w} + {}^nX_{\alpha_{gb}}\right) {}^{n+1}X_{\alpha}^{eq} - {}^nX_{\alpha_w}$ $t_{gb}^* = N_{gb} \sqrt{-\ln\left(1 - \frac{({}^nX_{\alpha_w} + {}^nX_{\alpha_{gb}}) / {}^{n+1}X_{\alpha}^{eq}}{({}^nX_{\beta} + {}^nX_{\alpha_w} + {}^nX_{\alpha_{gb}})}\right)} / k_{gb}$ $t_{gb}^{1\%} = 61.5e^{(-3.97e^{-3}T)} + 10^{-13}e^{(2.43e^{-2}T)}$ $t_{gb}^{95\%} = t_{gb}^{1\%} + 2.20$ $N_{gb} = \log_{10}\left(\frac{\ln(1 - 0.01)}{\ln(1 - 0.95)}\right) / \log_{10}\left(\frac{t_{gb}^{1\%}}{t_{gb}^{95\%}}\right)$ $k_{gb} = -\frac{\ln(1 - 0.01)}{(t_{gb}^{1\%})^{N_{gb}}}$																																	
F2	${}^{n+1}X_{\alpha_w} = \left(1 - e^{-k_w(t_w^* + \Delta t)^{N_w}}\right) \left({}^nX_{\beta} + {}^nX_{\alpha_w} + {}^nX_{\alpha_{gb}}\right) {}^{n+1}X_{\alpha}^{eq} - {}^nX_{\alpha_{gb}}$ $t_w^* = N_w \sqrt{-\ln\left(1 - \frac{({}^nX_{\alpha_w} + {}^nX_{\alpha_{gb}}) / {}^{n+1}X_{\alpha}^{eq}}{({}^nX_{\beta} + {}^nX_{\alpha_w} + {}^nX_{\alpha_{gb}})}\right)} / k_w$ <table border="1" style="width: 100%; text-align: center; border-collapse: collapse;"> <thead> <tr> <th style="border: none;">T[°C]</th> <th>0</th> <th>825</th> <th>850</th> <th>875</th> <th>900</th> <th>925</th> <th>950</th> <th>975</th> <th>1000</th> <th>1900</th> </tr> </thead> <tbody> <tr> <td style="border: none;">N_w</td> <td>1.10</td> <td>1.10</td> <td>1.10</td> <td>1.13</td> <td>1.16</td> <td>1.16</td> <td>1.16</td> <td>1.16</td> <td>1.16</td> <td>1.16</td> </tr> <tr> <td style="border: none;">$k_w [10^{-2}]$</td> <td>6.00</td> <td>6.00</td> <td>3.00</td> <td>1.70</td> <td>0.40</td> <td>0.30</td> <td>0.15</td> <td>10.0</td> <td>0.00</td> <td>0.00</td> </tr> </tbody> </table>	T[°C]	0	825	850	875	900	925	950	975	1000	1900	N_w	1.10	1.10	1.10	1.13	1.16	1.16	1.16	1.16	1.16	1.16	$k_w [10^{-2}]$	6.00	6.00	3.00	1.70	0.40	0.30	0.15	10.0	0.00	0.00
T[°C]	0	825	850	875	900	925	950	975	1000	1900																								
N_w	1.10	1.10	1.10	1.13	1.16	1.16	1.16	1.16	1.16	1.16																								
$k_w [10^{-2}]$	6.00	6.00	3.00	1.70	0.40	0.30	0.15	10.0	0.00	0.00																								
F3	${}^{n+1}X_{\alpha_m} = \begin{cases} (1 - e^{-b_{km}(T_{ms} - T)}) ({}^nX_{\beta} + {}^nX_{\alpha_m}); & \text{if } (\dot{T} > 410^\circ\text{C/s}) \\ (1 - e^{-b_{km}(T_{ms} - T)}) ({}^nX_{\beta} + {}^nX_{\alpha_m} - {}^{n+1}X_{\alpha}^{eq}); & \text{if } (20^\circ\text{C/s} > \dot{T} > 410^\circ\text{C/s}) \end{cases}$ $b_{km} = 5.0e^{-3}; T_{ms} = 851.0^\circ\text{C}$																																	

Table 1: Models and parameters for α -phase formation.

5.5. Dissolution of α Phase

The α_m phase formed by instantaneous transformation is unstable and therefore undergoes a diffusional transformation to α_w and β phases based on its current equilibrium composition. The incremental formulation of classical JMAK model by Charles Murgau et al. (2012) and its parameters are given in row D1 of table 2. During heating or reaching non-equilibrium phase composition, α_w and α_{gb} can transform to β -phase controlled by a the diffusion of vanadium at the $\alpha - \beta$ interface. A parabolic equation developed by Kelly (2004); Kelly et al. (2005) derived in its incremental form by Charles Murgau et al. (2012) is used here (see rows D2 and D3 of table 2).

D1	${}^{n+1}X_{\alpha_m} = \frac{({}^{n+1}X_{\alpha_m}^{eq} - e^{-k_m(t_m^* + \Delta t)} N_m)}{({}^n X_{\beta} + {}^n X_{\alpha_m} - {}^{n+1}X_{\alpha_m}^{eq})}$ $t_m^* = N_m \sqrt{-\ln \left(\frac{({}^n X_{\alpha} - {}^{n+1}X_{\alpha_m}^{eq})}{({}^n X_{\beta} + {}^n X_{\alpha_m} - {}^{n+1}X_{\alpha_m}^{eq})} \right) / k_m}$ ${}^{n+1}X_{\alpha_w} = {}^n X_{\alpha_w} + \Delta^n X_{\alpha_m} (1 - {}^{n+1}X_{\beta}^{eq})$ ${}^{n+1}X_{\beta} = {}^n X_{\beta} + \Delta^n X_{\alpha_m} {}^{n+1}X_{\beta}^{eq}$ <table border="1" style="margin-left: auto; margin-right: auto;"> <thead> <tr> <th>T [°C]</th> <th>0</th> <th>400</th> <th>500</th> <th>700</th> <th>800</th> <th>1900</th> </tr> </thead> <tbody> <tr> <td>N_m</td> <td>1.019</td> <td>1.019</td> <td>1.015</td> <td>1.025</td> <td>1.031</td> <td>1.031</td> </tr> <tr> <td>k_m</td> <td>0.667</td> <td>0.667</td> <td>1.106</td> <td>1.252</td> <td>1.326</td> <td>1.326</td> </tr> </tbody> </table>	T [°C]	0	400	500	700	800	1900	N_m	1.019	1.019	1.015	1.025	1.031	1.031	k_m	0.667	0.667	1.106	1.252	1.326	1.326
	T [°C]	0	400	500	700	800	1900															
N_m	1.019	1.019	1.015	1.025	1.031	1.031																
k_m	0.667	0.667	1.106	1.252	1.326	1.326																
D2	${}^{n+1}(X_{\alpha_w} + X_{\alpha_{gb}}) = \begin{cases} {}^{n+1}X_{\alpha}^{eq} f_{diss}(T) \sqrt{\Delta t + t^*}; & \text{if } (0 < (\Delta t + t^*) < t_{crit}) \\ {}^{n+1}X_{\alpha}^{eq}; & \text{if } (\Delta t + t^* > t_{crit}) \end{cases}$																					
D3	$t^* = \left(\frac{{}^n X_{\beta}}{{}^{n+1}X_{\beta}^{eq} f_{diss}(T)} \right)$ $f_{diss}(T) = 2.2e^{-31T^{0.89}}$ $t_{crit} = \sqrt{f_{diss}(T)}$																					

Table 2: Models and parameters for α -phase dissolution.

6. Coupling of phase and flow stress models

The Young's modulus can be written according to Fan (1993); Lee and Welsch (1990) as a linear rule of mixtures. However, since the elastic modulus of the individual phases are not available at elevated temperatures, the effective modulus is used here. The results of measurement and data from Fukuhara and Sanpei (1993) are plotted in figure 3 along with the model by Wachtman et al. (1961) fitted to the measurement. Based on the Wachtman model, Young's Modulus can be written as,

$$E = E_0 - B(T + 273.15)e^{(-T_0/(T+273.15))} \quad (15)$$

where T is the temperature in Celsius, $E_0 = 107GPa$ is the modulus of elasticity at $0K$, $B = 0.2$ is the calibration parameter and $T_0 = 1300K$ is the temperature at which $E - T$ relationship becomes linear. Drawing from the fact that data for individual phases are not available, the Poisson's ratio is assumed to be constant for both phases. The measurement by Fukuhara and Sanpei (1993) and a linear model fitted to it are shown in figure 3. The model for Poisson's ratio can be written as,

$$\mu = 0.34 + 6.34 \cdot 10^{-5}T \quad (16)$$

where T is the temperature in Celsius. Swarnakar et al. (2011) using X-Ray diffraction measured the vol-

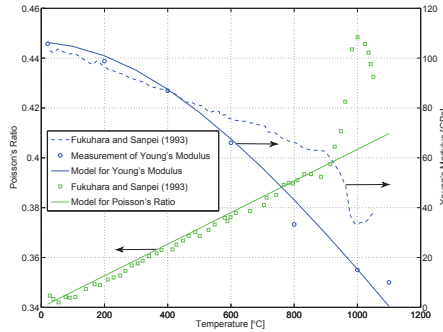


Figure 3: Youngs Modulus and Poisson's Ratio.

umetric expansion of unit cells of α and β phases during heating (see figure 4). Based on this, the average

coefficient of thermal expansion (CTE) of the phase mixture can be calculated using the rule of mixtures as in equation 17, where α_α and α_β gives the CTE of α and β phases respectively. The linear thermal strain can be computed using equation 18 is plotted in figure 4.

$$\alpha_{avg} = X_\alpha\alpha_\alpha + X_\beta\alpha_\beta \quad (17)$$

$$\varepsilon^{th} = \alpha_{avg}\Delta T \quad (18)$$

During α to β transformation, between (900-1000) $^\circ\text{C}$ the volume of the phase mixture undergoes a rapid increase. The yield strength of the phase mixture can be written according to the linear rule of mixtures as,

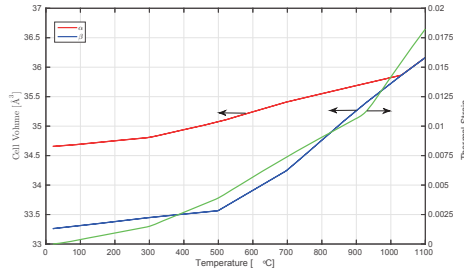


Figure 4: Thermal Expansion and Strain.

$$\sigma_y = X_\alpha\sigma_y^\alpha + X_\beta\sigma_y^\beta \quad (19)$$

Assuming iso-work principle, the distribution of plastic strain can be obtained. According to Bouaziz and Buessler (2004), this can be written as,

$$\sigma_y^\alpha \dot{\varepsilon}_\alpha = \sigma_y^\beta \dot{\varepsilon}_\beta \quad (20)$$

$$\dot{\varepsilon}^p = X_\alpha \dot{\varepsilon}_\alpha + X_\beta \dot{\varepsilon}_\beta \quad (21)$$

This ensures that the β phase with lower yield strength will get a larger share of plastic strain as compared to the stronger α phase

7. Calibration of constitutive models

The suitable parameters of the model are found by performing a calibration which poses a formidable challenge to the modeler. This is attributed to the fact that some of the parameters are temperature dependent which increases the number of parameters drastically and there exists multiple sets of valid parameters for the model. An in-house MatlabTM based toolbox using constrained minimization routine for optimization is developed for this task. It enables calibration of multiple experiments and easy interaction with the optimization process. This is done by using a gradient based algorithm which systematically chooses parameter values from between the given set.

The cost function to be minimized is formulated as the weighted sum of the difference between computed and experimental stress. This assures equal significance to all the data points of an experiment. Additionally, this tool allows the user to specify a custom weight for different parts of the curve. Compression tests performed at the nominal temperatures between 20 and 1100 $^\circ\text{C}$ and strain rates from 0.001s⁻¹ to 1.0s⁻¹ were used to calibrate the model. These data is already published in Babu and Lindgren (2013). The different parameters of the model obtained after calibration using σ - ε measurements are shown in Tables 4, 5 and 6.

Paper E

Parameter	Dimension	Value	Reference
T_{melt}	°C	1600	f
$T_{\beta-transus}$	°C	890	f
k	JK ⁻¹	$1.38 \cdot 10^{-23}$	f
b	m	$2.95 \cdot 10^{-10}$	a
$D_{\alpha 0}$	m ² s ⁻¹	$5 \cdot 10^{-6}$	d
$D_{\beta 0}$	m ² s ⁻¹	$3 \cdot 10^{-7}$	d
Q_{vf}	J	$1.9 \cdot 10^{-19}$	b
Q_{vm}	J	$2.49 \cdot 10^{-19}$	a
Q_{β}	J	$2.5 \cdot 10^{-19}$	d
Q_p	J	$1.61 \cdot 10^{-19}$	a
n_a^p	—	2	f
n_p	—	ρ_i	f
Ω_0	m ³	$1.76 \cdot 10^{-29}$	a
g_0	m	$2 \cdot 10^{-6}$	f
n	—	3	e
$\dot{\epsilon}_{ref}$	s ⁻¹	10 ⁶	a
ΔS_{vm}	JK ⁻¹	$1.38 \cdot 10^{-23}$	g

^aFrost and Ashby (1982)

^bNovikov et al. (1980)

^cConrad (1981)

^dMishin and Herzig (2000)

^eSargent et al. (2008)

^fCalculated or Measured Value

^gHernan et al. (2005)

Table 3: Parameters for the model from literature.

Parameter	Dimension	Value
D_{p0}	m ² s ⁻¹	10 ⁻⁸
N_a^l	—	10 ¹⁹
p	—	0.3
q	—	1.8
Ω	—	38
ρ_{eq}	m ⁻²	10 ¹⁰

Table 4: Calibrated parameters of the model.

T [°C]	25	100	200	300	400	500	600	700	800	900	1000	1100
α	2.30	1.92	1.90	1.90	2.10	2.15	1.70	0.80	1.00	1.15	1.20	1.10
C_γ [10 ⁻¹]	0.00	0.00	0.00	0.00	0.00	3.00	4.00	5.00	5.00	0.50	1.00	2.00
K_c [10 ²]	0.40	0.40	0.40	0.40	0.40	0.40	0.40	0.80	1.20	1.20	1.20	1.20
τ_0 [10 ⁻¹]	0.10	0.20	0.20	0.20	0.20	0.40	1.20	1.50	3.50	3.00	1.00	0.50
Δf_0	0.50	0.50	0.50	0.50	0.50	0.60	0.80	1.70	1.70	1.55	1.30	0.90
ρ_i^{init} [10 ¹⁴]	1.00	1.00	1.00	1.00	1.00	1.00	0.70	0.10	0.10	0.10	0.01	0.01
ρ_i^{crit} [10 ¹⁴]	5.00	5.00	5.00	5.00	2.24	2.00	1.50	0.20	0.20	0.20	0.10	0.10
B	1.00	1.00	1.00	1.00	0.50	0.50	0.50	0.60	0.50	0.10	0.01	0.01
k	2.00	2.00	2.00	2.00	2.00	2.00	1.00	1.50	2.00	2.00	2.00	2.00
M [10 ²]	0.00	0.00	0.00	0.00	0.00	1.00	6.00	6.00	1.00	1.00	1.00	1.00
ψ	0.00	0.00	0.00	0.00	0.05	0.05	0.60	2.00	8.00	1.00	1.00	1.00
K [10 ⁻¹⁹]	0.00	0.00	0.00	0.00	0.00	0.05	0.25	6.50	8.00	8.00	8.00	8.00

Table 5: Calibrated temperature-dependent parameters of the α -phase model.

α	C_γ [10 ⁻¹]	K_c [10 ²]	τ_0 [10 ⁻¹]	Δf_0	ρ_i^{int} [10 ¹²]
1.15	1.00	1.20	3.00	1.30	1.00

Table 6: Calibrated temperature-dependent parameters of the β -phase model.

8. Demonstration of the model

The stress-strain relationship predicted by the model for varying strain rates and temperature are given in figures 5.

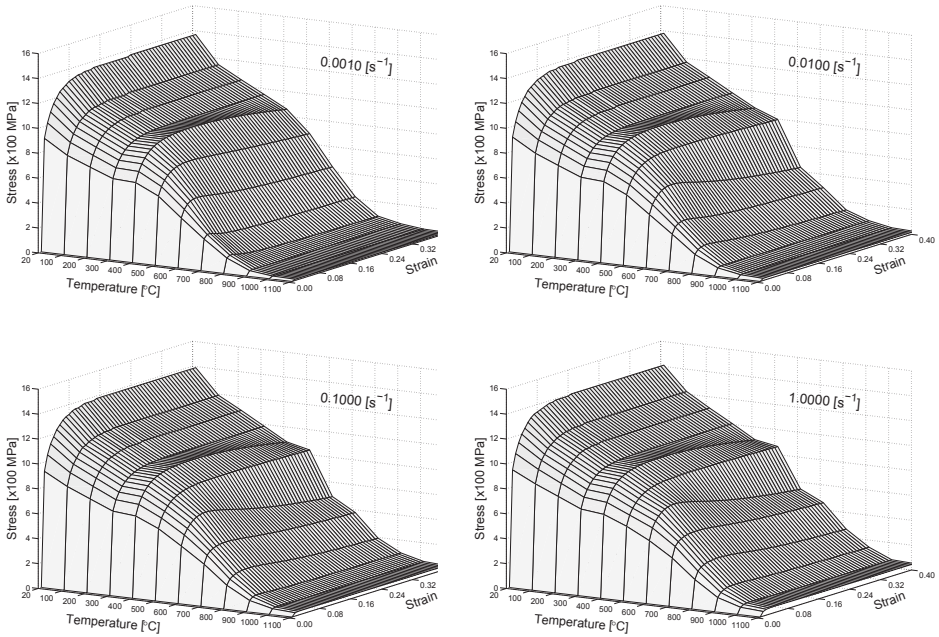


Figure 5: Stress-strain-temperature relationship at $\dot{\epsilon} = (1e^{-3} - 1)s^{-1}$.

A set of numerical tests were performed in order to compute the behavior of the microstructure model during cyclic heating and cooling. Figure 6 shows the computed total α -phase fraction (X_α) during cyclic heating from 600°C to 1050°C followed by cooling and heating at rates varying between (1 to 100)°C/s

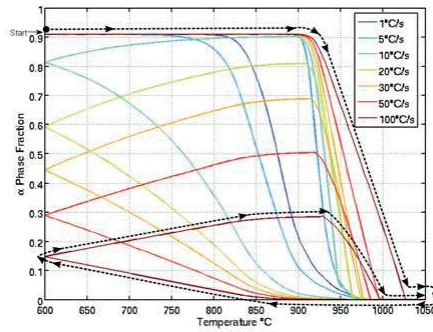


Figure 6: Computed phase transformation during cyclic Heating-Cooling-Heating.

9. Validation of the constitutive model

Experiments were performed to evaluate the validity of the model. Using the Gleeble-3800 machine, compression tests at varying rates were performed on cylindrical specimens which were subjected to continuous cooling from 1000 °C at rates varying between 50°C/min to 10°C/min. See figure 7 where dotted lines indicate applied strain and continuous lines the controlled temperature. Malinov et al. (2001a) performed a DSC study on Ti-6Al-4V at the same cooling rates and measured the phase fractions. Their data together with the computed phase fraction from the model is given in figure 8 where dots denote measurement and lines the model. During the compression test, stress and strain is recorded and is plotted along with computed values in figure 9 with dots denoting measurement and lines, the computed model. The model predictions for stress-strain behavior during faster cooling rates (50-30°C/min) follows the measurements much better than the slower cooling rates (10-20°C/min). One reason for this behavior could be because of the prolonged exposure to oxygen, (an α stabilizer) altering the phase transformation kinetics which is not included in the model. Another uncertainty is in the amount of $\alpha - \beta$ phases present in the as-received test material at room temperature.

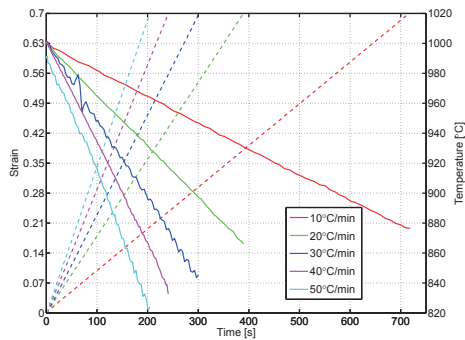


Figure 7: Deformation during continuous cooling (points-strain; lines-temperature).

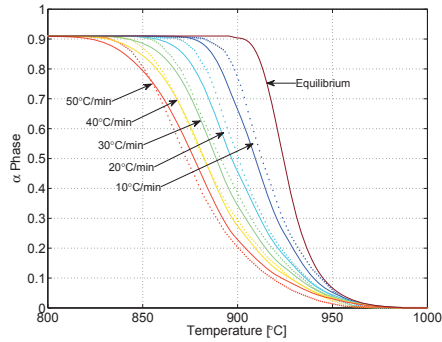


Figure 8: Phase Transformation during continuous cooling.

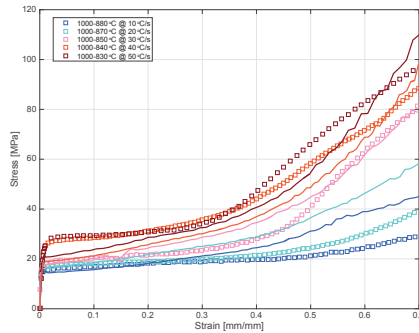


Figure 9: Measured and computed stress-strain curve during continuous cooling.

10. Conclusions

This article presents a calibrated thermo-mechanical-microstructural model for Ti-6Al-4V alloy to be used in simulations of involving arbitrary thermo-mechanical loading. Compared to the earlier work by Babu and Lindgren (2013) for equilibrium phase compositions, the non-equilibrium phase evolution model coupled with flow stress model developed in the current work allows us to simulate complex transient and cyclic loading situations that emerge during manufacturing processes like welding, metal deposition etc.

References

- Avrami, M., 1939. Kinetics of Phase Change. I General Theory. *The Journal of Chemical Physics* 7, 1103–1112.
- Babu, B., Lindgren, L.E., 2013. Dislocation density based model for plastic deformation and globularization of Ti-6Al-4V. *International Journal of Plasticity* 50, 94–108.
- Backman, D., Wei, D., Whitis, D., Buczek, M., Finnigan, P., Gao, D., 2006. ICME at GE: Accelerating the insertion of new materials and processes. *JOM* 58, 36–41.

Paper E

- Bergström, Y., 1969. Dislocation model for the stress-strain behaviour of polycrystalline alpha-iron with special emphasis on the variation of the densities of mobile and immobile dislocations. *Materials Science & Engineering* 5, 193–200.
- Bergström, Y., 1983. The plastic deformation of metals - A dislocation model and its applicability. *Reviews on Powder Metallurgy and Physical Ceramics* , 79–83.
- Bouaziz, O., Buessler, P., 2004. Iso-work Increment Assumption for Heterogeneous Material Behaviour Modelling. *Advanced Engineering Materials* 6, 79–83.
- Calamaz, M., Coupard, D., Nouari, M., Girot, F., 2011. Numerical analysis of chip formation and shear localisation processes in machining the Ti-6Al-4V titanium alloy. *The International Journal of Advanced Manufacturing Technology* 52, 887–895.
- Charles Murgau, C., Pederson, R., Lindgren, L., 2012. A model for Ti-6Al-4V microstructure evolution for arbitrary temperature changes. *Modelling and Simulation in Materials Science and Engineering* 20, 055006.
- Committee on Integrated Computational Materials Engineering, N.R.C., 2008. *Integrated Computational Materials Engineering: A Transformational Discipline for Improved Competitiveness and National Security*. The National Academies Press.
- Conrad, H., 1981. Effect of interstitial solutes on the strength and ductility of titanium 26, 123.
- Crespo, A., Deus, A., Vilar, R., 2008. Modeling of phase transformations and internal stresses in laser powder deposition.
- Fan, Z., 1993. On the young's moduli of Ti-6Al-4V alloys. *Scripta Metallurgica et Materialia* 29, 1427–1432.
- Frost, H.J., Ashby, M.F., 1982. *Deformation-Mechanism Maps: The Plasticity and Creep of Metals and Ceramics*. Paperback.
- Fukuhara, M., Sanpei, A., 1993. Elastic moduli and internal frictions of Inconel 718 and Ti-6Al-4V as a function of temperature. *Journal of Materials Science Letters* 12, 1122–1124.
- Gao, C., Zhang, L., Yan, H., 2011. A new constitutive model for HCP metals. *Materials Science and Engineering: A* 528, 4445–4452.
- Hernan, R.D., Maria, G.L., Maria, M.A., 2005. Self-diffusion in the hexagonal structure of Zirconium and Hafnium: computer simulation studies. *Materials Research* 8, 431–434.
- Holt, D.L., 1970. Dislocation cell formation in metals. *Journal of applied physics* 41, 3197.
- Johnson, W., Mehl, R., 1939. Reaction Kinetics in Processes of Nucleation and Growth. *Trans. Soc. Pet. Eng.* 135, 416.
- Karpát, Y., 2011. Temperature dependent flow softening of titanium alloy Ti6Al4V: An investigation using finite element simulation of machining. *Journal of Materials Processing Technology* 211, 737–749.
- Katzarov, I., Malinov, S., Sha, W., 2002. Finite element modeling of the morphology of (beta) to (alpha) phase transformation in Ti-6Al-4V alloy. *Metallurgical and Materials Transactions A* 33A, 1027.
- Kelly, S.M., 2004. *Thermal and Microstructure Modeling of Metal Deposition Processes with Application to Ti-6Al-4V*. Phd thesis. Virginia Polytechnic Institute and State University.
- Kelly, S.M., Babu, S.S., David, S.A., Zacharia, T., Kampe, S.L., 2005. A microstructure model for laser processing of Ti-6Al-4V, in: *24th International Congress on Applications of Lasers and Electro-Optics, ICALEO 2005, Laser Institute of America, Orlando, FL 32826, United States, Miami, FL, United States*. pp. 489–496.

Paper E

- Khan, A.S., Yu, S., 2012. Deformation induced anisotropic responses of Ti-6Al-4V alloy. Part I: Experiments. *International Journal of Plasticity* 38, 1–13.
- Khan, A.S., Yu, S., Liu, H., 2012. Deformation induced anisotropic responses of Ti-6Al-4V alloy Part II: A strain rate and temperature dependent anisotropic yield criterion. *International Journal of Plasticity* 38, 14–26.
- Kocks, U., 1976. Laws for Work-Hardening and Low-Temperature Creep. *Journal of Engineering Materials and Technology, Transactions of the ASME* 98 Ser H, 76–85.
- Kocks, U.F., Argon, A.S., Ashby, M.F., 1975. Thermodynamics and Kinetics of Slip. volume 19 of *Progress in Material Science*. Pergamon Press.
- Kolmogorov, A., 1937. A statistical theory for the recrystallisation of metals, *Akad Nauk SSSR, Izv. Izv. Akad. Nauk. SSSR* 3.
- Lee, Y., Welsch, G., 1990. Young's modulus and damping of Ti6Al4V alloy as a function of heat treatment and oxygen concentration. *Materials Science and Engineering A* 128, 77–89.
- Liu, R., Melkote, S., Pucha, R., Morehouse, J., Man, X., Marusich, T., 2013. An enhanced constitutive material model for machining of Ti-6Al-4V alloy. *Journal of Materials Processing Technology* 213, 2238–2246.
- Longuet, A., Robert, Y., Aebly-Gautier, E., Appolaire, B., Mariage, J., Colin, C., Cailletaud, G., 2009. A multiphase mechanical model for Ti-6Al-4V: Application to the modeling of laser assisted processing. *Computational Materials Science* In Press, Corrected Proof, –.
- Lütjering, G., 1998. Influence of processing on microstructure and mechanical properties of ($\alpha + \beta$) titanium alloys. *Materials Science and Engineering: A* 243, 32–45.
- Malinov, S., Guo, Z.X., Sha, W., Wilson, A., 2001a. Differential scanning calorimetry study and computer modeling of beta to alpha phase transformation in a Ti-6Al-4V alloy. *Metallurgical and Materials Transactions: A* 32A, 879.
- Malinov, S., Markovskiy, P.E., Sha, W., Guo, Z.X., 2001b. Resistivity study and computer modelling of the isothermal transformation kinetics of Ti-6Al-4V and Ti-6Al-2Sn-4Zr-2Mo-0.08Si alloys. *Journal of Alloys and Compounds* 314, 181.
- Mecking, H., Estrin, Y., 1980. The effect of vacancy generation on plastic deformation. *Scripta Metallurgica* 14, 815.
- Mecking, H., Kocks, U., 1981. Kinetics of flow and strain-hardening. *Acta Metallurgica* 29, 1865–1875.
- Mi, G., Wei, Y., Zhan, X., Gu, C., Yu, F., 2014. A coupled thermal and metallurgical model for welding simulation of Ti-6Al-4V alloy. *Journal of Materials Processing Technology* 214, 2434–2443.
- Militzer, M., Sun, W.P., Jonas, J.J., 1994. Modelling the effect of deformation-induced vacancies on segregation and precipitation. *Acta Metallurgica et Materialia* 42, 133.
- Mishin, Y., Herzig, C., 2000. Diffusion in the Ti-Al system. *Acta Materialia* 48, 589–623.
- Nemat-Nasser, S., Guo, W.G., Cheng, J.Y., 1999. Mechanical properties and deformation mechanisms of a commercially pure titanium. *Acta Materialia* 47, 3705.
- Novikov, I.I., Roshchupkin, V.V., Semashko, N.A., Fordeeva, L.K., 1980. Experimental investigation of vacancy effects in pure metals. *Journal of Engineering Physics and Thermophysics* V39, 1316.
- Picu, R.C., Majorell, A., 2002. Mechanical behavior of Ti-6Al-4V at high and moderate temperatures–Part II: constitutive modeling. *Materials Science and Engineering A* 326, 306–316.

Paper E

- Porntadawit, J., Uthaisangasuk, V., Choungthong, P., 2014. Modeling of flow behavior of Ti-6Al-4V alloy at elevated temperatures. *Materials Science and Engineering: A* 599, 212–222.
- Przybyla, C.P., McDowell, D.L., 2011. Simulated microstructure-sensitive extreme value probabilities for high cycle fatigue of duplex Ti-6Al-4V. *International Journal of Plasticity* 27, 1871–1895.
- Sandstrom, R., Lagneborg, R., 1975. A model for hot working occurring by recrystallization. *Acta Metallurgica* 23, 387.
- Sargent, G., Zane, A., Fagin, P., Ghosh, A., Semiatin, S., 2008. Low-Temperature Coarsening and Plastic Flow Behavior of an Alpha/Beta Titanium Billet Material with an Ultrafine Microstructure. *Metallurgical and Materials Transactions A* 39, 2949–2964.
- Seeger, A., 1956. The mechanism of Glide and Work Hardening in FCC and HCP Metals, in: Fisher, J., Johnston, W.G., Thomson, R., Vreeland, T.J. (Eds.), *Dislocations and Mechanical Properties of Crystals*, pp. 243–329.
- Seetharaman, V., Semiatin, S.L., 2002. Effect of the lamellar grain size on plastic flow behavior and microstructure evolution during hot working of a gamma titanium aluminide alloy. *Metallurgical and Materials Transactions A* 33A, 3817.
- Semiatin, S.L., Seetharaman, V., Ghosh, A.K., 1999a. Plastic flow, microstructure evolution, and defect formation during primary hot working of titanium and titanium aluminide alloys with lamellar colony microstructures. *Philosophical Transactions: Mathematical, Physical and Engineering Sciences* 357, 1487 – 1512.
- Semiatin, S.L., Seetharaman, V., Weiss, I., 1999b. Flow behavior and globularization kinetics during hot working of Ti-6Al-4V with a colony alpha microstructure. *Materials Science and Engineering A* 263, 257.
- Shafaat, M.A., Omidvar, H., Fallah, B., 2011. Prediction of hot compression flow curves of Ti-6Al-4V alloy in $\alpha + \beta$ phase region. *Materials & Design* 32, 4689–4695.
- Swarnakar, A.K., der Biest, O.V., Baufeld, B., 2011. Thermal expansion and lattice parameters of shaped metal deposited Ti-6Al-4V. *Journal of Alloys and Compounds* 509, 2723–2728.
- Thomas, R.B., Nicolaou, P.D., Semiatin, S.L., 2005. An Experimental and Theoretical Investigation of the Effect of Local Colony Orientations and Misorientation on Cavitation during Hot Working of Ti-6Al-4V. *Metallurgical and Materials Transactions A* 36A, 129.
- Wachtman, J.B., Tefft, W.E., Lam, D.G., Apstein, C.S., 1961. Exponential Temperature Dependence of Young's Modulus for Several Oxides. *Phys. Rev.* 122, 1754–1759.
- Williams, J.C., Lutjering, G., 2003. *Titanium*. Springer - Verlag.

